Magnetized accretion disks around compact objects

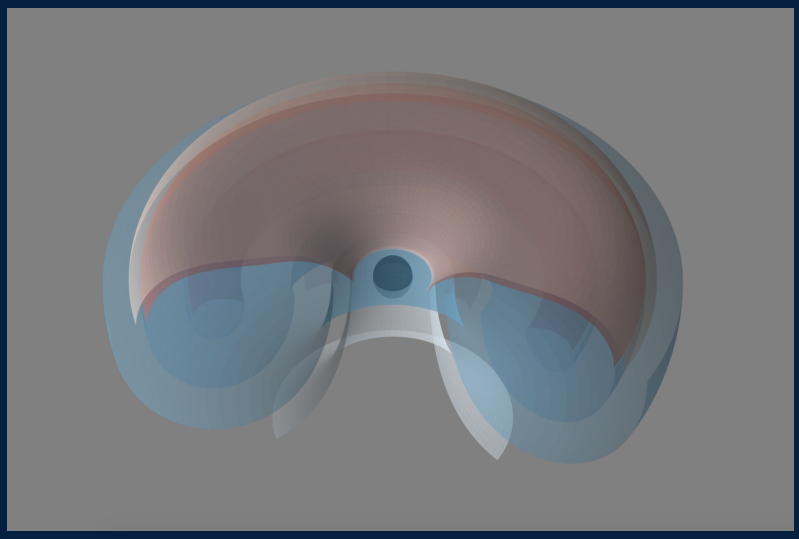

Sergio Gimeno Soler

Director:

José Antonio Font Roda

Doctorat en Física

Departament d'Astronomia i Astrofísica

Universitat de València

TESIS DOCTORAL

Septiembre 2021

VNIVERSITAT DE VALÈNCIA

Magnetized accretion disks around compact objects

Sergio Gimeno Soler

Doctorat en Física
Departament d'Astronomia i Astrofísica
Universitat de València

TESIS DOCTORAL

Director:
José Antonio Font Roda

Septiembre 2021

DECLARACIÓN

Dr. JOSÉ ANTONIO FONT RODA, Catedrático de Astronomía y Astrofísica de la Universitat de València

CERTIFICA:

Que la presente memoria, titulada *Magnetized accretion disks around compact objects*, ha sido realizada bajo su dirección en el Departamento de Astronomía y Astrofísica de la Universitat de València por Sergio Gimeno Soler y constituye su tesis doctoral para optar al título de Doctor por la Universitat de València una vez cursados los estudios en el Doctorado en Física.

Y para que así conste, en cumplimiento de la legislación vigente, firmo el presente certificado en Valencia, a 28 de septiembre de 2021.

JOSE ANTONIO| FONT|RODA

Firmado digitalmente por JOSE ANTONIO| FONT|RODA
Fecha: 2021.12.02 21:27:47 -08'00'

Fdo: José Antonio Font Roda

A mis padres y a mi hermana Laura.
A Paloma.

Acknowledgements

Esta tesis doctoral no habría sido posible sin el apoyo y consejo de muchas personas.

En primer lugar, quiero agradecer a mi director Prof. Toni Font por su guía y apoyo durante estos años. Sus consejos y su comprensión durante este periodo trabajando juntos que empezó con el Trabajo Final de Grado, han sido sin duda imprescindibles para la realización de este trabajo. Además de proponer ideas y presentarme a colaboradores, siempre me ha permitido investigar en las direcciones que me han parecido interesantes. Aunque ahora se termina mi etapa de estudiante, siento que todavía tengo mucho que aprender de él.

Likewise, I want to thank Prof. Carlos Herdeiro and Prof. Eugen Radu for introducing me to the world of self-gravitating bosonic fields (in the form of both bosonic stars and black holes with synchronized bosonic hair) which has become a core part of my research and in particular of this thesis.

I would like to thank Prof. Patryk Mach, Dr. Alejandro Cruz-Osorio and Dr. Sayantani Lahiri for letting me be a part of the different works we co-authored. It has been a real pleasure to work with all of you and I hope that we can keep collaborating in the future.

También a todo el Departamento de Astronomía y Astrofísica, en especial a José María Ibáñez, que me dió a conocer la existencia de la magnetohidronámica en relatividad general cuando solo era un estudiante de 1º de licenciatura y, años más tarde fue quien me presentó a Toni. También a Juan Antonio Morales, por conseguir que me enamorara otra vez de la relatividad general durante sus clases del máster. No me puedo olvidar tampoco de Manel y Feli, los cuales me han ayudado mucho con los problemas burocráticos desde el principio.

A mis compañeros y amigos del departamento (y de fuera de él), Nico, Álex, Adri, Isa, Tomek, Jens, Joan, Fabrizio, Pancho, Rebecca, Alejandro Mus, David, Miquel Miravet, Davide y especialmente a mis compañeros de despacho, Héctor, Alejandro Cruz, Jose y Miquel Llorens por los desayunos con tomate, los menús

de Farmacia, las pizzetas, los billares, el buen ambiente que hemos tenido todos estos años y muchas más cosas.

A mis amigos de la carrera Héctor, Adrián y Javi por su amistad durante todos estos años, las interesantísimas conversaciones y también, por qué no decirlo, las chorradas. También al resto de mis amigos, en especial al *Costureig* (Cris, Emmanuel y Lari), a David H. y a Alejandro N. por todas las cosas que hemos hecho juntos.

Por supuesto, a toda mi familia y en particular a mis padres y a mi hermana Laura por su apoyo, su comprensión y su cariño incondicional. Si he podido realizar esta tesis, es sin duda gracias a ellos.

Por último quiero darle las gracias a Paloma. Por su paciencia, por estar ahí tanto en los buenos momentos como en los malos, por querer lo mejor para mí y saber qué necesito cuando ni siquiera yo mismo lo sé y, en definitiva, por quererme y apoyarme. También quiero dar las gracias a su familia (Ramón, Silvia, Rosana...) por su cariño y por hacerme sentir parte de la familia.

Abstract

The recent observational breakthroughs accomplished by the LIGO-Virgo-KAGRA Collaboration – with the historical first detections of gravitational waves from mergers of compact binaries – and by the Event Horizon Telescope Collaboration – with the image of the supermassive black hole lurking in the centre of the M87 galaxy – have provided an unprecedented opportunity to investigate the physics of strong gravity and to even test Einstein's General Theory of Relativity in such a extreme situation. This thesis discusses one particular relativistic astrophysical system which is often invoked as a paradigmatic example of such strong-gravity realm – a black hole surrounded by a geometrically thick accretion disk (or torus). New prescriptions to build initial data of magnetized accretion disks around compact objects are presented, extending the current state-of-the-art in several directions, namely accommodating diverse magnetic field configurations, angular momentum distributions, and types of spacetimes (including Kerr black holes, black holes with scalar hair, and Yukawa black holes) where the fluid evolves. The results reported in this thesis provide insight on the effects that adding different physics has in the system's morphological and physical properties. In addition, this research offers large new samples of open-source initial data to conduct time-dependent general-relativistic, magneto-hydrodynamical simulations of black hole-torus systems.

Resumen

Los recientes avances observacionales logrados por la colaboración LIGO-Virgo-KAGRA – con las primeras detecciones históricas de ondas gravitacionales de fusiones de sistemas binarios de objetos compactos – junto con la colaboración *Event Horizon Telescope* - con la imagen del agujero negro supermasivo que reside en el centro de la galaxia M87 - han brindado una oportunidad sin precedentes para investigar la física de la gravedad en el regimen de campo intenso e incluso analizar la Teoría General de la Relatividad de Einstein en esta situación tan extrema. En esta tesis se discute un caso particular de sistema astrofísico relativista que suele considerarse como el ejemplo paradigmático de sistema en el régimen de campo intenso – un agujero negro rodeado de un disco grueso de acreción (o toro). Se presentan nuevas prescripciones para construir datos iniciales de discos de acreción magnetizados alrededor de objetos compactos, extendiendo el estado actual del tema en varias direcciones, a saber, acomodando diferentes configuraciones de campo magnético, distribuciones de momento angular, y tipos de espacio-tiempo (incluyendo agujeros negros de Kerr, agujeros negros con pelo escalar y agujeros negros de Yukawa) sobre los que evoluciona el fluido. Los resultados obtenidos en esta tesis nos proporcionan valiosa información sobre los efectos que tiene añadir diferentes fenómenos físicos en las propiedades morfológicas y físicas del sistema. Además, los resultados de esta investigación también proporcionan una amplia muestra de datos iniciales de dominio público para que puedan ser usados en simulaciones evolutivas del sistema toro de acreción-agujero negro, gobernado por las ecuaciones de la magnetohidrodinámica relativista .

Introducción

Motivación

El sistema compuesto por un objeto compacto rodeado de materia es omnipresente en astrofísica, ya que aparece en un rango de masas muy grande, desde masas comparables a la masa del Sol que se pueden encontrar en binarias de rayos X o fusiones de binarias de objetos compactos, hasta miles de millones de masas solares que se pueden encontrar en el centro de las galaxias. En el caso más que probable de que la materia posea momento angular, la acreción de materia sobre el objeto compacto tendrá lugar a través de un disco (o un toro). Para describir la física de estos sistemas, y ya que estamos tratando con objetos compactos (es decir, $M/R \sim 1$, donde M es la masa del objeto y R su radio) y campos de materia que se mueven en su cercanía, tenemos que emplear la teoría de la gravedad más avanzada y que mejor ha superado los test observacionales a nuestra disposición, es decir, la teoría de la relatividad general de Einstein (GR, por sus siglas en inglés, *general relativity*) [Einstein 1915]. Desde un punto de vista macroscópico, podemos considerar que los campos de materia se comportan como un fluido y si además consideramos que, potencialmente, puede haber presencia de campos magneticos, llegamos al marco teórico que vamos a utilizar a lo largo de toda esta tesis: la magnetohidrodinámica en relatividad general (GRMHD por sus siglas en inglés, *general relativistic magnetohydrodynamics*), que determina la dinámica de un fluido magnetizado junto con las ecuaciones del campo gravitatorio de la relatividad general.

Desde hace unos años estamos siendo testigos de una era muy interesante para la física de los fluidos en acreción sobre objetos compactos en el régimen de gravedad intensa. Recientes avances observacionales han brindado una oportunidad sin precedentes para investigar la física de la gravedad intensa en diferentes contextos físicos y rangos de masa. Por un lado, las observaciones de la colaboración *Event Horizon Telescope* (EHT) de las proximidades del objeto

compacto supermasivo situado en el núcleo de la galaxia M87, con la capacidad de resolver la sombra creada por el objeto central cuando su disco de acreción actúa como fuente de luz [Event Horizon Telescope Collaboration et al. 2019a, Event Horizon Telescope Collaboration et al. 2019c], ha proporcionado información muy útil sobre la gravedad en el régimen de campo intenso. A saber, el patrón de lente gravitacional (la curvatura de los rayos de luz) creado por el objeto compacto proporciona información sobre la estructura de las geodésicas nulas (el camino seguido por los fotones) en la región del espacio-tiempo en las cercanías del objeto central. El flujo de energía medido por la red de radiotelescopios proporciona información sobre las propiedades morfológicas y físicas (como la temperatura, la densidad, la tasa de acreción y el campo magnético, a través de medidas de polarimetría) del disco de acreción que se infieren a partir de las observaciones utilizando simulaciones por ordenador del fluido que está acretando alrededor del objeto compacto. Los resultados de las observaciones del EHT son compatibles con lo que esperaríamos de un disco de acreción magnetizado caliente de baja densidad compuesto de materia ordinaria (en una configuración comúnmente conocida como *Magnetically Arrested Disk* (MAD)[1] [Narayan, Igumenshchev, and Abramowicz 2003, Igumenshchev, Narayan, and Abramowicz 2003]) alrededor de un agujero negro de Kerr supermasivo ($M = 6.5 \times 10^9 M_\odot$) (es decir, una solución de vacío estacionaria y axisimétrica de las ecuaciones de campo de Einstein de la relatividad general que describen un agujero negro con masa y momento angular distintos de cero [Kerr 1963]). Es un hecho ampliamente aceptado que la solución de Kerr es la que describe todos los agujeros negros astrofísicos aislados (por lo tanto, es una solución de vacío), una afirmación comúnmente conocida como la "hipótesis de Kerr". Esta hipótesis está respaldada por los teoremas de unicidad de los agujeros negros (ver Chruściel, Costa, and Heusler [2012] para un artículo de revisión sobre este tema) y por la conjetura de no-pelo [Bekenstein 1995]. Los próximos resultados observacionales de la colaboración EHT de la radio-fuente compacta SgrA* ubicada en el centro de nuestra propia galaxia, proporcionarán nuevos datos sobre la naturaleza del objeto compacto oscuro y de la materia en acreción a su alrededor. El hecho de que la masa de SgrA* sea alrededor de tres órdenes de magnitud menor que la masa de M87* permitirá comparar la observación del mismo fenómeno (un disco de acreción alrededor de un objeto compacto oscuro supermasivo) en una escala de masa diferente.

[1] El régimen MAD en un disco de acreción se logra cuando se acumula un campo magnético poloidal intenso cerca del agujero negro, lo que provoca una interrupción del flujo de acreción hasta un cierto radio. Dentro de ese radio, la materia cae a una velocidad lenta como pequeñas gotas independientes. Este tipo de acreción es energéticamente muy eficiente.

Además, las observaciones de la estrella S2 que orbita alrededor de SgrA* [Do et al. 2019, Gravity Collaboration et al. 2019] aportan información sobre la distribución de la materia que es barrida a lo largo su órbita, restringiendo así las propiedades del espacio-tiempo en una región que está lo suficientemente cerca del objeto central como para que los efectos de la relatividad general se noten a lo largo de la órbita, pero lo suficientemente lejos del objeto central como para que no se puedan sondear los efectos debidos a la gravedad intensa en la zona cercana al objeto compacto (el periápside de la órbita de S2 está a unas 150 UA del objeto central, es decir, $\sim 2800\, r_g$, donde r_g es el radio gravitacional del objeto[2] [Gravity Collaboration et al. 2020]). Estos resultados son compatibles con la presencia de un objeto compacto supermasivo con una masa de $\sim 4 \times 10^6 M_\odot$ consistente con un agujero negro tal y como lo describe la relatividad general. Además, hay indicios observacionales que sugieren que no hay una masa extendida con más de $\sim 0.1\%$ de la masa central en el interior de la órbita de S2.

Asimismo, para objetos compactos menos masivos (es decir, objetos con masas del rango estelar $\sim 1M_\odot - 100M_\odot$) el estudio del régimen de campo gravitatorio intenso ha sido posible recientemente a través de las innovadoras observaciones de ondas gravitacionales (GWs, del inglés *gravitational waves*) de fusión de binarias de objetos compactos realizadas por la red de detectores de ondas gravitacionales *Advanced LIGO*, *Advanced Virgo* y KAGRA (LVK) [Abbott et al. 2019, Abbott et al. 2020b, Abbott et al. 2021a]. La mayoría de las detecciones de LVK están asociadas a *sucesos puramente de vacío*, es decir, fusiones de binarias de agujeros negros (BBH, del inglés *binary black holes*), pero también se han observado un par de coalescencias de sistemas de binarias mixtas (que comprenden una estrella de neutrones y un agujero negro; BHNS) y varias fusiones de binarias de estrellas de neutrones (BNS, del inglés *binary neutron stars*). En particular, el evento de fusión de BNS GW170817 merece una mención especial, ya que no solo fue la primera observación de ondas gravitacionales de una fusión de BNS, sino que también estuvo acompañado de radiación electromagnética que fue observada por docenas de telescopios en todo el mundo y dio lugar al nacimiento del campo de la Astronomía Multimensajero [Abbott et al. 2017]. En esta tesis estamos más interesados en las fusiones de binarias compactas que implican campos de materia, es decir, las fusiones de BNS y BHNS (junto con las supernovas asociadas al colapso de su núcleo que aún no se han observado en ondas gravitacionales). En todos estos casos, el resultado más probable del

[2] $r_g = GM/c^2$, donde G es la constante de la gravitación de Newton y c es la velocidad de la luz.

evento de fusión es un objeto compacto (ya sea un agujero negro o una estrella de neutrones) rodeado de materia. Estos eventos son también excelentes candidatos para detecciones multimensajero, tanto en el espectro electromagnético como en neutrinos, ya que estos sistemas están asociados a los fenómenos astrofísicos conocidos como estallidos de rayos gamma (GRBs, del inglés *Gamma-ray bursts*). En particular, los GRBs cortos ($t \sim 0.2$s) se asocian con fusiones de BNS y/o BHNS mientras que los GRBs largos ($t \sim 20$s) con el colapso gravitacional de estrellas masivas (ver Berger [2014] para un artículo de revisión). La naturaleza de los eventos de fusión de binarias de objetos compactos y sus parámetros físicos se infieren a partir de las señales de ondas gravitacionales, comparando los datos con plantillas de ondas obtenidas utilizando la relatividad general para la señal de *Inspiral-Merger-Ringdown*. Al igual que las observaciones de la Colaboración EHT y de las orbitas de estrellas alrededor del centro galáctico, las observaciones de la colaboración LVK proporcionan fuertes indicios que apoyan la validez de la relatividad general en el régimen de campo intenso, así como la hipótesis de Kerr.

Por lo tanto, los indicios observacionales actualmente disponibles apuntan hacia una confirmación de la relatividad general, la hipótesis de Kerr y, en el caso particular de los objetos compactos supermasivos, el modelo MAD de disco de acreción. Sin embargo, a pesar de los avances recientes logrados en el ámbito observacional, hay preguntas que siguen sin respuesta y también nuevas preguntas que uno podría plantearse a la luz de las nuevas observaciones. Enumeramos aquí algunas de las más relevantes para esta tesis.

- *¿Sirve la sombra del agujero negro para investigar la geometría del horizonte de sucesos?* Una pregunta natural que surge cuando se estudian las sombras es si la observación desde el infinito (lejos de la fuente) de la sombra producida por un agujero negro puede dar información sobre la estructura del horizonte de sucesos, y servir así como test de la hipótesis de Kerr. Desgraciadamente, la respuesta a esta pregunta es negativa: hay algunos contraejemplos presentes en la bibliografía que muestran que diferentes objetos pueden proyectar la misma sombra que un agujero negro. Por ejemplo, en Junior et al. [2021] los autores construyen soluciones que son degeneradas tanto con la geometría de Schwarzschild como con la de Kerr, En Herdeiro et al. [2021] se muestra que bajo ciertas condiciones de observación, un tipo de objeto compacto exótico oscuro conocido como estrella de Proca (PS) (una solución solitónica autogravitante de las ecuaciones de campo de Einstein acopladas con un campo vectorial masivo) puede imitar la sombra de Schwarzschild. A pesar de estos contraejemplos,

cabe destacar que aún se desconoce si simulaciones numéricas GRMHD de discos de acreción en dichos espacio-tiempos podrá ayudar a romper esta degeneración o no (véase Olivares et al. [2020] para un ejemplo en el que la sombra producida por una estrella de bosones no rotante puede distinguirse de la producida por un agujero negro). También debemos mencionar el trabajo de Gralla [2021] en el que el autor plantea algunas dudas sobre la capacidad de las observaciones del EHT para estudiar la geometría del espacio-tiempo.

- *¿Pueden dos discos diferentes proyectar la misma sombra?*: En un sistema agujero negro - toro de acreción, la parte del fluido es la más compleja de describir debido a la física implicada y a la falta de un conocimiento completo. Desde el punto de vista de la física, sabemos que un tratamiento realista debe incluir campos magnéticos, viscosidad, transporte radiativo y de neutrinos, una ecuación de estado (EOS) realista para el fluido, etc. Sin embargo, actualmente es imposible considerar todos estos efectos en las simulaciones GRMHD, ya que es inviable desde el punto de vista del coste computacional. El enfoque que se suele adoptar es el de descartar algunos de los procesos considerados como menos relevantes y simplificar otros (por ejemplo, no considerándolos durante la evolución, sino en una etapa de post-procesado). Este es el caso de los cálculos de transporte radiativo realizados por la colaboración EHT para obtener las imágenes sintéticas de las sombras. Además, existe otra fuente de incertidumbre al respecto, ya que aún se desconoce hasta qué punto la forma de prescribir los datos iniciales de una simulación GRMHD afecta a la evolución temporal y a su resultado. También hay muchos parámetros libres a tener en cuenta cuando se construyen los datos iniciales de un disco de acreción magnetizado, a saber, la EOS, la intensidad, topología y modo de prescribir la forma exacta del campo magnético, la ley de rotación del plasma y las ubicaciones de los radios interior y exterior del disco, entre otros. Es muy importante evaluar el impacto de los datos iniciales en la evolución porque una fuerte dependencia de los datos iniciales podría llevar a resultados poco realistas. En consecuencia, parece probable la existencia de posibles degeneraciones en el proceso de estimación de los parámetros físicos de un disco de acreción a través de la observación de su sombra. La simulación de una mayor cantidad de modelos de discos diferentes y futuras campañas de observación podrían ayudar a romper algunas de esas degeneraciones.

- *¿Todos las ondas gravitacionales de LIGO/Virgo son producidos por agujeros negros (BHs) y estrellas de neutrones (NSs) canónicos?* Si bien es cierto que las señales de ondas gravitacionales observadas por la colaboración LVK ponen fuertes restricciones sobre algunos de los efectos que deberían estar presentes en algunas teorías alternativas de la gravedad (desviaciones de la velocidad de propagación de las ondas gravitacionales, modos longitudinales de propagación, etc) [Abbott et al. 2021b], también es cierto que la cuestión de la degeneración también está presente aquí, al menos hasta cierto punto. El hecho de que los catálogos de formas de onda gravitacional para las búsquedas con filtro de coincidencia sean limitados (y en su mayoría restringidos a fusiones con órbitas cuasi-circulares) puede afectar a nuestra capacidad de inferir correctamente los parámetros físicos de algunos eventos. Esto es particularmente cierto para el reciente evento GW190521 [Abbott et al. 2020a], el evento más masivo anunciado por la colaboración LVK hasta hoy, con una masa total de $\sim 150M_{\odot}$, dentro del ámbito de los agujeros negros de masa intermedia. La fuente de GW190521 se identifica como una fusión de BBHs con al menos uno de los agujeros negros componentes con una masa $M > 65M_{\odot}$ que es mayor que la masa máxima que los modelos de supernova permiten para que una estrella masiva colapse en un agujero negro (debido a la llamada inestabilidad de pares). En la literatura han aparecido explicaciones alternativas a este suceso; por ejemplo, en Calderón Bustillo et al. [2021b] se muestra que esta señal es compatible con la fusión de dos PS con un campo vectorial ultraligero de masa $\mu_V = 8,7 \times 10^{-13}$ eV, siendo la masa total del sistema mayor que la estimada para los BBH, $\sim 230M_{\odot}$. También observamos que Calderón Bustillo et al. [2021a] señalan que la inferencia estándar de parámetros puede confundir eventos por debajo (por encima) del umbral de inestabilidad de pares si la fusión es altamente excéntrica en lugar de cuasi-circular. Una mayor investigación sobre las aproximaciones de la forma de onda para las binarias no cuasi-circulares ayudará a mitigar las incertidumbres en la interpretación de futuros eventos similares a GW190521 que podrían detectarse en las próximas campañas de observación de la colaboración LVK.

- *¿Son los agujeros negros iguales en todo el rango de masas?*: Si nos limitamos a los agujeros negros de Kerr aislados, estos son objetos bastante simples y una de sus propiedades definitorias es que escalan con su masa, es decir, los agujeros negros parecen iguales en todas las escalas de masa. Sin embargo, la introducción de campos de materia cambia esta situación.

Si consideramos la existencia potencial de campos fundamentales bosónicos masivos oscuros (tanto escalares como vectoriales), podemos ver que, si el parámetro de masa μ del campo es lo suficientemente pequeño (es decir, su longitud de onda, $\sim \mu^{-1}$, es lo suficientemente grande) el campo puede extraer energía del agujero negro en un proceso análogo al proceso de Penrose, llamado *inestabilidad superradiante* [Starobinsky 1973]. A través de este proceso, los agujeros negros de Kerr pueden perder momento angular y sincronizarse con el campo (es decir, la frecuencia del campo ω es igual a la velocidad angular del horizonte de sucesos $\Omega_{\rm H}$) y formar un estado ligado de un agujero negro de Kerr con pelo bosónico llamado *agujero negro con pelo* (HBH, del inglés *hairy black hole*) [Herdeiro and Radu 2014b]. Esta situación elude el llamado teorema de no pelo [Israel 1967, Carter 1971]. El crecimiento no lineal y la saturación de la inestabilidad superradiante se ha demostrado en las simulaciones de relatividad numérica de East, Ramazanoğlu, and Pretorius [2014], East and Pretorius [2017], and East [2017]. Este tipo de estados ligados también puede formarse por fusiones de estrellas bosónicas [Sanchis-Gual et al. 2020] que a su vez pueden formarse a través del colapso de una nube de materia bosónica [Di Giovanni et al. 2018] (para una discusión sobre la estabilidad no lineal de estas estrellas ver Sanchis-Gual et al. [2019] and Di Giovanni et al. [2020]). El punto clave a notar aquí es que dependiendo del parámetro de masa del campo bosónico, es posible que haya HBHs y estrellas bosónicas en una escala de masa particular y no en otra. Estos campos bosónicos suelen estar asociados a extensiones del modelo estándar de la física de partículas [Freitas et al. 2021] o del *axiverso* de la teoría de cuerdas [Arvanitaki et al. 2010] y han sido propuestos en Cosmología como candidatos a materia oscura. También vale la pena mencionar, por la relevancia para esta tesis, que las propiedades físicas de los discos de acreción alrededor de los agujeros negros a diferentes escalas de masa son también muy diferentes. Por ejemplo, las densidades de un disco formado a partir de una fusión BNS y las de un disco alrededor de un agujero negro supermasivo están a muchos órdenes de magnitud de distancia, por lo que pueden considerarse como fluidos muy diferentes. Si el disco es suficientemente masivo, puede incluso afectar a la geometría del agujero negro (véase Mach et al. [2019] and Kulczycki, Mach, and Malec [2021]).

De la discusión anterior se desprende que la mayoría de las cuestiones abiertas están relacionadas con las degeneraciones intrínsecas que existen cuando se intenta inferir parámetros físicos de objetos compactos oscuros a partir de datos

observacionales. Los futuros desarrollos, ya sean teóricos, computacionales (recursos computacionales más potentes) y observacionales, como el *Next Generation EHT* (ngEHT), la *Laser Interferometer Space Antenna* (LISA), el aumento de la red de detectores de GW de segunda generación (con la incorporación de KAGRA y LIGO-India) o los interferómetros de GW de tercera generación *Einstein Telescope* y *Cosmic Explorer* ayudarán a romper algunas de las degeneraciones actuales.

Esta tesis aborda el estudio teórico de sistemas de agujeros negros-toro de acreción en relatividad general, aumentando el conocimiento actual del campo. En esta tesis, me he centrado en construir soluciones de equilibrio (independientes del tiempo) de discos gruesos de acreción magnetizados alrededor de diferentes tipos de objetos compactos, cambiando tanto los ingredientes físicos presentes en los discos como la naturaleza del objeto compacto central. El objetivo de este trabajo es doble: en primer lugar, obtener información sobre los efectos que la consideración de física adicional tiene en las propiedades morfológicas y físicas del sistema, y en segundo lugar, proporcionar un gran volumen de datos iniciales de código abierto para realizar simulaciones GRMHD dependientes del tiempo de sistemas agujero negro-toro de acreción.

Antes de discutir en la siguiente sección las investigaciones específicas que componen este trabajo, vale la pena dedicar unas palabras a explorar el significado del término "equilibrio" al principio del párrafo anterior. Es muy importante distinguir entre los términos "equilibrio", el cual sólo significa que la solución es independiente del tiempo, y "estable", que significa que la solución es un atractor dinámico del sistema bajo posibles perturbaciones que puedan aparecer durante una evolución temporal. Nuestros modelos de equilibrio no son, pues, necesariamente estables y, en particular, pueden ser inestables bajo un conjunto conocido de inestabilidades del disco, a saber:

- *Inestabilidad runaway (RI)*: Esta inestabilidad dinámica puede ocurrir en un sistema formado por un toro de acreción que llena su lóbulo de Roche[3] alrededor de un agujero negro. Cuando la masa cae en el agujero negro a través del punto de Lagrange L_1, la masa del mismo aumenta, lo que hace que el punto L_1 se adentre más en el toroide, llegando a ser acretado por completo. Este proceso es muy rápido y puede destruir el disco en una escala de tiempo dinámica (sólo unos milisegundos para un agujero negro de masa estelar), lo que supone una amenaza para los sistemas agujero

[3]El lóbulo de Roche de un cuerpo en un sistema binario se define como la región del espacio dentro de la materia en órbita que está gravitatoriamente ligada a dicho cuerpo.

negro-toro como progenitores de GRBs cortos. La RI fue descubierta por primera vez por Abramowicz, Calvani, and Nobili [1983]. Las simulaciones numéricas en relatividad general (despreciando la autogravedad del disco) que se realizaron en Font and Daigne [2002] y Daigne and Font [2004] demostraron que efectivamente la inestabilidad se produce para discos de momento angular específico constante, $l = -u_\phi/u_t$, donde u_ϕ y u_t son las componentes azimutal y temporal de la 4-velocidad, pero se suprime si la distribución del momento angular no es constante (por ejemplo, una ley de potencia). Estudios posteriores mostraron que la consideración de la autogravedad no era determinante para la aparición de la RI: las simulaciones axisimétricas realizadas por Montero, Font, and Shibata [2010] indicaron que para discos con momento angular constante y no constante la RI estaba suprimida. Asimismo, la RI no aparece (en una escala de tiempo dinámica) en los sistemas BH-toro de acreción producidos tras la fusión de estrellas de neutrones de masa desigual [Rezzolla et al. 2010] ni en simulaciones tridimensionales de discos de momento angular constante en un espacio-tiempo completamente dinámico [Korobkin et al. 2011]. Sin embargo, en Korobkin et al. [2013] la RI sí aparece en simulaciones que utilizan una configuración similar a la empleada por Korobkin et al. [2011] pero con condiciones más favorables (un valor menor para el momento angular específico l). En conclusión, una condición suficiente para la aparición de la RI en una escala de tiempo dinámica requiere que el toro esté cerca de llenar su lóbulo de Roche y que obedezca a una distribución de momento angular constante suficientemente pequeña (el valor del momento angular específico debe permitir la existencia de discos estacionarios que llenen el lóbulo de Roche). Observamos que estas condiciones favorables no parecen darse en el contexto de las fusiones de BNS, como puede verse en Rezzolla et al. [2010] y Most et al. [2021].

- *Inestabilidad de Papaloizou-Pringle (PPI)*: Descubierta por Papaloizou and Pringle [1984], la PPI es una inestabilidad dinámica no axisimétrica que fragmenta el toro en m sobredensidades o "planetas" (para un modo de orden m) y sirve como mecanismo para transportar momento angular a las regiones exteriores del disco. Esta inestabilidad se manifiesta de manera más fuerte en los discos delgados, pero también puede estar presente en los discos gruesos, en particular en los discos de momento angular constante [Blaes 1987, Hawley 1991]. El mecanismo de generación de la PPI es la propagación de ondas asociadas con un cierto modo m y con la presencia de un radio de corotación relacionado con dicho modo

(que también define una región prohibida para la propagación de ondas) [Goldreich, Goodman, and Narayan 1986]. Estos modos se amplifican por la interacción a través de la región prohibida y por la reflexión de las ondas en los bordes interiores y exteriores del disco. Por lo tanto, el desencadenamiento de la acreción (es decir, la eliminación del borde interior del disco) satura la PPI a bajas amplitudes o incluso impide por completo su crecimiento [Blaes 1987, Hawley 1991, De Villiers and Hawley 2002]. Además, la asimetría persistente que la PPI puede inducir en un disco grueso puede desencadenar la emisión de ondas gravitacionales, como demostraron por primera vez Kiuchi et al. [2011] (véase también Mewes et al. [2016] para una discusión relacionada en el contexto de los discos de acreción inclinados). El modo más rápido de la PPI puede competir con la RI si esta última se suprime lo suficiente como para retrasar su aparición, de modo que la PPI tenga tiempo de establecerse. Esto puede desencadenar interacciones no lineales entre las dos inestabilidades. Por ejemplo, la PPI tiene el potencial de redistribuir el momento angular y eso podría suprimir el crecimiento de la RI (como mencionamos anteriormente) [Korobkin et al. 2011]. También merece la pena mencionar la notable similitud entre la PPI y la inestabilidad en forma de barra que aparece en el contexto de las estrellas de neutrones en rotación y las estrellas de bosones [Cerdá-Durán, Quilis, and Font 2007, Baiotti et al. 2007, Di Giovanni et al. 2020], que también presenta el radio de corotación, el transporte de momento angular a las regiones exteriores y una similitud morfológica con el modo $m = 2$ (nótese que el modo $m = 1$ está prohibido para estos objetos).

- *Inestabilidad Magnetorotacional (MRI)*: Originalmente descubierta por Chandrasekhar [1960] y posteriormente redescubierta por Balbus and Hawley [1991], la MRI aparece en dos situaciones diferentes: una inestabilidad axisimétrica producida por un campo magnético poloidal y una inestabilidad no axisimétrica que se desencadena por la presencia de un campo magnético toroidal [Balbus and Hawley 1992]. La turbulencia introducida por esta inestabilidad sirve como mecanismo para transportar y redistribuir el momento angular y desencadenar la acreción. En particular, un disco de momento angular constante puede redistribuir su momento angular hasta volverse casi kepleriano (véase por ejemplo Bugli et al. [2018]) y un campo magnético puede amplificarse o reducirse dependiendo de su intensidad inicial [Fragile and Sądowski 2017] (véase también Wielgus et al. [2015], McKinney and Blandford [2009], and Fragile et al. [2007]). También es relevante señalar que la MRI puede interactuar con la PPI,

ya que la escala de tiempo de crecimiento de los modos más rápidos de ambas inestabilidades son similares, como muestra Bugli et al. [2018] que encontró que la PPI se suprime en su mayor parte en presencia de un campo magnético (toroidal) en simulaciones GRMHD tridimensionales, incluso cuando las condiciones para su crecimiento son favorables (valor pequeño del momento angular constante).

De los párrafos anteriores se desprende que llevar a cabo estudios posteriores de la (in)estabilidad de los modelos de disco presentados en esta tesis como datos iniciales, es un tema relevante a seguir. Algunos de los procesos astrofísicos que hay que modelar requieren que el disco viva durante un tiempo suficientemente largo (por ejemplo, aquellos que actúan como fuente de luz de las sombras observadas por el EHT) mientras que, por otro lado, para desencadenar la acreción sobre el agujero negro central se requiere que el disco esté en un estado inestable (de hecho, los datos iniciales empleados en las simulaciones numéricas de la colaboración EHT están construidos para ser inestables bajo la MRI). Por lo tanto, el estudio de las posibles inestabilidades que pueden afectar a los modelos de equilibrio de discos gruesos presentados en esta tesis es muy relevante para comprobar su viabilidad como datos iniciales para evoluciones no lineales.

Discos de acreción gruesos magnetizados: soluciones de equilibrio

Como se ha dicho anteriormente, esta tesis se centra principalmente en la construcción y discusión de soluciones de equilibrio de discos de acreción gruesos magnetizados alrededor de objetos compactos. En particular, los discos que aquí se presentan pertenecen a la clase de discos comúnmente conocidos como *Donuts polacos* dotados de un campo magnético toroidal. El modelo del donut polaco fue desarrollado por Abramowicz, Jaroszynski, and Sikora [1978], Kozlowski, Jaroszynski, and Abramowicz [1978], Jaroszynski, Abramowicz, and Paczynski [1980], and Paczyńsky and Wiita [1980]. En su forma original un disco de este tipo consistía en una solución estacionaria y axisimétrica de las ecuaciones de conservación de energía-momento $\nabla_\mu T^{\mu\nu} = 0$ cuando $T^{\mu\nu}$ es el tensor de energía-momento de un fluido perfecto barotrópico ($p = p(\rho)$) no autogravitante moviéndose sobre la métrica de Kerr y dada una distribución constante del momento angular específico $l = -u_\phi/u_t$. Es importante señalar que existen otras definiciones posibles del momento angular específico. Por ejemplo, el momento angular específico también se indica como $j = u^t u_\phi$ y si se toma

$j =$ constante también se obtienen discos gruesos (véase por ejemplo Fishbone and Moncrief [1976]). Sin embargo, l y j están relacionados de forma sencilla, a saber, $j = \frac{l}{1-\Omega l}$, por lo que es fácil trasladar una elección particular de j a un formalismo que utilice l.

Este formalismo se ha extendido para considerar discos con momento angular específico no constante (véase, por ejemplo, Daigne and Font [2004] and Qian et al. [2009]). Hay que señalar que para discos con momento angular no constante, la integración de las ecuaciones de movimiento requiere una condición extra en la distribución de la velocidad angular (que se satisface automáticamente para discos de l constante) que es $\Omega = \Omega(l)$, es decir, las superficies de velocidad angular constante deben coincidir con las de momento angular constante. Esta condición, conocida como la versión del teorema de von Zeipel en relatividad general [von Zeipel 1924, Abramowicz 1971], se cumple si el fluido es barotrópico ($p = p(\rho)$). Puede verse que, dada una distribución concreta del momento angular en el plano ecuatorial del agujero negro, la condición $\Omega = \Omega(l)$ da lugar a una familia de superficies cilíndricas (conocidas como cilindros de von Zeipel) a lo largo de las cuales Ω y l son constantes (un ejemplo de los cilindros de von Zeipel en el espacio-tiempo de Kerr puede verse en Daigne and Font [2004]). Además, considerar una distribución (radial) no constante de l es clave para ajustar las características geométricas del toro de acreción, como la extensión radial y la altura. Por último, tener en cuenta el momento angular no constante también es necesario para poder acomodar discos con $j =$ constante, ya que es evidente que si j es constante l debe ser no constante.

La extensión más relevante del modelo del *donut polaco* para el trabajo desarrollado en esta tesis es la solución de Komissarov [Komissarov 2006], donde el toro se acopla a un campo magnético puramente toroidal y las ecuaciones a resolver son las de la GRMHD ideal. Esta solución es particularmente interesante ya que es una solución analítica de las ecuaciones de la GRMHD que es muy útil por varias razones: como dato inicial fácil de construir para los códigos de evolución no lineal (algunos ejemplos se presentan en Montero et al. [2007], Wielgus et al. [2015], Fragile and Sądowski [2017], and Bugli et al. [2018]), para probar la precisión de dichos códigos debido a su naturaleza analítica (ver por ejemplo Porth et al. [2017]) e incluso para calcular imágenes sintéticas del agujero negro cuando la luz es emitida por el disco de acreción (ver Vincent et al. [2015]). Para integrar las ecuaciones de movimiento para el caso magnetizado, hay que tomar una suposición extra (además de la barotropicidad). La elección de Komissarov al respecto fue asumir una 'EOS politrópica' para la presión

magnética (que se define como $p_{\rm m} = b^2/2$), pero hay otras posibilidades, como demostró Zanotti and Pugliese [2015].

Por último, es relevante señalar que se espera que los discos gruesos magnetizados aparezcan en escenarios astrofísicos realistas, como el remanente de las fusiones de BNS o BHNS (véase, por ejemplo, Baiotti and Rezzolla [2017] y Most et al. [2021]). Por lo tanto, es muy importante construir, comprender y mejorar los modelos de equilibrio de discos de acreción gruesos magnetizados. De esta manera, si utilizamos datos iniciales suficientemente precisos, se puede estudiar la física de los sistemas disco+agujero negro sin necesidad de realizar las computacionalmente costosas simulaciones *ab initio* de su formación.

Configuraciones de fluido perfecto

Métrica de Kerr

Dado que el espacio-tiempo de Kerr es la métrica canónica de agujero negro en el marco de la relatividad general, es natural esperar que la mayoría de las extensiones de la solución de Komissarov se hayan estudiado para los agujeros negros de Kerr. En primer lugar, en Montero et al. [2007] los autores utilizaron una EOS para el fluido de la forma $p = K\rho^{\Gamma}$, en lugar de la presentada por Komissarov [2006], que es $p = Kw^{\Gamma}$ (donde w es la entalpía del fluido[4]). La consecuencia de esto es que la solución deja de ser analítica (la ecuación a resolver para obtener las distribuciones de presión y densidad pasa a ser trascendente) por lo que se requiere de métodos numéricos para resolverla. Wielgus et al. [2015] introdujo una distribución de momento angular no constante considerando que la velocidad angular es una ley de potencia del momento angular específico para estudiar la aparición de modos inestables bajo la MRI cuando un disco magnetizado está sometido a perturbaciones no axisimétricas. Más recientemente, en Pimentel, Lora-Clavijo, and Gonzalez [2018] se ha presentado una extensión de la solución de Komissarov para incluir la posibilidad de que la materia del disco tenga una susceptibilidad magnética no nula. Dicha solución permite que el disco esté polarizado magnéticamente.

En Gimeno-Soler and Font [2017] se incorporó a la solución de Komissarov la distribución de momento angular específico no constante propuesta por Qian et al. [2009]. En concreto, esta implementación del ansatz de momento angular específico propuesto en Qian et al. [2009] para este trabajo se corresponde a un modelo de dos parámetros (fijamos uno de los tres parámetros originales).

[4]La entalpía del fluido w se define como $w = \rho h$.

El ansatz en el plano ecuatorial consiste en una parte constante para $r \leq r_{\rm ms}$[5] y una ley de potencia para el momento angular $l(r) \propto l_{\rm K}(r)^{\beta}$ cuando $r > r_{\rm ms}$, donde β es un parámetro del modelo y $l_{\rm K}(r)$ es el momento angular kepleriano. El otro parámetro del ansatz controla el decrecimiento de l cuando $\theta \neq \pi/2$. Esta elección de parámetros es muy interesante porque permite modificar la morfología de los discos, ya que la modificación del valor del primer parámetro implica un cambio del espesor del disco y cambiar el valor del segundo implica una variación de su extensión radial, como se puede observar tanto en Qian et al. [2009] como en esta tesis. La libertad para ajustar la morfología del disco puede hacer que este tipo de soluciones sean útiles para ser utilizadas como datos iniciales en códigos de evolución para explorar cómo diferentes morfologías de disco pueden afectar a diferentes procesos físicos y al resultado de la simulación.

Para comprender mejor esta familia de soluciones de equilibrio, exploré una amplia región del espacio de parámetros de 4 dimensiones (dos parámetros para la distribución del momento angular específico, el parámetro de espín del agujero negro y la relación entre la presión magnética y la presión del fluido (en adelante, parámetro de magnetización)). Este estudio reveló algunas propiedades de las soluciones de equilibrio (i) el comportamiento cualitativo del disco ante cambios en los parámetros de momento angular o de magnetización es independiente del parámetro de espín del agujero negro; (ii) la solución es sensible a cambios en el parámetro de magnetización entre $\sim 10^{-3}$ y $\sim 10^{3}$. Fuera de ese rango, las cantidades físicas relevantes y la morfología son constantes; (iii) se obtuvieron algunas propiedades universales (independientes de la distribución del momento angular y del espín del agujero negro) de las soluciones tipo Komissarov. En el capítulo 2 del manuscrito se ofrecen ejemplos.

También es relevante mencionar que el método que utilizamos para obtener estas soluciones se basa en el cálculo de un gran número de curvas equipotenciales, las suficientes como para mapear el disco con una 'densidad' de curvas suficiente (utilizamos ~ 100 curvas por unidad de longitud). Además, para calcular estas curvas utilizamos un algoritmo Runge-Kutta de 4º orden que requiere un paso de integración muy pequeño, ya que las curvas equipotenciales divergen en el plano ecuatorial. Por lo tanto, este método de cálculo de las soluciones de equilibrio de los discos magnetizados de momento angular no constante es costoso computacionalmente cuando se compara con otros métodos disponibles (como los métodos basados en mallas numéricas que utilizaremos más adelante en esta tesis). Como consecuencia, no seguimos este enfoque en el resto de la tesis.

[5] aquí, donde $r_{\rm ms}$ denota la órbita marginalmente estable para las partículas masivas.

Agujeros negros de Kerr con pelo escalar

Como se mencionó anteriormente, el espacio-tiempo de Kerr es la solución canónica que se considera para los escenarios astrofísicos que involucran agujeros negros, pero hay alternativas a ese paradigma que se están considerando en la literatura. Dentro del marco de la relatividad general, hay una clase de soluciones alternativas para los agujeros negros que desafían la hipótesis de Kerr al evitar los llamados teoremas de no pelo y, por esa razón, estas soluciones se conocen como agujeros negros con pelo (en inglés *hairy* BHs; HBHs). En particular, en los capítulos 3 y 4 de esta tesis consideraremos la clase de HBHs conocida como agujeros negros de Kerr con pelo escalar (KBHsSH) [Herdeiro and Radu 2014b, Herdeiro and Radu 2015a], que son soluciones estacionarias y axisimétricas de las ecuaciones de campo de Einstein con un horizonte de sucesos, cuando el tensor de energía-momento es el de un campo escalar complejo, el campo escalar está sincronizado con el horizonte del BH (es decir, la frecuencia del campo y la velocidad angular del horizonte de sucesos se relacionan a través de $\omega = m\Omega_{\rm H}$, donde ω es la frecuencia del campo, m su índice armónico azimutal y $\Omega_{\rm H}$ es la velocidad angular del horizonte de sucesos) y se puede expresar como

$$\psi = \varphi(r,\theta)e^{{\rm i}(-\omega t + m\phi)}. \tag{1}$$

Esta definición hace evidente que el campo no tiene las mismas simetrías que el espacio-tiempo, y ese es precisamente el hecho que permite a esta solución eludir los teoremas de no pelo. La falta de simetrías del campo no constituye un problema, ya que el tensor de energía-momento que se deriva de él será estacionario y axisimétrico.

La solución de KBHSH original de Herdeiro and Radu [2014b] se ha extendido de varias maneras, para incluir la autointeracción del campo [Herdeiro, Radu, and Rúnarsson 2015], estados excitados [Wang, Liu, and Wei 2019], o valores más altos de m [Delgado, Herdeiro, and Radu 2019]. Esas soluciones también se han utilizado para calcular la sombra producida por el agujero negro en Vincent et al. [2016] and Cunha et al. [2015]. Hay que señalar que el mismo tipo de solución se puede construir para campos vectoriales masivos [Herdeiro, Radu, and Rúnarsson 2016].

Cabe destacar que las soluciones HBH construidas de esta forma requieren un valor muy pequeño del parámetro de masa para ser relevantes en procesos que involucren agujeros negros astrofísicos ($\mu \sim 10^{-10} - 10^{-20}$eV). Aunque actualmente no sabemos si tales campos existen, hay argumentos teóricos para su existencia (véase Arvanitaki et al. [2010] and Freitas et al. [2021]). Además, se

sabe que los agujeros negros con pelo bosónico sincronizado se forman (dinámicamente) de varias maneras, como por ejemplo a través de la fusión de estrellas binarias bosónicas (soluciones sin horizonte de las mismas ecuaciones), y por el mecanismo conocido como superradiancia (ver Cardoso et al. [2004] y sus referencias) en el que un campo que cumple $\omega < m\Omega_{\rm H}$ aumenta su frecuencia a costa del momento angular del agujero negro. Además, en la región en la que existen tanto agujeros negros de Kerr como KBHsSH, estos últimos se ven favorecidos entrópicamente. Por lo tanto, es muy probable que si este tipo de campos bosónicos ultraligeros existen en la naturaleza, entonces los HBHs también existirán. Como suponemos que estos campos no interactúan con la materia ordinaria de ninguna manera no gravitacional y en vista de que pueden formar y afectar a objetos astrofísicamente relevantes, los campos bosónicos ultraligeros se han propuesto de forma natural como candidatos a materia oscura.

En Gimeno-Soler et al. [2019] and Gimeno-Soler et al. [2021] se construyeron modelos de equilibrio de discos gruesos magnetizados alrededor de KBHsSH. En particular, se consideraron modelos con momento angular específico constante y no constante. Aquí, nos apartamos del trabajo previamente discutido [Gimeno-Soler and Font 2017] al considerar la EOS para el fluido propuesta por Montero et al. [2007] y, para los casos de distribución de momento angular no constante, una combinación de los enfoques en Gimeno-Soler and Font [2017] (en el plano ecuatorial) y el seguido por Daigne and Font [2004] (para calcular la distribución del momento angular fuera del plano ecuatorial calculando los ya mencionados cilindros de von Zeipel). En estos dos artículos intenté comprender la influencia que tiene la presencia del pelo escalar en la estructura del disco. Para ello, exploré diferentes espacio-tiempos de KBHsSH, diferentes valores y distribuciones del momento angular específico y valores del parámetro de magnetización. Esto condujo al descubrimiento de varios hechos interesantes: (i) La solución de Komissarov puede verse como una aproximación de la considerada en Montero et al. [2007] (debido a que se considera implícitamente $h \simeq 1$ cuando se toma $p = Kw^{\Gamma}$). Esto funciona bien para discos magnetizados cuando el pozo de potencial del disco es suficientemente poco profundo, pero para KBHsSH este puede dejar de ser el caso); (ii) aunque la morfología individual de los discos para diferentes modelos de KBHSH difiere, la morfología de la mayoría de los modelos de disco cambia de la misma manera cualitativa cuando la magnetización o la distribución de momento angular varía, mostrando un comportamiento similar al que ocurre cuando consieramos un agujero negro de Kerr; (iii) existen interesantes efectos morfológicos debidos a la presencia del campo gravitatorio del pelo que modifica la estructura del disco hasta el punto de provocar incluso la aparición

de un segundo máximo en la densidad de energía gravitatoria. Este efecto es más importante para los discos de momento angular no constante; (iv) se obtuvieron cotas astrofísicas para los diferentes modelos considerando varios valores adecuados para el parámetro de masa del campo escalar. Las cotas se calcularon para agujeros negros en el rango estelar y supermasivo y se basaron en los límites de la masa total del disco y su densidad máxima.

Como los espacio-tiempos de KBHsSH calculados en Herdeiro and Radu [2015a] son numéricos, para calcular estas soluciones de equilibrio escribí un código basado en una malla numérica que resultó ser mucho más eficiente y preciso que el utilizado en Gimeno-Soler and Font [2017]. Este código es capaz de calcular discos magnetizados en equilibrio con distribución de momento angular constante y no constante dado un cierto espacio-tiempo que puede ser analítico (por ejemplo, Kerr) o numérico. Hay planes para hacer este código disponible para el uso público.

Agujeros negros de Yukawa

Hasta ahora, sólo hemos considerado los espacio-tiempos de agujero negro en el marco de la relatividad general, pero también existen soluciones de agujero negro en el marco de teorías alternativas de la gravedad. En particular, las teorías de la gravedad de la familia $f(R)$ (en las que la acción estándar de Einstein-Hilbert de la relatividad general se modifica para incluir una función del escalar de Ricci) pueden producir soluciones de agujero negro no rotatantes conocidas como agujeros negros de Yukawa (YBH), nombre que se debe a que los potenciales métricos se modifican para incluir un término similar al de Yukawa $e^{-\alpha r}/r$. El YBH es una solución analítica del campo gravitatorio con tres parámetros (la masa del agujero negro, una escala de longitud y un parámetro de intensidad del campo gravitatorio). Por lo tanto, nos permite construir, de forma sencilla, modelos de equilibrio de discos de acreción para explorar posibles desviaciones respecto a la métrica de Kerr tanto en las soluciones estacionarias como utilizando códigos de evolución. A continuación, esto podría utilizarse para comparar los resultados de la simulación con los datos observacionales reales (por ejemplo, los datos de la colaboración EHT de M87*) para poner restricciones a la relatividad general. Esta solución se analizó en el contexto de la precesión del periastro en De Martino, Lazkoz, and De Laurentis [2018] and De Laurentis, De Martino, and Lazkoz [2018].

En el trabajo que se presenta en el Capítulo 5, construimos discos magnetizados de momento angular constante alrededor de diferentes YBH, utilizando el mismo enfoque que en el Capítulo 3. Nuestro principal objetivo aquí es evaluar

la influencia de las desviaciones de la relatividad general en el disco y sus potenciales efectos observacionales. Para ello, calculamos discos magnetizados para un amplio rango de parámetros del YBH. Observamos que el comportamiento cualitativo de los discos bajo cambios de la magnetización es el mismo que el observado en los trabajos anteriores. Sin embargo, también notamos que las desviaciones observadas en la geometría de los discos se deben a que el potencial de Yukawa actúa como una función de masa efectiva, por lo que los discos de acreción *ven* una masa diferente para cada esfera de radio r. Además, también calculamos el tamaño del anillo de fotones asociado a los YBHs para acotar los valores de los parámetros de los YBHs especificando los resultados a M87* y SgrA*.

Para obtener estos resultados utilizamos el módulo para calcular datos iniciales del *Black Hole Accretion Code* de la colaboración EHT (BHAC) [Porth et al. 2017] que fue modificado en Cruz-Osorio, Gimeno-Soler, and Font [2020] para implementar el mismo enfoque que el que utilicé en el Capítulo 2 [Gimeno-Soler et al. 2019]. La inclusión de las soluciones YBH en mi código de datos iniciales está todavía pendiente.

Discos autogravitantes

En todos los trabajos anteriores nos limitamos a la aproximación de fluido de prueba, en la que el fluido vive en un espacio-tiempo de fondo, pero su presencia no tiene ninguna reacción sobre el mismo. Sin embargo, esta aproximación no siempre está justificada, en particular cuando la masa del disco es comparable a la masa del agujero negro. En tal caso, hay que tener en cuenta la contribución a la curvatura del espacio-tiempo debida a la autogravedad del disco. Las simulaciones de relatividad numérica han revelado (véase, por ejemplo, Rezzolla et al. [2010]) que, en el contexto de las fusiones de BNS, la masa del disco final puede ser mayor que $\sim 10\%$ de la masa del agujero negro.

Entre los trabajos anteriores que tratan de la construcción de discos autogravitantes en equilibrio alrededor de un agujero negro se encuentran los de Nishida and Eriguchi [1994], Ansorg and Petroff [2005], Shibata [2007], Stergioulas [2011a], Stergioulas [2011b], and Kiuchi et al. [2011]. Destacamos en particular el artículo de [Shibata 2007] ya que es la investigación más relevante para nuestro propio trabajo, porque utilizamos el mismo formalismo. El trabajo de Shibata utiliza el llamado formalismo *puncture* para calcular discos de acreción puramente hidrodinámicos alrededor de agujeros negros en rotación. El formalismo *puncture* es muy conveniente para este tipo de cálculos, ya que evita los posibles

problemas numéricos debidos a la singularidad de curvatura dentro del agujero negro.

En el capítulo 6 presentamos nuestros resultados para discos autogravitantes con una ley de rotación kepleriana ($j = j(\Omega)$) propuesta por Karkowski et al. [2018a] and Karkowski et al. [2018b] y un campo magnético toroidal que se prescribe de forma diferente a la seguida anteriormente (no obstante, cumple la condición de integrabilidad de von Zeipel, ya que es uno de los casos considerados en Zanotti and Pugliese [2015]). Calculamos familias de soluciones para cuatro valores diferentes del parámetro de espín del agujero negro: un agujero negro que rota en sentido contrario al disco, un agujero negro de Schwarzschild y dos casos corrotantes con el disco con un valor del espín muy alto. En nuestra investigación descubrimos que (i) en contraste con el caso de fluido de prueba, los discos keplerianos autogravitantes no son infinitamente delgados y pueden ser bastante gruesos; (ii) los agujeros negros con rotación moderada producen una morfología del disco de acreción muy similar para un amplio rango de valores del parámetro de espín. Hay que fijarse en las cantidades métricas para poder discriminar realmente entre los casos; (iii) el grosor del disco puede depender del parámetro de magnetización. Este no es el caso para los discos en el régimen de fluido prueba; (iv) el aumento del parámetro de magnetización del disco (manteniendo el resto de parámetros constantes) cambian la masa y el momento angular del disco y del agujero negro de manera diferente si el disco es de rotación moderada o alta. Sin embargo, el cambio en la estructura radial del BH con respecto a la magnetización es el mismo para todos los casos y similar al observado para discos en el régimen de fluido prueba.

Para calcular los modelos de discos autogravitantes modificamos el código utilizado en Karkowski et al. [2018b] para tener en cuenta los efectos del campo magnético. Los detalles del código se presentan en el capítulo 6.

Discos con viscosidad

En los modelos discutidos hasta ahora hemos considerado configuraciones de fluido perfecto para los discos, construidos en diferentes fondos espacio-temporales. Sin embargo, en el capítulo 7 de esta tesis nos apartamos de esta aproximación introduciendo efectos disipativos en los discos en forma de tensiones de corte. Se sabe que al incluir efectos disipativos se obtienen ecuaciones de movimiento no hiperbólicas para el fluido [Romatschke 2010] y las configuraciones de equilibrio que se obtienen a partir de ellas son inestables bajo perturbaciones lineales [Hiscock and Lindblom 1985]. Este carácter patológico se atribuyó a la existencia

de gradientes de primer orden de las variables hidrodinámicas en las magnitudes disipativas y se eludió mediante la inclusión de gradientes de segundo orden. Este formalismo fue desarrollado primero por Muller [1967] (para el caso no relativista) y extendido a los fluidos relativistas por Israel [1976]. Las ecuaciones de movimiento resultantes son hiperbólicas y linealmente estables [Rezzolla and Zanotti 2013]. Recientemente, una nueva formulación causal de segundo orden de la hidrodinámica relativista disipativa que además puede ser escrita como un sistema de leyes de conservación dentro del formalismo $3+1$ fue presentada en Chabanov, Rezzolla, and Rischke [2021].

En el contexto de los discos de acreción alrededor de agujeros negros, los efectos de la viscosidad utilizando este enfoque fueron estudiados por primera vez por Lahiri and Lämmerzahl [2019] utilizando un esquema perturbativo para discos de acreción no magnetizados y de momento angular constante en la geometría de Schwarzschild. Este trabajo mostró que los modelos estacionarios de discos gruesos viscosos sólo pueden construirse en el contexto del enfoque causal en relatividad general utilizando el esquema de expansión del gradiente [Lahiri 2020]. Vale la pena observar que la inclusión de gradientes de segundo orden introduce explícitamente la curvatura de Riemann en las ecuaciones (la curvatura de Ricci también estaría presente para un espacio-tiempo no plano en el sentido de Ricci) como uno de los muchos gradientes de segundo orden. Como resultado, la curvatura de la geometría del espacio-tiempo influye directamente en la solución.

En Lahiri et al. [2021] presentamos una extensión de los resultados de Lahiri and Lämmerzahl [2019] para incluir campos magnéticos puramente toroidales (prescritos de la misma manera que en Komissarov [2006]). En particular, nos centramos en los discos magnetizados que desbordan sus lóbulos de Roche. En este estudio encontramos las siguientes propiedades de tales soluciones (i) la adición de la viscosidad modifica los valores de la presión del fluido y de la presión magnética de la misma manera. Por lo tanto, puede verse que, en primer orden en teoría de perturbaciones, la magnetización no se ve afectada por la viscosidad; (ii) las correcciones de primer orden a la presión y a la densidad de energía debidas a la viscosidad son más relevantes cuando las componentes de orden cero son más pequeñas (por ejemplo, cerca de la superficie del disco o cerca de la superficie isobárica crítica). Además, esto también induce un cambio en la localización del punto de cruce de la superficie isobárica crítica (es decir, la cúspide); (iii) estas correcciones de primer orden tienen signo negativo, por lo que la aparición de regiones de presión y densidad de energía negativas nos permite poner cotas superiores sobre los valor máximos de los parámetros de viscosidad.

Para calcular los modelos de disco con viscosidad, utilizamos el hecho de que las ecuaciones que deben resolverse para obtener la corrección de primer orden de la presión del fluido son PDEs de primer orden. A continuación, implementé en el código de datos iniciales el método de las características que es considerablemente más eficiente y preciso en comparación con otros métodos disponibles. En particular, las condiciones de contorno del problema (que de otro modo pueden ser muy difíciles de cumplir) se implementan fácilmente utilizando este enfoque.

Discos de acreción gruesos magnetizados: evoluciones no lineales

Comparar el resultado de diferentes simulaciones numéricas para diferentes conjuntos de datos iniciales de discos de acreción es una cuestión importante para validar o falsear los modelos teóricos frente a las observaciones. Una cuestión igualmente relevante es la comparación de los resultados de las simulaciones numéricas entre conjuntos similares de datos iniciales. Comprobar la validez de ciertas aproximaciones y la consistencia del resultado de las simulaciones es esencial para ayudar a tomar las decisiones adecuadas a la hora de prescribir los datos iniciales.

Esto es lo que se intentó en Cruz-Osorio, Gimeno-Soler, and Font [2020] y se discute en el capítulo 8 de esta tesis. Aquí, a diferencia de los capítulos anteriores, tratamos las evoluciones numéricas reales de los discos de acreción gruesos magnetizados en axisimetría dentro de la aproximación del fluido de prueba. Las simulaciones de GRMHD se realizaron con el código BHAC [Porth et al. 2017]. Para ello, implementamos en BHAC las ecuaciones necesarias para calcular los datos iniciales descritos en Gimeno-Soler et al. [2019]. El objetivo de esta investigación fue comparar tres formas diferentes de construir toros de momento angular constante dotados de un campo magnético toroidal: (i) un toro que se construye inicialmente sin campo magnético siguiendo la prescripción de Font and Daigne [2002] y el campo magnético se añade posteriormente como una perturbación después del primer paso de tiempo (introduciendo un cierto potencial vector magnético); (ii) un toro magnetizado siguiendo el método de Komissarov, en el que el campo magnético está en equilibrio con el fluido; (iii) la versión termodinámicamente relativista ($h > 1$) de la solución de Komissarov siguiendo el método expuesto en Montero et al. [2007] and Gimeno-Soler et al. [2019]. En particular, nos centramos en el seguimiento de la evolución de

diferentes cantidades del disco como la masa del disco, los perfiles radiales de la densidad, la magnetización y el momento angular para los diferentes valores de la magnetización alrededor de un agujero negro de Kerr $a = 0.9$ durante ~ 100 períodos orbitales (medidos en el centro del disco). Como el campo magnético es puramente toroidal pero las simulaciones se realizan en axisimetría, no se espera que aparezcan modos de la MRI. Sin embargo, es importante recordar que los modos no axisimétricos de la MRI aparecerían después de pocos periodos orbitales si no impusiéramos axisimetría.

La comparación de la evolución de diferentes datos iniciales reveló algunos efectos interesantes: (i) como era de esperar, si el campo magnético se introduce como una perturbación y la intensidad del campo es lo suficientemente grande (es decir, $\beta_{\rm m} \lesssim 0.1$) el disco puede ser perturbado de manera significativa o incluso ser destruido por completo. Alternativamente, si la magnetización es pequeña, la evolución del 'modelo perturbativo' es muy similar a la de los otros dos casos; (ii) durante la evolución del disco, el momento angular es transportado y el disco desarrolla una distribución de momento angular no constante: (iii) el campo magnético también se redistribuye. En particular, se puede observar que, si $\beta_{\rm m} \gtrsim 1$ el disco se magnetiza un poco más y, si $\beta_{\rm m} \lesssim 1$, el disco tiende a desmagnetizarse en la región interior, pero desarrolla una corona altamente magnetizada. Esto sugiere la existencia de un valor de la magnetización que da lugar a una distribución del campo magnético que sería constante durante la evolución; (iv) las dos aproximaciones en las que se prescribe el campo magnético evolucionan consistentemente de forma muy similar. Se espera que estas dos aproximaciones coincidan completamente cuando el disco está fuertemente magnetizado, pero se espera que discrepen ligeramente cuando el disco está débilmente magnetizado y el pozo de potencial es suficientemente profundo. La discrepancia debería aparecer para agujeros negros de Kerr casi extremales (es decir, $a \to 1$) y en algunos de los espacio-tiempos de KBHsSH considerados en Gimeno-Soler et al. [2019], pero un parámetro de espín de $a = 0.9$ no es suficiente para que este efecto sea perceptible en nuestras simulaciones.

Conclusiones

En esta tesis me he centrado en mejorar nuestro conocimiento de las propiedades físicas de las configuraciones de equilibrio de fluidos magnetizados alrededor de objetos compactos en relatividad general. En particular, se han obtenido nuevas prescripciones para construir datos iniciales de discos de acreción magnetizados alrededor de objetos compactos. Estas soluciones pueden utilizarse como datos iniciales para realizar simulaciones numéricas en escenarios dinámicos. De hecho, extender los tipos de datos iniciales disponibles para las simulaciones de discos de acreción en diferentes direcciones (acomodando, por ejemplo, diversas configuraciones de campo magnético, distribuciones de momento angular y tipos de espacio-tiempos donde vive el fluido) es un tema oportuno. Las instalaciones astronómicas de que disponemos en la actualidad nos presentan una oportunidad sin precedentes para empezar a analizar nuestras teorías sobre el espacio-tiempo y la verdadera naturaleza de los agujeros negros en el régimen de campo intenso, por ejemplo, mediante la astronomía de ondas gravitacionales [Abbott et al. 2019, Abbott et al. 2020b, Abbott et al. 2021a] y la astrometría de precisión de las estrellas alrededor del agujero negro supermasivo en el centro de nuestra galaxia [Do et al. 2019, Gravity Collaboration et al. 2019]. Además, la física de los fluidos en acreción en las proximidades de los objetos compactos está ahora al alcance de la experimentación gracias a las observaciones en radio del agujero negro supermasivo en el núcleo de la galaxia M87 [Event Horizon Telescope Collaboration et al. 2019a]. Llevar a cabo simulaciones numéricas que cubran un amplio rango del espacio de parámetros del problema son muy necesarias para inferir correctamente las propiedades físicas de tales sistemas agujero negro-toro de acreción a partir de los datos observacionales. Todas estas oportunidades observacionales han sido una de las motivaciones para el trabajo que aquí se presenta.

En el capítulo 2 extendimos la solución de Komissarov de un disco de acreción magnetizado y grueso (un 'donut polaco' magnetizado) al caso de

distribuciones de momento angular no constantes. En este estudio describimos el comportamiento de los discos de acreción magnetizados bajo cambios del parámetro de magnetización para diferentes parámetros de espín de los agujeros negros y la distribución del momento angular. También caracterizamos algunas propiedades de las soluciones de equilibrio que son independientes del parámetro de Kerr y de la distribución de momento angular considerada.

El capítulo 3 trató un tipo diferente de objeto compacto conocido como agujero negro de Kerr con pelo escalar [Herdeiro and Radu 2014b]. Se trata de una generalización del agujero negro de Kerr canónico (pero todavía dentro del marco de la relatividad general) que tiene en cuenta la presencia de un campo escalar complejo ultraligero que está sincronizado con el horizonte del agujero negro. Aquí nos centramos primero en los discos de momento angular constante y en las peculiaridades morfológicas y termodinámicas introducidas por la presencia del campo escalar. Una extensión de este estudio, discutida en el capítulo 4, consideró discos de momento angular no constante. En conjunto, estos dos trabajos revelaron las peculiares características morfológicas y termodinámicas de algunas de las soluciones (en particular cuando el campo escalar almacena la mayor parte de la masa y el momento angular del sistema). Observamos que la evolución temporal no lineal de estos modelos sigue siendo necesaria para obtener rasgos distintivos potencialmente observables de este tipo de sistemas de disco-agujero negro con pelo.

Dejando un momento de lado la relatividad general, en el capítulo 5 consideramos una solución de agujero negro en el marco de las teorías de gravedad $f(R)$, conocida como agujero negro de Yukawa. Aquí estudiamos discos magnetizados de momento angular constante para evaluar el impacto de las desviaciones de la relatividad general en la estructura y las propiedades físicas de los toros. Efectivamente, observamos desviaciones morfológicas que son características de este tipo de soluciones. Además, también calculamos los anillos de fotones asociados al agujero negro de Yukawa y pusimos algunas restricciones observacionales a los valores de sus parámetros.

Considerar los efectos de la autogravedad del disco de acreción es relevante cuando la masa del disco es comparable con la masa del agujero negro alrededor del cual gira. En el capítulo 7 estudiamos el impacto de la inclusión de la autogravedad en discos gruesos magnetizados con rotación kepleriana. Nuestro estudio reveló diferencias morfológicas entre los discos de fluido prueba y los discos con autogravedad. También caracterizamos el impacto que tienen los discos en la métrica del espacio-tiempo para diferentes valores del parámetro de espín de los agujeros negros y de la magnetización de los discos.

Hasta este punto de la tesis sólo habíamos considerado configuraciones de fluido perfecto. Sin embargo, en determinadas circunstancias, los efectos disipativos pueden ser importantes. Por esta razón, en el capítulo 7 introdujimos la presencia de viscosidad utilizando un enfoque perturbativo y consideramos una secuencia de discos magnetizados de momento angular constante en la geometría de Schwarzschild. En este trabajo observamos que la introducción de la viscosidad no modifica la magnetización del disco (al menos a primer orden en teoría de perturbaciones) y que las correcciones que la viscosidad introduce en la presión y la densidad de energía son negativas. Además, también caracterizamos la forma en que la viscosidad modifica la estructura del disco, en particular en la región cercana a la cúspide, poniendo cotas superiores a los valores de los parámetros del modelo.

Por último, en el capítulo 8 consideramos evoluciones temporales de diferentes discos de momento angular constante en un espacio-tiempo de Kerr de espín alto. En particular, comparamos tres formas de prescribir los datos iniciales. Una de ellas introduce el campo magnético como una perturbación de una solución no magnetizada. Las otras dos son la solución de Komissarov y una versión termodinámicamente relativista de dicha solución en la que el campo magnético está acoplado al fluido. Nuestro estudio puso límites al valor de la magnetización inicial del disco para el primer método (que se puede considerar inconsistente). También encontramos acuerdo entre las dos formas consistentes de prescribir los datos iniciales. Además, las simulaciones mostraron la presencia de redistribución del momento angular y del campo magnético. En concreto, encontramos una amplificación del campo magnético para los discos ligeramente magnetizados y un decrecimiento del campo magnético para los casos fuertemente magnetizados. Esto apunta a la existencia de un punto de equilibrio para el que el campo magnético será aproximadamente constante durante la evolución.

La mayoría de los resultados presentados en esta tesis se han obtenido con un código numérico que he desarrollado desde cero. Este código me ha permitido construir soluciones de equilibrio de discos magnetizados en espacio-tiempos estacionarios y axisimétricos genéricos. El código se está ampliando constantemente para tener en cuenta física adicional y actualmente hay varios proyectos en curso. En un futuro próximo tenemos previsto publicar el código como una herramienta de código abierto disponible para la comunidad.

En cuanto a las extensiones de los modelos estacionarios presentados aquí, ya se está trabajando para extender los discos polarizados magnéticamente de Pimentel, Lora-Clavijo, and Gonzalez [2018] al caso de momento angular no

constante descrito en Gimeno-Soler et al. [2021]. Además, se están calculando modelos de discos magnetizados alrededor de estrellas de Proca, una clase de objetos compactos exóticos sin horizonte que han sido propuestos como imitadores de agujeros negros [Brito et al. 2016]. Este tipo de estrellas bosónicas permite extender los discos cerca del eje de rotación. Esto conduce a la posibilidad de construir las llamadas *estrellas mixtas* (estrellas formadas tanto por campos bosónicos como por materia fermiónica ordinaria, véase por ejemplo [Di Giovanni et al. 2020]) usando herramientas propias de los discos de acreción. Otros trabajos en curso incluyen la extensión de nuestros resultados sobre discos con viscosidad al caso de Kerr. Dado que los gradientes de segundo orden considerados en Lahiri et al. [2021] incluyen componentes del tensor de Riemann, esperamos encontrar nuevos efectos cuando se considere el espacio-tiempo de Kerr, en particular en lo que respecta a la ubicación de la cúspide para los discos alrededor de agujeros negros de rotación máxima. Desde un punto de vista teórico, en colaboración con el Dr. Patryk Mach, también estamos interesados en averiguar la posibilidad de desarrollar un marco que permita la inclusión de campos magnéticos poloidales de forma consistente como el que utilizamos para los campos toroidales. Como se cree que los campos poloidales son clave para ciertos procesos físicos, como la MRI y la generación de chorros relativistas, esta adición sería muy relevante.

En cuanto a las posibles comparaciones con observaciones reales, los resultados de esta tesis, así como nuestras extensiones previstas, constituyen un punto de partida. Como primer paso, planeamos utilizar códigos de transporte radiativo en relatividad general (GRRT del inglés *general relativistic radiative transfer*) para obtener las sombras proyectadas por el agujero negro iluminado por la luz emitida por el disco de acreción, una línea sobre la que hemos empezado a trabajar en colaboración con los doctores Ziri Younsi, Alejandro Cruz-Osorio y Sayantani Lahiri. Sin embargo, considerar una solución de disco en equilibrio no es demasiado realista, ya que los flujos de acreción reales pueden ser muy dinámicos. Por lo tanto, el siguiente paso natural en mi investigación sería evolucionar nuestros modelos iniciales utilizando códigos de evolución, tanto en la aproximación de fluido de prueba con BHAC, como en relatividad general completa utilizando el *Einstein Toolkit* [Löffler et al. 2012]. Estas extensiones no solo me permitirían estudiar las propiedades de estabilidad y los procesos físicos de los modelos iniciales discutidos en esta tesis, sino también utilizar modelos de disco totalmente dinámicos para calcular las sombras con códigos de GRRT.

Contents

Chapter 1

Introduction

1.1 Motivation

The system composed of a compact object surrounded by matter is ubiquitous in astrophysics as it is present in a very large mass range, from masses comparable to the mass of the Sun that can be found in X-ray binaries or compact binary mergers, to the billions of solar masses that can be found at the center of galaxies. In the most likely event that the matter possesses angular momentum, the accretion of matter onto the compact object will take place through a disk (or a torus). For the physical description of these systems, as we are dealing with compact objects (i.e. $M/R \sim 1$, where M is the mass of the object and R its radius) and matter fields moving close to them, we need to employ the most advanced and observationally well-tested theory of gravity at our disposal, i.e. Einstein's general theory of relativity (GR) [Einstein 1915]. From a macroscopical point of view, we can consider that the matter fields behave as a fluid and if we also consider the potential presence of magnetic fields, we arrive at the theoretical framework that we are going to use throughout this whole thesis: *General relativistic magnetohydrodynamics* (GRMHD), which determines the dynamics of a magnetized fluid coupled with the gravitational field equations of GR.

Since a few years we are witnessing a very interesting era for the physics of accretion flows in the strong-gravity regime. Recent observational breakthroughs have provided an unprecedented opportunity to investigate the physics of strong gravity in different physical contexts and mass ranges. On the one hand, the Event Horizon Telescope (EHT) Collaboration observation of the vicinity of the compact supermassive central object at the core of the M87 galaxy, with the

capacity to resolve the shadow created by the central object when its accretion disk acts as a source of light [Event Horizon Telescope Collaboration et al. 2019a, Event Horizon Telescope Collaboration et al. 2019c], has offered very useful information about gravity in the strong-field regime. Namely, the lensing pattern (the bending of the light rays) created by the compact object gives information about the structure of null geodesics (the path followed by photons) in the region of spacetime close to the central object. The energy flux measured by the telescope network yields information about the morphological and physical properties (such as temperature, density, accretion rate and magnetic field, through polarimetric measurements) of the accretion disk that are inferred from the observations making use of time-dependent computer simulations of the accretion flow around the compact object. The results from the EHT observations are compatible with what we would expect from a hot, low-density, magnetized accretion disk of regular matter (in a configuration commonly known as *Magnetically Arrested Disk* (MAD)[1] [Narayan, Igumenshchev, and Abramowicz 2003, Igumenshchev, Narayan, and Abramowicz 2003]) around a supermassive ($M = 6.5 \times 10^9 M_\odot$) Kerr black hole (i.e. a stationary and axisymmetric vacuum solution of the Einstein field equations of GR that describe a black hole with nonzero mass and angular momentum [Kerr 1963]). It is broadly accepted that the Kerr solution is the one that describes all isolated (hence, vacuum) astrophysical black holes, a statement commonly known as the "Kerr hypothesis". This hypothesis is supported by the black hole uniqueness theorems (see Chruściel, Costa, and Heusler [2012] for a review on this topic) and by the no-hair conjecture [Bekenstein 1995]. Upcoming observational results from the EHT collaboration of the compact radio source Sgr A* located at the center of our very own galaxy will provide new information about the nature of the dark compact object and the accretion flows around it. The fact that the mass of Sgr A* is around three orders of magnitude smaller than the mass of M87* will allow for the comparison of the observation of the same phenomenon (an accretion disk around a supermassive dark compact object) in a different mass scale.

Furthermore, observations of the S2 star orbiting around Sgr A* [Do et al. 2019, Gravity Collaboration et al. 2019] yield information about the matter distribution that is swept during its orbit, constraining the properties of the spacetime in a region that is sufficiently close to the central object so that the effects of GR are noticeable along the orbit, but far enough from the central

[1] The MAD regime in an accretion disk is achieved when a strong poloidal magnetic field is accumulated close to the black hole, which causes a disruption of the accretion flow up to a certain radius. Inside that radius, matter falls at a slow speed as discrete blobs. This kind of accretion is energetically very efficient.

object so that the strong-gravity effects close to the compact body cannot be tested (the periapsis of the orbit of S2 is at around 150 AU from the central object, i.e. $\sim 2800\, r_g$, where r_g is the gravitational radius of the object[2] [Gravity Collaboration et al. 2020]). These results are compatible with the presence of a supermassive compact object with a mass of $\sim 4 \times 10^6 M_\odot$ consistent with a black hole as described by GR. Moreover, there is observational evidence suggesting that there is no extended mass with more than $\sim 0.1\%$ of the central mass inside the orbit of S2.

Likewise, for less massive compact objects (i.e. objects with masses in the stellar-mass range $\sim 1M_\odot - 100M_\odot$) access to the strong-field regime of gravity has been recently possible through the groundbreaking observations of gravitational waves (GWs) from compact binary mergers accomplished by the network of GW detectors Advanced LIGO, Advanced Virgo, and KAGRA (LVK) [Abbott et al. 2019, Abbott et al. 2020b, Abbott et al. 2021a]. The majority of LVK detections are associated with *purely vacuum events*, i.e. binary black hole (BBH) mergers, but there have also been observations of a couple of mixed binary merger systems (comprising a neutron star and a black hole; BHNS) and several binary neutron star (BNS) mergers. In particular, the BNS merger event GW170817 deserves special mention as not only it was the first observation ever of GWs from a BNS merger but it was also accompanied by electromagnetic radiation which was observed by dozens of telescopes worldwide and brought forth the field of Multi-Messenger Astronomy [Abbott et al. 2017]. In this thesis we are more interested in compact binary mergers involving matter fields, i.e. BNS and BHNS mergers (along with core-collapse supernovae (CSSN) not yet observed in GWs). In all of these cases, the most likely outcome of the merger event is a compact object (either a black hole or a neutron star) surrounded by matter. These events are also excellent candidates for multi-messenger detections, both in the electromagnetic spectrum and in neutrinos, as these systems are associated with the astrophysical phenomena known as *Gamma-ray bursts* (GRBs). In particular, short GRBs ($t \sim 0.2$s) are associated with BNS and/or BHNS mergers while long GRBs ($t \sim 20$s) with the gravitational collapse of massive stars (see Berger [2014] for a review). The nature of binary merger events and their physical parameters are inferred from the GW signals by comparing the data to waveform templates obtained using general relativity for the Inspiral-Merger-Ringdown signal. As with the observations by the EHT Collaboration and of the orbital motions around the Galactic center, the LVK GW observations provide strong evidence supporting GR in the strong-field regime as well as the Kerr hypothesis.

[2] $r_g = GM/c^2$, where G is Newton's gravitational constant and c is the speed of light.

Therefore, currently available observational evidences point towards a confirmation of GR, the Kerr hypothesis and, in the particular case of the supermassive compact-object range, the MAD model of disk accretion. However, despite the tremendous recent progress achieved in the observational front there are questions that still remain unanswered and also new questions one could ask in light of the new observations. We list here some of those that are most relevant for this thesis.

- *Is the shadow of the black hole a probe of the event horizon geometry?*: A natural question that arises when studying shadows is if the observation from infinity (far away from the source) of the shadow produced by a black hole can give information about the structure of the event horizon, and thus serve as a test of the Kerr hypothesis. Unfortunately, the answer to this question is negative: there are some counterexamples present in the literature that show that different objects can cast the same shadow as a black hole. For instance, in Junior et al. [2021] the authors construct solutions that are shadow-degenerate with both the Schwarzschild and Kerr geometries, In Herdeiro et al. [2021] it is shown that under certain observational conditions, a type of dark exotic compact object (ECO) known as a Proca star (PS) (a self-gravitating solitonic solution of the Einstein field equations coupled with a massive vector field) can mimic the Schwarzschild shadow. Despite these counterexamples, it is worth remarking that it is still unknown if performing GRMHD simulations of a disk in those spacetimes will break this degeneracy or not (see Olivares et al. [2020] for an example in which the shadow produced by a non-rotating boson star can actually be distinguished from the one produced by a black hole). We should also mention the work of Gralla [2021] in which the author raises some concerns about the capability of the EHT observations to probe GR.

- *Can two different disks cast the same shadow?*: In a black hole - torus system, the fluid part is the most complex to describe because of the physics involved and the lack of a complete knowledge. From the physics side, we know that a realistic treatment must include magnetic fields, viscosity, radiative and neutrino transport, a realistic equation of state (EOS) for the fluid, etc. However, it is currently impossible to consider all of these effects in GRMHD simulations, as it is computationally unfeasible. The approach that is commonly taken is to dismiss some of the deemed less relevant processes and to simplify some others (for instance, not considering

them during the evolution, but rather in a post-processing stage.) This is the case of the radiative transfer computations conducted by the EHT Collaboration to obtain the shadow images. Furthermore, there is another source of uncertainty regarding this, as it is still unknown to what extent the way the initial data of a GRMHD simulation is prescribed affects the time evolution and its outcome. There are also many free parameters to take into account when building the initial data of a magnetized accretion disk, namely the EOS, the intensity, topology and the way to prescribe the exact form of the magnetic field, the rotation law of the plasma and the locations of the inner and outer radii of the disk, among others. It is very important to assess the impact of the initial data in the evolution because a strong dependence on the initial data could lead to unrealistic outcomes. As a result, possible degeneracies in the process of estimating the physical parameters of an accretion disk through the observation of its shadow would seem likely. The simulation of a larger quantity of different disk models and future observational campaigns might help break some of those degeneracies.

- *Do all LIGO/Virgo GWs are produced by canonical black holes (BHs) and neutron stars (NSs)?* While it is true that the GW signals observed by the LVK Collaboration place strong constraints in some of the effects that should be present in some alternative theories of gravity (deviations of the speed of propagation of the gravitational waves, longitudinal modes of propagation, etc) [Abbott et al. 2021b], it is also true that the issue of degeneracy is also present here, at least to some extent. The fact that the catalogs of GW approximants for match-filtered searches is limited (and mostly restricted to quasi-circular orbital mergers) may impact our capability of inferring correctly the physical parameters of some events. This is particularly true for the recent event GW190521 [Abbott et al. 2020a], the most massive event announced by the LVC as of today, with a total mass of $\sim 150M_{\odot}$, in the realm of the intermediate-mass black holes. The source of GW190521 is identified as a BBH merger with at least one of the component BHs with a mass $M > 65M_{\odot}$ which is greater than the maximum mass that supernova models allow for a massive star to collapse into a black hole (due to the so-called pair instability). Alternative explanations to this event have appeared in the literature; for instance in Calderón Bustillo et al. [2021b] it is shown that this signal is compatible with the merger of two PS with an ultralight vector mass of $\mu_V = 8.7{\times}10^{-13}$ eV and the total mass of the system being larger than the estimate for

BBHs, $\sim 230 M_{\odot}$. We also note that Calderón Bustillo et al. [2021a] point out that standard parameter inference may confuse events below (above) the pair-instability threshold if the merger is highly eccentric instead of quasi-circular. Further research on waveform approximants for non-quasi-circular binaries will help mitigate uncertainties in the interpretation of future GW190521-like events that might be detected in upcoming LVK observational campaigns.

- *Are BHs the same at all mass scales?*: If we restrict ourselves to isolated Kerr BHs, black holes are quite simple objects and one of their defining properties is that they scale with their mass, i.e. black holes look the same at all mass scales. But it turns out that the introduction of matter fields changes this situation. If we consider the potential existence of massive dark bosonic fundamental fields (both scalar and vectorial), one can see that, if the mass parameter μ of the field is small enough (i.e. its wavelength, $\sim \mu^{-1}$, is large enough) the field can extract energy from the black hole in a process analogous to the Penrose process, called *superradiant instability* [Starobinsky 1973]. Through this process, Kerr black holes can lose angular momentum and synchronize with the field (i.e. the frequency of the field ω equals the angular velocity of the event horizon $\Omega_{\rm H}$) and form a bound state of a Kerr black hole with bosonic hair called *hairy black hole* (HBH) [Herdeiro and Radu 2014b]. This situation circumvents the so-called no-hair theorem [Israel 1967, Carter 1971]. The non-linear growth and saturation of the superradiant instability has been shown in the numerical-relativity simulations of East, Ramazanoğlu, and Pretorius [2014], East and Pretorius [2017], and East [2017]. This kind of bound states can also be formed by mergers of bosonic stars [Sanchis-Gual et al. 2020] which in turn can be formed through the collapse of a cloud of bosonic matter [Di Giovanni et al. 2018] (for a discussion regarding the non-linear stability of these stars see Sanchis-Gual et al. [2019] and Di Giovanni et al. [2020]). The key point to notice here is that depending on the mass parameter of the bosonic field, it is possible that there are HBHs and bosonic stars in one particular mass scale and not in another one. These bosonic fields are usually associated with extensions of the standard model of particle physics [Freitas et al. 2021] or the string theory's *axiverse* [Arvanitaki et al. 2010] and have been proposed in Cosmology as dark-matter candidates. It is also worth mentioning, for the relevance to this thesis, that the physical properties of accretion disks around black holes at different mass scales are also very different. For instance, the

densities of a disk formed from a BNS merger and those of a disk around a supermassive black hole are many orders of magnitude apart, so they can be regarded as very different kind of fluids. If the disk is sufficiently massive, it can even affect the geometry of the black hole (see Mach et al. [2019] and Kulczycki, Mach, and Malec [2021]).

From the previous discussion it follows that most of the open issues are related to the intrinsic degeneracies that exist when one tries to infer physical parameters of dark compact objects from observational data. Future developments, either theoretical, computational (more powerful computational resources) and observational, such as the *Next Generation EHT* (ngEHT), the *Laser Interferometer Space Antenna* (LISA), the increased second-generation GW detector network (with the addition of KAGRA and LIGO-India) or the third-generation GW interferometers *Einstein Telescope* and *Cosmic Explorer* will help to break some of the current degeneracies.

This thesis deals with the theoretical study of black hole-torus systems in full GR, increasing the current state-of-the-art of the field. In this thesis, I have focused in building equilibrium (time-independent) solutions of magnetized accretion thick disks around different types of compact objects, changing both the physical ingredients present in the disks as well as the nature of the central compact object. The goal of this work is twofold: first, to gain insight on the effects that adding different physics has in the system's morphological and physical properties, and second, to provide large new samples of open-source initial data to conduct time-dependent GRMHD simulations of BH-torus systems.

Before discussing in the next section the specific investigations that comprise this work it is worth spending a few words exploring the meaning of the term "equilibrium" at the beginning of the previous paragraph. It is very important to distinguish between the terms "equilibrium", that only means the solution is time-independent, and "stable" that means the solution is a dynamical attractor of the system under potential perturbations that might appear during a time evolution. Our equilibrium models are then, not necessarily stable and, in particular, can be unstable under a known set of disk instabilities, namely:

- *Runaway instability (RI)*: This dynamical instability can happen in a system consisting of an accretion torus filling its Roche lobe[3] around a black hole. When the mass falls into the BH through the Lagrange L_1 point,

[3]The Roche lobe of a body on a binary system is defined as the region of space within the orbiting matter that is gravitationally bound to that body.

the BH mass increases, which makes the L_1 point to move deeper into the torus, eventually being accreted entirely. This process is very fast and can destroy the disk in a dynamical timescale (just a few milliseconds for a stellar mass BH) which poses a threat to BH-torus systems as progenitors of short GRBs. The RI was first discovered by Abramowicz, Calvani, and Nobili [1983]. Numerical time evolutions in GR (neglecting the self-gravity of the disk) were performed in Font and Daigne [2002] and Daigne and Font [2004] where it was shown that the instability does indeed happen for constant specific angular momentum disks, $l = -u_\phi/u_t$, where u_ϕ and u_t are the azimuthal and temporal components of the 4-velocity, but it is supressed if the angular momentum distribution is non-constant (e.g. a power law). Further studies showed that considering self-gravity was not determinant to the onset of the RI: the axisymmetric simulations performed by Montero, Font, and Shibata [2010] indicated that for disks with constant and nonconstant angular momentum the RI was suppressed. Likewise, the RI does not appear (in a dynamical time scale) in the BH-torus systems produced after the merger of unequal mass neutron stars [Rezzolla et al. 2010] nor in three-dimensional simulations of constant angular momentum disks in a fully dynamical spacetime [Korobkin et al. 2011]. However, in Korobkin et al. [2013] the RI does indeed appear in simulations using a similar setup than the one employed by Korobkin et al. [2011] but with more favorable conditions (a smaller value for the specific angular momentum l). In conclusion, a sufficient condition for the appearance of the RI in a dynamical timescale requires the torus to be close to filling its Roche lobe and obeying a sufficiently small constant angular momentum distribution (the value of the specific angular momentum must allow the existence of Roche-lobe-filling stationary disks). We note that these favorable conditions do not seem to arise in the context of BNS mergers, as it can be seen in Rezzolla et al. [2010] and Most et al. [2021].

- *Papaloizou-Pringle instability (PPI)*: Discovered by Papaloizou and Pringle [1984], the PPI is a non-axisymmetric dynamical instability that fragments the torus into m overdensities or "planets" (for a mode of order m) and serves as a mechanism to transport angular momentum to the outer regions of the disk. This instability manifests in a stronger way for slender disks but it can be present for thick disks as well, in particular for constant angular momentum disks [Blaes 1987, Hawley 1991]. The mechanism of generation for the PPI is the propagation of waves associated with some mode m and with the presence of a corotation radius related to

that mode (which also defines a forbidden region for wave propagation) [Goldreich, Goodman, and Narayan 1986]. These modes are amplified by interaction through the forbidden region and by the reflection of the waves in the inner and outer edges of the disk. Therefore, the triggering of accretion (i.e. removing the inner edge of the disk) saturates the PPI at low amplitudes or even altogether prevents its growth [Blaes 1987, Hawley 1991, De Villiers and Hawley 2002]. Moreover, the persistent asymmetry that the PPI can induce in a thick disk may trigger the emission of GWs as first shown by Kiuchi et al. [2011] (see also Mewes et al. [2016] for a related discussion in the context of tilted accretion disks). The PPI's fastest mode can compete with the RI if the latter is sufficiently suppressed to delay its appearance so the PPI has the time to set in. This can trigger non-linear interactions between the two instabilities. For instance, the PPI has the potential to redistribute angular momentum and that could suppress the growth of the RI (as we mentioned above) [Korobkin et al. 2011]. It is also worth mentioning the remarkable similarity between the PPI and the bar-mode instability that appears in the context of rotating neutron stars and boson stars [Cerdá-Durán, Quilis, and Font 2007, Baiotti et al. 2007, Di Giovanni et al. 2020], which also presents the corotating radius, angular momentum transport to the outer regions and a morphological similarity to the mode $m = 2$ (the $m = 1$ mode is forbidden for these objects).

- *Magnetorotational instability (MRI)*: Originally discoverd by Chandrasekhar [1960] and later rediscovered by Balbus and Hawley [1991], the MRI appears in two different instances: an axisymmetric instability produced by a poloidal magnetic field and a non-axisymmetric instability that is triggered by the presence of a toroidal magnetic field [Balbus and Hawley 1992]. The turbulence introduced by this instability serves as a mechanism to transport and redistribute angular momentum and triggering accretion. In particular, a constant angular momentum disk can redistribute its angular momentum to become almost Keplerian (see for instance Bugli et al. [2018]) and a magnetic field can be amplified or reduced depending on its initial intensity [Fragile and Sądowski 2017] (see also Wielgus et al. [2015], McKinney and Blandford [2009], and Fragile et al. [2007]). It is also relevant to note that the MRI can interact with the PPI as the growth timescale of the fastest modes of both instabilities are similar, as shown by Bugli et al. [2018] who found that the PPI is mostly suppressed in the presence of a (toroidal) magnetic field in 3D GRMHD simulations

even when the conditions for its growth are favorable (small value of the constant angular momentum).

From the above paragraphs it becomes apparent that the subsequent study of the (in)stability of the disk models reported in this thesis as initial data is a relevant topic to pursue. Some of the astrophysical processes one needs to model require that the disk lives for a long enough time (e.g. those that are the source of light for the shadows observed by the EHT) while, in addition, to trigger accretion onto the central black hole it is required that the disk is in an unstable state (in fact, the initial data employed in the numerical simulations of the EHT collaboration are built to be MRI unstable). Therefore, the study of the potential instabilities that may affect the equilibrium models of thick disks reported in this thesis is very relevant to check their viability as initial data for non-linear evolutions.

1.2 Magnetized thick accretion disks: equilibrium solutions

As previously stated, this thesis is mainly focused in construction and discussing equilibrium solutions of magnetized thick accretion disks around compact objects. In particular, the disks presented here belong to the class of disks commonly known as *Polish doughnuts* endowed with a toroidal magnetic field. The Polish doughnut model was developed by Abramowicz, Jaroszynski, and Sikora [1978], Kozlowski, Jaroszynski, and Abramowicz [1978], Jaroszynski, Abramowicz, and Paczynski [1980], and Paczyński and Wiita [1980]. In its original form one such disk consisted of a stationary and axisymmetric solution of the energy-momentum conservation equations $\nabla_\mu T^{\mu\nu} = 0$ when $T^{\mu\nu}$ is the energy-momentum tensor of a perfect, barotropic ($p = p(\rho)$) non-self-gravitating fluid on a Kerr geometry background and given a constant distribution of the specific angular momentum $l = -u_\phi/u_t$. It is important to note that there are other possible definitions of the specific angular momentum. For instance, the specific angular momentum is also reported as $j = u^t u_\phi$ and taking $j =$ constant also yield thick disks (see for instance Fishbone and Moncrief [1976]). However, l and j are related in a simple way, namely $j = \frac{l}{1-\Omega l}$, so it is easy to translate a particular choice of j to a formalism that uses l.

This formalism has been extended to consider non-constant specific angular momentum disks (see, for instance, Daigne and Font [2004] and Qian et al. [2009]). It must be remarked that for non-constant angular momentum disks,

integrating the equations of motion requires an extra condition in the angular velocity distribution (that is automatically satisfied for constant l disks) which is $\Omega = \Omega(l)$, i.e. the constant angular velocity surfaces must coincide with the constant angular momentum ones. This condition, known as the general relativistic form of the von Zeipel theorem [von Zeipel 1924, Abramowicz 1971], is fulfilled if the fluid is barotropic ($p = p(\rho)$). It can be seen that, given a specific angular momentum distribution at the equatorial plane of the black hole, the condition $\Omega = \Omega(l)$ yields a family of cylinder-like surfaces (known as von Zeipel cylinders) along which Ω and l are constant (an example of the von Zeipel cylinders in the Kerr spacetime can be seen in Daigne and Font [2004]). Besides this, considering a (radially) non-constant distribution of l is key to adjust the geometrical characteristics of the accretion torus, such as the radial extent and the height. Lastly, taking into account non-constant angular momentum is also required to be able to accommodate $j =$ constant disks, as it is apparent that if j is constant l must be non-constant.

The most relevant extension of the Polish doughnut model for the work developed in this thesis is the Komissarov solution [Komissarov 2006], where the torus is coupled with a purely toroidal magnetic field and the equations to be solved are the ones of ideal GRMHD. This solution is particularly interesting since it is an analytical solution of the GRMHD equations which is very useful for several reasons: as an easy to build initial data for nonlinear evolution codes (some examples are reported in Montero et al. [2007], Wielgus et al. [2015], Fragile and Sądowski [2017], and Bugli et al. [2018]), to test the accuracy of such codes due to its analytic nature (see for instance Porth et al. [2017]) and even to compute synthetic images of the black hole when the light is emitted by the accretion disk (see Vincent et al. [2015]). To integrate the equations of motion for the magnetized case, an extra assumption must be taken (in addition to barotropicity). Komissarov's choice regarding this was to assume a 'polytropic EOS' for the magnetic pressure (that is defined as $p_{\rm m} = b^2/2$) but there are other possibilities, as was shown by Zanotti and Pugliese [2015].

Lastly, it is relevant to note that magnetized thick disks are expected to appear in realistic astrophysical scenarios, such as the remnant of BNS or BHNS mergers (see e.g. Baiotti and Rezzolla [2017] and Most et al. [2021]). Therefore, it is very important to build, understand and improve equilibrium models of magnetized thick accretion disks. In that way, if we use sufficiently accurate initial data, one can study the physics of disk+BH systems without the need to perform the computationally expensive *ab initio* simulations of their formation.

1.2.1 Perfect fluid configurations

Kerr metric

As the Kerr spacetime is the canonical BH metric within the framework of GR, it is natural to expect that most extensions of Komissarov's solution were studied for Kerr BHs. First, in Montero et al. [2007] the authors used an EOS of the fluid of the form $p = K\rho^{\Gamma}$, instead of the one presented by Komissarov [2006], which is $p = Kw^{\Gamma}$ (where w is the fluid enthalpy[4]). The consequence of this is that the solution is no longer analytic (the equation to solve to obtain the pressure and density distributions becomes trascendental) so it requires numerical methods to solve it. Wielgus et al. [2015] introduced a non-constant angular momentum distribution by considering the angular velocity to be a power law of the specific angular momentum to study the appearance of unstable MRI modes when a magnetized disk is subject to non-axisymmetric perturbations. More recently, in Pimentel, Lora-Clavijo, and Gonzalez [2018] an extension of the Komissarov solution to include the possibility that the matter of the disk has a non-zero magnetic susceptibility has been presented. Such solution allows for the disk to be magnetically polarized.

In Gimeno-Soler and Font [2017], the non-constant specific angular momentum distribution proposed by Qian et al. [2009] was incorporated into the Komissarov solution. The actual implementation of the specific angular momentum ansatz proposed in Qian et al. [2009] for this work is a two parameter model (we fixed one of the three original parameters). The ansatz at the equatorial plane consists of a constant part for $r \leq r_{\rm ms}$[5] and a power law for the angular momentum $l(r) \propto l_{\rm K}(r)^{\beta}$ when $r > r_{\rm ms}$, where β is a model parameter and $l_{\rm K}(r)$ is the Keplerian angular momentum. The other parameter of the ansatz controls the decay of l when $\theta \neq \pi/2$. This choice of parameters is very interesting because it allows to modify the morphology of the disks, as the modification of the value of the first parameter implies a change of the thickness of the disk and changing the value of the second one implies a variation of its radial extent, as it can be noticed both in Qian et al. [2009] and in this thesis. The freedom to adjust the morphology of the disk can make this kind of solutions useful to be used as initial data in evolution codes to explore how different disk morphologies can affect different physical processes and the outcome of the simulation.

To better understand this family of equilibrium solutions, I explored a wide range of the 4 dimensional parameter space (two parameters for the specific

[4]The fluid enthalpy w is defined as $w = \rho h$.

[5]Here, $r_{\rm ms}$ denotes the innermost marginally stable orbit for massive particles.

angular momentum distribution, the spin parameter of the black hole and the ratio between the magnetic pressure and the fluid pressure (henceforth known as the magnetization parameter)). This study revealed some properties of the equilibrium solutions: (i) the qualitative behaviour of the disk under changes of the angular momentum parameters or the magnetization is independent of the spin parameter of the black hole; (ii) the solution is sensitive to changes in the magnetization parameter between $\sim 10^{-3}$ and $\sim 10^{3}$. Outside that range, the relevant physical quantities and the morphology are constant; (iii) some universal properties (independent of the angular momentum distribution and spin of the BH) of Komissarov-like solutions were obtained. Examples are provided in Chapter 2 of the manuscript.

It is also relevant to mention that the method we use to obtain these solutions is based on computing a large number of equipotential curves, enough to map the disk with sufficient 'density' of curves (we used ~ 100 curves per unit of lenght). Moreover, to compute these curves we use a 4th-order Runge-Kutta algorithm that requires a very small integration step, as the equipotential curves diverge at the equatorial plane. Therefore, this method of computing equilibrium solutions of magnetized, non-constant angular momentum disks is computationally expensive when compared to other avalaible methods (as the grid-based methods we will use later in this thesis). As a consequence, we do not follow this approach in the rest of the thesis.

Kerr black holes with scalar hair

As previously mentioned, the Kerr spacetime is the canonical solution that is considered for astrophysical scenarios involving black holes, but there are alternatives to that paradigm that are being considered in the literature. Within GR, there is a class of alternative BH solutions that challenge the Kerr hypothesis by avoiding the so-called no-hair theorems and for that reason, these solutions are known as *hairy* BHs (HBHs). In particular, in Chapters 3 and 4 of this thesis we will consider the class of HBHs known as Kerr BHs with scalar hair (KBHsSH) [Herdeiro and Radu 2014b, Herdeiro and Radu 2015a], that are horizon-possessing stationary and axisymmetric solutions of the Einstein field equations when the energy-momentum tensor is that of a complex scalar field and the scalar field is synchronized with the horizon of the BH (i.e. the frequency of the field and the angular velocity of the event horizon are related through $\omega = m\Omega_{\rm H}$, where ω is the frequency of the field, m its azimuthal harmonic index

and $\Omega_{\rm H}$ is the angular velocity of the event horizon) and it can be expressed as

$$\psi = \varphi(r,\theta)e^{{\rm i}(-\omega t+m\phi)}. \tag{1.1}$$

This definition makes apparent that the field has not the same symmetries as the spacetime, and that is precisely the fact that allows this solution to circumvent the no-hair theorems. The lack of symmetries of the field does not constitute a problem, as the energy-momentum tensor that is derived from it will be stationary and axisymmetric.

The original KBHSH solution of Herdeiro and Radu [2014b] has been extended in several ways, to include self-interaction of the field [Herdeiro, Radu, and Rúnarsson 2015], excited states [Wang, Liu, and Wei 2019], or higher values of m [Delgado, Herdeiro, and Radu 2019]. Those solutions have also been used to compute the shadow of the BH in Vincent et al. [2016] and Cunha et al. [2015]. It must be noted that the same kind of solution can be built for massive vector fields [Herdeiro, Radu, and Rúnarsson 2016].

It is worth highlighting that HBH solutions contructed in this way require a very small value of the mass parameter to become relevant in processes involving astrophysical BHs ($\mu \sim 10^{-10} - 10^{-20}\,$eV). Although we currently do not know if such fields exist, there are theoretical arguments for their existence (see Arvanitaki et al. [2010] and Freitas et al. [2021]). Additionally, BHs with synchronized bosonic hair are known to (dynamically) form in several ways, such as through the merger of binary bosonic stars (horizonless solutions of the same equations), and by the mechanism known as superradiance (see Cardoso et al. [2004] and references therein) in which a field that fulfills $\omega < m\Omega_{\rm H}$ increases its frequency at the expense of the angular momentum of the black hole. Moreover, in the region in which there exist both Kerr BHs and KBHsSH, the latter are entropically favored. Therefore, it is very likely that if this kind of ultralight bosonic fields exist in nature, HBHs will exist as well. As we are assuming that these fields do not interact with regular matter in any non-gravitational way and in view of the fact that they can form and affect astrophysically relevant objects, ultralight bosonic fields have been naturally proposed as dark-matter candidates.

In Gimeno-Soler et al. [2019] and Gimeno-Soler et al. [2021] equilibrium models of magnetized thick disks around KBHsSH were constructed. In particular, models with both constant and non-constant specific angular momentum were considered. Here, we departed from the work previously discussed [Gimeno-Soler and Font 2017] by considering the EOS for the fluid proposed by Montero et al. [2007] and, for the non-constant angular momentum distribution cases, a

combination of the approaches in Gimeno-Soler and Font [2017] (at the equatorial plane) and the one followed by Daigne and Font [2004] (to compute the angular momentum distribution outside the equatorial plane by computing the aforementioned von Zeipel's cylinders). In these two articles I attempted to understand the influence that the presence of the scalar hair has in the disk structure. For this reason, I explored different KBHsSH spacetimes, different values and distributions of the specific angular momentum and values of the magnetization parameter. This led to the discovery of several interesting facts: (i) Komissarov's solution can be seen as an approximation of the one considered in Montero et al. [2007] (due to the fact that $h \simeq 1$ is considered implicitly when $p = Kw^{\Gamma}$ is taken). This works well for magnetized disks when the potential well of the disk is sufficiently shallow, but for KBHsSH this may no longer be the case); (ii) although the individual morphology of the disks for different models of KBHSH difers, the morphology of most disk model changes in the same qualitative way when the magnetization or the angular momentum distribution varies when compared to the Kerr; (iii) there are interesting morphological effects due to the presence of the hair's gravitational field that modifies the disk structure to the point of even causing the appearance of a second maximum in the gravitational energy density. This effect is more important for non-constant angular momentum disks; (iv) astrophysical constraints on the different models were obtained by considering various suitable values for the mass parameter of the scalar field. The constraints were computed for BHs in both, the stellar and supermassive range and were based on limits of total disk mass and maximum density.

As the KBHsSH spacetimes computed in Herdeiro and Radu [2015a] are numerical, to compute the torus solutions I wrote a grid-based code that turned out to be much more efficient and accurate than the one used in Gimeno-Soler and Font [2017]. The code is able to compute equilibrium magnetized disks with constant and non-constant angular momentum distribution given some spacetime that can be analytical (e.g. Kerr) or numerical. There are plans to make this code available for public use.

Yukawa black holes

Until now, we only considered BH spacetimes within the framework of GR, but BH solutions exist for alternative theories of gravity as well. In particular, theories of gravity of the $f(R)$ family (where the standard Einstein-Hilbert action of GR is modified to include a function of the Ricci scalar) can produce non-rotating BH solutions known as Yukawa BHs (YBHs), the name being due

to the metric potentials being modified to include a Yukawa-like term $e^{-\alpha r}/r$. The YBH is a three parameter (the mass of the BH, a length scale, and a field strength parameter), analytic solution of the gravitational field. Therefore, it offers a way to build equilibrium models of accretion disks to explore potential deviations from the Kerr case in both the stationary solutions and using evolution codes. Then, this could be used to compare the results of the simulation with actual observational data (e.g. the EHT collaboration data of M87*) to put constraints on GR. This solution was analyzed in the context of periastron advance in De Martino, Lazkoz, and De Laurentis [2018] and De Laurentis, De Martino, and Lazkoz [2018].

In the work reported in Chapter 5, we build constant angular momentum, magnetized disks around different YBH, using the same approach as in Chapter 3. Our main objective here is to assess the influence of the deviations from GR in the disk and their potential observational effects. To this end, we computed magnetized disks for a wide range of YBH parameters. We noticed that the qualitative behavior of the disks under changes of the magnetization is the same as the one we observed in the previous works. However, we noticed that the deviations observed in the geometry of the disks are due to the Yukawa potential acting as an effective mass function, so the accretion disks *sees* a different mass for each sphere of radius r. Moreover, we also computed the photon ring size associated with the YBHs to put constraints on the YBH parameters by specifying the results to M87* and SgrA*.

To obtain these results we used the module to compute inital data of the EHT Collaboration's *Black Hole Accretion Code* (BHAC) [Porth et al. 2017] that was modified in Cruz-Osorio, Gimeno-Soler, and Font [2020] to implement the same approach as the one I used in Chapter 2 [Gimeno-Soler et al. 2019]. The inclusion of YBH solutions in my initial data code is work in progress.

Self-gravitating disks

In all previous works we restricted ourselves to the test fluid approximation, where the fluid lives in a background spacetime, but its presence has no backreaction in the spacetime whatsoever. However, this approximation is not always justified, in particular when the disk mass is comparable to the BH mass. In such case the contribution to the spacetime curvature due to the self-gravity of the disk must be taken into account. Numerical relativity simulations have revealed (see, for instance, Rezzolla et al. [2010]) that, in the context of BNS mergers, the mass of the final disk can be greater than $\sim 10\%$ of the mass of the BH.

Previous works dealing with the construction of equilibrium, self-gravitating disks around a BH include those from Nishida and Eriguchi [1994], Ansorg and Petroff [2005], Shibata [2007], Stergioulas [2011a], Stergioulas [2011b], and Kiuchi et al. [2011]. We highlight in particular the article by [Shibata 2007] since it is the most relevant investigation for our own work, as we use the same formalism. Shibata's work uses the so-called puncture framework to compute purely hydrodynamical accretion disks around rotating BHs. The puncture framework is very convenient for this kind of computations, as it avoids the potential numerical issues due to the curvature singularity inside the BH.

In Chapter 6 we present our results for self-gravitating disks with a Keplerian rotation law ($j = j(\Omega)$) proposed by Karkowski et al. [2018a] and Karkowski et al. [2018b] and a toroidal magnetic field that is prescribed in a different way than the one previously followed (it nevertheless fulfills the von Zeipel integrability condition, as it is one of the cases considered in Zanotti and Pugliese [2015]). We computed families of solutions for four different values of the BH spin parameter, one counterrotating, a non-rotating BH, and two highly co-rotating cases. In our investigation we found out that (i) in contrast to the test-fluid case, Keplerian self-gravitating disks are not infinitely thin and can be quite thick; (ii) mildly rotating BHs yield a very similar accretion disk morphology for a wide range of the spin parameter values. One must look at the metric quantities to actually be able to discriminate between cases; (iii) the thickness of the disk can be dependent on the magnetization parameter. This is not the case for test-fluid disks; (iv) increasing the magnetization parameter of the disk (and keeping the other parameters constant) change the disk and BH mass and angular momentum in a different way if the disk is either mildly or highly rotating. However, the change in the radial structure of the BH with respect of the magnetization is the same for all cases and similar to the one observed for test-fluid disks.

To compute the self-gravitating disk models we modified the code used in Karkowski et al. [2018b] to account for the effects of the magnetic field. Details of the code are reported in Chapter 6.

1.2.2 Viscous disks

In the models so far discussed we have considered *perfect fluid* configurations for the disks, built in different spacetime backgrounds. However, in Chapter 7 of this thesis we depart from this matter model by introducing dissipative effects in the disks in the form of shear stresses. It is known that including dissipative effects yields non-hyperbolic equations of motion for the fluid [Romatschke 2010]

and the equilibrium configurations that are obtained from them are unstable under linear perturbations [Hiscock and Lindblom 1985]. This pathological nature was attributed to the existence of first-order gradients of hydrodynamical variables in the dissipative quantities and was circumvented by the inclusion of second-order gradients. This formalism was developed first by Muller [1967] (for the non-relativistic case) and extended to relativistic fluids by Israel [1976]. The resulting equations of motion are hyperbolic and linearly stable [Rezzolla and Zanotti 2013]. More recently a new causal formulation of relativistic second-order dissipative hydrodynamics that can be written in 3+1 flux-conservative form was proposed by Chabanov, Rezzolla, and Rischke [2021].

In the context of accretion disks around BHs, the effects of shear viscosity using this approach were first studied by Lahiri and Lämmerzahl [2019] using a perturbative scheme for non-magnetized, constant angular momentum accretion disks in the Schwarzschild geometry. This work showed that stationary models of viscous thick disks can only be constructed in the context of the general relativistic causal approach by using the gradient expansion scheme [Lahiri 2020]. It is worth observing that the inclusion of second-order gradients introduce explicitly the Riemann curvature in the equations (the Ricci curvature would also be present for a non Ricci-flat spacetime) as one of many second-order gradients. As a result, the curvature of the spacetime geometry directly influences the solution.

In Lahiri et al. [2021] we presented an extension of the results of Lahiri and Lämmerzahl [2019] to include purely toroidal magnetic fields (prescribed in the same way as in Komissarov [2006]). In particular, we focused on magnetized disks that overflow their Roche lobes. In this study we found the following properties of such solutions: (i) the addition of shear viscosity modifies the values of the fluid pressure and of the magnetic pressure in the same way. Therefore it can be seen that, at first order, the magnetization is unaffected by viscosity; (ii) the first-order corrections to the pressure and energy density due to the viscosity are more relevant when the zeroth-order components are smaller (e.g. close to the surface of the disk or near the self-crossing isobaric surface). Furthermore, this also induces a change on the location of the self-crossing point of the critical isobaric surface (i.e. the cusp); (iii) these first-order correction have negative sign, so the appearance of negative pressure and energy density regions allows us to put constraints on the maximum value of the viscosity parameters.

To compute viscous disk models we used the fact that the equations that must be solved to obtain the first-order correction to the fluid pressure are first-order PDEs. I then implemented in the initial data code the method of

characteristics that is considerably more efficient and accurate when compared to other available methods. In particular, the boundary conditions of the problem (that can be otherwise very hard to enforce) are easily implemented using this approach.

1.3 Magnetized thick accretion disks: non-linear evolutions

Comparing the outcome of different numerical simulations for different sets of accretion disk initial data is an important issue to validate/falsify theoretical models against observations. An equally relevant issue is the comparison of the results of numerical simulations between *similar* sets of initial data. Testing the validity of certain approximations and the consistency of the outcome of the simulations is essential to help make appropriate choices when prescribing the initial data.

This was attempted in Cruz-Osorio, Gimeno-Soler, and Font [2020] and it is discussed in Chapter 8 of this thesis. Here, contrary to the previous chapters, we deal with actual numerical evolutions of magnetized thick accretion disks in axisymmetry within the test-fluid approximation. The GRMHD simulations were carried out with the BHAC code [Porth et al. 2017]. To this end, we implemented in BHAC the equations required to compute the initial data described in Gimeno-Soler et al. [2019]. The goal of this investigation was to compare three different ways to build constant angular momentum tori endowed with a toroidal magnetic field: (i) a torus that is initially built without a magnetic field following the prescription of Font and Daigne [2002] and the magnetic field is added as a perturbation after the first time step (by introducing a magnetic vector potential); (ii) a magnetized torus following Komissarov's method, in which the magnetic field is in equilibrium with the fluid; (iii) the thermodynamically relativistic ($h > 1$) version of Komissarov's solution following the method laid out in Montero et al. [2007] and Gimeno-Soler et al. [2019]. In particular, we focused on tracking the evolution of different disk quantities such as the mass of the disk, the radial profiles of the density, magnetization and angular momentum for the different values of the magnetization around a $a = 0.9$ Kerr BH during ~ 100 orbital periods (measured at the center of the disk). As the magnetic field is purely toroidal but the simulations are performed in axisymmetry, MRI modes are not expected to appear. However, we have to mention that non-axisymmetric

MRI modes would appear after a few orbital periods if our simulations were performed without enforcing axisymmetry.

Comparing the evolution of different initial data revealed some interesting effects: (i) as expected, if the magnetic field is introduced as a perturbation and the field strength is sufficiently large (i.e. $\beta_{\rm m} \lesssim 0.1$) the disk can be perturbed in a significant way or even destroyed entirely. Alternatively, if the magnetization is small, the evolution of the 'perturbative model' is very similar to that of the other two cases; (ii) during the disk's evolution, angular momentum gets transported and the disk develops a non-constant angular momentum distribution: (iii) the magnetic field is also redistributed. In particular, it can be observed that, if $\beta_{\rm m} \gtrsim 1$ the disk becomes slightly more magnetized and, if $\beta_{\rm m} \lesssim 1$, the disk tends to demagnetize in the inner region, but develops a highly magnetized corona. This suggests the existence of a value of the magnetization that yields a magnetic field distribution that would be constant during the evolution; (iv) the two approaches in which the magnetic field is prescribed consistently evolve in a very similar way. These two approaches are expected to completely coincide when the disk is strongly magnetized, but are expected to slightly disagree when the disk is weakly magnetized and the potential well is sufficiently deep. The discrepancy should appear for nearly extremal Kerr BHs (i.e. $a \to 1$) and in some of the KBHsSH spacetimes considered in Gimeno-Soler et al. [2019], but a spin parameter of $a = 0.9$ is not enough for this effect to be noticeable in our simulations.

Chapter 2

Magnetised Polish doughnuts revisited

This chapter is based on the following publication: S. Gimeno-Soler & J. A. Font. Magnetised Polish doughnuts revisited, *A&A* 607, A68 (2017), DOI: 10.1051/0004-6361/201730935.

2.1 Introduction

Matter accretion on to black holes is the most efficient form of energy production known in nature. The conversion of the gravitational energy of the infalling matter into heat and radiation may reach efficiencies of about 43% in the case of maximally rotating (Kerr) black holes. For this reason, systems formed by a black hole surrounded by an accretion disc are deemed responsible for many of the most energetic astronomical phenomena observed in the cosmos. In particular, (geometrically) thick accretion discs (or tori) are believed to be present in quasars and other active galactic nuclei, some X-ray binaries and microquasars, as well as in the central engine of gamma-ray bursts. The latter are alluded to in connection with mergers of neutron star binaries and black hole neutron star binaries, as well as with the rotational collapse that ensues at the end of the life of some massive stars. As numerical simulations show, such events often result in a black hole surrounded by a torus (see e.g. [Rezzolla et al. 2010, Sekiguchi and Shibata 2011, Faber and Rasio 2012, Shibata and Taniguchi 2011a, Baiotti and Rezzolla 2017]).

The investigation of this type of systems, either by analytical or numerical means, may rely on the ability to construct suitable representations based on physical assumptions. The construction of equilibrium models of stationary discs around black holes has indeed a long tradition (see [Abramowicz and Fragile 2013] and references therein). In particular, the so-called "Polish doughnuts" [Abramowicz, Jaroszynski, and Sikora 1978, Kozlowski, Jaroszynski, and Abramowicz 1978] provide a very general method to build equilibrium configurations of perfect fluid matter orbiting around a Kerr black hole. This fully relativistic model assumes that the disc is non-magnetised and that the matter obeys a constant specific angular momentum distribution. This method was later extended by Komissarov [2006] by adding a purely azimuthal magnetic field to build magnetised tori around rotating black holes. Dynamical evolutions of magnetized tori built with the Komissarov solution were first reported by Montero et al. [2007]. On the other hand, assuming different distributions of angular momentum in the discs, Qian et al. [2009] presented a method to build sequences of black hole thick accretion discs in dynamical equilibria, restricted however to the purely hydrodynamical case.

In this paper we combine the two approaches considered in Komissarov [2006] and Qian et al. [2009] to build new sequences of equilibrium tori around Kerr black holes. Building on these works, we present here the extension of the models of Qian et al. [2009] to account for discs endowed with a purely toroidal magnetic field. In our procedure we hence assume a form of the angular momentum distribution that departs from the constant case considered by Komissarov [2006] and from which the location and morphology of the equipotential surfaces can be numerically computed. As we shall show below, for the particular case of constant angular momentum distributions, our method is in good agreement with the results of Komissarov [2006]. We also note the recent work of Wielgus et al. [2015] where Komissarov's solution was extended for the particular case of power-law distributions of angular momentum. Moreover, the magnetised tori of Wielgus et al. [2015] were used to explore the growth of the magneto-rotational instabilty (MRI) through time-dependent numerical simulations. In particular, the long-term evolution of those tori has been recently investigated by Fragile and Sądowski [2017], who paid special attention to the decay of their magnetisation.

The organization of the paper is as follows: Section 2.2 presents the analytic framework to build the discs while Section 2.3 explains the corresponding numerical procedure. The sequences of models are discussed in Section 2.4. Finally, the conclusions are summarized in Section 2.5, where we also briefly

indicate potential extensions of this work we plan to inspect. In our work we assume that the test-fluid approximation holds, thus neglecting the self-gravity of the fluid, and further assume that the spacetime is described by the Kerr metric. In mathematical expressions below Greek indices are spacetime indices running from 0 to 3 and Latin indices are only spatial. We use geometrized units where $G = c = 1$.

2.2 Framework

Equilibrium tori around Kerr black holes are built assuming that the spacetime gravitational potentials and the fluid fields are stationary and axisymmetric. In all the derivations presented below, the Kerr metric is implicitly written using standard Boyer-Lindquist coordinates. It is convenient to introduce a number of relevant characteristic radii, such as the radius of the marginally stable circular orbit, $r_{\rm ms}$, and the radius of the marginally bound circular orbit, $r_{\rm mb}$, given by

$$r_{\rm ms} = M\left(3 + Z_2 - [(3 - Z_1)(3 + Z_1 + 2Z_2)]^{1/2})\right) , \tag{2.1}$$

$$r_{\rm mb} = 2M\left(1 - \frac{a_*}{2} + \sqrt{1 - a_*}\right) , \tag{2.2}$$

where we have defined the following quantities, $Z_1 = 1 + (1 - a_*^2)^{1/3}[(1 + a_*)^{1/3} + (1 - a_*)^{1/3}]$, $Z_2 = (3a_*^2 + Z_1^2)^{1/2}$, and $a_* = a/M$, with a and M being the spin Kerr parameter and the black hole mass, respectively.

2.2.1 Distribution of angular momentum

We introduce the specific angular momentum l and the angular velocity Ω employing the standard definitions,

$$l = -\frac{u_\phi}{u_t}, \quad \Omega = \frac{u^\phi}{u^t}, \tag{2.3}$$

where u^μ is the fluid four-velocity. The relationship between l and Ω is given by the equations

$$l = -\frac{\Omega g_{\phi\phi} + g_{t\phi}}{\Omega g_{t\phi} + g_{tt}}, \quad \Omega = -\frac{l g_{tt} + g_{t\phi}}{l g_{t\phi} + g_{\phi\phi}}, \tag{2.4}$$

where $g_{\mu\nu}$ is the metric tensor and we are assuming circular motion, i.e. the four-velocity can be written as

$$u^\mu = (u^t, 0, 0, u^\phi) . \tag{2.5}$$

We also introduce the Keplerian angular momentum (for prograde motion) in the equatorial plane $l_{\rm K}$, defined as

$$l_{\rm K}(r) = \frac{M^{1/2}(r^2 - 2aM^{1/2}r^{1/2} + a^2)}{r^{3/2} - 2Mr^{1/2} + aM^{1/2}}\,. \tag{2.6}$$

Jaroszynski, Abramowicz, and Paczynski [1980] argued that the slope of the specific angular momentum should range between two limiting cases, namely $l = \text{const.}$ and $\Omega = \text{const.}$ Following Qian et al. [2009] we assume an angular momentum distribution ansatz given by

$$l(r,\theta) = \begin{cases} l_0 \left(\frac{l_{\rm K}(r)}{l_0}\right)^{\beta} \sin^{2\gamma}\theta & \text{for } r \geq r_{\rm ms} \\ l_{\rm ms}(r)\sin^{2\gamma}\theta & \text{for } r < r_{\rm ms} \end{cases} \tag{2.7}$$

where constants l_0 and $l_{\rm ms}(r)$ are defined by $l_0 \equiv \eta l_{\rm K}(r_{\rm ms})$ and $l_{\rm ms}(r) \equiv l_0[l_{\rm K}(r_{\rm ms})/l_0]^{\beta}$. Therefore, the model for the distribution of angular momentum has three free parameters, β , γ and η, whose range of variation is given by [Qian et al. 2009]

$$0 \leq \beta \leq 1, \quad -1 \leq \gamma \leq 1, \quad 1 \leq \eta \leq \eta_{\rm max}, \tag{2.8}$$

with $\eta_{\rm max} = l_{\rm K}(r_{\rm mb})/l_{\rm K}(r_{\rm ms})$. In this paper, and as it is done for hydrodynamical discs in Qian et al. [2009], we choose $\eta = \eta_{\rm max}$, and then we can write l_0 as $l_0 = l_{\rm K}(r_{\rm mb})$. For this choice of η, we can find the location of the cusp of the disc within the range $r_{\rm mb} \leq r_{\rm cusp} \leq r_{\rm ms}$ (for $0 \leq \beta \leq 1$). The cusp is defined as the circle in the equatorial plane on which the pressure gradient vanishes and the angular momentum of the disc equals the Keplerian angular momentum. Moreover, this value of η guarantees that constant angular momentum discs ($\beta = \gamma = 0$) with their inner edge located at the cusp ($r_{\rm in} = r_{\rm cusp}$) have no outer boundary, i.e they are infinite discs (see also [Font and Daigne 2002]).

2.2.2 Magnetised discs

The equations of ideal general relativistic MHD are the following conservation laws, $\nabla_\mu T^{\mu\nu} = 0$, $\nabla_\mu {}^*F^{\mu\nu} = 0$, and $\nabla_\mu(\rho u^\mu) = 0$, where ∇_μ is the covariant derivative and

$$T^{\mu\nu} = (w + b^2)u^\mu u^\nu + \left(p + \frac{1}{2}b^2\right) g^{\mu\nu} - b^\mu b^\nu, \tag{2.9}$$

is the energy-momentum tensor of a magnetised perfect fluid, w and p being the fluid enthalpy density and fluid pressure, respectively. Moreover, ${}^*F^{\mu\nu} = b^\mu u^\nu - b^\nu u^\mu$ is the (dual of the) Faraday tensor relative to an observer with four-velocity u^μ, and b^μ is the magnetic field in that frame, with $b^2 = b^\mu b_\mu$.

Assuming the magnetic field is purely azimuthal, i.e. $b^r = b^\theta = 0$, and taking into account that the flow is stationary and axisymmetric, the conservation of the current density and of the Faraday tensor follow. Contracting Eq. (2.9) with the projection tensor $h^\alpha_{\ \beta} = \delta^\alpha_{\ \beta} + u^\alpha u_\beta$, we arrive at

$$(w + b^2)u_\nu \partial_i u^\nu + \partial_i \left(p + \frac{b^2}{2} \right) - b_\nu \partial_i b^\nu = 0 \,, \tag{2.10}$$

where $i = r, \theta$. Following Komissarov [2006] we rewrite this equation in terms of the specific angular momentum l and of the angular velocity Ω, to obtain

$$\partial_i (\ln |u_t|) - \frac{\Omega \partial_i l}{1 - l\Omega} + \frac{\partial_i p}{w} + \frac{\partial_i (\mathcal{L} b^2)}{2\mathcal{L} w} = 0 \,, \tag{2.11}$$

where $\mathcal{L} = g_{t\phi}^2 - g_{tt} g_{\phi\phi}$. To integrate Eq. (2.11) we first assume a barotropic equation of state $w = w(p)$ of the form

$$p = K w^\kappa, \tag{2.12}$$

with K and κ constants. Then, we define the magnetic pressure as $p_\mathrm{m} = b^2/2$, and introduce the definitions $\tilde{p}_\mathrm{m} = \mathcal{L} p_\mathrm{m}$ and $\tilde{w} = \mathcal{L} w$, in order to write an analogue equation to Eq. (2.12) for $\tilde{p}_\mathrm{m}$ [Komissarov 2006]

$$\tilde{p}_\mathrm{m} = K_\mathrm{m} \tilde{w}_\mathrm{m}^\lambda, \tag{2.13}$$

or, in terms of the magnetic pressure p_m

$$p_\mathrm{m} = K_\mathrm{m} \mathcal{L}^{\lambda - 1} w^\lambda, \tag{2.14}$$

where K_m and λ are constants. This particular choice of barotropic relationships, $w = w(p)$ and $\tilde{w} = \tilde{w}(\tilde{p}_\mathrm{m})$, fulfill the general relativistic version of the von Zeipel theorem for a toroidal magnetic field [von Zeipel 1924, Zanotti and Pugliese 2015], i.e. the surfaces of constant Ω and constant l coincide.

We can now integrate Eq. (2.11) to obtain

$$\ln |u_t| - \int_0^l \frac{\Omega \mathrm{d}l}{1 - \Omega l} + \int_0^p \frac{\mathrm{d}p}{w} + \int_0^{\tilde{p}_\mathrm{m}} \frac{\mathrm{d}\tilde{p}_\mathrm{m}}{\tilde{w}} = \text{const.} \tag{2.15}$$

On the surface of the disc, and particularly on its inner edge, the conditions $p = \tilde{p}_\mathrm{m} = 0$, $u_t = u_{t,\mathrm{in}}$, $l = l_\mathrm{in}$ are satisfied and, therefore, the integration constant is simply given by

$$\text{const.} = \ln |u_t| - \int_{l_\mathrm{in}}^l \frac{\Omega \mathrm{d}l}{1 - \Omega l} \,. \tag{2.16}$$

We can also introduce the total (gravitational plus centrifugal) potential W [Abramowicz, Jaroszynski, and Sikora 1978] and write the integral form of the equation of

motion (the relativistic Euler equation) as

$$W - W_{\rm in} = \ln|u_t| - \ln|u_{t,\rm in}| - \int_{l_{\rm in}}^{l} \frac{\Omega {\rm d}l}{1-\Omega l}, \tag{2.17}$$

where $W_{\rm in}$ is the potential at the inner edge of the disc (in the equatorial plane). With this definition, we can write Eq. (2.15) as

$$W - W_{\rm in} = \int_0^p \frac{{\rm d}p}{w} + \int_0^{\tilde{p}_{\rm m}} \frac{{\rm d}\tilde{p}_{\rm m}}{\tilde{w}}, \tag{2.18}$$

which for a barotropic equation of state can be easily integrated to give

$$W - W_{\rm in} + \frac{\kappa}{\kappa-1}\frac{p}{w} + \frac{\lambda}{\lambda-1}\frac{p_{\rm m}}{w} = 0\,. \tag{2.19}$$

Replacing p and $p_{\rm m}$ by equations (2.12) and (2.14), the previous equation reduces to

$$W - W_{\rm in} + \frac{\kappa}{\kappa-1}Kw^{\kappa-1} + \frac{\lambda}{\lambda-1}K_{\rm m}(\mathcal{L}w)^{\lambda-1} = 0, \tag{2.20}$$

which relates the distribution of the potential with the distribution of the enthalpy density.

2.3 Methodology

To construct our models of magnetised discs we follow the approach described in Qian et al. [2009]. First, we find the radial location of the cusp and of the centre of the disc in the equatorial plane, $r_{\rm cusp}$ and $r_{\rm c}$, defined as the solutions to the equation $l(r) - l_{\rm K} = 0$. Next, we compute the partial derivatives of the potential, Eq. (2.17)

$$\partial_r W = \partial_r \ln|u_t| - \frac{\Omega\partial_r l}{1-\Omega l}\,, \tag{2.21}$$

and

$$\partial_\theta W = \partial_\theta \ln|u_t| - \frac{\Omega\partial_\theta l}{1-\Omega l}\,. \tag{2.22}$$

Then, we integrate the radial partial derivative of the potential along the segment $[r_{\rm cusp}, r_{\rm c}]$ (assuming $W_{\rm cusp} = 0$) at the equatorial plane, thus obtaining the equatorial distribution of the potential between $r_{\rm cusp}$ and $r_{\rm c}$

$$W_{\rm eq}(r) = \int_{r_{\rm cusp}}^{r_{\rm c}} \left(\partial_r \ln|u_t| - \frac{\Omega\partial_r l}{1-\Omega l}\right). \tag{2.23}$$

Following Qian et al. [2009] (see also Jaroszynski, Abramowicz, and Paczynski [1980]) we can divide equations (2.21) and (2.22) to obtain

$$F(r,\theta) = -\frac{\partial_r W}{\partial_\theta W} = \frac{{\rm d}\theta}{{\rm d}r}\,, \tag{2.24}$$

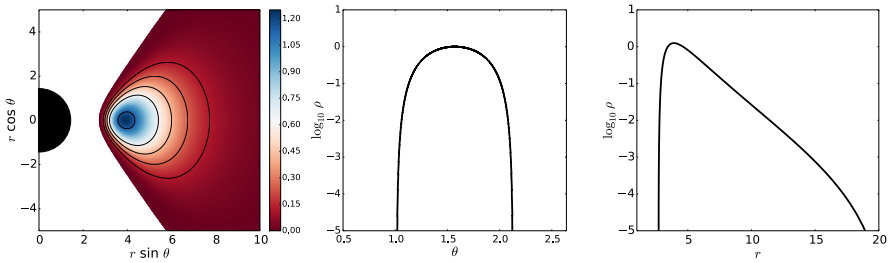

Figure 2.1 Comparison with Komissarov's solution for a constant angular momentum model. The left panel shows the rest-mass density distribution in logarithm scale for all radii and all angles while the middle and right panels show, respectively, the angular profile of the logarithm of the rest-mass density at the centre of the disc and the radial profile of the logarithm of the rest-mass density at the equatorial plane.

where function $F(r,\theta)$ is known in closed form for the Kerr metric once an assumption for the angular momentum distribution has been made (cf. Eq. ((2.7))). For this reason, Eq. ((2.24)) also takes the form of an ordinary differential equation for the surfaces of constant potential, $\theta = \theta(r)$, which, upon integration, yields the location of those surfaces. Note that in Qian et al. [2009] these are surfaces of constant *fluid pressure* instead, since their discs are purely hydrodynamical.

Next, we choose all the initial radial values for the integration of Eq. (2.24) to lie between $r_{\rm cusp}$ and $r_{\rm c}$ ($\theta = \pi/2$). Since we are only interested in the equipotential surfaces inside the Roche lobe of the disc, our choice of initial values provides us a mapping of the equipotential surfaces of the torus. Given that we have already obtained both the equipotential surfaces $\theta(r)$ which cross the segment $[r_{\rm cusp}, r_{\rm c}]$ at the equatorial plane and the values of the potential in that segment, we can obtain the complete potential distribution for the torus (outside of that segment). Once we have the potential distribution, we can find the fluid pressure at the centre of the disc from Eq. (2.20),

$$p_{\rm c} = w_{\rm c}(W_{\rm in} - W_{\rm c})\left(\frac{\kappa}{\kappa - 1} + \frac{\lambda}{\lambda - 1}\frac{1}{\beta_{\rm m_c}}\right)^{-1}, \tag{2.25}$$

where $w_{\rm c}$ is the enthalpy density at the centre and

$$\beta_{\rm m} = p/p_{\rm m}, \tag{2.26}$$

is the magnetisation parameter ($\beta_{\rm m_c}$ being the magnetisation parameter at the centre of the disc). Using this definition, we can find the magnetic pressure at the centre,

$$p_{\rm m_c} = p_{\rm c}/\beta_{\rm m_c}\,. \tag{2.27}$$

With both pressures known at the centre, fluid and magnetic, we can now find the constants K and $K_{\rm m}$ using equations (2.12) and (2.14). Therefore, for a given inner radius of the disc $r_{\rm in}$ we can obtain the potential $W_{\rm in}$. We now finally have all the ingredients required to find the enthalpy density distribution (Eq. (2.20)), the fluid pressure and magnetic pressure distributions (Eqs. (2.12) and (2.14)), and the rest-mass density distribution, which can be trivially obtained inverting the barotropic relation, $p = K\rho^{\kappa}$. We note that the fluid enthalpy density w includes the rest-mass density ρ, and can thus be defined as $w = \rho h$ where h is the specific enthalpy. The relativistic definition of this quantity is $h = 1+\varepsilon+p/\rho$, where ε is the specific internal energy. From a thermodynamical point of view a non-relativistic fluid satisfies $h = 1$. Therefore, since we use poytropic equations of state (relating p with either w or ρ in the same functional form) we are implicitly assuming that $h = 1$, i.e. the discs we build in our procedure are non-relativistic from a thermodynamical point of view.

For the integration of Eq. (2.23) we use the composite Simpson's rule. It is important to use a very small integration step because the slope is very steep. In this work, we use a step $\Delta r = 10^{-6}$. Using the analytic, constant angular momentum case for comparison, we tested that a larger value of Δr gives unacceptable accuracy losses. On the other hand, to integrate the ordinary differential equation (2.24) we use a fourth-order Runge-Kutta method. Again, it is also important here to choose a suitable step of integration, especially at the outer end of the disc, because Eq. (2.24) diverges at the equatorial plane (the equipotential surfaces cross the equatorial plane perpendicularly). We show the proof of this statment in Appendix 2.6.

2.4 Results

To reduce the number of free parameters to build the initial models we do as in Komissarov [2006] and fix the values of the equation of state exponents, κ and λ, and of the enthalpy density at the disc centre, $w_{\rm c}$. More precisely, we choose $\kappa = \lambda = 4/3$ and $w_{\rm c} = 1$. This still leaves us with five parameters to control the size, shape, thickness, and magnetisation of the disc, namely the magnetisation parameter $\beta_{\rm m_c}$, the parameters of the angular momentum distribution β and γ, the black hole spin parameter a, and the inner radius of the disc $r_{\rm in}$. We build a series of 45 models, whose main features are summarised in Table 2.1 (for $\beta_{\rm m_c} = 10^3$, i.e. models where the effects of the magnetisation are unimportant), Table 2.2 ($\beta_{\rm m_c} = 1$, i.e. equipartition models), and Table 2.3 ($\beta_{\rm m_c} = 10^{-3}$, i.e. highly-magnetised models). We note that we can build models with very

Table 2.1 List of models for $\beta_{\mathrm{m_c}} = 10^3$. From left to right the columns report: the model name (with A, B and C standing for black hole spin $a = 0.5$, 0.9 and 0.99, respectively), the parameters of the angular momentum distribution β and γ, the corresponding radii of the maximum fluid pressure and magnetic pressure, r_{max} and $r_{\mathrm{m,max}}$, the gravitational potential difference between the centre and the inner radius, $\Delta W \equiv W_{\mathrm{c}} - W_{\mathrm{in}}$, and the inner and outer radii of the discs, r_{in} and r_{out}.

	β	γ	r_{max}	$r_{\mathrm{m,max}}$	ΔW $(\times 10^{-2})$	r_{in}	r_{out}
A1	0.0	0.0	7.15	8.14	−6.35	2.91	–
A2	0.5	0.5	7.15	7.65	−2.27	3.20	11.8
A3	0.9	0.9	7.15	7.45	−0.30	3.70	9.58
A4	0.0	0.9	7.15	8.32	−6.35	2.91	9.68
A5	0.9	0.0	7.15	7.28	−0.30	3.70	–
B1	0.0	0.0	3.59	3.98	−12.9	1.73	–
B2	0.5	0.5	3.59	3.83	−4.32	1.86	5.35
B3	0.9	0.9	3.59	3.73	−0.54	2.08	4.52
B4	0.0	0.9	3.59	3.85	−12.9	1.73	4.54
B5	0.9	0.0	3.59	3.81	−0.54	2.08	–
C1	0.0	0.0	1.98	2.28	−24.6	1.21	–
C2	0.5	0.5	1.98	2.09	−7.34	1.26	2.50
C3	0.9	0.9	1.98	2.04	−0.85	1.35	2.25
C4	0.0	0.9	1.98	2.10	−24.6	1.21	2.26
C5	0.9	0.0	1.98	2.08	−0.85	1.35	–

Table 2.2 List of models for $\beta_{\mathrm{m_c}} = 1$. The naming of the models and the parameters reported in the columns are as in Table 2.1.

	β	γ	r_{max}	$r_{\mathrm{m,max}}$	ΔW $(\times 10^{-2})$	r_{in}	r_{out}
A1	0.0	0.0	6.00	6.49	−6.35	2.91	–
A2	0.5	0.5	6.25	6.66	−2.27	3.20	11.8
A3	0.9	0.9	6.50	6.80	−0.30	3.70	9.58
A4	0.0	0.9	6.00	6.49	−6.35	2.91	9.68
A5	0.9	0.0	6.50	6.80	−0.30	3.70	–
B1	0.0	0.0	3.02	3.26	−12.9	1.73	–
B2	0.5	0.5	3.16	3.35	−4.32	1.86	5.35
B3	0.9	0.9	3.29	3.43	−0.54	2.08	4.52
B4	0.0	0.9	3.02	3.26	−12.9	1.73	4.54
B5	0.9	0.0	3.29	3.43	−0.54	2.08	–
C1	0.0	0.0	1.68	1.80	−0.246	1.21	–
C2	0.5	0.5	1.77	1.86	−7.34	1.26	2.50
C3	0.9	0.9	1.84	1.91	−0.85	1.35	2.25
C4	0.0	0.9	1.68	1.80	−24.6	1.21	2.26
C5	0.9	0.0	1.84	1.91	−0.85	1.35	–

small values of $\beta_{\rm m_c}$, such as e.g. $\beta_{\rm m_c} = 10^{-20}$ (extremely high magnetisation) without encountering numerical difficulties. No qualitative differences in the structure of the discs are found once $\beta_{\rm m_c}$ becomes smaller than a sufficiently small value, about $\beta_{\rm m_c} = 10^{-3}$. This is the reason why we choose that particular value as our lower limit in the figures and tables of the manuscript.

We note in particular that the radii of the maximum fluid pressure and magnetic pressure, $r_{\rm max}$ and $r_{\rm m,max}$, respectively, for the same value of $\beta_{\rm m_c}$, never coincide. This also reflects the fact that constant fluid pressure surfaces do not coincide with constant magnetic pressure surfaces.

We start by assessing our procedure by first building an extra disc model that can be directly compared with one of the two models in Komissarov [2006]. This is shown in Figure 2.1, which corresponds to the same constant specific angular momentum model A presented by Komissarov [2006]. The parameters of this model are $a = 0.9$, $\beta_{\rm m_c} = 0.1$, and $l = 2.8$. The visual comparison shows that our approach can reproduce those previous results with good agreement. The rest-mass density distribution in the $(r\sin\theta, r\cos\theta)$ plane shown in the left panel of Fig. 2.1 is remarkably similar to that shown in the left panel of Fig. 2 in Komissarov [2006]. Not only the morphology of both models is nearly identical but also the range of variation of the rest-mass density and the location of the disc centre agree well in both cases. This can be most clearly seen in the middle and right panels of Fig. 2.1 which show, repectively, the angular profile at $r_{\rm c}$ and the radial profile at $\theta = \pi/2$. The middle figure can be directly compared with Fig. 3 of Komissarov [2006]. It is relevant to mention that very small changes in the location of the inner radius $r_{\rm in}$ have a significant effect on the maximum value of the rest-mass density, which explains the small differences between our figures and the ones presented in Komissarov [2006].

A representative sample of the isodensity surfaces for some of our models appears in Figure 2.2. We plot, in particular, the models of Table 2.3, for which the magnetisation is highest ($\beta_{\rm m_c} = 10^{-3}$). From left to right the columns of this figure correspond to increasing values of the black hole spin, namely, $a = 0.5$, 0.9 and 0.99, while from top to bottom the rows correspond to different combinations of the γ and β parameters that characterize the ansatz for the angular momentum distribution of Qian et al. [2009] (the particular values are indicated in the caption of the figure). A rapid inspection shows that the structure of the discs noticeable changes when the parameters change. Notice that the spatial scale in all of the plots of this figure has been chosen so as to facilitate the visualization of the discs (which can be fairly small in some cases) and, as such, is different in each plot. A typical Polish doughnut is represented

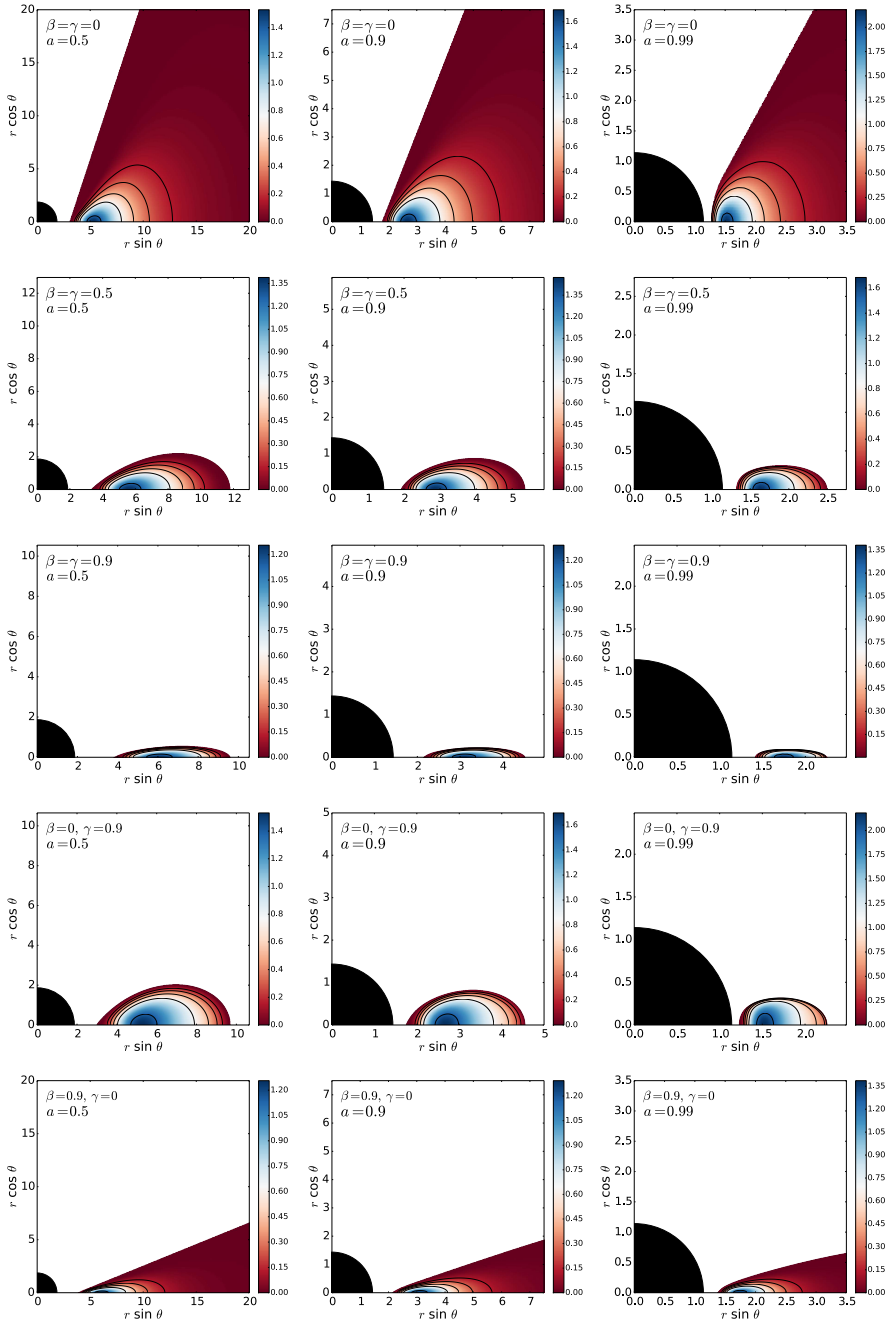

Figure 2.2 Isodensity distributions for all models of Table 2.3. From left to right the columns correspond to increasing values of the black hole spin: $a = 0.5$, 0.9 and 0.99. From top to bottom the rows correspond to the following parameter combinations: a) $\gamma = \beta = 0$; b) $\gamma = \beta = 0.5$; c) $\gamma = \beta = 0.9$; d) $\gamma = 0.9$, $\beta = 0$; e) $\gamma = 0$, $\beta = 0.9$. Note that the spatial scale of the plots differs as it has been chosen to facilitate the visualization of the discs.

Table 2.3 List of models for $\beta_{\rm m_c} = 10^{-3}$. The naming of the models and the parameters reported in the columns are as in Table 2.1.

	β	γ	$r_{\rm max}$	$r_{\rm m,max}$	ΔW $(\times 10^{-2})$	$r_{\rm in}$	$r_{\rm out}$
A1	0.0	0.0	5.11	5.51	−6.35	2.91	–
A2	0.5	0.5	5.55	5.80	−2.27	3.20	11.8
A3	0.9	0.9	5.95	6.15	−0.30	3.70	9.58
A4	0.0	0.9	5.21	5.51	−6.35	2.91	9.68
A5	0.9	0.0	5.90	6.10	−0.30	3.70	–
B1	0.0	0.0	2.53	2.73	−12.9	1.73	–
B2	0.5	0.5	2.81	2.91	−4.32	1.86	5.35
B3	0.9	0.9	3.03	3.13	−0.54	2.08	4.52
B4	0.0	0.9	2.65	2.80	−12.9	1.73	4.54
B5	0.9	0.0	3.03	3.13	−0.54	2.08	–
C1	0.0	0.0	1.46	1.51	−24.6	1.21	–
C2	0.5	0.5	1.56	1.61	−7.34	1.26	2.50
C3	0.9	0.9	1.70	1.75	−0.85	1.35	2.25
C4	0.0	0.9	1.50	1.57	−24.6	1.21	2.26
C5	0.9	0.0	1.72	1.77	−0.85	1.35	–

by the model in the top-left panel. As the black hole spin increases, the discs are closer to the black hole and its relative size with respect to the black hole is smaller for all values of γ and β. For $\gamma = 0$ the discs are infinite, irrespective of the value of a and β. As γ and β increase from 0 to 0.9 (compare the three top rows) the discs become significantly thinner and radially smaller (see also Fig. 2.5 below). It is also interesting to note that the maximum value of the rest-mass density is higher (with respect to the value at the disc centre) as the spin increases.

Figure 2.3 shows the effects of changing the parameter $\beta_{\rm m_c}$ (the magnetisation) in the structure of the discs. From left to right the values plotted in each panel are $\beta_{\rm m_c} = 10^3$, 1, and 10^{-3}. The model chosen corresponds to $a = 0.9$ and $\gamma = \beta = 0.5$. The larger the value of $\beta_{\rm m_c}$ the less important the effects of the magnetisation in the disc structure. Figure 2.3 shows that, at least for the kind of magnetic field distribution we are considering, the effects of the magnetisation are minor. The disc structure remains fairly similar for all values of $\beta_{\rm m_c}$ and the only quantitative differences are found in the location of the centre of the disc (which moves inward with decreasing $\beta_{\rm m_c}$) and of the range of variation of the isodensity contours (the maximum being slightly larger with decreasing $\beta_{\rm m_c}$). This can be more clearly visualized in Figure 2.4 which displays the radial

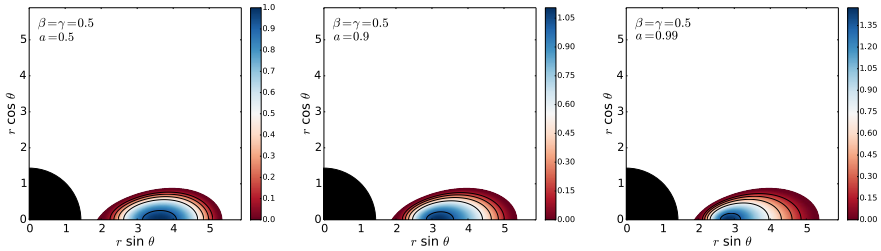

Figure 2.3 Effects of the magnetisation in the structure of the disc. From left to right the values are $\beta_{\rm m_c} = 10^3$, 1, and 10^{-3}.

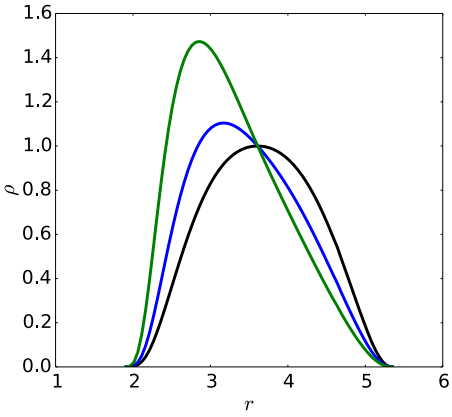

Figure 2.4 Radial profiles of the rest-mass density in the equatorial plane for $\beta_{\rm m_c} = 10^3$ (black curve), 1 (blue curve), and 10^{-3} (green curve).

profile at the equatorial plane of the rest-mass density for the same three cases plotted in Fig. 2.3.

Next, we show in Fig. 2.5 the corresponding radial profiles at the equatorial plane for the models with black hole spin $a = 0.9$. We consider the case $\beta_{\rm m_c} = 10^{-3}$ (highest magnetisation) and the same combination of the γ and β parameters that we employed in Fig. 2.2. Therefore, this plot depicts the radial profiles of the models occupying the central column of Fig. 2.2. These profiles allow for a clearer quantification of the radial extent of the discs with γ and β. As mentioned in the description of Fig. 2.2 as γ and β increase from 0 to 0.9 (compare black, blue, and green curves) the discs become gradually smaller. At the same time, the radial location of the rest-mass density maximum increases and the maximum value of the central rest-mass density (and pressure) decreases. It is worth noticing that the radial profiles of some of the models

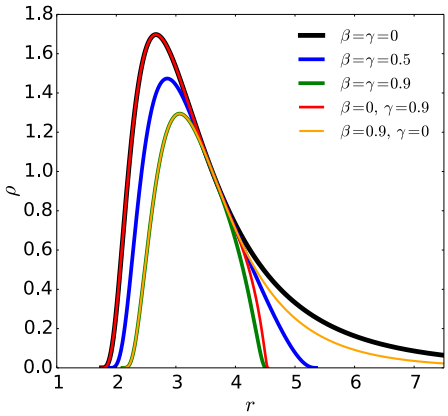

Figure 2.5 Radial profiles at the equatorial plane for models with $a = 0.9$, $\beta_{\mathrm{m_c}} = 10^{-3}$, and same combination of the γ and β parameters as in the rows of Fig. 2.2 (the specific values are indicated in the legend).

overlap below a certain radius. More precisely, the black and red curves overlap below $r \sim r_{\mathrm{c}}$ (which corresponds to $\rho \sim 1$) and also the green and orange curves. In addition, this figure clearly shows that, besides modifying the thickness of the disc, β is the parameter which determines the value of the rest-mass density (and pressure) maximum. On the other hand, the parameter γ is only relevant for controlling the radial size of the discs.

In order to provide a quantitative comparison of the structural differences that appear along the sequence of equilibrium models, we plot in Fig. 2.6 the variation of the maximum of the rest-mass density (left panel), the radial location of the maximum of the fluid pressure (middle panel), and the radial location of the maximum of the magnetic pressure (right panel) as a function of the magnetisation parameter $\beta_{\mathrm{m_c}}$. All quantities plotted are measured at the equatorial plane. Let us first consider the left panel. The line type used indicates the value of the black hole spin a, namely, a dotted line is for $a = 0.5$, a dashed line for $a = 0.9$, and a solid line for $a = 0.99$. Correspondingly, the colour of the lines indicates the value of β and γ used, namely, red curves correspond to $\gamma = \beta = 0$, the blue ones to $\gamma = \beta = 0.5$, and the black ones to $\gamma = \beta = 0.9$. All curves show the same monotonically decreasing trend with $\beta_{\mathrm{m_c}}$, yet for small enough and large enough values of $\beta_{\mathrm{m_c}}$ the value of the rest-mass density maximum does not change. However, in the interval $10^{-2} \leq \beta_{\mathrm{m_c}} \leq 10^{2}$, ρ_{max} changes abruptly. The larger the black hole spin the larger the drop in the maximum of the rest-mass density. For sufficiently large values of $\beta_{\mathrm{m_c}}$ (small

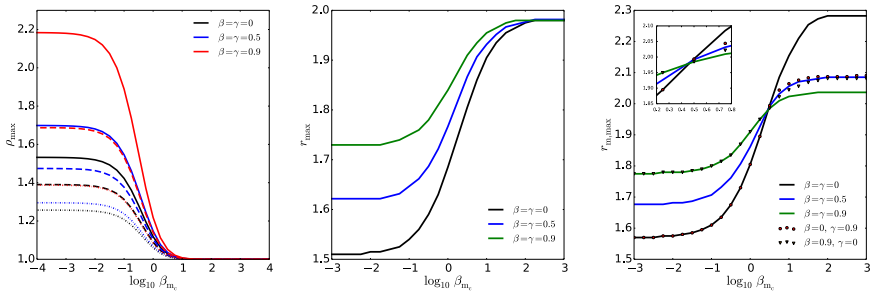

Figure 2.6 Effects of $\beta_{\mathrm{m_c}}$. Left panel: variation of the value of the maximum rest-mass density with respect to the logarithm of the magnetisation parameter. The solid, dashed, and dotted lines refer to $a = 0.99$, 0.9 and 0.5, respectively, and the colour code refers to the models shown in the legend. Middle panel: variation of the location of the rest-mass density maximum (and fluid pressure) with respect to the logarithm of the magnetisation parameter for the three models shown in the legend with $a = 0.99$. Right panel: variation (also for $a = 0.99$) of the location of the maximum of the magnetic pressure with respect to the logarithm of $\beta_{\mathrm{m_c}}$.

magnetisation) the value of $\rho_{\max}$ stays constant to the same value irrespective of the black hole rotation.

In the middle panel of Fig. 2.6 we show the radial location of the maximum of the fluid pressure as a function of $\beta_{\mathrm{m_c}}$. The black hole spin is $a = 0.99$ and the values of β and γ are indicated in the legend. For all values of β and γ, the maximum of the location of the disc fluid pressure decreases with decreasing $\beta_{\mathrm{m_c}}$. Below $\beta_{\mathrm{m_c}} \sim 10^{-3}$ the location of the maximum does no longer change. The panel also shows that above $\beta_{\mathrm{m_c}} \sim 10^{3}$ the constant value of $r_{\max}$ is the same irrespective of β and γ, as expected, because for purely hydrodynamic discs, $r_{\max} = r_{\mathrm{c}}$.

The dependence of the location of the maximum of the magnetic pressure with $\beta_{\mathrm{m_c}}$ is shown in the right panel of Fig. 2.6. While this location also decreases with decreasing $\beta_{\mathrm{m_c}}$, the constant value achieved for values above $\beta_{\mathrm{m_c}} \sim 10^{3}$ does depend on the specific values of β and γ, contrary to what happens with the fluid pressure. It must be noted that the location of the maximum of the magnetic pressure is identical for all models considered when $\beta_{\mathrm{m_c}} \equiv 1/(\lambda - 1) = 3$, as we show in Appendix 2.7. At this value of $\beta_{\mathrm{m_c}}$ all models cross at $r_{\mathrm{m}_{\max}} = r_{\mathrm{c}}$, as it is more clearly shown in the inset of the right panel of Fig. 2.6.

As a final remark we note that in the left and middle panels of Fig. 2.6 we do not show the data for models with $\beta \neq \gamma$ as they coincide with the respective models with the same value of β. Moreover, the middle and right panels only show the data for $a = 0.99$ because changing the value of the spin parameter of the black hole only yields a change of scale. Therefore, if we chose the range

of the graph accordingly, the plots would be identical (same relative differences between the curves) irrespective of the value of a.

2.5 Conclusions

In this paper we have presented a procedure to build equilibrium sequences of magnetised, non-self-gravitating discs around Kerr black holes which combines the two existing approaches of Komissarov [2006] and Qian et al. [2009]. On the one hand we have followed Qian et al. [2009] and have assumed a form of the angular momentum distribution in the disc from which the location and morphology of surfaces of equal potential can be computed. As a limiting case, this ansatz includes the constant angular momentum case originally employed in the construction of thick tori – or Polish doughnuts [Abramowicz, Jaroszynski, and Sikora 1978, Kozlowski, Jaroszynski, and Abramowicz 1978] – and was already used by Qian et al. [2009] to build equilibrium sequences of purely hydrodynamical models. On the other hand, our discs are endowed with a purely toroidal magnetic field, as in the work of Komissarov [2006], which provides the methodology we have followed to handle the magnetic terms. On a similar note, we cite the work of Wielgus et al. [2015] who have recently extended the solution of Komissarov [2006] to include non-constant specific angular momentum tori. These authors limited their consideration to power-law distributions and were particularly focused on the stability of such tori to the MRI. The approach discussed in our work differs from that of Wielgus et al. [2015] and, moreover, we have explored a much wider parameter space.

We have discussed the properties of the new models and their dependence on the initial parameters, namely the magnetisation parameter $\beta_{\mathrm{m_c}}$, the parameters β and γ describing the angular momentum distribution, the black hole spin parameter a, and the inner radius of the disc r_{in}. We have shown the effects of changing β and γ beyond the purely hydrodynamical case considered in Qian et al. [2009]. The morphology of the solutions we have built no longer changes for magnetisation values above $\beta_{\mathrm{m_c}} \sim 10^3$ and below $\beta_{\mathrm{m_c}} \sim 10^{-3}$. These cases can thus be considered as the hydrodynamical and MHD limiting cases, respectively. The new sequences of magnetised discs around black holes presented in this work can be used as initial data for magnetohydrodynamical evolutions in general relativity. In the near future, we plan to extend this work along two main directions, namely (i) including the self-gravity of the discs, following the approach laid out in Stergioulas [2011a], and (ii) constructing accretion discs

around hairy black holes, both, with scalar and Proca hair [Herdeiro and Radu 2014b, Herdeiro, Radu, and Rúnarsson 2016].

2.6 Appendix: Divergence of equation (2.24) at $\theta = \pi/2$

To prove that Eq. (2.24) diverges at $\theta = \pi/2$ we need to show that Eq. (2.22) vanishes at the equator, i.e.

$$\partial_\theta W = \partial_\theta \ln|u_t| - \frac{\Omega \partial_\theta l}{1-\Omega l} = 0. \tag{2.28}$$

Then, we have to prove that either the two terms of this equation are equal or they are identically zero at $\theta = \pi/2$. We shall see that the latter is true. First, we take the derivative of the angular momentum distribution $\partial_\theta l$. From Eq. (7) we can write the angular momentum distribution as $l(r,\theta) = l(r)\sin^{2\gamma}\theta$, so that the derivative reads

$$\partial_\theta l = 2\gamma l(r)\sin^{2\gamma-1}\theta\cos\theta\,. \tag{2.29}$$

Taking $\theta = \pi/2$ leads to $\partial_\theta l = 0$, so the second term equals to zero. To show that the first term is also zero, we write it as

$$\partial_\theta \ln|u_t| = \partial_\theta \ln\left(\frac{\mathcal{L}}{\mathcal{A}}\right)^{\frac{1}{2}}, \tag{2.30}$$

where $\mathcal{L} = g_{t\phi}^2 - g_{tt}g_{\phi\phi}$ and $\mathcal{A} = g_{\phi\phi} + 2lg_{t\phi} + l^2 g_{tt}$, and we have dropped the absolute value, as it is irrelevant to this discussion. Then, the derivative is

$$\partial_\theta \ln|u_t| = \frac{1}{2}\frac{\mathcal{A}}{\mathcal{L}}\frac{\mathcal{A}\partial_\theta\mathcal{L} - \mathcal{L}\partial_\theta\mathcal{A}}{\mathcal{A}^2} = \frac{1}{2}\frac{\mathcal{A}\partial_\theta\mathcal{L} - \mathcal{L}\partial_\theta\mathcal{A}}{\mathcal{A}\mathcal{L}}\,. \tag{2.31}$$

We use Boyer-Lindquist coordinates, for which the metric components read

$$\begin{aligned} g_{tt} &= -\left(1 - \frac{2Mr}{\rho^2}\right),\ g_{t\phi} = -\frac{2Mar\sin^2\theta}{\rho^2}, \\ g_{\phi\phi} &= \left(r^2 + a^2 + \frac{2Ma^2 r\sin^2\theta}{\rho^2}\right)\sin^2\theta\,, \end{aligned} \tag{2.32}$$

where $\rho^2 = r^2 + a^2\cos^2\theta$. Therefore, we obtain $\mathcal{L} = \Delta\sin^2\theta$, where $\Delta = r^2 - 2Mr + a^2$, and its derivative $\partial_\theta\mathcal{L} = 2\Delta\sin\theta\cos\theta$, which is zero for $\theta = \pi/2$.

Next, we take the derivative of $\mathcal{A}$

$$\partial_\theta \mathcal{A} = \partial_\theta g_{\phi\phi} + 2(\partial_\theta l) g_{t\phi} + 2l\partial_\theta g_{t\phi} + 2l(\partial_\theta l) g_{tt} + l^2 \partial_\theta g_{tt} = \\ = \partial_\theta g_{\phi\phi} + 2l\partial_\theta g_{t\phi} + l^2 \partial_\theta g_{tt}\,, \tag{2.33}$$

where we have used the previous result that $\partial_\theta l = 0$ at $\theta = \pi/2$. By inspecting the metric components, it is easy to see that all terms depending on θ are functions of $\sin^2\theta$ or $\cos^2\theta$. This means their θ derivatives will have at least a $\cos\theta$ multiplying. Then $\partial_\theta \mathcal{A} = 0$ at $\theta = \pi/2$. Therefore, $\partial_\theta \ln|u_t|$ is also zero at $\theta = \pi/2$.

2.7 Appendix: Value of the magnetisation parameter for $r_{\mathrm{m}_{\mathrm{max}}} = r_{\mathrm{c}}$

In this appendix we derive the condition $\beta_{\mathrm{m_c}} = 1/(\lambda - 1)$ for $r_{\mathrm{m}_{\mathrm{max}}} = r_{\mathrm{c}}$. First, we can use Eq. (2.14) to write

$$\frac{\partial p_{\mathrm{m}}(r)}{\partial r} = \partial_r \left(K_{\mathrm{m}} \mathcal{L}^{\lambda-1} w^\lambda \right) = 0\,, \tag{2.34}$$

which yields

$$\partial_r p_{\mathrm{m}} = K_{\mathrm{m}} \mathcal{L}^{\lambda-2} w^\lambda [(\lambda - 1)(\partial_r \mathcal{L}) w + \lambda \mathcal{L}(\partial_r w)] = 0\,. \tag{2.35}$$

Inside the disc $K_{\mathrm{m}} \mathcal{L}^{\lambda-2} w^\lambda \neq 0$. Therefore, to fulfill the extremum condition (2.34) we need

$$(\lambda - 1)(\partial_r \mathcal{L}) w + \lambda \mathcal{L}(\partial_r w) = 0\,. \tag{2.36}$$

To evaluate this expression, we need to compute the partial derivatives $\partial_r \mathcal{L}$ and $\partial_r w$. The derivative of $\mathcal{L}$ is straightforward, since $\mathcal{L} = \Delta \sin^2\theta$,

$$\partial_r \mathcal{L} = 2(r - M)\sin^2\theta\,. \tag{2.37}$$

Let us now discuss $\partial_r w$. From Eq. (2.20) we have

$$w = \left[-\Delta W \left(\frac{\lambda - 1}{\lambda} \right) \frac{1}{K + K_{\mathrm{m}} \mathcal{L}^{\lambda-1}} \right]^{\frac{1}{\lambda-1}}\,. \tag{2.38}$$

Taking its derivative we obtain

$$\partial_r w = \frac{w}{\lambda - 1} \left[-\Delta W \left(\frac{\lambda - 1}{\lambda} \right) \frac{1}{K + K_{\mathrm{m}} \mathcal{L}^{\lambda-1}} \right]^{-1} \\ \times \left[\left(-\partial_r W \left(\frac{\lambda - 1}{\lambda} \right) \frac{1}{K + K_{\mathrm{m}} \mathcal{L}^{\lambda-1}} \right) \right.$$

$$+ \quad \left(-\Delta W \left(\frac{\lambda-1}{\lambda}\right) \frac{-(\lambda-1)K_{\mathrm{m}}\mathcal{L}^{\lambda-2}\partial_r\mathcal{L}}{(K+K_{\mathrm{m}}\mathcal{L}^{\lambda-1})^2}\right] . \tag{2.39}$$

Since at $r = r_{\mathrm{c}}$ the derivative of the potential is zero, $\partial_r W(r, \pi/2)|_{r=r_{\mathrm{c}}} = 0$, we can simplify the above expression to obtain

$$\begin{aligned} \partial_r w &= \frac{w}{\lambda-1}\left[-\Delta W\left(\frac{\lambda-1}{\lambda}\right)\frac{1}{K+K_{\mathrm{m}}\mathcal{L}^{\lambda-1}}\right]^{-1} \\ &\times \left(-\Delta W\left(\frac{\lambda-1}{\lambda}\right)\frac{1}{K+K_{\mathrm{m}}\mathcal{L}^{\lambda-1}}\right) \\ &\times \left[\frac{-(\lambda-1)K_{\mathrm{m}}\mathcal{L}^{\lambda-2}\partial_r\mathcal{L}}{K+K_{\mathrm{m}}\mathcal{L}^{\lambda-1}}\right] , \end{aligned} \tag{2.40}$$

which can be further simplified to the following form

$$\partial_r w = -w\left[\frac{K_{\mathrm{m}}\mathcal{L}^{\lambda-2}\partial_r\mathcal{L}}{K+K_{\mathrm{m}}\mathcal{L}^{\lambda-1}}\right] . \tag{2.41}$$

Next, by inserting this expression in Eq. (2.36) we obtain

$$(\partial_r\mathcal{L})w[(\lambda-1)(K+K_{\mathrm{m}}\mathcal{L}^{\lambda-1}) - \lambda K_{\mathrm{m}}\mathcal{L}^{\lambda-1}] = 0 . \tag{2.42}$$

Since $(\partial_r\mathcal{L})w \neq 0$ inside the disc, the above equation leads to

$$K(\lambda-1) = K_{\mathrm{m}}\mathcal{L}^{\lambda-1} . \tag{2.43}$$

Moreover, we can use Eqs. (2.12), (2.14) and (2.26) at the centre (remember that $w_{\mathrm{c}} = 1$) to write K as $K = \beta_{\mathrm{m_c}} K_{\mathrm{m}}\mathcal{L}^{\lambda-1}$. Therefore, this allows us to obtain the following simple expression for the value of the magnetisation parameter at the centre of the disc

$$\beta_{\mathrm{m_c}} = \frac{1}{\lambda-1} . \tag{2.44}$$

It is relevant to note that the only reference to the explicit form of the metric is done to show that $\mathcal{L} \neq 0$ and $\partial_r\mathcal{L} \neq 0$ inside the disc. This means that our result holds for any stationary and axisymmetric metric if the aforementioned inequalities hold. Moreover, the result is also true for any angular momentum distribution that allows for the existence of a cusp and a centre (and $r_{\mathrm{c}} \neq r_{\mathrm{cusp}}$).

Chapter 3

Magnetized accretion disks around Kerr black holes with scalar hair: Constant angular momentum disks

This chapter is based on the following publication: S. Gimeno-Soler, J. A. Font, C. Herdeiro & E. Radu. Magnetized accretion disks around Kerr black holes with scalar hair: Constant angular momentum disks, *Physical Review D* 99, 043002 (2019), DOI: 10.1103/PhysRevD.99.043002.

3.1 Introduction

In recent years, new families of stationary, asymptotically flat black holes (BHs) avoiding the so-called "no hair" theorems, have been obtained both in general relativity and in modified gravity (see e.g. [Herdeiro and Radu 2015b] and references therein). Among those, Kerr BHs with synchronised hair [Herdeiro and Radu 2014b, Herdeiro, Radu, and Rúnarsson 2016] are a counterexample to the no hair conjecture resulting from minimally coupling Einstein's gravity to simple (bosonic) matter fields obeying all energy conditions. The physical conditions and stability properties of these classes of *hairy* BHs (HBHs) have been recently investigated to assess their potential viability as alternatives to astrophysical

Kerr BHs. On the one hand, Kerr BHs with Proca hair have been shown to form dynamically as the end-product of the superradiant instability [East and Pretorius 2017, Herdeiro and Radu 2017] (see also [Sanchis-Gual et al. 2016, Bosch, Green, and Lehner 2016] for the case of a charged scalar field around a charged BH in spherical symmetry). On the other hand, even though the hairy BHs themselves are (like Kerr BHs) afflicted by superradiant instabilities [Herdeiro and Radu 2014a, Ganchev and Santos 2018], these instabilities are weaker than for Kerr and, at least in some regions of parameter space, are inefficient for astrophysical time scales, making the hairy BHs *effectively* stable against superradiance [Degollado, Herdeiro, and Radu 2018].

In the observational arena, the LIGO/Virgo detection of gravitational waves from binary BHs [Abbott et al. 2016, Abbott et al. 2016, Abbott et al. 2017a, Abbott et al. 2017b, Abbott et al. 2017a] and the exciting prospects of observing the first image – the black hole *shadow* – of a BH by the Event Horizon Telescope (EHT) [Fish et al. 2016] opens the opportunity to test the true nature of BHs – the no-hair hypothesis – and, in particular, the astrophysical relevance of HBHs. It is not yet known whether the LIGO/Virgo binary BH signals are consistent with alternative scenarios, such as the merger of ultracompact boson stars or non-Kerr BHs, because the latter possibilities remain thus far insufficiently modelled. Likewise, Kerr BHs with scalar hair (KBHsSH) can exhibit very distinct shadows from those of (bald) Kerr BHs, as shown by Cunha et al. [2015] and Vincent et al. [2016] for two different setups for the light source, either a celestial sphere far from the compact object or an emitting torus of matter surrounding the BH, respectively. It is therefore an intriguing open possibility if the very long baseline interferometric observations of BH candidates in Sgr A* and M87 envisaged by the EHT may constrain the astrophysical significance of HBHs.

The setup considered by Vincent et al. [2016] in which the light source producing the BH shadow is an accretion disk, is arguably more realistic than the distant celestial sphere of Cunha et al. [2015]. Thick accretion disks (or tori) are common systems in astrophysics, either surrounding the supermassive central BHs of quasars and active galactic nuclei or, at stellar scale, surrounding the compact objects in X-ray binaries, microquasars, and gamma-ray bursts (see [Abramowicz and Fragile 2013] and references therein). In this paper we present new families of stationary solutions of magnetized thick accretion disks around KBHsSH that differ from those considered by Vincent et al. [2016]. Our procedure, which combines earlier approaches put forward by Komissarov [2006] and Qian et al. [2009] was presented in Gimeno-Soler and Font [2017] for

the Kerr BH case. In Ref. [Gimeno-Soler and Font 2017] we built equilibrium sequences of accretion disks in the test-fluid approximation endowed with a purely toroidal magnetic field, assuming a form of the angular momentum distribution that departs from the constant case considered by Komissarov [2006] and from which the location and morphology of the equipotential surfaces can be numerically computed. Our goal in the present work is to extend this approach to KBHsSH and to assess the dependence of the morphology and properties of accretion disks on the type of BH considered, either Kerr BHs of varying spins or KBHsSH. In this first investigation we focus on disks with a constant distribution of specific angular momentum. In the purely hydrodynamical case, such a model is commonly refereed to as a 'Polish doughnut', after the seminal work by Abramowicz, Jaroszynski, and Sikora [1978] (but see also [Fishbone and Moncrief 1976]). In a companion paper we will present the non-constant (power-law) case, whose sequences have already been computed. The dynamical (non-linear) stability of these solutions as well as the analysis of the corresponding shadows will be discussed elsewhere.

The organization of this paper is as follows: Section 3.2 presents the mathematical framework we employ to build magnetized disks in the numerically generated spacetimes of KBHsSH. Section 3.3 discusses the corresponding numerical methodology to build the disks. Sequences of equilibrium models are presented in Section 3.4 along with the discussion of their morphological features and properties and the comparison with models around Kerr BHs. Finally, our conclusions are summarized in Section 3.5. Geometrized units ($G = c = 1$) are used throughout.

3.2 Framework

3.2.1 Spacetime metric and KBHsSH models

The models of KBHsSH we use in this study are built following the procedure described in Herdeiro and Radu [2015a]. The underlying theoretical framework is the Einstein-Klein-Gordon (EKG) field theory, describing a massive complex scalar field Ψ minimally coupled to Einstein gravity. KBHsSH solutions are obtained by using the following ansatz for the metric and the scalar field [Herdeiro and Radu 2014b]

$$\begin{aligned} \mathrm{d}s^2 &= e^{2F_1}\left(\frac{\mathrm{d}r^2}{N}+r^2\mathrm{d}\theta^2\right)+e^{2F_2}r^2\sin^2\theta(\mathrm{d}\phi-W\mathrm{d}t)^2 \\ &- e^{2F_0}N\mathrm{d}t^2\,, \end{aligned} \tag{3.1}$$

$$\Psi = \phi(r,\theta)e^{\mathrm{i}(m\varphi-\omega t)}\,, \tag{3.2}$$

with $N = 1 - r_{\rm H}/r$, where $r_{\rm H}$ is the radius of the event horizon of the BH, and W, F_1, F_2, F_0 are functions of r and θ. Moreover, ω is the scalar field frequency and m is the azimuthal harmonic index. We note that the radial coordinate r is related to the Boyer-Lindquist radial coordinate $r_{\rm BL}$ by $r = r_{\rm BL} - a^2/r_{\rm H,BL}$, in the Kerr limit, where $a = J/M$ stands for the spin of the BH and $r_{\rm H,BL}$ is the location of the horizon in Boyer-Lindquist coordinates.

The stationary and axisymmetric metric ansatz is a solution to the EKG field equations $R_{ab} - \frac{1}{2}Rg_{ab} = 8\pi(T_{\rm SF})_{ab}$ with

$$\begin{aligned}(T_{\rm SF})_{ab} &= \partial_a\Psi^*\partial_b\Psi + \partial_b\Psi^*\partial_a\Psi \\ &- g_{ab}\left(\frac{1}{2}g^{cd}(\partial_c\Psi^*\partial_d\Psi + \partial_d\Psi^*\partial_c\Psi) + \mu^2\Psi^*\Psi\right),\end{aligned} \tag{3.3}$$

where μ is the mass of the scalar field and superscript $(^*)$ denotes complex conjugation. The interested reader is addressed to [Herdeiro and Radu 2015a] for details on the equations of motion for the scalar field Ψ and the four metric functions W, F_0, F_1, F_2, along with their solution.

Table 3.1 lists the seven KBHsSH models we use in this work. The models have been selected to span all regions of interest in the parameter space. Model I corresponds to a Kerr-like model, with almost all the mass and angular momentum stored in the BH (namely, 94.7% of the total mass and 87.2% of the total angular momentum of the spacetime are stored in the BH), while model VII corresponds to a hairy Kerr BH with almost all the mass (98.15%) and angular momentum (99.76%) stored in the scalar field. It is worth mentioning that some of the models violate the Kerr bound (i.e. the normalized spin parameter is larger than unity) in terms of both ADM or horizon quantities. This is not a source of concern because, as shown in Herdeiro and Radu [2015c], the linear velocity of the horizon, $v_{\rm H}$, never exceeds the speed of light. For comparison, we also show in Table 3.1 the spin parameter $a_{\rm H_{eq}}$ corresponding to a Kerr BH with a horizon linear velocity $v_{\rm H}$. In the last column of Table 3.1 we indicate the horizon sphericity of the KBHsSH, defined in Delgado, Herdeiro, and Radu [2018] as the quotient of the equatorial and polar proper lengths of the event horizon

$$\mathfrak{s} = \frac{L_{\rm e}}{L_{\rm p}} = \frac{\int_0^{2\pi}\mathrm{d}\phi\, e^{F_2(r_{\rm H},\pi/2)}r_{\rm H}}{2\int_0^{\pi}\mathrm{d}\theta\, e^{F_1(r_{\rm H},\theta)}r_{\rm H}}\,. \tag{3.4}$$

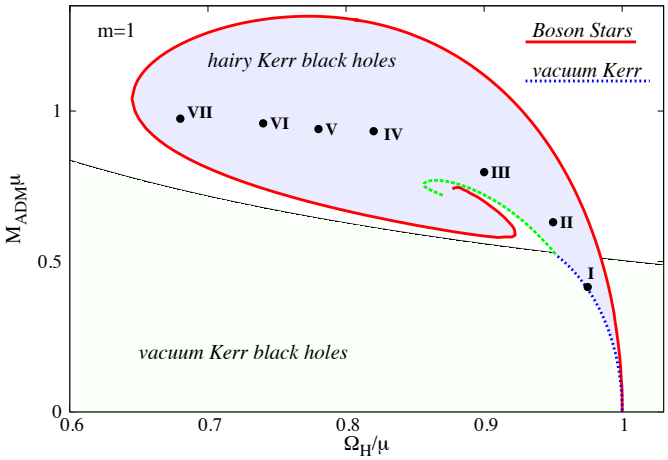

Figure 3.1 Domain of existence for KBHsSH (shaded blue area) in an ADM mass versus scalar field frequency diagram. The seven solutions to be studied herein are highlighted in this diagram.

In addition to the information provided in Table 3.1, Figure 3.1 plots the location of our models in the domain of existence of KBHsSH in an ADM mass versus scalar field frequency diagram.

3.2.2 Distribution of angular momentum in the disk

Equilibrium models of thick disks around Kerr BHs are built assuming that the spacetime metric and the fluid fields are stationary and axisymmetric (see, e.g. [Font and Daigne 2002, Daigne and Font 2004, Gimeno-Soler and Font 2017] and references therein). For disks around KBHsSH we can follow the same approach as the metric ansatz given by Eq. (3.1) is stationary and axisymmetric.

We start by introducing the specific angular momentum l and the angular velocity Ω employing the standard definitions,

$$l = -\frac{u_\phi}{u_t}, \quad \Omega = \frac{u^\phi}{u^t}, \tag{3.5}$$

where u^μ is the fluid four-velocity. The relationship between l and Ω is given by the equations

$$l = -\frac{\Omega g_{\phi\phi} + g_{t\phi}}{\Omega g_{t\phi} + g_{tt}}, \quad \Omega = -\frac{l g_{tt} + g_{t\phi}}{l g_{t\phi} + g_{\phi\phi}}, \tag{3.6}$$

where we are assuming circular motion, i.e. the four-velocity can be written as

$$u^\mu = (u^t, 0, 0, u^\phi)\,. \tag{3.7}$$

Table 3.1 List of models of KBHsSH used in this work. From left to right the columns report the name of the model, the ADM mass, $M_{\rm ADM}$, the ADM angular momentum, $J_{\rm ADM}$, the horizon mass, $M_{\rm H}$, the horizon angular momentum, $J_{\rm H}$, the mass of the scalar field, $M_{\rm SF}$, the angular momentum of the scalar field, $J_{\rm SF}$, the radius of the event horizon, $r_{\rm H}$, the values of the normalized spin parameter for the ADM quantities, $a_{\rm ADM}$, and for the BH horizon quantities, $a_{\rm H}$, the horizon linear velocity, $v_{\rm H}$, the spin parameter corresponding to a Kerr BH with a linear velocity equal to $v_{\rm H}$, $a_{\rm H_{eq}}$, and the sphericity of the horizon, $\mathfrak{s}$. Here $\mu = 1$.

Model	$M_{\rm ADM}$	$J_{\rm ADM}$	$M_{\rm H}$	$J_{\rm H}$	$M_{\rm SF}$	$J_{\rm SF}$	$r_{\rm H}$	$a_{\rm ADM}$	$a_{\rm H}$	$v_{\rm H}$	$a_{\rm H_{eq}}$	$\mathfrak{s}$
I	0.415	0.172	0.393	0.150	0.022	0.022	0.200	0.9987	0.971	0.7685	0.9663	1.404
II	0.630	0.403	0.340	0.121	0.290	0.282	0.221	1.0140	0.376	0.6802	0.9301	1.352
III	0.797	0.573	0.365	0.172	0.432	0.401	0.111	0.9032	1.295	0.7524	0.9608	1.489
IV	0.933	0.739	0.234	0.114	0.699	0.625	0.100	0.8489	2.082	0.5635	0.8554	1.425
V	0.940	0.757	0.159	0.076	0.781	0.680	0.091	0.8560	3.017	0.4438	0.7415	1.357
VI	0.959	0.795	0.087	0.034	0.872	0.747	0.088	0.8644	3.947	0.2988	0.5487	1.222
VII	0.975	0.850	0.018	0.002	0.957	0.848	0.040	0.8941	6.173	0.0973	0.1928	1.039

The approach we followed in Gimeno-Soler and Font [2017] for the angular momentum distribution of the disks was introduced by Qian et al. [2009], and it is characterized by three free parameters, β, γ, and η (see Eq. (7) in Gimeno-Soler and Font [2017]). In this work, for simplicity and to reduce the ample space of parameters of the system, we consider a constant angular momentum distribution, $l(r,\theta) = \text{const}$, which corresponds to setting $\beta = \gamma = 0$ in Gimeno-Soler and Font [2017]. This choice also allows for the presence of a cusp (and hence matter accretion onto the BH) and a centre. Following [Daigne and Font 2004], the specific value of the angular momentum corresponding to bound fluid elements ($-u_t < 1$) is computed as the minimum of the following equation

$$l_{\rm b}^{\pm}(r,\theta) = \frac{g_{t\phi} \pm \sqrt{(g_{t\phi}^2 - g_{tt}g_{\phi\phi})(1+g_{tt})}}{-g_{tt}}\,, \tag{3.8}$$

where the plus sign solution corresponds to prograde orbits and the minus sign solution to retrograde orbits. Our convention is that the angular momentum of the BH is positive and the matter of the disk rotates in the positive (negative) direction of ϕ for a prograde (retrograde) disk. Equation ((3.8)) is given by Daigne and Font [2004] for Kerr BHs, but it is valid for any stationary and axisymmetric spacetime. For prograde motion, the function has a minimum outside the event horizon. The location of this minimum corresponds with the marginally bound orbit $r_{\rm mb}$ (also known as ICO, innermost circular orbit, in the literature), and the angular momentum corresponds to the Keplerian angular momentum $l_{\rm mb}$ at that point. We show the proof of this statement in Appendix 3.6.

3.2.3 Magnetized disks

To account for the magnetic field in the disks we use the procedure described by Komissarov [2006] and Montero et al. [2007]. First, we write the equations of ideal general relativistic MHD as the following conservation laws, $\nabla_\mu T^{\mu\nu} = 0$, $\nabla_\mu {}^*F^{\mu\nu} = 0$, and $\nabla_\mu(\rho u^\mu) = 0$, where ∇_μ is the covariant derivative and

$$T^{\mu\nu} = (\rho h + b^2)u^\mu u^\nu + (p + p_{\rm m})g^{\mu\nu} - b^\mu b^\nu, \tag{3.9}$$

is the energy-momentum tensor of a magnetized perfect fluid, with h, ρ, p, and $p_{\rm m}$ being the fluid specific enthalpy, density, fluid pressure, and magnetic pressure, respectively, the latter defined as $p_{\rm m} = b^2/2$. The ratio of fluid pressure to magnetic pressure defines the magnetization parameter $\beta_{\rm m} = p/p_{\rm m}$. Moreover, ${}^*F^{\mu\nu} = b^\mu u^\nu - b^\nu u^\mu$ is the (dual of the) Faraday tensor relative to an observer with four-velocity u^μ, and b^μ is the magnetic field in that frame, with $b^2 = b^\mu b_\mu$ (see [Antón et al. 2006] for further details). Assuming the magnetic field is purely azimuthal, i.e. $b^r = b^\theta = 0$, and taking into account that the flow is stationary and axisymmetric, the conservation of the current density and of the Faraday tensor follow. Contracting the divergence of Eq. (3.9) with the projection tensor $h^\alpha_{\ \beta} = \delta^\alpha_{\ \beta} + u^\alpha u_\beta$, we arrive at

$$(\rho h + b^2)u_\nu \partial_i u^\nu + \partial_i\left(p + \frac{b^2}{2}\right) - b_\nu \partial_i b^\nu = 0\,, \tag{3.10}$$

where $i = r, \theta$. This equation can be rewritten in terms of the specific angular momentum l and of the angular velocity Ω,

$$\partial_i(\ln|u_t|) - \frac{\Omega\partial_i l}{1 - l\Omega} + \frac{\partial_i p}{\rho h} + \frac{\partial_i(\mathcal{L}b^2)}{2\mathcal{L}\rho h} = 0\,, \tag{3.11}$$

where $\mathcal{L} = g_{t\phi}^2 - g_{tt}g_{\phi\phi}$.

To integrate Eq. (3.11) we need to assume an equation of state (EOS). We assume a polytropic EOS of the form

$$p = K\rho^\Gamma, \tag{3.12}$$

with K and Γ constants. By introducing the definitions $\tilde{p}_{\rm m} = \mathcal{L}p_{\rm m}$, $w = \rho h$ and $\tilde{w} = \mathcal{L}(w)$, we can write equations equivalent to Eq. (3.12) for both $\tilde{p}_{\rm m}$ and $p_{\rm m}$

$$\tilde{p}_{\rm m} = K_{\rm m}\tilde{w}^q, \tag{3.13}$$

$$p_{\rm m} = K_{\rm m}\mathcal{L}^{q-1}(\rho h)^q, \tag{3.14}$$

where $K_{\rm m}$ and q are constants. Then we can integrate Eq. (3.11) as

$$W - W_{\rm in} + \ln\left(1 + \frac{\Gamma K}{\Gamma - 1}\rho^{\Gamma-1}\right) + \frac{q}{q-1}K_{\rm m}(\mathcal{L}\rho h)^{q-1} = 0, \tag{3.15}$$

where $W \equiv \ln|u_t|$ stands for the (gravitational plus centrifugal) potential and $W_{\rm in}$ is the potential at the inner edge of the disk.

We can also define the total energy density for the torus, $\rho_{\rm T} = -T^t_t + T^i_i$, and for the scalar field, $\rho_{\rm SF} = -(T_{\rm SF})^t_t + (T_{\rm SF})^i_i$. These are given by

$$\rho_{\rm T} = \frac{\rho h(g_{\phi\phi} - g_{tt}l^2)}{g_{\phi\phi} + 2g_{t\phi}l + g_{tt}l^2} + 2(p + p_{\rm m}), \tag{3.16}$$

$$\rho_{\rm SF} = 2\left(\frac{2e^{-2F_0}\omega(\omega - mW)}{N} - \mu^2\right)\phi^2. \tag{3.17}$$

Using these expressions, we can compute the total gravitational mass of the torus and the scalar field as the following expression

$$\mathcal{M} = \int \rho\sqrt{-g}\,{\rm d}^3x\,, \tag{3.18}$$

where g is the determinant of the metric tensor and $\rho \equiv \rho_{\rm T}, \rho_{\rm SF}$.

In this work we take an approach to construct the magnetized disks different to the one proposed by [Komissarov 2006] and used by Vincent et al. [2016] for building disks around KBHsSH. As noted by Gimeno-Soler and Font [2017], the approach of [Komissarov 2006] implicitly assumes that the specific enthalpy of the fluid is close to unity ($w = \rho h \simeq \rho$). This means that the polytropic EOS Eq. (3.12) can be written as $p = Kw^\Gamma$ (see Eq. (27) of Komissarov [2006]). We do not make this assumption here. To better understand the differences between these two approaches, we consider their behaviour in two limiting cases, namely the non-magnetized case and the extremely magnetized case.

For the former, we can rewrite Eq. (3.15) in the limiting case of $\beta_{\rm m_c} \to \infty$ ($K_{\rm m} \to 0$) as

$$W - W_{\rm in} + \ln\left(1 + \frac{\Gamma K}{\Gamma - 1}\rho^{\Gamma-1}\right) = 0. \tag{3.19}$$

Then, we can solve this equation for the specific enthalpy

$$h = e^{W_{\rm in} - W}. \tag{3.20}$$

Now, we want to obtain an analogous equation for the $h \simeq 1$ case. We start by considering Eq. (20) of Gimeno-Soler and Font [2017] and taking the limit $\beta_{\rm m_c} \to \infty$ (in this equation, this means $K_{\rm m} \to 0$), to obtain

$$W - W_{\rm in} + \frac{\Gamma K}{\Gamma - 1}w^{\Gamma-1}. \tag{3.21}$$

If we consider the $h \simeq 1$ approximmation, we can use the definition of h and solve the equation to arrive at

$$h = 1 + (W_{\rm in} - W). \tag{3.22}$$

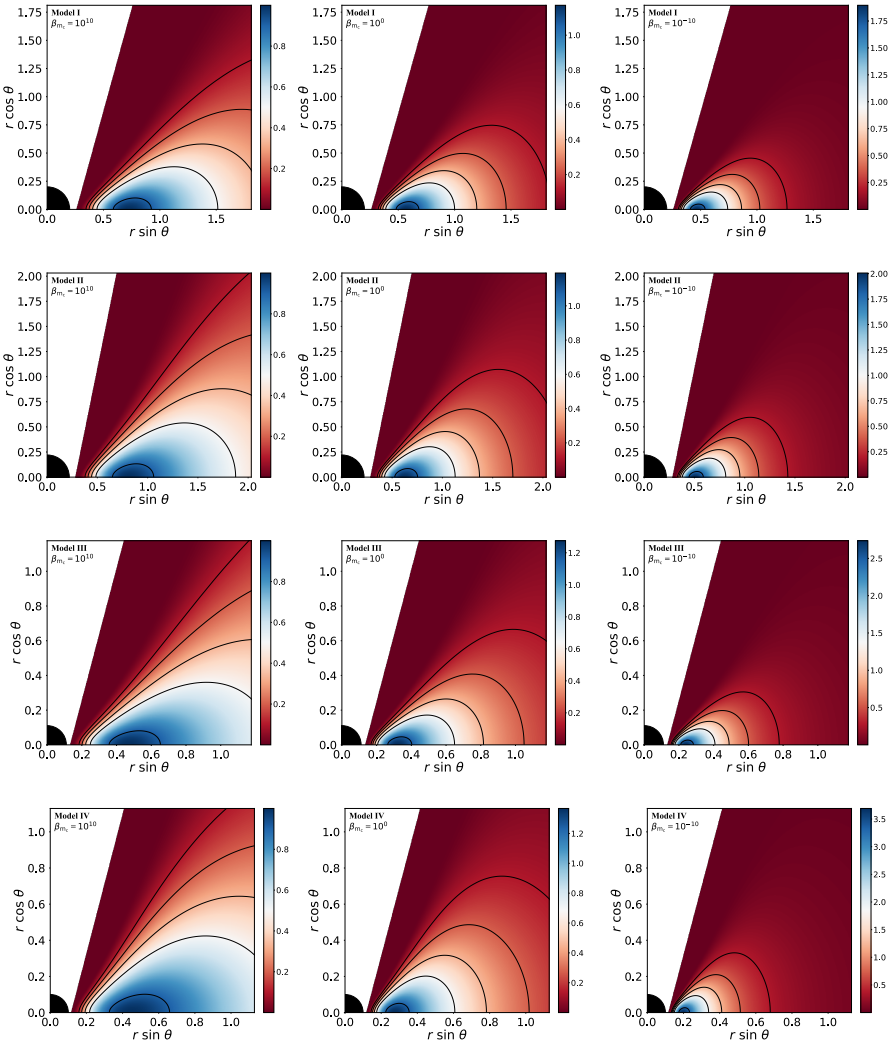

Figure 3.2 Distribution of the rest-mass density. From top to bottom the rows correspond to the first four models of KBHsSH (I, II, III and IV). From left to right the columns correspond to different values of the magnetization parameter, namely non-magnetized ($\beta_{\mathrm{m_c}} = 10^{10}$), mildly magnetized ($\beta_{\mathrm{m_c}} = 1$) and strongly magnetized ($\beta_{\mathrm{m_c}} = 10^{-10}$). Note that the range of the colour scale is not the same for all plots.

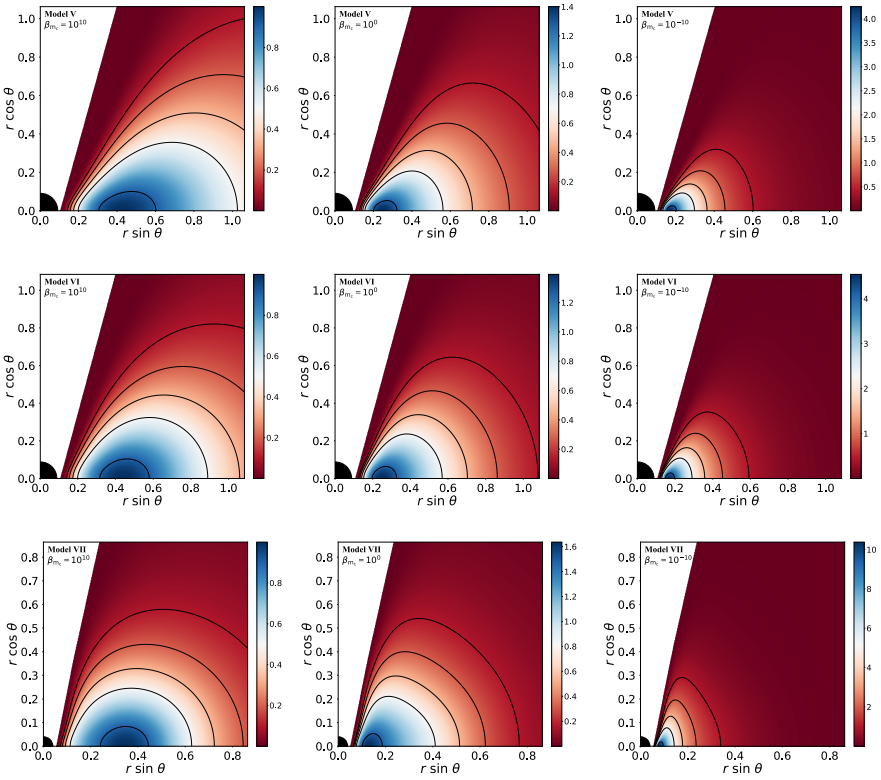

Figure 3.3 Same as Fig. 3.2 but for the last three models of KBHsSH (V, VI, and VII).

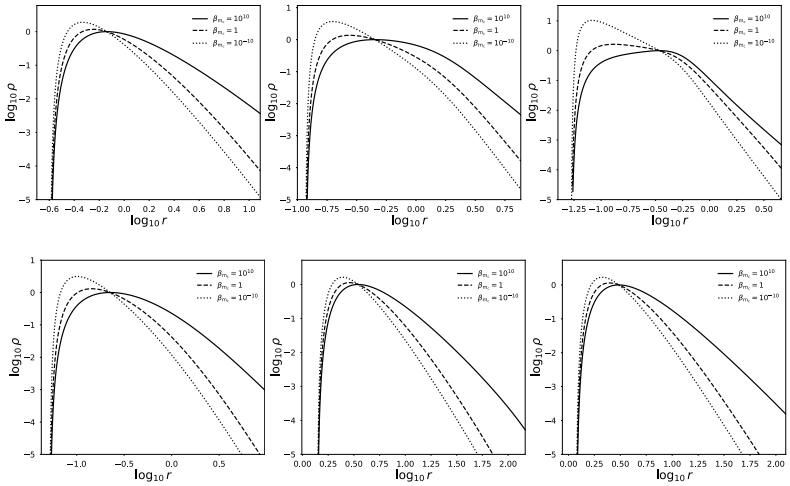

Figure 3.4 Size of the disks. Top panel: Effects of the magnetization on the radial profiles of the logarithm of the density at the equatorial plane for different KBHsSH models. From left to right we show model I, IV, and VII, respectively. Bottom panel: same as the top panel but for Kerr BHs. From left to right the cases shown have the same ADM quantities as the KBHsSH model I, IV, and VII, respectively, shown in the top panel. Note that the scale shown in the horizontal axes is different in all plots.

If we compare both results, we can see that Eq. (3.22) is the first-order Taylor series expansion of Eq. (3.20) for a sufficiently small value of $W_{\mathrm{in}} - W$.

For the extremely magnetised case, we consider again Eq. (3.15) and Eq. (20) of Gimeno-Soler and Font [2017], but this time around we take $\beta_{\mathrm{m_c}} \to 0$ ($K \to 0$). This yields the same result for both equations

$$W - W_{\mathrm{in}} + \frac{q}{q-1} K_{\mathrm{m}} (\mathcal{L}\rho h)^{q-1} = 0. \tag{3.23}$$

In addition, we could consider the expression for the specific enthalpy in terms of the density $h = 1 + \frac{K\Gamma\rho^{\Gamma-1}}{\Gamma-1}$ to see that we will have $h \to 1$. This shows that, for the extremely magnetized limit, the two approaches coincide.

Taking into account these two limits we can obtain the range of validity of the $h \simeq 1$ approximation: As magnetized disks exist between the two considered cases, for disks with a sufficiently small value of the potential well, $\Delta W \equiv W_{\mathrm{in}} - W_{\mathrm{c}}$, the $h \simeq 1$ approximation is valid. On the contrary, if the value of ΔW is large enough, the approximation does not hold even for disks with a fairly low value of magnetization.

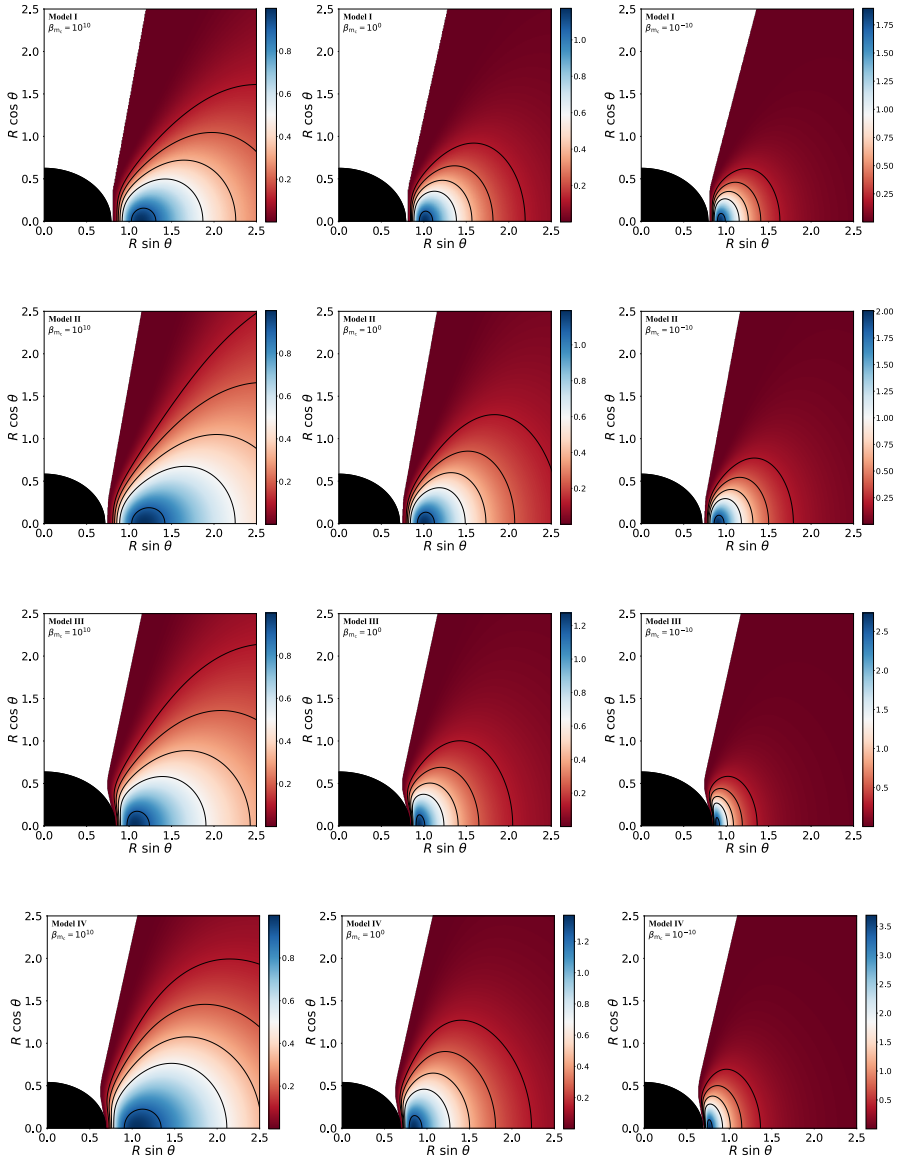

Figure 3.5 Same as Fig. 3.2 but using the perimeteral radial coordinate R.

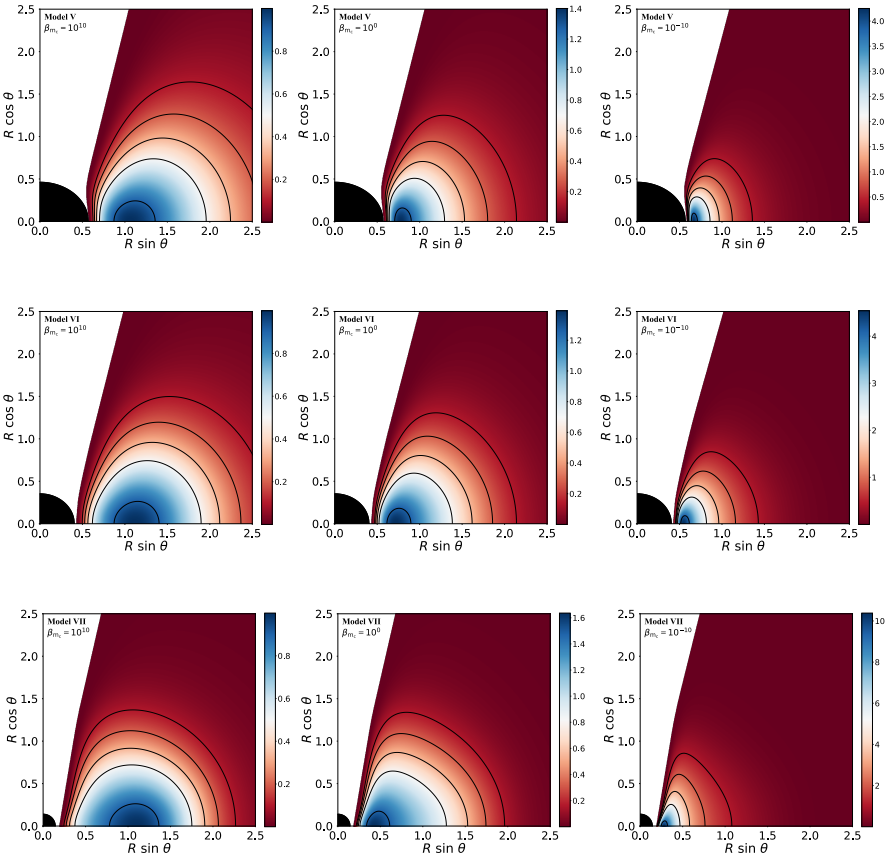

Figure 3.6 Same as Fig. 3.3 but using the perimeteral radial coordinate R.

3.3 Methodology

We now turn to describe the numerical methodology to build the disks. From the discussion in the preceding section it becomes apparent that the number of parameters defining the disk models is fairly large. In order to reduce the sample, in this work we set the mass of the scalar field to $\mu = 1$, the azimuthal harmonic index to $m = 1$, the exponents of the polytropic EOS to $q = \Gamma = 4/3$, the density at the centre of the disk to $\rho_{\rm c} = 1$, the specific angular momentum to $l = l_{\rm mb}$ and the inner radius of the disk to $r_{\rm in} = r_{\rm mb}$. Thus, we leave the magnetization at the centre, $\beta_{\rm m_c}$, as the only free parameter for each model of KBHsSH. With this information we can compute all relevant physical quantities.

In particular, our choice of specific angular momentum and inner radius is made to allow disks to have a cusp and a centre. These disks are marginally stable, as they completely fill their Roche lobe, and a small perturbation can trigger accretion onto the BH. In addition, the thermodynamical quantities of the disks reach their maxima for this particular choice of parameters, as they are related to the total potential well $|\Delta W|$. Our choice also implies that the resulting disks will be semi-infinite (they are closed at infinity) but this is not a source of concern, as the external layers of the disk have extremely low density.

Before building the models, it is important to note that we need a sufficiently fine numerical grid to fully capture the behaviour of the physical magnitudes at the innermost regions of the disk. For this reason, we use a non-uniform (r, θ) grid with a typical domain given by $[r_{\rm H}, 199.2] \times [0, \pi/2]$ and a typical number of points $N_r \times N_\theta = 2500 \times 300$. Those numbers are only representative as the actual numbers depend on the horizon radius $r_{\rm H}$ and on the specific model. The spacetime metric data on this grid is interpolated from the original data obtained by Herdeiro and Radu [2015a]. The original grid in Herdeiro and Radu [2015a] is a uniform $(x,\ \theta)$ grid (where x is a compactified radial coordinate) with a domain $[0, 1] \times [0, \pi/2]$ and a number of points of $N_x \times N_\theta = 251 \times 30$ [1]. To obtain our grid, we use the coordinate transformation provided in *http://gravitation.web.ua.pt/node/416* and interpolate the initial grid using cubic splines interpolation.

To build the disks we first need to find $l_{\rm mb}$ and $r_{\rm mb}$ as the minimum of Eq. (3.8) and the location of said minimum in terms of the radial coordinate respectively. Once this is done, we can compute the total potential distribution

[1] Some samples are presented in *http://gravitation.web.ua.pt/node/416*

as

$$W(r,\theta) \equiv \ln|u_t| = \frac{1}{2}\ln\left|\frac{g_{t\phi}^2 - g_{tt}g_{\phi\phi}}{g_{\phi\phi} + 2g_{t\phi}l + g_{tt}l^2}\right|. \tag{3.24}$$

With the total potential distribution, we can compute the location of the cusp $r_{\rm cusp}$ and the centre $r_{\rm c}$ as the extrema (maximum and minimum respectively) of the total potential in the equatorial plane. Also, we set $r_{\rm in} = r_{\rm cusp}$. For our choice of angular momentum distribution, this also means $W_{\rm in} = 0$. Having the total potential distribution and the characteristic radii of the disk, we can start to compute the thermodynamical quantities in the disk. First of all, we compute the polytropic constant K by evaluating Eq. (3.15) at the centre

$$W - W_{\rm in} + \ln\left(1 + \frac{\Gamma K}{\Gamma - 1}\rho_{\rm c}^{\Gamma-1}\right) + \frac{q}{q-1}\frac{K\rho_{\rm c}^{\Gamma}}{\beta_{\rm m_c}\left(\rho_{\rm c} + \frac{K\Gamma\rho_{\rm c}^{\Gamma}}{\Gamma-1}\right)} = 0\,, \tag{3.25}$$

where we have used the definition of magnetic pressure and the definition of the magnetization parameter β. Using their corresponding definitions, we can also compute $h_{\rm c}$, $p_{\rm c}$, $p_{\rm m_c}$ and the constant of the magnetic EOS $K_{\rm m}$. With both K and $K_{\rm m}$ obtained, we can now compute the thermodynamical quantities in all our numerical domain. For points with $W(r,\theta) > 0$ we set $\rho = p = p_{\rm m} = 0$ and for points with $W_{\rm c} < W(r,\theta) < 0$, we write Eq. (3.15) as

$$W - W_{\rm in} + \ln\left(1 + \frac{\Gamma K}{\Gamma - 1}\rho^{\Gamma-1}\right) + \frac{q}{q-1}K_{\rm m}\left(\mathcal{L}\left(\rho + \frac{K\Gamma\rho^{\Gamma}}{\Gamma-1}\right)\right)^{q-1} = 0\,, \tag{3.26}$$

to compute the rest-mass density ρ of said point. Then, we can use again Eqs. (3.12) and (3.13) and the definition of the specific enthalpy to compute the distribution of p, $p_{\rm m}$ and h.

It is relevant to note that Eqs. (3.25) and (3.26) are trascendental equations and that Eq. (3.26) in particular must be solved at each point of our numerical grid. To solve these equations we use the bisection method. To ensure the accuracy of our computations (particularly the accuracy of the maximum and central quantities we report) we choose our grid to have a difference between two adjacent points of $\Delta r(r \simeq r_{\rm c}) \simeq 0.001$ in the equatorial plane.

Table 3.2 Values of the relevant physical magnitudes of our models of magnetized, equilibrium tori around KBHsSH. All reported radii correspond to the perimeteral coordinate. For all cases, $R_{\rm in} = R_{\rm mb}$ and $l = l_{\rm mb}$. From left to right the columns report: the specific angular momentum, l, the potential at the centre of the disk, $W_{\rm c}$, the inner radius of the disk, $R_{\rm in}$, its centre, $R_{\rm c}$, the value of the magnetization parameter at the centre, $\beta_{\rm m_c}$, the maximum specific enthalpy, $h_{\rm max}$, density, $\rho_{\rm max}$, thermal pressure, $p_{\rm max}$, and magnetic pressure, $p_{\rm m,max}$, and the location of the maximum of the thermal pressure and magnetic pressure, $R_{\rm max}$ and $R_{\rm m,max}$, respectively.

Model	l	$W_{\rm c}$	$R_{\rm in}$	$R_{\rm c}$	$\beta_{\rm m_c}$	$h_{\rm max}$	$\rho_{\rm max}$	$p_{\rm max}$	$p_{\rm m,max}$	$R_{\rm max}$	$R_{\rm m,max}$
I	0.934	−0.188	0.81	1.14	10^{10}	1.21	1.00	5.16×10^{-2}	5.50×10^{-12}	1.14	1.26
					1	1.10	1.17	3.11×10^{-2}	2.68×10^{-2}	1.01	1.06
					10^{-10}	1.00	1.90	1.10×10^{-11}	7.80×10^{-2}	0.93	0.96
II	0.933	−0.205	0.75	1.18	10^{10}	1.23	1.00	5.69×10^{-2}	6.14×10^{-12}	1.18	1.36
					1	1.12	1.19	3.50×10^{-2}	2.97×10^{-2}	1.00	1.07
					10^{-10}	1.00	2.01	1.30×10^{-11}	8.99×10^{-2}	0.91	0.94
III	1.060	−0.362	0.84	1.07	10^{10}	1.44	1.00	1.09×10^{-1}	1.21×10^{-11}	1.07	1.22
					1	1.23	1.28	7.22×10^{-2}	5.76×10^{-2}	0.95	0.99
					10^{-10}	1.00	2.74	3.48×10^{-11}	2.06×10^{-1}	0.89	0.91
IV	1.160	−0.547	0.67	1.06	10^{10}	1.72	1.00	1.82×10^{-1}	2.09×10^{-11}	1.06	1.34
					1	1.38	1.37	1.29×10^{-1}	9.76×10^{-2}	0.85	0.91
					10^{-10}	1.00	3.70	7.83×10^{-11}	4.08×10^{-1}	0.76	0.78
V	1.200	−0.685	0.58	1.07	10^{10}	1.98	1.00	2.46×10^{-1}	2.76×10^{-11}	1.07	1.31
					1	1.51	1.40	1.78×10^{-1}	1.32×10^{-1}	0.78	0.87
					10^{-10}	1.00	4.26	1.18×10^{-10}	5.79×10^{-1}	0.67	0.69
VI	1.200	−0.832	0.43	1.12	10^{10}	2.30	1.00	3.24×10^{-1}	3.52×10^{-11}	1.12	1.32
					1	1.66	1.39	2.28×10^{-1}	1.69×10^{-1}	0.72	0.86
					10^{-10}	1.00	4.54	1.57×10^{-10}	7.40×10^{-1}	0.55	0.59
VII	0.920	−1.236	0.18	1.10	10^{-10}	3.44	1.00	6.10×10^{-1}	6.46×10^{-11}	1.10	1.25
					1	2.25	1.64	5.10×10^{-1}	3.22×10^{-1}	0.43	0.62
					10^{-10}	1.00	10.42	7.03×10^{-10}	0.24×10^{-1}	0.28	0.30

3.4 Results

3.4.1 2D Morphology

We start presenting the morphological distribution of the models in the $(r\sin\theta, r\cos\theta)$ plane in figures 3.2 and 3.3. These figures show the rest-mass density distribution for all our KBHsSH models for 3 different values of the magnetization parameter at the centre of the disks, $\beta_{\rm m_c}$, namely 10^{10} (unmagnetized, left column), 1 (mildly magnetized, middle column) and 10^{-10} (strongly magnetized, right column).

The structure of the disks is similar for all values of $\beta_{\rm m_c}$ with the only quantitative differences being the location of the centre of the disk, which moves closer to the BH as the magnetization increases, and the range of variation of the isodensity contours, whose upper ends become larger with decreasing $\beta_{\rm m_c}$. This behaviour is in complete agreement with that found for Kerr BHs in Gimeno-Soler and Font [2017] irrespective of the BH spin. For the particular case of Model VII, the maximum of the rest-mass density for the strongly magnetized

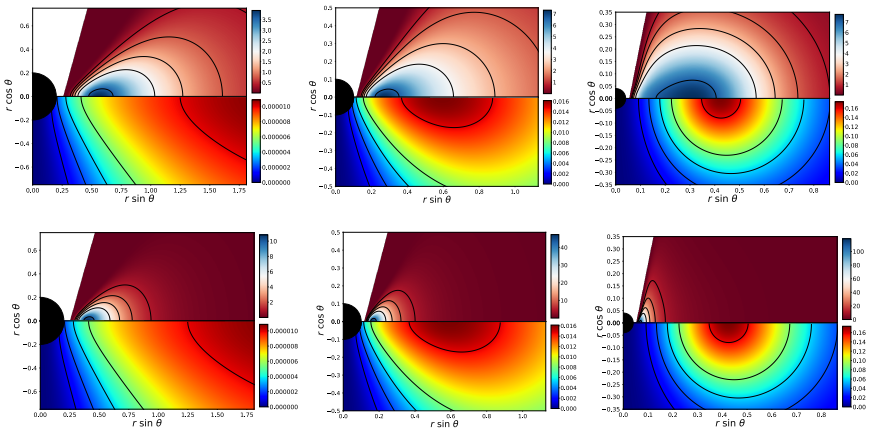

Figure 3.7 Energy density distribution for the torus $\rho_{\rm T}$ (upper half of the images) and for the scalar field $\rho_{\rm SF}$ (lower half). From left to right the columns correspond to models I, IV, and VII. The top row corresponds to non-magnetized models ($\beta_{\rm m_c} = 10^{10}$) and the bottom row to strongly magnetized models ($\beta_{\rm m_c} = 10^{-10}$).

case is significantly larger than for the other models and the spatial extent of the disk is fairly small.

The size of the disks can be best quantified by plotting the radial profiles of the rest-mass density on the equatorial plane. This is shown in the upper panels of Fig. 3.4 for models I, IV and VII and for the same three values of the magnetization parameter shown in Figs. 3.2 and 3.3. (The lower panels of this figure correspond to disks around Kerr BHs and will be discussed below.) From Fig. 3.4 we see that model I disks are significantly larger than models IV and VII, i.e. the hairier the models the more compact and smaller the disks become. We also note the presence of an extended region of high density in the unmagnetized model VII (the mildly-magnetized case also shows this feature but to a lesser extent). This could be related to the existence of an extra gravitational well due to the scalar field distribution that overlaps with the matter distribution of the disk (as can be seen in the right panel of Fig. 3.7 below).

In figures 3.5 and 3.6 we show the same morphological distribution of Figs. 3.2 and 3.3 but using, instead, a perimeteral radial coordinate R, related to the radial coordinate r according to $R = e^{F_2} r$. This perimeteral coordinate represents the proper length along the azimuthal direction, which constitutes a geometrically meaningful direction since it runs along the orbits of the azimuthal Killing vector field. Therefore, the proper size of a full ϕ orbit is given by $2\pi R$, i.e. R is the perimeteral radius. The most salient feature of the morphologies shown in Figs. 3.5 and 3.6, when comparing to those displayed in Figs. 3.2 and 3.3, is the

Table 3.3 Disk parameters and values of their relevant physical magnitudes for the Kerr BH case. For all models, $R_{\rm in} = R_{\rm mb}$, $l = l_{\rm mb}$ and $M_{\rm BH} = 1$. The meaning of the quantities reported is as in Table 3.2.

a	$\mathfrak{s}$	l	$W_{\rm c}$	$R_{\rm in}$	$R_{\rm c}$	$\beta_{\rm m_c}$	$h_{\rm max}$	$\rho_{\rm max}$	$p_{\rm max}$	$p_{\rm m,max}$	$R_{\rm max}$	$R_{\rm m,max}$
0	1	4.00	-4.32×10^{-2}	4.00	10.47	10^{10}	1.04	1.00	1.10×10^{-2}	1.15×10^{-12}	10.47	11.86
						1	1.02	1.11	6.29×10^{-3}	5.69×10^{-3}	8.81	9.52
						10^{-10}	1.00	1.48	1.83×10^{-12}	1.48×10^{-2}	7.70	8.14
0.5	1.053	3.41	-6.35×10^{-2}	2.99	7.12	10^{10}	1.07	1.00	1.64×10^{-2}	1.72×10^{-12}	7.19	8.14
						1	1.03	1.12	9.43×10^{-3}	8.47×10^{-3}	6.05	6.53
						10^{-10}	1.00	1.53	2.81×10^{-12}	2.23×10^{-2}	5.29	5.59
0.9	1.276	2.63	-0.129	2.18	3.78	10^{10}	1.14	1.00	1.64×10^{-2}	3.65×10^{-12}	3.78	4.23
						1	1.07	1.14	2.03×10^{-2}	1.78×10^{-2}	3.25	3.47
						10^{-10}	1.00	1.70	6.54×10^{-12}	4.92×10^{-2}	2.92	3.04
0.9999	1.629	2.02	-0.429	2.00015	2.034	10^{10}	1.54	1.00	1.34×10^{-1}	1.61×10^{-11}	2.034	2.094
						1	1.29	1.51	1.10×10^{-1}	7.52×10^{-2}	2.0075	2.014
						10^{-10}	1.00	6.17	1.22×10^{-10}	4.91×10^{-1}	2.0021	2.0030

deformation of the disks in their innermost regions. In general, the deformations become larger the higher the horizon sphericity $\mathfrak{s}$ and the closer the disk is to the horizon. Model III is the one showing the largest deformation, as $(R_{\rm in} - R_{\rm H})/R_{\rm H}$ attains the smallest value for this model. It is also worth noticing that the shape of the BH also changes when using the perimeteral coordinate. While in the r coordinate the horizon is spherical (cf. Figs. 3.2 and 3.3) in the perimeteral coordinate R is not always so. Moreover, the larger the value of $v_{\rm H}$, the more elliptic the horizon becomes, which in our sample corresponds to model III (cf. Table 3.1, $\mathfrak{s} = 1.489$).

In addition, an interesting geometrical property of the perimeteral coordinates is that, for the Kerr metric, $R_{\rm H} = 2M$ irrespective of the value of the angular momentum. However, for the KBHsSH cases, $2M_{\rm H} < R_{\rm H} < 2M_{\rm ADM}$, and the quotient $R_{\rm H}/2M_{\rm H}$ increases as more mass and angular momentum is stored in the scalar field.

Table 3.2 reports the relevant physical quantities for all of our disk models around KBHsSH. It is worth mentioning that KBHsSH can violate the Kerr bound for the potential $\Delta W \equiv W_{\rm in} - W_{\rm c}$. As shown in Abramowicz, Jaroszynski, and Sikora [1978], constant angular momentum disks arround Kerr BHs exhibit a maximum for $|\Delta W|$ when the spin parameter $a \to 1$. This value is $\Delta W_{\rm max} = -\frac{1}{2}\ln 3 \simeq -0.549$. Models V, VI, and VII of our sample violate that bound. As a result, the maximum values of the fluid quantities for disks around KBHsSH are significantly larger than in the Kerr BH case. In both cases, these values increase as $|\Delta W|$ increases, irrespective of the magnetization, as shown in Table 3.2.

In figure 3.7 we show the total energy density of the torus $\rho_{\rm T}$ (upper half of each image) and the total energy density of the scalar field $\rho_{\rm SF}$ (lower half) for models I, IV and VII and two values of the magnetization parameter at

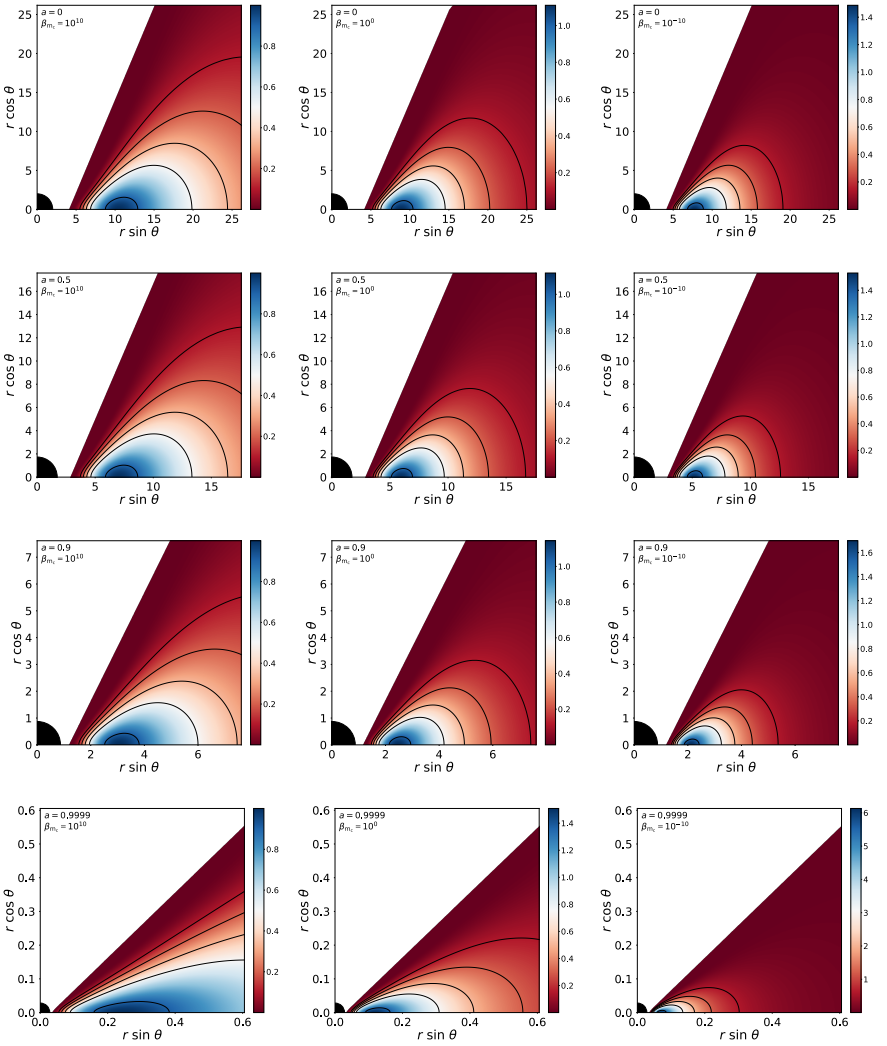

Figure 3.8 Rest-mass density distribution. From top to bottom the rows correspond to a sequence of Kerr BHs with increasing spin parameter a (0, 0.5, 0.9 and 0.9999). From left to right the columns correspond to different values of the magnetization parameter, namely non-magnetized ($\beta_{\rm mc} = 10^{10}$), mildly magnetized ($\beta_{\rm mc} = 1$) and strongly magnetized ($\beta_{\rm mc} = 10^{-10}$)

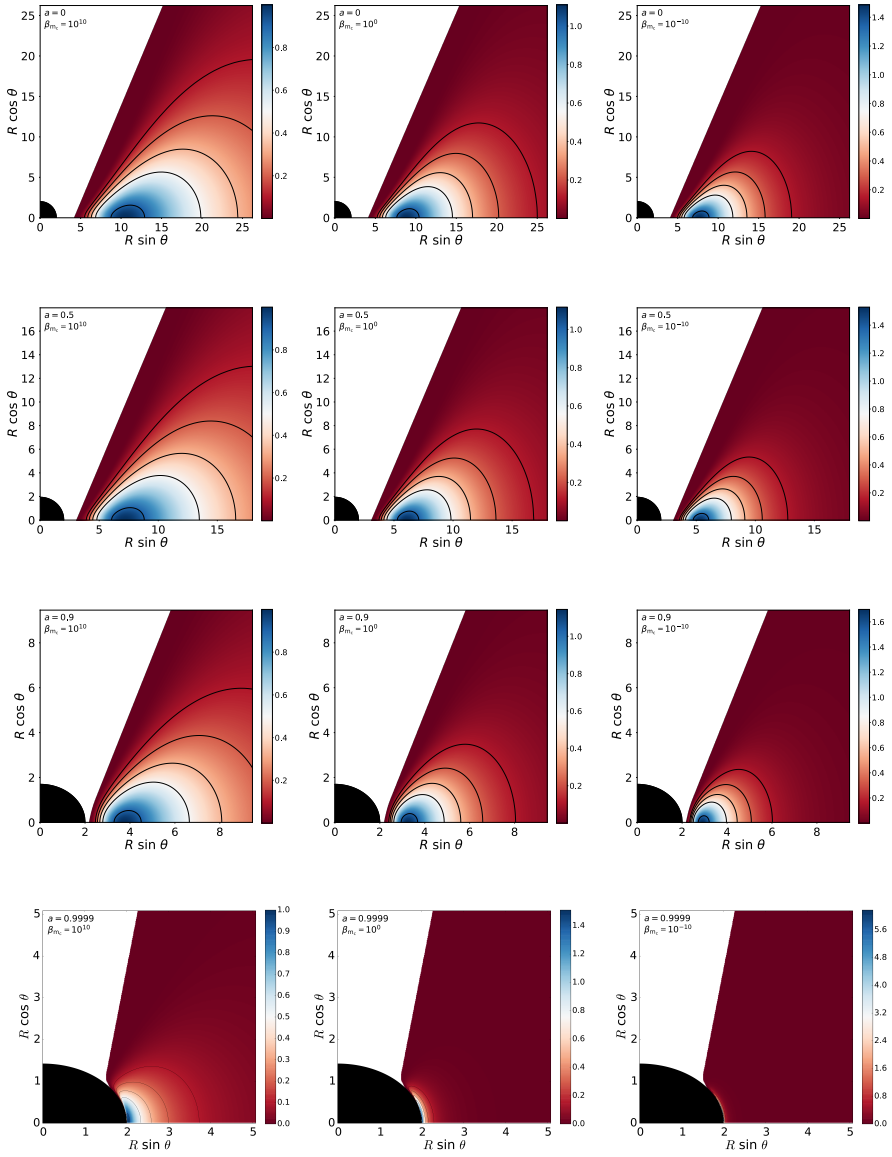

Figure 3.9 Rest-mass density distribution using perimeteral coordinates. From top to bottom the rows correspond to a sequence of Kerr BHs with increasing spin parameter a (0, 0.5, 0.9 and 0.9999). From left to right the columns correspond to different values of the magnetization parameter, namely non-magnetized ($\beta_{\rm mc} = 10^{10}$), mildly magnetized ($\beta_{\rm mc} = 1$) and strongly magnetized ($\beta_{\rm mc} = 10^{-10}$)

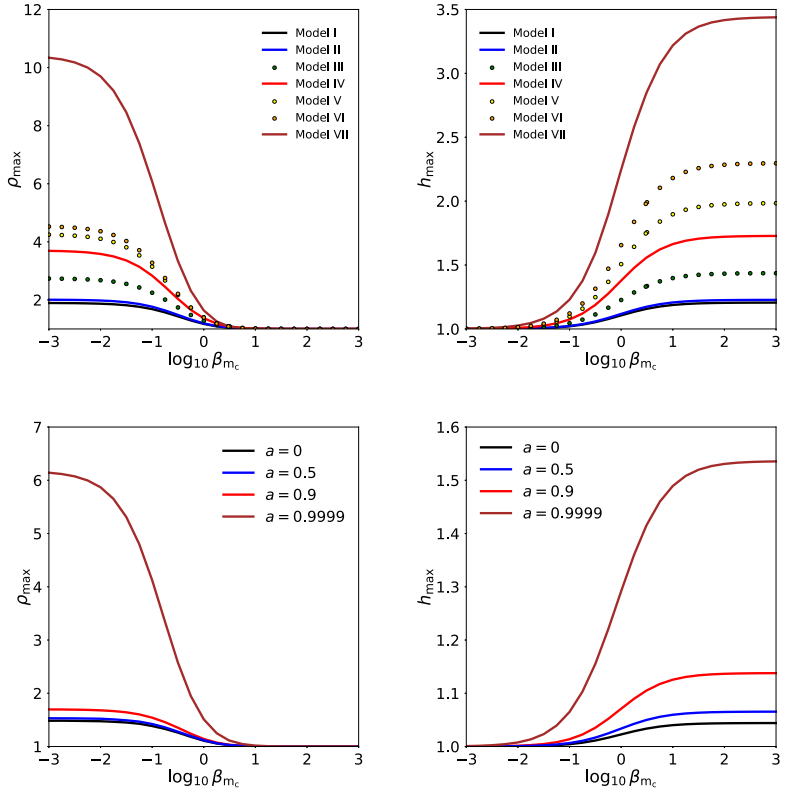

Figure 3.10 Effects of the magnetization on the values for the maximum density (left) and enthalpy (right) of the disks. In the first row, we show this for all of our KBHsSH models. In the second row, we show this for a sequence of Kerr BHs with increasing spin parameter.

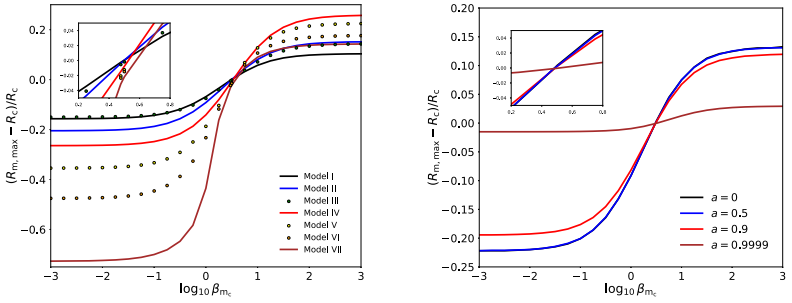

Figure 3.11 Effects of the magnetization on the perimeteral location of the magnetic pressure maximum (divided by the the perimeteral radius of the centre), $R_{\mathrm{mag,max}} - R_{\mathrm{c}})/R_{\mathrm{c}}$). Left panel: KBHsSH models. Right panel: A sequence of Kerr BHs with increasing spin parameter.

Table 3.4 Central density for the different models. A value of $r_{\rm in}$ such that $\Delta W = 0.9\Delta W_{\rm Total} \equiv W_{\rm cusp} - W_{\rm c}$ is chosen and a torus gravitational mass of $M_{\rm T} = 0.1 M_{\rm ADM}$ is assumed. In the third column, the value of the central density is reported in geometrized units ('g.u.') while in the fourth column this value is reported in cgs units. The fifth and sixth columns provide those values but for tori built around Kerr BHs with the same ADM quantities as the KBHsSH models. Finally, the last column reports the sphericity of the Kerr BH models.

Model	$\beta_{\rm m_c}$	$\rho_{\rm c}$ [g.u.]	$\rho_{\rm c}$ [g cm^{-3}]	$\rho_{\rm c}^{\rm K}$ [g.u.]	$\rho_{\rm c}^{\rm K}$ [g cm^{-3}]	$\mathfrak{s}^{\rm K}$
I	10^{10}	6.818×10^{-4}	1.739×10^{13}	3.752×10^{-3}	9.567×10^{13}	1.589
	1	2.185×10^{-3}	5.503×10^{13}	7.942×10^{-3}	2.025×10^{14}	
	10^{-10}	3.227×10^{-3}	8.229×10^{13}	7.641×10^{-3}	1.948×10^{14}	
II	10^{10}	3.216×10^{-4}	8.201×10^{12}	–	–	–
	1	1.651×10^{-3}	4.210×10^{13}	–	–	–
	10^{-10}	3.026×10^{-3}	7.716×10^{13}	–	–	–
III	10^{10}	8.120×10^{-4}	2.071×10^{13}	6.683×10^{-5}	1.704×10^{12}	1.278
	1	3.497×10^{-3}	8.917×10^{13}	2.075×10^{-4}	5.291×10^{12}	
	10^{-10}	5.452×10^{-3}	1.390×10^{14}	3.265×10^{-4}	8.325×10^{12}	
IV	10^{10}	1.197×10^{-3}	3.052×10^{13}	3.001×10^{-5}	7.652×10^{11}	1.219
	1	3.421×10^{-3}	8.723×10^{13}	9.512×10^{-5}	2.425×10^{12}	
	10^{-10}	5.135×10^{-3}	1.309×10^{14}	1.533×10^{-4}	3.909×10^{12}	
V	10^{10}	1.792×10^{-3}	4.569×10^{13}	3.152×10^{-5}	8.037×10^{11}	1.227
	1	3.883×10^{-3}	9.901×10^{13}	9.942×10^{-5}	2.535×10^{12}	
	10^{-10}	5.435×10^{-3}	1.386×10^{14}	1.596×10^{-4}	4.070×10^{12}	
VI	10^{10}	2.348×10^{-3}	5.987×10^{13}	3.232×10^{-5}	8.241×10^{11}	1.234
	1	4.106×10^{-3}	1.047×10^{14}	1.019×10^{-4}	2.598×10^{12}	
	10^{-10}	5.685×10^{-3}	1.450×10^{14}	1.632×10^{-4}	4.161×10^{12}	
VII	10^{10}	3.737×10^{-3}	9.529×10^{13}	4.114×10^{-5}	1.049×10^{12}	1.268
	1	5.356×10^{-3}	1.366×10^{14}	1.280×10^{-4}	3.264×10^{12}	
	10^{-10}	7.598×10^{-3}	1.937×10^{14}	2.021×10^{-4}	5.153×10^{12}	

the centre (10^{10}, top row, and 10^{-10}, bottom row). This figure shows that, for non-magnetized disks, the maximum of the total energy density of the disk $\rho_{\rm T}$ is closer to the maximum of the total energy density of the scalar field $\rho_{\rm SF}$ for increasing hair. This trend disappears with increasing magnetization, as the disk moves closer to the horizon in such case.

3.4.2 Comparison with Kerr BHs

For the sake of comparison we also build equilibrium sequences of magnetized disks around four Kerr BHs of the same mass ($M_{\rm BH} = 1$) and varying spins, from $a = 0$ to $a = 0.9999$. These models are more general than the corresponding ones presented in Gimeno-Soler and Font [2017] as the $h = 1$ assumption is now relaxed. Our numerical approach can handle BH spins as large as $|a - 1| = 10^{-7}$ without modifying the resolution of our numerical grid. However, for higher values of the spin parameter, we would need to increase our resolution (especially the resolution along the polar angle θ for the most highly magnetized case) but

such extreme cases do not add further relevant information to our discussion. Table 3.3 reports a summary of the values of the main physical quantities of these disks, whose morphology is displayed in Figs. 3.8 and 3.9. As for the disks built around KBHsSH, the maximum values of the enthalpy, density, pressure and magnetic pressure increase with increasing $|\Delta W|$, which, in the Kerr BH case, also means with increasing values of a. It can be seen that both the cusp and the centre move closer to the horizon with increasing a, i.e. the disks reduce their size and approach the BH as the spin parameter increases. (Note that, as we mentioned before, in the Kerr case the radial location of the horizon at the equatorial plane in perimeteral coordinates is $R_{\rm H} = 2M$ irrespective of the value of the BH spin.)

The comparison of the values of the physical quantities shows that, even for highly rotating Kerr BHs, the maximum values for h, p and $p_{\rm m}$ are lower than in the KBHsSH case. This is not a surprise, as these quantities are related to the value of $|\Delta W|$. Also, as in the case of KBHsSH, we observe a higher distortion of the shape of the disc in the near-horizon region with increasing sphericity $\mathfrak{s}$ (and spin, in this particular case). This is particularly noticeable when plotting the disk morphology in terms of the perimeteral coordinates (cf. Fig. 3.9). For the $a = 0.9999$ model the disk is extremely skewed and attached to the BH horizon, particularly in the highly magnetized case in which the values reported in Table 3.3 for $R_{\rm in}$ and $R_{\rm c}$ are very close to each other. The appearance of the solution is more disk-like when displayed in terms of the r coordinate, as shown in Fig. 3.8, as this radial coordinate expands the near-horizon region. While this coordinate is well suited to do the computations, this is not the case for visualization, where the perimeteral coordinate is preferred since it allows to directly compare the different models as the scale is the same.

To provide additional information for the comparison we show in the bottom panels of Fig. 3.4 three disk models around Kerr BHs with the same ADM mass and ADM angular momentum as the KBHsSH cases shown in the upper panels of the same figure. The model on the left plot corresponds to a near-extremal Kerr BH ($a = 0.9987$) and the other two have a similar value for the spin parameter ($a = 0.8489$ and $a = 0.8941$, for the middle and right plots, respectively). The comparison reveals interesting differences between these models regarding their compactness. The size of the disk in the Kerr case plotted on the left is considerably smaller than its hairy counterpart, KBHsSH model I. In this case, the presence of the scalar field has little effect on the morphology of the disk (as its gravitational field is small) but its effect is nonetheless noted in a reduction of the value of the sphericity (see Table 3.4), effectively reducing the

effect of the BH spin in the disk (i.e. increasing its shape). As the mass and angular momentum stored in the scalar field increase, the gravitational field of the scalar field affects the radial morphology of the disk, altering its shape and reducing its extent. Note that both KBHsSH models IV and VII have lesser radial extent than its Kerr BH counterparts with the same ADM mass and angular momentum, even though model VII attains a lower value of the sphericity. These conclusions hold irrespective of the value of the magnetization parameter.

3.4.3 Magnetization profiles

The dependence of the maximum specific enthalpy $h_{\rm max}$ and the maximum rest-mass density $\rho_{\rm max}$ with the magnetization parameter is shown in Fig. 3.10. The upper panels correspond to the KBHsSH models (I-VII) and the lower ones to our sequence of Kerr BHs with increasing spin parameter. For both cases, an increase in $|\Delta W|$ implies monotonically higher values for $h_{\rm max}$ (low magnetization) and also higher values for $\rho_{\rm max}$ (high magnetization). However, there are quantitative differences between the two cases. For the enthalpy, the values of $h_{\rm max}$ reached for disks around KBHsSH are much higher than those of the Kerr BH case. This implies that, while the $w = \rho h \simeq \rho$ approximation (employed in Komissarov [2006] and Gimeno-Soler and Font [2017]) is valid for magnetized disks ($\beta_{\rm m_c} \sim 1$) around Kerr BHs for values of the spin parameter as high as $a \sim 0.99$, that is not the case for disks around KBHsSH. We note that for the most extreme spin value we can build, $|a-1| = 10^{-7}$, the maximum enthalpy for the purely hydrodynamical case is $h_{\rm max} = 1.692$. For this case, the maximum density in the extremely magnetized limit reaches a value of $\rho_{\rm max} = 97$, significantly larger than the value displayed in the left panel of Fig. 3.10 for the $a = 0.9999$ model.

Figure 3.11 shows the relative variation of the quotient of the perimeteral radius of the magnetic pressure maximum and the perimeteral radius of the disk centre, $(R_{\rm m,max} - R_{\rm c})/R_{\rm c}$, with the decimal logarithm of the magnetization parameter at the centre of the disk, $\log_{10}\beta_{\rm m_c}$. The curves plotted correspond to the same KBHsSH and Kerr BH cases as those in figure 3.10. For all cases, the radial location of the magnetic pressure maximum decreases with decreasing $\beta_{\rm m_c}$. In Gimeno-Soler and Font [2017] we proved that for $h = 1$ disk models in stationary and axisymmetric BH spacetimes, the location of the maximum of the magnetic pressure is identical for all models when $\beta_{\rm m_c} \equiv 1/\Gamma - 1 = 3$. This condition is almost fulfilled for the Kerr BH case even when $h \neq 1$, with a

very slight deviation for cases with very high spin parameter. This cannot be seen clearly in Fig. 3.11 (even in the inset) but, as an example, for $a = 0.9999$, the relative difference of $(R_{\rm m,max} - R_{\rm c})/R_{\rm c}$ with the $h = 1$ case is about 0.1%. (We note that in the radial coordinate of the metric ansatz, the disks are not so skewed and attached to the horizon and the differences would be more visible.) On the other hand, the condition $R_{\rm m,max} = R_{\rm c}$ when $\beta_{\rm m_c} = 3$ is clearly not fulfilled (when $h \neq 1$) for disks built around KBHsSH (see inset in the left panel). At this point, it is relevant to remember that some of the KBHsSH models violate the Kerr bound in terms of the potential. As we mentioned previously, we need a small value of ΔW for the $h \simeq 1$ approximation to be valid in the non-magnetized regime. Now we can see that, in the KBHsSH case, this approximation is not valid even for mildly-magnetized disks.

3.4.4 Torus mass

In an attempt to gauge the astrophysical relevance of our models, in this section we drop the $\rho_{\rm c} = 1$ choice we have thus far considered to build the tori and compute their masses and, instead, we assume that the mass of the tori is $M_{\rm T} = 0.1 M_{\rm ADM}$ and ask ourselves what are the corresponding values of the central density of each model. The value selected for $M_{\rm T}$ is, broadly speaking, compatible with the torus masses found through numerical relativity simulations of binary neutron star mergers (see, e.g. [Rezzolla et al. 2010, Baiotti and Rezzolla 2017] and references therein). Moreover, to avoid complications due to the infinite size of our models, we choose the total potential well as the 90% of its maximum possible value.

Therefore, we compute the mass of the tori around KBHsSH and, for comparison, the corresponding mass for seven disk models around Kerr BHs, each one of them with the same ADM quantities as their KBHsSH counterparts. The resulting values are reported in Table 3.4. The variables corresponding to the Kerr case are indicated with a 'K' superindex in this table. The third and fifth columns of Table 3.4 indicate the resulting central densities for the KBHsSH and Kerr BH cases, respectively, in geometrized units. In order to compare these values with those from the end-products of binary neutron star mergers, we need to convert our results to cgs units. To this end, we first need to choose a mass for the scalar field μ, as the maximum ADM mass of KBHsSH depends on μ. In particular, we compute the maximum ADM mass with the following equation

(see [Herdeiro, Radu, and Rúnarsson 2015] and references therein)

$$M_{\rm ADM}^{\rm max} \simeq \alpha_{\rm BS} 10^{-19} M_\odot \left(\frac{\rm GeV}{\mu}\right) , \tag{3.27}$$

for a value of $\alpha_{\rm BS} = 1.315$ (corresponding to a value of the azimuthal harmonic index $m = 1$). The constant $\alpha_{\rm BS}$ is computed numerically for rotating boson stars. Note that Eq. (3.27) corresponds to the maximum mass of a boson star but, as mentioned in tHerdeiro:2015a, this is also the maximum mass for the corresponding hairy BH. Using a value of the mass of the scalar field of $\mu = 2.087 \times 10^{-11}$ eV yields values for the ADM mass of our models that increase from 2.043 $M_\odot$ to 4.799 $M_\odot$, from model I to VII. This value of μ is within the mass range suggested by the *axiverse* of string theory (see [Arvanitaki et al. 2010]) portraying a large number of scalar fields in a mass range from 10^{-33} eV to 10^{-10} eV. In addition, as mentioned in Ramazanoglu and Pretorius [2016], the value of μ we choose is compatible with the scalar-field mass range allowed by the observational tests in scalar-tensor theories of gravity. Although in this paper we are working within general relativity, for the low values of the trace of the energy-momentum tensor of our models (in comparison with the values reached for neutron stars) both theories should be indistinguishable. We should note as well that Eq. ((3.27)) is valid for non self-interacting scalar hair. Adding self-interaction terms would produce astrophysically relevant solutions for less extreme values of the scalar-field mass μ [Delgado, Herdeiro, and Radu 2018].

Once we compute the new values of the central density in geometrized units, we use the following equation [Rezzolla and Zanotti 2013]

$$\rho_{\rm cgs} = 6.17714 \times 10^{17} \left(\frac{G}{c^2}\right) \left(\frac{M_\odot}{M}\right)^2 \rho_{\rm geo} , \tag{3.28}$$

to obtain the value of the central density in cgs units for the different models. These values are reported in columns four and six of Table 3.4. The range of values is fairly broad, spanning from $\sim 10^{11}$ g cm^{-3} to $\sim 10^{14}$ g cm^{-3}. This is due to the significant differences in size of the different disks, especially between the Kerr and KBHsSH cases. Comparing these values with those reported in the literature (see [Rezzolla et al. 2010, Baiotti and Rezzolla 2017]) we conclude that, despite our assumptions, they are in the same ballpark than the central densities found in disks consistently formed through ab-initio simulations of binary neutron star mergers. In particular, changing the distribution of the specific angular momentum from our simplistic constant prescription to a more realistic power-law distribution, may help improve the accuracy of our results.

3.5 Conclusions

Astrophysical BHs are commonly surrounded by accretion disks, either at stellar-mass scales or at supermassive scales. In the former case, stellar-mass BHs surrounded by thick disks (or tori) are broadly accepted as natural end results of catastrophic events involving the coalescence and merger of compact objects, namely binary neutron stars and BH-neutron star systems (see e.g. [Faber and Rasio 2012, Paschalidis 2017, Baiotti and Rezzolla 2017] and references therein). These systems are traditionally described using the paradigmatic BHs of general relativity, where the spacetime metric is given by the Kerr metric, solely characterized by the BH mass and spin. Upcoming observational campaigns may, however, provide data to discriminate those canonical BH solutions from exotic alternatives as, e.g. those in which the BHs are endowed with scalar or vector (Proca) hair, recently obtained by Herdeiro and Radu [2014b] and Herdeiro, Radu, and Rúnarsson [2016]. It is conceivable that testing the no-hair hypothesis of BHs will become increasingly more precise in the next few years as new observational data is collected in both the gravitational-wave channel and in the electromagnetic channel.

In this paper we have considered numerically generated spacetimes of Kerr BHs with synchronised scalar hair and have built stationary models of magnetized tori around them. Those disks are assumed to be non-self-gravitating, to obey a polytropic equation of state, and to be marginally stable, i.e. the disks completely fill their Roche lobe. In addition, and for the sake of simplicity, the distribution of the specific angular momentum in the disks has been assumed to be constant. The models have been constructed building on existing approaches presented in Komissarov [2006] and Gimeno-Soler and Font [2017] which dealt with (hairless) Kerr BHs. An important generalization of the present work compared to the methodology presented in previous works has had to do with the fluid model: while the matter EOS we use is still rather simplistic (a polytropic EOS) the models are allowed to be thermodinamically relativist, as the specific enthalpy of the fluid can adopt values significantly larger than unity. That has led to interesting differences with respect to the findings reported in Gimeno-Soler and Font [2017] for the purely Kerr BH case.

We have studied the dependence of the morphology and properties of the accretion tori on the type of BH system considered, from purely Kerr BHs with varying degrees of spin parameter (namely from a Schwarzschild BH to a nearly extremal Kerr case) to KBHsSH with different ADM mass and horizon angular velocity. Comparisons between the disk properties for both types of BHs

have been presented. The sequences of magnetized, equilibrium disks models discussed in this study can be used as initial data for numerical relativity codes to investigate their dynamical (non-linear) stability and can be used in tandem with ray-tracing codes to obtain synthetic images of black holes (i.e. shadows) in astrophysically relevant situations where the light source is provided by an emitting accretion disk (first attempted by Vincent et al. [2016]). In a companion paper we will present the non-constant (power-law) case, whose sequences have already been computed. The dynamical (non-linear) stability of these solutions as well as the analysis of the corresponding shadows will be discussed elsewhere.

3.6 Appendix: Finding $l_{\rm mb}$ and $r_{\rm mb}$

We start by considering the Lagrangian of a stationary and axisymmetric spacetime

$$\mathcal{L} = \frac{1}{2}\left[g_{tt}(\dot{t})^2 + 2g_{t\phi}\dot{t}\dot{\phi} + g_{rr}(\dot{r})^2 + g_{\theta\theta}(\dot{\theta})^2 + g_{\phi\phi}(\dot{\phi})^2\right] \ , \tag{3.29}$$

where $\dot{x^\alpha} = \mathrm{d}x^\alpha/\mathrm{d}\lambda$ denotes the partial derivative of the coordinates with respect to an affine parameter λ. We can note that we have two cyclic coordinates (t and ϕ). Then, the canonically conjugate momentum of each coordinate is conserved, namely

$$p_t = \frac{\partial L}{\partial \dot{t}} = -E \ , \tag{3.30}$$

$$p_\phi = \frac{\partial L}{\partial \dot{\phi}} = L \ , \tag{3.31}$$

where we identify the constants of motion as the energy and angular momentum of a test particle.

If we assume motion in the equatorial plane (i.e. $\theta = \pi/2$, $\dot{\theta} = 0$) we can write the relativistic four-momentum (of a massive particle) normalisation as

$$p_t p^t + p_r p^r + p_\phi p^\phi = -m^2 \ , \tag{3.32}$$

where m is the mass of a test particle. Using the defintions of the energy and angular momentum of the particle and taking into account that $p^\alpha = \dot{x^\alpha}$, we can rewrite the above equation as

$$-E\dot{t} + L\dot{\phi} + g_{rr}\dot{r}^2 = -m^2. \tag{3.33}$$

Now, we can find the expressions for the contravariant momenta p^t and p^ϕ from $p_\alpha = g_{\alpha\beta}p^\beta$

$$p^t = \frac{g_{\phi\phi}E + g_{t\phi}}{g_{t\phi}^2 - g_{tt}g_{\phi\phi}} \ , \tag{3.34}$$

$$p^\phi = -\frac{g_{tt}L + g_{t\phi}}{g_{t\phi}^2 - g_{tt}g_{\phi\phi}} \ , \tag{3.35}$$

replace these expressions into Eq. (3.32) and write the expression for the radial velocity $\dot{r}$

$$\dot{r} = \left(-m^2 + \frac{g_{\phi\phi}E^2 + 2g_{t\phi}LE + g_{tt}L^2}{g_{t\phi}^2 - g_{tt}g_{\phi\phi}} \right)^{\frac{1}{2}} . \tag{3.36}$$

We want to consider circular orbits, so the radial velocity must be $\dot{r} = 0$. Then, we arrive at

$$g_{t\phi}^2 - g_{tt}g_{\phi\phi} = g_{\phi\phi}e^2 + 2g_{t\phi}le + g_{tt}l^2 \ , \tag{3.37}$$

where we have introduced the specific energy per unit mass ($e = E/m$) and the specific angular momentum per unit mass ($l = L/m$). Additionally, we are interested in bound orbits. Specifically, we want marginally bound orbits ($e = 1$). Taking this into account, we get the following expression for the specific angular momentum

$$l_{\rm b}^{\pm} = \frac{g_{t\phi} \pm \sqrt{(g_{t\phi}^2 - g_{tt}g_{\phi\phi})(1 + g_{tt})}}{-g_{tt}} \tag{3.38}$$

which corresponds to Eq. (3.8). It is well-known that in BH spacetimes there is an innermost circular marginally bound orbit for test particles. Naturally, a marginally bound particle at the innermost circular orbit has to have the smallest possible value of the specific angular momentum (i.e. a minimum of Eq. (3.38)). The radial location of said minimum is, obviously, the innermost circular marginally bound radius $r_{\rm mb}$.

Chapter 4

Magnetized accretion disks around Kerr black holes with scalar hair: Nonconstant angular momentum disks

This chapter is based on the following publication: S. Gimeno-Soler, J. A. Font, C. Herdeiro & E. Radu. Magnetized accretion disks around Kerr black holes with scalar hair: Nonconstant angular momentum disks, *Physical Review D* 104, 103008 (2021), DOI: 10.1103/PhysRevD.104.103008.

4.1 Introduction

The Event Horizon Telescope (EHT) Collaboration has recently resolved the shadow of the supermassive dark compact object at the center of the giant elliptical galaxy M87 Event Horizon Telescope Collaboration et al. 2019a. The image shows a remarkable similarity with the shadow a Kerr black hole from general relativity would produce. The observational capabilities offered by the EHT, thus, allow to measure strong-field lensing patterns from accretion disks which can be used to test the validity of the black hole hypothesis. Further

evidences in support of such hypothesis are provided by the Advanced LIGO and Advanced Virgo observations of gravitational waves from compact binary coalescences Abbott et al. 2019, Abbott et al. 2020b and by the study of orbital motions of stars near SgrA* at the center of the Milky Way Ghez et al. 2008, Genzel, Eisenhauer, and Gillessen 2010, Gravity Collaboration et al. 2018.

While the black hole hypothesis is thus far supported by current data, the available experimental efforts also place within observational reach the exploration of additional proposals that are collectively known as *exotic* compact objects (ECOs, see Cardoso and Pani 2019 and references therein). Indeed, recent examples have shown the intrinsic degeneracy between the prevailing Kerr black hole solutions of general relativity and bosonic star solutions, a class of horizonless, dynamically robust ECOs, using both actual gravitational-wave data Calderón Bustillo et al. 2021b and electromagnetic data Herdeiro et al. 2021 (see also Olivares et al. 2020). Likewise, testing the very nature of gravity in the strong-field regime is becoming increasingly possible using gravitational-wave observations Abbott et al. 2019, The LIGO Scientific Collaboration, the Virgo Collaboration, and Abbott 2021. Moreover, proofs of concept of the feasibility of testing general relativity, or even the existence of new particles via EHT observations have been reported in, *e.g.* Mizuno et al. 2018, Cunha, Herdeiro, and Radu 2019a, Cunha, Herdeiro, and Radu 2019b, Cruz-Osorio et al. 2021, Völkel et al. 2020, Psaltis et al. 2020, Kocherlakota et al. 2021.

Those observational advances highly motivate the development of theoretical models to explain the available data. In particular, and in connection with the EHT observations, the establishing of sound theoretical descriptions of dark compact objects surrounded by accretion disks is much required. Disks act as illuminating sources leading through gravity to potentially observable strong-field lensing patterns and shadows. Indeed, a few proposals have recently discussed the observational appearance of the shadows of black holes and boson stars by analyzing the lensing patterns produced by a light source - an accretion disk - with identical morphology Cunha et al. 2015, Cunha et al. 2016, Vincent et al. 2016, Olivares et al. 2020. While boson star spacetimes lack an innermost stable circular orbit for timelike geodesics (which would prevent the occurence of the shadow as the disk can only terminate in the centre of the dark star) the general relativistic MHD simulations of Olivares et al. 2020 have shown the existence of an *effective* shadow at a given areal radius at which the angular velocity of the orbits attains a maximum. The intrinsic unstable nature of the spherical boson star model employed in Olivares et al. 2020 has been discussed in Herdeiro et al.

2021 who found that a degenerate (effective) shadow comparable to that of a Schwarzschild black hole can exist for spherical *vector* (a.k.a. Proca) boson stars.

Despite the significance of the accretion disk model for the computation of lensing patterns as realistic as possible, existing studies are based on rigidly-rotating (geometrically thick) disks, assuming as an initial condition for the dynamical evolutions a constant radial profile of the specific angular momentum of the plasma. In this paper we present stationary solutions of magnetized thick disks (or tori) whose angular momentum distribution deviates from a simplistic constant angular momentum law. We introduce a new way to prescribe the distribution of the disk's angular momentum based on a combination of two previous proposals Daigne and Font 2004, Qian et al. 2009, Gimeno-Soler and Font 2017 and compute the angular momentum distribution employing the so-called von Zeipel cylinders, i.e. the surfaces of constant specific angular momentum and constant angular velocity, which coincide for a barotropic equation of state. A major simplification of our approach is that the self-gravity of the disk is neglected and the models are built within the background spacetime provided by a particular class of ECO, namely the spacetime of a Kerr black hole with synchronised scalar hair. (We note in passing that building such disks around bosonic stars, extending the models of Vincent et al. 2016, Olivares et al. 2020 would be straightforward in our approach.) Kerr black holes with synchronised scalar hair (KBHsSH) result from minimally coupling Einstein's gravity to bosonic matter fields Herdeiro and Radu 2014b, Herdeiro and Radu 2015a and provide a sound counterexample to the no-hair conjecture Herdeiro and Radu 2015b[1]. Such hairy black holes have been shown to form dynamically (in the vector case) as the end-product of the superradiant instability East and Pretorius 2017 (but see also Sanchis-Gual et al. 2020 for an alternative formation channel through the post-merger dynamics of bosonic star binaries) and to be effectively stable against superradiance in regions of the parameter space Degollado, Herdeiro, and Radu 2018. As we show below, the effect of the scalar hair on the black hole spacetime can introduce significant differences in the properties and morphology of the disks compared to what is found in a purely Kerr spacetime. The models discussed in this paper can be used as initial

[1]The solutions studied here are the fundamental states of the minimal Einstein-Klein-Gordon model without self-interactions. Different generalizations can be obtained, including charged Delgado et al. 2016 and excited states in the same model Wang, Liu, and Wei 2019, Delgado, Herdeiro, and Radu 2019, as well as cousin solutions in different scalar Herdeiro, Radu, and Rúnarsson 2015, Herdeiro et al. 2018, Herdeiro et al. 2019, Brihaye and Ducobu 2019, Kunz, Perapechka, and Shnir 2019, Collodel, Doneva, and Yazadjiev 2020, Delgado, Herdeiro, and Radu 2021 or Proca models Herdeiro, Radu, and Rúnarsson 2016, Santos et al. 2020.

data for general-relativistic MHD codes and employed as illuminating sources to compute shadows of KBHsSH that might be confronted with prospective new observational data.

The organization of this paper is as follows: Section 4.2 briefly describes the spacetime properties of KBHsSH, the combined approaches we employ to prescribe the angular momentum distribution in the disk, along with the way the magnetic field is incorporated in the models. The numerical procedure to build the tori and our choice of parameter space is discussed in Section 4.3. The equilibrium models are presented and analyzed in Section 4.4. This section also contains the discussion of the morphological features of the disks along with potential astrophysical implications of our models. Finally, our conclusions are summarized in Section 4.5. Geometrized units ($G = c = 1$) are used throughout the paper.

4.2 Framework

4.2.1 Spacetime metric and KBHsSH models

As in Gimeno-Soler et al. 2019 (hereafter Paper I) we use the KBHsSH models built using the procedure described in Herdeiro and Radu 2015a where the interested reader is addressed for further details. In the following we briefly review their basic properties.

KBHsSH are asymptotically flat, stationary and axisymmetric solutions of the Einstein-(complex)Klein-Gordon (EKG) field equations

$$R_{ab} - \frac{1}{2} R g_{ab} = 8\pi (T_{\rm SF})_{ab} \,, \tag{4.1}$$

describing a massive, complex scalar field Ψ minimally coupled to Einstein gravity. The metric and the scalar field can be written using the ansatz (see Herdeiro and Radu 2014b)

$$\begin{aligned} {\rm d}s^2 &= e^{2F_1} \left(\frac{{\rm d}r^2}{N} + r^2 {\rm d}\theta^2 \right) + e^{2F_2} r^2 \sin^2\theta ({\rm d}\phi - \mathcal{W}{\rm d}t)^2 \\ &- e^{2F_0} N {\rm d}t^2 \,, \end{aligned} \tag{4.2}$$

$$\Psi = \varphi(r,\theta) e^{{\rm i}(m\phi - \omega t)} \,, \tag{4.3}$$

where $\mathcal{W}$, F_1, F_2, F_0 are functions of r and θ, ω is the scalar field frequency, and m is the azimuthal harmonic index. The latter two are related through

Table 4.1 List of models of KBHsSH used in this work. From left to right the columns report the name of the model, the ADM mass, $M_{\rm ADM}$, the ADM angular momentum, $J_{\rm ADM}$, the horizon mass, $M_{\rm H}$, the horizon angular momentum, $J_{\rm H}$, the mass of the scalar field, $M_{\rm SF}$, the angular momentum of the scalar field, $J_{\rm SF}$, the radius of the event horizon, $r_{\rm H}$, the values of the normalized spin parameter for the ADM quantities, $a_{\rm ADM}$, and for the BH horizon quantities, $a_{\rm H}$, the horizon linear velocity, $v_{\rm H}$, the spin parameter corresponding to a Kerr BH with a linear velocity equal to $v_{\rm H}$, $a_{\rm H_{eq}}$, and the sphericity of the horizon as defined in Delgado, Herdeiro, and Radu [2018], $\mathfrak{s}$. Here $\mu = 1$.

Model	$M_{\rm ADM}$	$J_{\rm ADM}$	$M_{\rm H}$	$J_{\rm H}$	$M_{\rm SF}$	$J_{\rm SF}$	$r_{\rm H}$	$a_{\rm ADM}$	$a_{\rm H}$	$v_{\rm H}$	$a_{\rm H_{eq}}$	$\mathfrak{s}$
I	0.415	0.172	0.393	0.150	0.022	0.022	0.200	0.9987	0.971	0.7685	0.9663	1.404
IV	0.933	0.739	0.234	0.114	0.699	0.625	0.100	0.8489	2.082	0.5635	0.8554	1.425
VII	0.975	0.850	0.018	0.002	0.957	0.848	0.040	0.8941	6.173	0.0973	0.1928	1.039

$\omega/m = \Omega_{\rm H}$, where $\Omega_{\rm H}$ is the angular velocity of the event horizon. Moreover $N = 1 - r_{\rm H}/r$, where $r_{\rm H}$ is the radius of the event horizon of the black hole. The energy-momentum tensor acting as a source of the EKG equations can be written as

$$\begin{aligned}(T_{\rm SF})_{ab} &= \partial_a\Psi^*\partial_b\Psi + \partial_b\Psi^*\partial_a\Psi \\ &- g_{ab}\left(\frac{1}{2}g^{cd}(\partial_c\Psi^*\partial_d\Psi + \partial_d\Psi^*\partial_c\Psi) + \mu^2\Psi^*\Psi\right),\end{aligned} \tag{4.4}$$

where μ is the mass of the scalar field and superscript $(^*)$ denotes complex conjugation.

Table 4.1 reports the properties of the three KBHsSH models we use in this work. The corresponding models are plotted in Fig. 4.1 within the domain of existence of KBHsSH in an ADM mass versus scalar field frequency diagram. As we consider a subset of the models we used in Paper I we keep the same labels so that the comparison with the previous results for constant angular momentum disks is easier to do. In particular, model I corresponds to a Kerr-like model, with almost all the mass and angular momentum stored in the BH (namely, 94.7% of the total mass and 87.2% of the total angular momentum of the spacetime are stored in the BH), while model VII corresponds to a hairy Kerr BH with almost all the mass (98.15%) and angular momentum (99.76%) stored in the scalar field. Moreover, it is worth noting that, even though KBHsSH can violate the Kerr bound in terms of the horizon quantities (i.e. the normalized spin of the BH $a_{\rm H}$ can be greater than one), this fact does not have the same implications as in Kerr spacetime. In particular, the linear velocity of the horizon, $v_{\rm H}$, never exceeds the speed of light [Herdeiro and Radu 2015c].

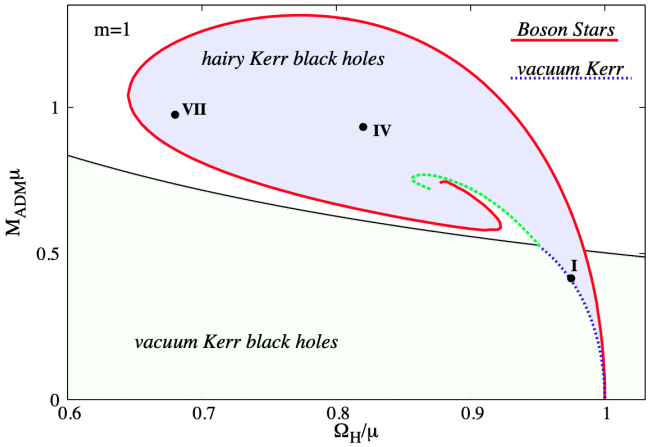

Figure 4.1 Domain of existence for KBHsSH (shaded blue area) in an ADM mass versus scalar field frequency diagram. The three solutions to be studied herein are highlighted in this diagram.

4.2.2 Angular momentum distributions in the disk

As in Paper I equilibrium solutions of thick accretion disks are built assuming stationarity and axisymmetry in both the spacetime and in the matter fields (i.e. $\partial_t f(r,\theta) = \partial_\phi f(r,\theta) = 0$ when $f(r,\theta)$ is a fluid quantity). We use the standard definitions of the specific angular momentum $l = -u_\phi/u_t$ and of the angular velocity $\Omega = u^\phi/u^t$, where we further assume circular motion, i.e. the 4-velocity of the fluid is given by $u^\mu = (u^t, 0, 0, u^\phi)$. It is straightforward to obtain the relationship between l and Ω,

$$l = -\frac{\Omega g_{\phi\phi} + g_{t\phi}}{\Omega g_{t\phi} + g_{tt}}, \quad \Omega = -\frac{l g_{tt} + g_{t\phi}}{l g_{t\phi} + g_{\phi\phi}}. \tag{4.5}$$

In this work we depart from Paper I by introducing a non-constant distribution of specific angular momentum in the disk. This new prescription is the result of combining two different approaches: one to formulate the angular momentum distribution in the equatorial plane, and another one to do so outside the equatorial plane. The reason for this split will be explained below.

4.2.2.1 Angular momentum distribution in the equatorial plane

To obtain the specific angular momentum distribution in the equatorial plane, $\theta = \pi/2$, we consider the following procedure

$$l\left(r, \frac{\pi}{2}\right) = \begin{cases} l_0 \left(\frac{l_{\rm K}(r)}{l_{\rm K}(r_{\rm ms})}\right)^\alpha & \text{for } r \geq r_{\rm ms} \\ l_0 & \text{for } r < r_{\rm ms} \end{cases} \tag{4.6}$$

Table 4.2 Values of the relevant physical magnitudes of our results for model I. From left to right, the columns correspond to: the constant part of the specific angular momentum distribution l_0, the exponent of the angular momentum distribution α, the depth of the potential well at the center $\Delta W_{\rm c}$, the values of the perimeteral radial coordinate at the inner edge of the disk $R_{\rm in}$, at the outer edge of the disk $R_{\rm out}$ and at the center of the disk $R_{\rm c}$, the value of the magnetization parameter at the center of the disk $\beta_{\rm m,c}$, the maximum values of the rest-mass density $\rho_{\rm max}$, specific enthalpy $h_{\rm max}$, fluid pressure $p_{\rm max}$ and magnetic pressure $p_{\rm m,max}$, the location of the maximum of the fluid pressure and the magnetic pressure $R_{\rm max}$, $R_{\rm m,max}$.

l_0	α	$\Delta W_{\rm c}$	$R_{\rm in}$	$R_{\rm out}$	$R_{\rm c}$	$\beta_{\rm m,c}$	$\rho_{\rm max}$	$h_{\rm max}$	$p_{\rm max}$	$p_{\rm m,max}$	$R_{\rm max}$	$R_{\rm m,max}$
0.934	0	-9.37×10^{-2}	0.858	3.56	1.14	10^{10}	1.00	1.10	2.46×10^{-2}	2.54×10^{-12}	1.14	1.20
						1	1.09	1.05	1.37×10^{-2}	1.25×10^{-2}	1.06	1.09
						10^{-10}	1.43	1.00	3.76×10^{-12}	3.09×10^{-2}	1.00	1.03
0.922	0	-9.37×10^{-2}	0.818	3.08	1.08	10^{10}	1.00	1.10	2.46×10^{-2}	2.55×10^{-12}	1.08	1.13
						1	1.10	1.05	1.38×10^{-2}	1.26×10^{-2}	1.01	1.04
						10^{-10}	1.48	1.00	3.93×10^{-12}	3.17×10^{-2}	0.953	0.975
1.14	0	-9.37×10^{-2}	1.24	∞	2.17	10^{10}	1.00	1.10	2.46×10^{-2}	2.56×10^{-12}	2.17	2.40
						1	1.10	1.05	1.38×10^{-2}	1.26×10^{-2}	1.89	2.01
						10^{-10}	1.44	1.00	3.81×10^{-12}	3.14×10^{-2}	1.72	1.79
0.930	0.25	-7.57×10^{-2}	0.864	3.94	1.17	10^{10}	1.00	1.08	1.97×10^{-2}	2.04×10^{-12}	1.17	1.24
						1	1.10	1.04	1.10×10^{-2}	1.01×10^{-2}	1.08	1.12
						10^{-10}	1.45	1.00	3.10×10^{-12}	2.53×10^{-2}	1.02	1.05
0.918	0.25	-7.57×10^{-2}	0.821	3.32	1.10	10^{10}	1.00	1.08	1.97×10^{-2}	2.04×10^{-12}	1.10	1.16
						1	1.11	1.04	1.11×10^{-2}	1.01×10^{-2}	1.02	1.05
						10^{-10}	1.50	1.00	3.25×10^{-2}	2.60×10^{-2}	0.963	0.986
1.09	0.25	-7.57×10^{-2}	1.24	∞	2.27	10^{10}	1.00	1.08	1.97×10^{-2}	2.06×10^{-12}	2.27	2.56
						1	1.11	1.04	1.12×10^{-2}	1.01×10^{-2}	1.95	2.08
						10^{-10}	1.49	1.00	3.22×10^{-12}	2.61×10^{-2}	1.75	1.83
0.923	0.5	-5.46×10^{-2}	0.874	4.52	1.23	10^{10}	1.00	1.06	1.40×10^{-2}	1.46×10^{-12}	1.23	1.31
						1	1.11	1.03	7.97×10^{-3}	7.22×10^{-3}	1.12	1.16
						10^{-10}	1.48	1.00	2.30×10^{-12}	1.86×10^{-2}	1.05	1.08
0.913	0.5	-5.46×10^{-2}	0.826	3.65	1.13	10^{10}	1.00	1.06	1.40×10^{-2}	1.46×10^{-12}	1.13	1.46
						1	1.11	1.03	8.03×10^{-3}	7.24×10^{-3}	1.04	1.08
						10^{-10}	1.53	1.00	2.40×10^{-12}	1.90×10^{-2}	0.977	1.00
1.03	0.5	-5.46×10^{-2}	1.24	∞	2.42	10^{10}	1.00	1.06	1.40×10^{-2}	1.48×10^{-12}	2.42	2.79
						1	1.13	1.03	8.17×10^{-3}	7.28×10^{-3}	2.03	2.19
						10^{-10}	1.56	1.00	2.47×10^{-12}	1.95×10^{-2}	1.81	1.89
0.913	0.75	-2.96×10^{-2}	0.892	5.51	1.31	10^{10}	1.00	1.03	7.50×10^{-3}	7.83×10^{-13}	1.31	1.41
						1	1.11	1.02	4.31×10^{-3}	3.88×10^{-3}	1.18	1.24
						10^{-10}	1.51	1.00	1.29×10^{-12}	1.03×10^{-3}	1.09	1.13
0.906	0.75	-2.96×10^{-2}	0.836	4.14	1.18	10^{10}	1.00	1.03	7.50×10^{-3}	7.84×10^{-13}	1.18	1.26
						1	1.12	1.02	4.33×10^{-3}	3.88×10^{-3}	1.07	1.12
						10^{-10}	1.55	1.00	1.32×10^{-12}	1.04×10^{-2}	1.00	1.03
0.967	0.75	-2.96×10^{-2}	1.26	∞	2.65	10^{10}	1.00	1.03	7.50×10^{-3}	8.00×10^{-13}	2.65	3.15
						1	1.15	1.02	4.48×10^{-3}	3.93×10^{-3}	2.17	2.36
						10^{-10}	1.66	1.00	1.45×10^{-12}	1.11×10^{-2}	1.89	2.00

where l_0 is a constant, $l_{\rm K}(r)$ is the Keplerian specific angular momentum, $r_{\rm ms}$ is the radius of the innermost stable circular orbit (ISCO) and the exponent α (where $0 \leq \alpha < 1$) is a parameter which controls how *Keplerian* the angular momentum profile on the equatorial plane is. The value $\alpha = 0$ would produce a constant profile and $\alpha = 1$ would produce a Keplerian profile. This prescription, extended outside the equatorial plane, was first introduced for so-called Polish-doughnuts in Qian et al. 2009. We also used this recipe in the context of magnetized accretion disks around Kerr black holes in Gimeno-Soler and Font 2017.

In contrast with the Kerr case, for KBHsSH spacetimes we do not have a simple expression for the Keplerian angular momentum distribution $l_{\rm K}(r)$ or for the radius of the ISCO $r_{\rm ms}$. However, it can be shown (see, for instance [Dyba,

Table 4.3 Same as in Table 4.2 but for model IV.

l_0	α	ΔW_c	$R_{\rm in}$	$R_{\rm out}$	R_c	$\beta_{\rm m,c}$	$\rho_{\rm max}$	$h_{\rm max}$	$p_{\rm max}$	$p_{\rm m,max}$	$R_{\rm max}$	$R_{\rm m,max}$
1.16	0	−0.273	0.725	3.85	1.06	10^{10}	1.00	1.31	7.86×10^{-2}	8.52×10^{-12}	1.06	1.21
						1	1.22	1.16	4.95×10^{-2}	4.10×10^{-2}	0.908	0.967
						10^{-10}	2.21	1.00	1.97×10^{-11}	0.130	0.827	0.852
1.14	0	−0.273	0.701	3.70	1.01	10^{10}	1.00	1.31	7.86×10^{-2}	8.56×10^{-12}	1.01	1.15
						1	1.24	1.16	5.04×10^{-2}	4.13×10^{-2}	0.865	0.920
						10^{-10}	2.38	1.00	2.17×10^{-11}	0.138	0.792	0.815
1.83	0	−0.273	1.42	∞	2.44	10^{10}	1.00	1.31	7.86×10^{-2}	8.13×10^{-12}	2.44	2.61
						1	1.09	1.16	4.29×10^{-2}	3.94×10^{-2}	2.17	2.29
						10^{-10}	1.43	1.00	1.10×10^{-11}	9.08×10^{-2}	1.98	2.06
1.16	0.25	−0.233	0.729	4.06	1.12	10^{10}	1.00	1.26	6.57×10^{-2}	7.17×10^{-12}	1.12	1.29
						1	1.24	1.14	4.23×10^{-2}	3.46×10^{-2}	0.935	1.01
						10^{-10}	2.33	1.00	1.80×10^{-11}	0.116	0.842	0.870
1.14	0.25	−0.233	0.703	3.86	1.05	10^{10}	1.00	1.26	6.57×10^{-2}	7.22×10^{-12}	1.05	1.22
						1	1.26	1.14	4.33×10^{-2}	3.49×10^{-2}	0.881	0.944
						10^{-10}	2.52	1.00	2.00×10^{-11}	0.124	0.800	0.825
1.61	0.25	−0.233	1.31	∞	2.44	10^{10}	1.00	1.26	6.57×10^{-2}	6.83×10^{-12}	2.44	2.64
						1	1.11	1.13	3.67×10^{-2}	3.32×10^{-2}	2.13	2.26
						10^{-10}	1.52	1.00	1.02×10^{-11}	8.13×10^{-2}	1.91	1.99
1.15	0.5	−0.179	0.736	4.35	1.21	10^{10}	1.00	1.20	4.91×10^{-2}	5.38×10^{-12}	1.21	1.42
						1	1.25	1.10	3.24×10^{-2}	2.61×10^{-2}	0.980	1.07
						10^{-10}	2.46	1.00	1.49×10^{-11}	9.35×10^{-2}	0.867	0.901
1.13	0.5	−0.179	0.705	4.07	1.11	10^{10}	1.00	1.20	4.91×10^{-2}	5.45×10^{-12}	1.11	1.32
						1	1.28	1.10	3.33×10^{-2}	2.63×10^{-2}	0.907	0.983
						10^{-10}	2.68	1.00	1.67×10^{-11}	0.100	0.812	0.840
1.42	0.5	−0.179	1.20	∞	2.44	10^{10}	1.00	1.20	4.91×10^{-2}	5.14×10^{-12}	2.44	2.68
						1	1.13	1.10	2.83×10^{-2}	2.51×10^{-2}	2.08	2.24
						10^{-10}	1.64	1.00	8.71×10^{-12}	6.65×10^{-2}	1.82	1.92
1.14	0.75	−0.103	0.753	4.79	1.37	10^{10}	1.00	1.11	2.72×10^{-2}	2.98×10^{-12}	1.37	1.62
						1	1.26	1.06	1.83×10^{-2}	1.46×10^{-2}	1.07	1.19
						10^{-10}	2.55	1.00	9.03×10^{-12}	5.53×10^{-2}	0.922	0.968
1.12	0.75	−0.103	0.712	4.29	1.21	10^{10}	1.00	1.11	2.72×10^{-2}	3.03×10^{-12}	1.21	1.47
						1	1.30	1.06	1.90×10^{-2}	1.48×10^{-2}	0.956	1.05
						10^{-10}	2.84	1.00	1.04×10^{-11}	6.06×10^{-2}	0.839	0.873
1.25	0.75	−0.103	1.10	∞	2.48	10^{10}	1.00	1.11	2.72×10^{-2}	2.88×10^{-12}	2.48	2.78
						1	1.16	1.06	1.63×10^{-2}	1.41×10^{-2}	2.05	2.24
						10^{-10}	1.82	1.00	5.75×10^{-12}	4.14×10^{-2}	1.73	1.85

Kulczycki, and Mach 2020]) that in a stationary and axisymmetric spacetime, the Keplerian angular momentum (for prograde motion) takes the general form

$$l_{\rm K}(r) = -\frac{\mathcal{B}g_{\phi\phi} + \partial_r g_{\phi\phi} g_{t\phi}}{\mathcal{B}g_{t\phi} + \partial_r g_{\phi\phi} g_{tt}} \,, \tag{4.7}$$

where $\mathcal{B}$ is defined as

$$\mathcal{B} = -\partial_r g_{t\phi} + \sqrt{(\partial_r g_{t\phi})^2 - \partial_r g_{tt} \partial_r g_{\phi\phi}}. \tag{4.8}$$

It can also be seen that for most BH spacetimes $l_{\rm K}(r)$ only has one minimum outside the event horizon and this minimum coincides with the location of the ISCO. Examples where this condition is not fulfilled are discussed in Dyba, Kulczycki, and Mach 2020, Dyba, Mach, and Pietrzynski 2021 in the context of self-gravitating accretion disks.

Our ansatz for the angular momentum law brings some advantages when compared to a simpler choice. For instance, one could consider a power-law radial dependence like the one discussed in Daigne and Font 2004

$$l(r) = kr^{\alpha}. \tag{4.9}$$

Table 4.4 Same as in Table 4.2 but for model VII.

l_0	α	ΔW_c	R_{in}	R_{out}	R_c	$\beta_{m,c}$	ρ_{max}	h_{max}	p_{max}	$p_{m,max}$	R_{max}	$R_{m,max}$
0.920	0	−0.618	0.227	2.51	1.10	10^{10}	1.00	1.85	0.214	2.23×10^{-11}	1.10	1.21
						1	1.32	1.44	0.144	0.108	0.574	0.863
						10^{-10}	4.77	1.00	1.24×10^{-10}	0.555	0.363	0.400
0.895	0	−0.618	0.189	2.50	1.08	10^{10}	1.00	1.85	0.214	2.23×10^{-11}	1.08	1.20
						1	1.39	1.44	0.153	0.109	0.519	0.820
						10^{-10}	5.84	1.00	1.62×10^{-10}	0.670	0.326	0.360
1.92	0	−0.618	1.01	∞	1.64	10^{10}	1.00	1.85	0.214	2.18×10^{-11}	1.64	1.71
						1	1.08	1.41	0.109	0.102	1.52	1.57
						10^{-10}	1.34	1.00	2.29×10^{-11}	0.196	1.41	1.45
0.916	0.25	−0.531	0.234	2.54	1.16	10^{10}	1.00	1.70	0.175	1.82×10^{-11}	1.16	1.27
						1	1.30	1.36	0.116	8.85×10^{-2}	0.629	0.931
						10^{-10}	4.57	1.00	1.01×10^{-10}	0.453	0.383	0.425
0.887	0.25	−0.531	0.192	2.50	1.14	10^{10}	1.00	1.70	0.175	1.82×10^{-11}	1.14	1.25
						1	1.37	1.36	0.125	8.96×10^{-2}	0.552	0.876
						10^{-10}	5.75	1.00	1.37×10^{-10}	0.561	0.339	0.375
1.44	0.25	−0.531	0.672	∞	1.63	10^{10}	1.00	1.70	0.175	1.80×10^{-11}	1.63	1.71
						1	1.09	1.34	9.23×10^{-2}	8.51×10^{-2}	1.47	1.55
						10^{-10}	1.46	1.00	2.20×10^{-11}	0.178	1.31	1.38
0.903	0.5	−0.374	0.253	2.59	1.29	10^{10}	1.00	1.45	0.113	1.17×10^{-11}	1.29	1.38
						1	1.23	1.23	7.15×10^{-2}	5.72×10^{-2}	0.785	1.12
						10^{-10}	3.93	1.00	5.80×10^{-11}	0.268	0.438	0.493
0.867	0.5	−0.374	0.198	2.48	1.24	10^{10}	1.00	1.45	0.113	1.18×10^{-11}	1.24	1.34
						1	1.30	1.24	7.65×10^{-2}	5.78×10^{-2}	0.663	1.03
						10^{-10}	5.18	1.00	8.39×10^{-11}	0.346	0.367	0.412
1.10	0.5	−0.374	0.460	∞	1.67	10^{10}	1.00	1.45	0.113	1.17×10^{-11}	1.67	1.75
						1	1.11	1.22	6.22×10^{-2}	5.64×10^{-2}	1.48	1.57
						10^{-10}	1.66	1.00	1.84×10^{-11}	0.134	0.973	1.34
0.829	0.75	−0.111	0.380	3.07	1.65	10^{10}	1.00	1.12	2.95×10^{-2}	3.02×10^{-12}	1.65	1.71
						1	1.07	1.06	1.60×10^{-2}	1.49×10^{-2}	1.53	1.59
						10^{-10}	1.37	1.00	4.24×10^{-12}	3.50×10^{-2}	1.34	1.44
0.795	0.75	−0.111	0.233	2.29	1.47	10^{10}	1.00	1.12	2.95×10^{-2}	3.01×10^{-12}	1.47	1.52
						1	1.08	1.06	1.60×10^{-2}	1.49×10^{-2}	1.31	1.40
						10^{-10}	1.92	1.00	6.62×10^{-12}	3.85×10^{-2}	0.594	0.843
0.861	0.75	−0.111	0.643	∞	1.95	10^{10}	1.00	1.12	2.95×10^{-2}	3.08×10^{-12}	1.95	2.06
						1	1.10	1.06	1.66×10^{-2}	1.51×10^{-2}	1.81	1.87
						10^{-10}	1.48	1.00	4.69×10^{-12}	3.79×10^{-2}	1.67	1.73

Due to the explicit dependence on the radial coordinate in Eq. (4.9) it is apparent that this functional form is not coordinate independent. This fact should be no more than a minor inconvenience when dealing with solutions of the Kerr family where algebraic coordinate transformations exist. However, this becomes an insurmountable problem in our case, as there is no way of *translating* a specific choice of angular momentum distribution to a different spacetime in such a way that the physical meaning of Eq. (4.9) is preserved (e.g. from KBHsSH in our coordinate ansatz to a Kerr BH in Boyer-Lindquist coordinates). The angular momentum ansatz used in this work, Eq. (4.6), could be seen as a power law in the same way as Eq. (4.9) (for $r \geq r_{ms}$) if we consider that $k = l_0/l_K(r_{ms})^\alpha$ and $l_K(r)$ plays the role of the radial coordinate. This choice is particularly good as $l_K(r)$ captures the relevant physical information about circular orbits and it is strictly increasing with r, as a well-chosen radial coordinate should be. Furthermore, if l_0 is expressed in terms of quantities determined by the kinematics of the disk, one specific choice of angular momentum will have the same physical meaning irrespective of the particular spacetime we considered.

4.2.2.2 Angular momentum distribution outside the equatorial plane - von Zeipel's cylinders

To obtain the specific angular momentum outside the equatorial plane ($\theta \neq \pi/2$) we take the same approach as in Daigne and Font 2004. This approach considers that l is constant along curves of constant angular velocity Ω that cross the equatorial plane at a particular point $(r_0, \pi/2)$. The specific angular momentum distribution outside the equatorial plane $l(r,\theta)$ is hence obtained by considering $\Omega(r,\theta) = \Omega(r_0, \pi/2)$. By replacing this condition in Eq. (4.5) we arrive at

$$\begin{aligned}
&[g_{tt}(r,\theta)\tilde{g}_{t\phi}(r_0) - \tilde{g}_{tt}(r_0)g_{t\phi}(r,\theta)]l^2_{\rm eq}(r_0) \\
+&[g_{tt}(r,\theta)\tilde{g}_{\phi\phi}(r_0) - \tilde{g}_{tt}(r_0)g_{\phi\phi}(r,\theta)]l_{\rm eq}(r_0) \\
+&[g_{t\phi}(r,\theta)\tilde{g}_{\phi\phi}(r_0) - \tilde{g}_{t\phi}(r_0)g_{\phi\phi}(r,\theta)] = 0\,,
\end{aligned} \tag{4.10}$$

where $l_{\rm eq}(r_0)$ is the specific angular momentum at the point $(r_0, \pi/2)$ and the metric components $\tilde{g}_{\alpha\beta}(r_0)$ refer to quantities evaluated at the equatorial plane. Solving Eq. (4.10) for different values r_0 yields the equation of the curves along which $l(r,\theta) = l_{\rm eq}(r_0)$, i.e. the so-called von Zeipel cylinders.

It is worth remarking that this approach to compute the angular momentum distribution outside the equatorial plane is a better choice for our case than the approach considered in Gimeno-Soler and Font 2017 where a set of equipotential surfaces were computed to map the disk. On the one hand, this approach is computationally cheaper when compared to the one followed in Gimeno-Soler and Font 2017, where a large number of equipotential surfaces and a very small integration step were required to compute the physical quantities in the disk with an acceptable accuracy. On the other hand, one could argue that this approach can be seen as a more natural way of building the angular momentum distribution, as it is built from the integrability conditions of Eq. (4.18) instead of an *ad-hoc* assumption about the form of the angular momentum distribution outside the equatorial plane.

4.2.3 Magnetized disks

As in Paper I we consider that the matter in the disk is described within the framework of ideal, general relativistic MHD. Starting from the conservation laws $\nabla_\mu T^{\mu\nu} = 0$, $\nabla_\mu {}^*F^{\mu\nu} = 0$ and $\nabla_\mu(\rho u^\mu) = 0$, where ∇_μ is the covariant derivative, ${}^*F^{\mu\nu} = b^\mu u^\nu - b^\nu u^\mu$ is the (dual of the) Faraday tensor, b^μ is the magnetic field 4-vector and

$$T^{\mu\nu} = (\rho h + 2p_{\rm m})u^\mu u^\nu + (p + p_{\rm m})g^{\mu\nu} - b^\mu b^\nu, \tag{4.11}$$

is the energy-momentum tensor of a magnetized perfect fluid. In the latter h, ρ, p, and $p_{\rm m} = b^\mu b_\mu/2$ are the fluid specific enthalpy, density, fluid pressure, and magnetic pressure, respectively. It is also convenient to define the magnetization parameter, that is the ratio of fluid pressure to magnetic pressure

$$\beta_{\rm m} = p/p_{\rm m}\,. \tag{4.12}$$

Assuming that the magnetic field is purely azimuthal i.e. $b^r = b^\theta = 0$ and stationarity and axisymmetry of the flow, it immediately follows that the conservation equations of the current density and of the Faraday tensor are trivially satisfied. Contracting the divergence of Eq. (4.11) with the projection tensor $h^\alpha_{\ \beta} = \delta^\alpha_{\ \beta} + u^\alpha u_\beta$ and rewriting the result in terms of the specific angular momentum l and of the angular velocity Ω, we arrive at

$$\partial_i(\ln|u_t|) - \frac{\Omega\partial_i l}{1-l\Omega} + \frac{\partial_i p}{\rho h} + \frac{\partial_i(\mathcal{L}b^2)}{2\mathcal{L}\rho h} = 0\,, \tag{4.13}$$

where $i = r, \theta$ and $\mathcal{L} = g_{t\phi}^2 - g_{tt}g_{\phi\phi}$. To integrate Eq. (4.13) we need to assume an equation of state (EoS). As in Paper I we assume a polytropic EoS of the form

$$p = K\rho^\Gamma\,, \tag{4.14}$$

with K and Γ constants. For the magnetic part, we can write an EoS equivalent to Eq. (4.14), but for $\tilde{p}_{\rm m} = \mathcal{L}p_{\rm m}$

$$\tilde{p}_{\rm m} = K_{\rm m}\tilde{w}^q\,, \tag{4.15}$$

where $K_{\rm m}$ and q are constants and $w = \rho h$. Thus, we can express the magnetic pressure $p_{\rm m}$ as

$$p_{\rm m} = K_{\rm m}\mathcal{L}^{q-1}(\rho h)^q\,. \tag{4.16}$$

Now, we can integrate Eq. (4.13) to arrive at

$$W - W_{\rm in} + \ln\left(1 + \frac{\Gamma K}{\Gamma-1}\rho^{\Gamma-1}\right) + \frac{q}{q-1}K_{\rm m}(\mathcal{L}\rho h)^{q-1} = 0, \tag{4.17}$$

where W stands for the (gravitational plus centrifugal) potential and is defined as

$$W(r,\theta) - W_{\rm in} = \ln|u_t| - \ln|u_{t,{\rm in}}| - \int_{l_{\rm in}}^{l}\frac{\Omega\,dl}{1-l\Omega}\,, \tag{4.18}$$

where subscript 'in' denotes that the corresponding quantity is evaluated at the inner edge of the disk i.e. $(r_{\rm in}, \pi/2)$. We also need to introduce the total gravitational energy density for the disk, $\rho_{\rm T} = -T^t_t + T^i_i$, and for the scalar field,

$\rho_{\rm SF} = -(T_{\rm SF})^t_t + (T_{\rm SF})^i_i$. These are given by

$$\rho_{\rm T} = \frac{\rho h(g_{\phi\phi} - g_{tt}l^2)}{g_{\phi\phi} + 2g_{t\phi}l + g_{tt}l^2} + 2(p + p_{\rm m}), \tag{4.19}$$

$$\rho_{\rm SF} = 2\left(\frac{2e^{-2F_0}\omega(\omega - m\mathcal{W})}{N} - \mu^2\right)\varphi^2. \tag{4.20}$$

Using these expressions we can compute the total gravitational mass of the torus and of the scalar field as the following integral

$$\mathcal{M} = \int \rho\sqrt{-g}\,{\rm d}^3x\,, \tag{4.21}$$

where g is the determinant of the metric tensor and $\rho \equiv \rho_{\rm T}, \rho_{\rm SF}$.

4.3 Methodology

In this section we briefly discuss the space of parameters of the models and our various choices of specific angular momentum distribution. Technical details regarding the computations and other issues are reported in the appendix

In this work, as mentioned before, we only consider a subset of the KBHsSH spacetimes considered in Paper I (namely, spacetimes I, IV and VII). This choice is made to keep the number of free parameters of our models reasonably tractable. Likewise, as in Paper I we fix the mass of the scalar field to $\mu = 1$, the exponents of the polytropic EoS to $q = \Gamma = 4/3$, and the density at the center of the disk to $\rho_{\rm c} = 1$. We also consider only three representative values for the magnetization parameter at the center of the disk $\beta_{\rm m,c}$, namely 10^{10} (which effectively corresponds to a nonmagnetized disk), 1 (mildly magnetized) and 10^{-10} (strongly magnetized).

From Eq. (4.6) it is apparent that the parameter space in the angular momentum sector can be fairly large, i.e. both the constant part of the angular momentum distribution l_0 and the exponent α are continuous parameters. To reduce this part of the parameter space, first we restrict ourselves to four values of the exponent α, namely 0, 0.25, 0.5 and 0.75. To obtain the constant part of the angular momentum distribution, l_0, we consider three different criteria that yield three values of l_0 for each value of α:

1.- l_0 is such that $W_{\rm cusp} = 0$ and $r_{\rm in}$ is chosen such that $\Delta W_{\rm c} = 0.5 W_{\rm c,1}$

2.- l_0 is such that $W_{\rm cusp} < 0$ and $\Delta W_{\rm c} = 0.5 W_{\rm c,1}$

3.- l_0 is such that $W_{\rm cusp} > 0$ and $\Delta W_{\rm c} = 0.5 W_{\rm c,1}$,

In the previous expressions $W_{\rm cusp}$ is the value of the potential at the point where the isopotential surfaces cross (forming a cusp). That point corresponds to a maximum of the potential. In addition $\Delta W_{\rm c}$ is defined as

$$\Delta W_{\rm c} = \begin{cases} W_{\rm c} - W_{\rm in} & \text{if } W_{\rm in} < 0 \\ W_{\rm c} & \text{if } W_{\rm in} \geq 0\,, \end{cases} \tag{4.22}$$

where $W_{\rm c}$ is the potential at the center of the disk and $W_{\rm c,1}$ is the value of the potential at the center when $W_{\rm cusp} = 0$. This value also corresponds to the maximum possible value of $|\Delta W_{\rm c}|$ for a specific choice of α.

4.4 Results

Taking into account the different parameters that characterize our problem setup, we build a total of 108 models of thick disks around KBHsSH, 36 for each of the three hairy BH spacetimes we consider. The main thermodynamical and geometrical characteristics of the models are reported in tables 4.2, 4.3 and 4.4, for spacetimes I, IV, and VII, respectively. For all models the various physical quantities listed in the tables follow qualitatively similar trends when compared to the results in Paper I for constant angular-momentum tori. In particular, for increasing magnetization the maximum of the rest-mass density increases, and the location of the fluid and magnetic pressure maximum shifts towards the black hole. This is accompanied by a global reduction in the size of the disks, only visible for the finite-size disks corresponding to the $l_0, 1$ and $l_0, 2$ cases. Moreover, since the value of $\Delta W_{\rm c}$ is the same for the three values of l_0, for each spacetime and value of the exponent α the maximum specific enthalpy $h_{\rm max}$ and the fluid pressure maximum $p_{\rm max}$ are equal when the disk is unmagnetized ($\beta_{\rm m,c} = 10^{10}$). When the magnetization increases, $h_{\rm max} \to 1$ but at a different rate for each value of l_0 (although the differences can be very small depending on the spacetime and the value of α). We also observe that increasing the magnetization also increases the value of $\rho_{\rm max}$ in a different way depending on the value of l_0. We conclude that the specific value of $\rho_{\rm max}$ achieved when $\beta_{\rm m,c} \to 0$ does not depend on the value of $\Delta W_{\rm c}$, but depends only on the disk model and on the spacetime. Quantitative features and differences between the models are discussed below.

4.4.1 Morphology of the disks

The morphology of the disks in the $(R\sin\theta, R\cos\theta)$ plane is shown in figures 4.2, 4.3, and 4.4. Respectively, they correspond to spacetimes I, IV, and VII.

These figures depict the distribution of the rest-mass density ρ for our three values of the central magnetization parameter $\beta_{\rm m,c}$ (one per column) and for our three values of the constant part of the specific angular momentum l_0 (one per row). In all three figures the exponent α of the specific angular momentum law is fixed to $\alpha = 0.5$, as an illustrative example. The morphological trends observed in this case also apply to the other values of α we scanned. Specific information about the radial size of the disks for all α values are reported in the tables.

The figures reveal that the size of the disks is similar for the two cases $l_{0,1}$ and $l_{0,2}$ and it is remarkably different for $l_{0,3}$. In the latter, disks are significantly larger (in fact the outermost isodensity contour closes at infinity, as shown in the value of $R_{\rm out}$ in the tables). This trend applies to all values of the magnetization parameter, to all three spacetimes, and to all values of α, as can be determined from the tables. The fact that the morphological differences for $l_{0,1}$ and $l_{0,2}$ are minor is related to the fact that the angular momentum profiles along the equatorial plane are fairly similar for those two cases (as shown in Fig. 4.9). Actually, the $l_{0,2}$ models resemble a slightly smaller version of the $l_{0,1}$ disks, attaining larger values of $\rho_{\rm max}$ and $p_{\rm max}$ when the magnetization starts becoming relevant.

As in the constant angular momentum models of Paper I the location of the centre of the disk moves closer to the black hole as the magnetization increases, and the upper values of the isodensity contours also become larger. Moreover, the inner radius of the disks also shift closer to the black hole for $l_{0,1}$ and $l_{0,2}$ than for $l_{0,3}$. Both of these trends are observed for all three spacetimes. Specific values of those radii are reported in the tables.

Fig. 4.5 shows the gravitational energy density, Eqs. (4.19) and (20), for both the fluid matter (top half of each panel) and for the scalar field (bottom half). We compare the distribution of the energy density in the three KBHsSH spacetimes for the particular case $\alpha = 0.75$, $\beta_{\rm m,c} = 10^{-10}$ as an illustrative example. The top panels correspond to $l_0 = l_{0,2}$ and the bottom panels to $l_0 = l_{0,3}$. We note that, in general, the location of the area where the maximum values for the energy density for the fluid and for the scalar field are attained do not coincide. The most striking morphological difference appears in spacetime VII where, in some cases, a second maximum in the gravitational energy density distribution of the fluid appears (see top-right plot of Fig. 4.5). The region of the parameter space in which this situation occurs is discussed below.

In Fig. 4.6 we plot the radial profiles of the rest-mass density at the equatorial plane in double logarithmic scale. Models built for spacetimes I and IV (top

and central rows) show very similar qualitative profiles in all cases (i.e. different values of α and $\beta_{\rm m,c}$). Those profiles are also fairly similar to those expected of a constant angular momentum torus around a Kerr black hole (see Gimeno-Soler et al. 2019). Again, the most prominent differences are apparent for spacetime VII shown in the bottom row: for spacetime I and IV, the rest-mass density maximum is close to the inner edge of the disk while for spacetime VII and for unmagnetized disks (solid lines), this maximum is significantly further away. This is related to the fact that most of the mass and angular momentum of spacetime VII are stored in the scalar field. Moreover, compared to spacetimes I and IV, for spacetime VII the location of the density maximum for models $l_0 = l_{0,2}$ and $l_0 = l_{0,3}$ in the unmagnetized case ($\beta_{\rm m,c} = 10^{10}$) are very close to each other (see solid black and blue curves).

Focusing on the unmagnetized case, the bottom row of the figure shows that the rest-mass density is higher in the region where the hair has most of its gravitational energy density ($\log_{10} R \sim 0.1$; see vertical line), irrespective of l_0. The central and right panel reveal an interesting effect. Compared to the left panel, the profile of the $l_0 = l_{0,2}$ case in the central panel is similar but that of the $l_0 = l_{0,3}$ case develops a low-density inner region (notice the change in slope in the blue solid curves). When the magnetization increases the maximum of the distribution shifts towards the black hole (central panel, blue dotted curve) but the profile flattens and a significant fraction of the mass is left around $R_{\rm c}$ (signalled by the maximum of the solid lines).

If we now focus on the right panel, we observe that what we have just discussed for the $l_{0,3}$ case for $\alpha = 0.5$ (i.e. the flattening of the profile) occurs for the $l_{0,2}$ case in the $\alpha = 0.75$ case. The flattening in the distribution implies the appearance of a second maximum in the gravitational energy density of the torus, $\rho_{\rm T}$, which is roughly located in the same region where the $\rho_{\rm SF}$ maximum is attained (see top-right panel in Fig. 4.5). Correspondingly, for the $l_{0,3}$ case (blue dashed and dotted curves) we see that the location of $\rho_{\rm max}$ does not move all the way down to the inner edge of the disk and a low density region is left even in the highly magnetized case.

We note that this trend is expected to happen also for the $l_0 = l_{0,2}$ (black curves) if we increase the value of α. We have tested this by building models with $\alpha = 0.8$. It seems that large enough values of α the gravitational well of the hair can act as a barrier preventing the maximum of the rest-mass density to reach the inner edge of the disk. This effect seems to appear first (i.e. for smaller values of α) for $l_{0,3}$, then for $l_{0,1}$ (radial profiles not shown in Fig. 4.6) and lastly for $l_{0,2}$.

We close this section by noting that some models for spacetime VII bear some morphological resemblance with the findings of Dyba, Kulczycki, and Mach 2020, Dyba, Mach, and Pietrzynski 2021 for self-gravitating massive tori. In particular, this similarity is found for nonmagnetized disks and when the maximum of the rest-mass density is close to the maximum of gravitational energy density of the field. Some of their massive models also present a second ergoregion as in our spacetime VII (see [Herdeiro and Radu 2015a]) but due to the self-gravity of the disk. This resemblance can be explained by the fact that in our case, the scalar field distribution can mimic the self-gravity of the disk.

4.4.2 Effects of the magnetization

In Fig. 4.7 we discuss the effects of the magnetization on the disk properties, for a subset of the models reported in Tables 4.2, 4.3 and 4.4. The top row of Fig. 4.7 shows the deviation in the location of the maximum of the magnetic pressure $R_{\rm m,c}$ (reached at the equatorial plane) with respect the location of the center of the disk $R_{\rm c}$. This is a relevant quantity to analyze because our previous results in Gimeno-Soler and Font 2017 and Paper I showed that $R_{\rm m,c} > R_{\rm c}$ for weakly magnetized disks and $R_{\rm m,c} < R_{\rm c}$ for strongly magnetized disks. The exact value of $\beta_{\rm m,c}$ for which $R_{\rm m,c} = R_{\rm c}$ is related to the exponent of the EoS Γ and to the value of the potential gap at the center of the disk $\Delta W_{\rm c}$ (or to the maximum value of the specific enthalpy $h_{\rm max}$ when $\beta_{\rm m,c} \to \infty$). In particular, in reference Gimeno-Soler and Font 2017 it was shown that, if $\Delta W_{\rm c}$ is sufficiently small, then $h \to 1$ and the value of the magnetization parameter such that $R_{\rm m,c} = R_{\rm c}$ is $\beta_{\rm m,c} = 1/(\Gamma - 1)$. In the rightmost part of the top panels (which correspond to cases increasingly less magnetized) we observe that most models can be ordered by their value of $(R_{\rm m,c} - R_{\rm c})/R_{\rm c}$ irrespective of α, the greatest deviation being observed for spacetime IV and $l_0 = l_{0,2}$ (blue solid curve) and the smallest for spacetime VII and $l_0 = l_{0,3}$ (red dashed curve). The only exception to this trend is spacetime VII for $l_0 = l_{0,2}$ where the value of $(R_{\rm m,c} - R_{\rm c})/R_{\rm c}$ goes from the second highest for $\alpha = 0$ (left column) to the smallest for $\alpha = 0.75$ (right column). In the inset of all three plots in the top row we display the region around $R_{\rm m,c} = R_{\rm c}$ and $\beta_{\rm m,c} = 3$. In particular, we find that, as expected, models with a smaller value of $\Delta W_{\rm c}$ pass closer to the point $(\log_1 03, 0)$. This can be seen both for each spacetime with constant α and for each model when changing the value of α. Moreover, we also observe that in general, the models with $l_0 = l_{0,3}$ pass closer to the point $(\log_{10} 3, 0)$ when compared to their counterparts with $l_0 = l_{0,3}$, with the exceptions of model I for $\alpha = 0$ where they almost coincide

(see the black curves in the top left panel) and of model I for $\alpha = 0.75$, where this behaviour is inverted (top right panel).

On the other hand, in the leftmost part of each plot in the top row (which correspond to highly magnetized cases) we find that for $\alpha = 0$ and 0.75 (left and central panels), the value of $(R_{\rm m,c} - R_{\rm c})/R_{\rm c}$ also provides a neat ordering of the models, from spacetime VII, $l_0 = l_{0,2}$ (red solid line) with the highest deviation, to spacetime I, $l_0 = l_{0,2}$ (black solid curve) with the smallest. However, for $\alpha = 0.75$ (top left panel) we find that spacetime IV, $l_{0,3}$ now has a slightly larger deviation than spacetime I, $l_{0,3}$, and for spacetime VII it is found that $l = l_{0,3}$ has the smaller deviation and that for $l = l_{0,2}$ the behavior of $(R_{\rm m,c} - R_{\rm c})/R_{\rm c}$ with respect $\log_{10}\beta_{\rm m,c}$ is abnormal when compared to the other models. The discrepancies observed for the highly magnetized models for spacetime VII can be related to the peculiarities we discussed in the radial profiles in Fig. 4.6.

In the central row of Fig. 4.7 we show the dependence of the maximum of the specific enthalpy $h_{\rm max}$ on the magnetization of the disk. For each model the value of $h_{\rm max}$ goes from $e^{\Delta W_{\rm c}}$ for unmagnetized disks ($\beta_{\rm m,c} \to \infty$) to 1 for extremely magnetized disks ($\beta_{\rm m,c} \to 0$) (for a discussion on this topic see, for instance [Gimeno-Soler et al. 2019, Cruz-Osorio, Gimeno-Soler, and Font 2020]). It is apparent that, as expected, the value of $h_{\rm max}$ is consistently higher for models with a higher value of $\Delta W_{\rm c}$ up to small values of $\beta_{\rm m,c}$. Moreover, we can see that models with $l_0 = l_{0,2}$ (solid curves) have slightly higher values of $h_{\rm max}$ for values of $\log_{10}\beta_{\rm m,c}$ between 0 and -2. This difference could be related to the fact that, even though the value of $\Delta W_{\rm c}$ is the same for both $l_{0,2}$ and $l_{0,3}$ models, the gravitational potential distribution that they feel is quite different (see Fig. 4.9).

Finally, the bottom row of Fig. 4.7 depicts the dependence of the maximum of the rest-mass density $\rho_{\rm max}$ on the magnetization of the disk. The observed behaviour is related, when the magnetization begins to be relevant in the disk, to two factors, namely, the shift of the maximum of the rest-mass density with respect the center of the disk and the radial extent of the high density region of the disk. We find that, in general, tori with a value of $R_{\rm in}$ ($l_{0,2}$) closer to the horizon of the black hole exhibit larger values of $\rho_{\rm max}$. This is related to the fact that this kind of disks tend to have $\rho_{\rm max}$ closer to the inner edge of the disk and lesser radial extent of the high density region, as it can be noticed from the central rows of Figs.4.2, 4.3 and 4.4. When comparing between KBHsSH spacetimes, we find that larger values of $\rho_{\rm max}$ are attained for larger values of $\Delta W_{\rm c}$. However, there are particular models that do not obey this trend. In the case of spacetime I, (black lines), the solid and dashed lines are almost coincident

for $\alpha = 0$ and $\alpha = 0.5$ (left and central panels), and for $\alpha = 0.75$ (right panel) the value of $\rho_{\rm max}$ is larger for $l_{0,3}$. This can be explained taking into account that the size of the high-density region for spacetime I, $l_0 = l_{0,2}$ does not change much for increasing magnetization. Other cases that behave in a different way are spacetime VII, $l_0 = l_{0,2}$ (red solid curve) for $\alpha = 0.75$ and $l_0 = l_{0,3}$ (red dashed curve) for $\alpha = 0.5$. In the first case, the value of $\rho_{\rm max}$ is the smallest for $\beta_{\rm m,c} = 0$. However, when the magnetization increases, $\rho_{\rm max}$ grows faster and it ends up reaching the second highest value for $\beta_{\rm m,c} = 10^3$. A similar effect (but in a smaller scale) can be observed for spacetime VII, $l_0 = l_{0,3}$, $\alpha = 0.5$. In this case the effect is due to the flattening of the rest-mass density distribution that we described in the preceding section, where a significant fraction of the mass is left around $R_{\rm c}$, thus reducing the value of $\rho_{\rm max}/\rho_{\rm c}$ (i.e. $\rho_{\rm max}$ as $\rho_{\rm c} = 1$ by construction). It is also worth remarking that with the exception of spacetime VII, if we fix the spacetime and l_0, the value of $\rho_{\rm max}$ in the extremely magnetized case is larger for increasing α, in agreement with what was found for purely Kerr black holes in Gimeno-Soler and Font 2017.

4.4.3 Astrophysical implications

We turn next to discuss possible astrophysical implications of our models. To do so we compute the maximum value of the rest-mass density and of the mass of the disk in physical units. To this end, we recall (see Paper I) that the density in cgs units is related to the density in geometrized units by

$$\rho_{\rm cgs} = 6.17714 \times 10^{17} \left(\frac{G}{c^2}\right) \left(\frac{M_\odot}{M}\right)^2 \rho_{\rm geo}\,. \tag{4.23}$$

We can rewrite this equation in a more convenient way making the following considerations: The ADM mass of the spacetime is expressed in solar-mass units $M_{\rm ADM} = nM_\odot$. The mass of the accretion disk is expressed as a fraction of the ADM mass $M_{\rm T} = qM_{\rm ADM}$. Now, we define the function $\overline{\rho_{\rm T}}$ such that we can rewrite Eq. (4.21) as

$$M_{\rm T} = \rho_{\rm max} \int \overline{\rho_{\rm T}}\, \sqrt{-g}\, {\rm d}x^3\,, \tag{4.24}$$

where $\rho_{\rm max}$ is the maximum value of the rest-mass density in the disk. It is relevant to note that, as $\rho_{\rm T}$ in Eq. (4.19) does not depend linearly in ρ, some dependence on $\rho_{\rm max}$ is left in $\overline{\rho_{\rm T}}$, but the contribution of the nonlinear terms is very small for all the cases we are considering (the deviation between the exact formula and Eq. (4.24) is $< 10^{-6}$ for all our cases). Then, one can see that the ratio $M_{\rm T}/\rho_{\rm max}$ is constant if all the parameters but $\rho_{\rm c}$ are kept constant.

This fact allows us to write the value of the maximum rest-mass density in geometrized units for an accretion torus of mass $M_{\rm T}$ as

$$\rho^{\rm max}_{\rm geo} = \frac{M_{\rm T}\rho_{\rm max}}{M_{\rm T}(\rho_{\rm c}=1)} = \frac{qM^{\rm geo}_{\rm ADM}\rho_{\rm max}}{M_{\rm T}(\rho_{\rm c}=1)}\,, \tag{4.25}$$

where we have used that $M_{\rm T} = qM_{\rm ADM}$, $M_{\rm T}(\rho_{\rm c}=1)$ and $\rho_{\rm max}$ are the mass and the maximum rest-mass of the torus when $\rho_{\rm c}=1$ and $M^{\rm geo}_{\rm ADM}$ is the ADM mass of the spacetime in geometrized units (i.e. the ADM mass as is reported in Table 4.1). Now, we can rewrite Eq. (4.23) as

$$\rho^{\rm max}_{\rm cgs} = 6.17714\times10^{17}\left(\frac{1}{n}\right)^2\frac{qM^{\rm geo}_{\rm ADM}\rho_{\rm max}}{M_{\rm T}(\rho_{\rm c}=1)}\,. \tag{4.26}$$

This equation allows us to compute the maximum value of the rest-mass density in cgs units in terms of the disk mass fraction q provided that we know n, $M^{\rm geo}_{\rm ADM}$ (parameters of the model), $\rho_{\rm max}$, and $M_{\rm T}(\rho_{\rm c}=1)$ (results of our computations).

Figure 4.8 depicts double logarithmic plots of Eq. (4.26) showing the relation between the maximum value of the rest-mass density and $M_{\rm T}/M_{\rm ADM}$ for a subset of our parameter space and two different ADM masses for each KBHsSH spacetime. One is in the stellar mass regime ($M_{\rm ADM} = 5M_\odot$; top panels) and another one is in the supermassive range ($M_{\rm ADM} = 6.2\times10^9 M_\odot$, i.e. the mass of the central black hole in M87; bottom panels). In the top panels we explore the limits of both our disk models and our approach to build them. The shaded region corresponds to the physically admissible solution space, and it is bounded by a horizontal line that represents unrealistically dense solutions ($\rho_{\rm max} = 10^{15}{\rm gcm}^{-3}$) and by a vertical line that represents the point when the test fluid approximation for the disk begins to break down ($M_{\rm T} = 0.1M_{\rm ADM}$) and our approach becomes unsuitable to construct accretion tori. These top panels show interesting properties of our models that we should highlight here: First, it can be seen that, irrespective of the value of the magnetization parameter at the center $\beta_{\rm m,c}$, for a given value of $q = M_{\rm T}/M_{\rm ADM}$, the models with $l_0 = l_{0,3}$ (triangle markers) have smaller values of $\rho_{\rm max}$ when compared to the models with $l_0 = l_{0,2}$ (circle markers). This is due to the fact that the models that are constructed following criterion 3 are significantly more radially extended than the ones built using criterion 2. It can be seen as well that increasing the magnetization parameter increases the value of $\rho_{\rm max}$ for constant q. This is caused by the change of morphology of the disk (the higher rest-mass density region moves towards the black hole and then its volume decreases), but this effect does not change the value of $\rho_{\rm max}$ in the same way for all the models. In particular, we observe that, in general, models with $\alpha = 0.75$ suffer a greater

Table 4.5 Mass parameter of the scalar field μ in eV for our three KBHsSH models if the ADM mass of each spacetime is $M_{\rm ADM} = 5M_\odot$ (first row) and $M_{\rm ADM} = 6.2 \times 10^9 M_\odot$ (i.e. the mass of the central black hole in M87; second row).

	Model I	Model IV	Model VII
$M_{\rm ADM} = 5M_\odot$			
$\mu[eV]$	8.33×10^{-11}	1.87×10^{-11}	1.95×10^{-11}
$M_{\rm ADM} = 6.2 \times 10^9 M_\odot$			
$\mu[eV]$	6.69×10^{-21}	1.50×10^{-20}	1.57×10^{-20}

increase of $\rho_{\rm max}$. In some cases, the difference is very small (e.g. Models I and IV for $l_0 = l_{0,2}$) but it can also be considerably large (e.g. Model VII for $l_0 = l_{0,3}$). This is due to the fact that models with $\alpha = 0.75$ have a greater value of $R_{\rm in}$ than their counterparts with $\alpha = 0$, and then, the decrease of volume of the high rest-mass density region is bigger. However, the difference in magnitude of these changes are caused by the particular features of each spacetime. In particular, Model VII for $l_0 = l_{0,2}$ and $\alpha = 0.75$ is the only case that deviates from the behavior described above. The reason for this deviation is the presence of a second maximum of the gravitational energy density $\rho_{\rm T}$ (see top right panel of Fig. 4.5). This second maximum suppresses the increase of $\rho_{\rm T}$ that would be present due to the high rest-mass density region moving toward the black hole. We also note that the most dense models should affect the hair distribution. In particular in cases I and IV, where less mass and angular momentum are stored in the field.

We conclude that, for a stellar-mass black hole, the values spanned by $\rho_{\rm max}$ are consistent with the maximum densities found in disks formed in numerical-relativity simulations of binary neutron star mergers (see Rezzolla et al. 2010, Baiotti and Rezzolla 2017, Most et al. 2021). This result, which had already been found in the constant angular momentum models of Paper I, is corroborated when using the improved angular momentum distributions analyzed in the present work.

In the bottom panels of Fig. 4.8 we consider the case of a supermassive black hole and only show the two lines (the top line and the bottom line for each case) that bound the parameter space spanned by our results. We also expand the horizontal axis to take into account the extremely low rest-mass densities (between $\sim 10^{-17}$ and $\sim 10^{-19} \mathrm{g\,cm^{-3}}$) in the disk inferred by matching the results of general relativistic magneto-hydrodynamic (GRMHD) simulations with observations (see The Event Horizon Collaboration 2021 and also Chael, Narayan, and Johnson 2019). As we can see in this figure these values of

$\rho_{\max}$ correspond to extremely low values of q (from $< 10^{-11}$ for $\beta_{\rm m,c} = 10^{10}$ to $\lesssim 10^{-13}$ for $\beta_{\rm m,c} = 10^{-10}$). However, it is important to note that the disks in the aforementioned references are not stationary solutions (unlike ours) but are evolved dynamically instead, which means that they are subject to various processes that cause matter redistribution, angular momentum transport and magnetic field amplification -for low magnetized disks- or suppression -for strongly magnetized disks. (Some instances of these processes can be seen in Cruz-Osorio, Gimeno-Soler, and Font 2020.). These effects would change the value of the integral Eq. (4.24) in a non trivial way, as the exact form the evolution affects the disk can depend on the characteristics of the spacetime.

It is also relevant to recall the formula that relates the maximum ADM mass of the KBHsSH with the mass parameter of the scalar field μ (see Herdeiro, Radu, and Rúnarsson 2015 and references therein),

$$M_{\rm ADM}^{\rm max} \simeq \alpha_{\rm BS} 10^{-19} M_\odot \left(\frac{\rm GeV}{\mu}\right) , \tag{4.27}$$

with $\alpha_{\rm BS} = 1.315$ (corresponding to a value of the azimuthal harmonic index $m = 1$). Using the previous definitions, we can rewrite this formula as

$$\mu[\rm eV] = 10^{-10} \frac{M_{\rm ADM}^{\rm geo}}{n} . \tag{4.28}$$

The values of μ for the two astrophysical scenarios we have considered in this section are reported in Table 4.5. These values of μ are within the mass range suggested by the *axiverse* of string theory (see Arvanitaki et al. 2010) portraying a large number of scalar fields in a mass range from 10^{-33} eV to 10^{-10} eV.

4.5 Conclusions

Recent observational data from the LIGO-Virgo-KAGRA Collaboration and from the EHT Collaboration is allowing to probe the black hole hypothesis – black holes apparently populate the Cosmos in large numbers and are regarded as the canonical dark compact objects. While this hypothesis is thus far supported by current data, the ongoing efforts also place within observational reach the exploration of additional proposals for alternative, and *exotic*, compact objects. Indeed, possible model degeneracies have been already pointed out in Calderón Bustillo et al. 2021b, Herdeiro et al. 2021. In this paper we have considered a particular class of ECOs, namely Kerr black holes with synchronised hair resulting from minimally coupling Einstein's gravity to bosonic matter fields Herdeiro and Radu 2014b, Herdeiro, Radu, and Rúnarsson 2016. Such hairy black holes

provide a counterexample to the no-hair conjecture and they have been shown to form dynamically (in the vector case) as the end-product of the superradiant instability East and Pretorius 2017 (but see also Sanchis-Gual et al. 2020 for an alternative formation channel through the post-merger dynamics of bosonic star binaries) and to be effectively stable themselves against superradiance Degollado, Herdeiro, and Radu 2018. In this work we have presented new equilibrium solutions of stationary models of magnetized thick disks (or tori) around Kerr black holes with synchronised scalar hair. The models reported are based on ideas put forward in our previous work Gimeno-Soler et al. 2019 which focused on models following a constant radial distribution of the specific angular momentum along the equatorial plane. The models reported in the present paper, however, greatly extend those of Gimeno-Soler et al. 2019 by accounting for fairly general and astrophysically motivated distributions of the specific angular momentum. In particular, we have introduced a new way to prescribe the distribution of the disk's angular momentum based on a combination of two previous proposals discussed in Daigne and Font 2004 and Qian et al. 2009. Due to the intrinsic higher complexity of the new models, the methodology employed for their construction is markedly different to that employed in Gimeno-Soler et al. 2019. Following Daigne and Font 2004, our approach has been based on the use of the so-called von Zeipel cylinders as a suitable (and computationally efficient) means to compute the angular momentum distribution outside the equatorial plane. Within this framework, we have chosen a fairly large parameter space (amounting to a total of 108 models) that has allowed us to directly compare among different spacetimes with the same choice of specific angular momentum distribution, and to compare between different rotation profiles in the same spacetime.

While our models show some similarities to the constant angular momentum disks of Paper I (which we recover here as a particular limiting case of our improved distributions) important morphological differences also arise. We have found that, due to the scalar hair effect on the spacetime, the disk morphology and physical properties can be quite different than expected if the spacetime was purely Kerr. This has been revealed quite dramatically for KBHsSH spacetime VII which most deviates from the Kerr spacetime (as most of the mass and angular momentum of this spacetime is actually stored in the scalar field). Some of the tori built within this spacetime exhibit the appearance of a secondary maximum in the gravitational energy density with implications in the radial profile distributions of the thermodynamical quantities of the disks. We have also discussed possible astrophysical implications of our models, computing the

maximum value of the rest-mass density and of the mass of the disk in physical units for the case of a stellar-mass black hole and a supermassive black hole. Comparisons with the results from mergers of compact binaries and GRMHD simulations performed by the EHT collaboration yield values compatible with our numbers, again pointing out possible model degeneracies. Finally, our study has also allowed us to provide estimates for the mass of the bosonic particle.

The two-parameter specific angular momentum prescription we have discussed here could be particularly useful for further studies, possibly including time-dependent evolutions, as it allows to build disks with different morphological features (different degrees of thickness and radial extent of the disk). Our models could be used as initial data for numerical evolutions of GRMHD codes to study their dynamics and stability properties. In addition, perhaps most importantly, these disks could be used as illuminating sources to build shadows of Kerr black holes with scalar hair which might further constrain the no-hair hypothesis as new observational data is collected, following up on Cunha et al. 2015, Cunha et al. 2016, Cunha, Herdeiro, and Radu 2019a. Those aspects are left for future research and will be presented elsewhere.

4.6 Appendix: Technical details of our methodology

4.6.1 Angular momentum and potential at the equatorial plane

Our choice for the three values of the constant part of the angular momentum distribution l_0 introduced in Section 4.3 is particularly useful because it allows us to get rid of the dependence on $\Delta W_{\rm c}$ of the physical quantities in the disk computed with each criterion. As it can be seen when inspecting Eq. (4.17), the rest-mass density ρ and the specific enthalpy h (and the pressure p and the magnetic pressure $p_{\rm m}$ which are computed from them) are only dependent on the potential distribution, the magnetization parameter $\beta_{\rm m,c}$ and the geometry of the spacetime (for fixed Γ and q). Therefore, if we remove the dependence on $\Delta W_{\rm c}$, the disk morphology and the physical quantities in the disk only depend on the angular momentum distribution, $l(r,\theta)$, the magnetization parameter at the center of the disk $\beta_{\rm m,c}$ and the geometry of the spacetime. It is also worth to mention that this way of prescribing the angular momentum distribution only depends on the metric parameters and their derivatives (through the potential,

the Keplerian angular momentum and the definition of the von Zeipel cylinders). Therefore, if we compare two solutions built in different spacetimes, but following the same criterion to prescribe the angular momentum distribution, we can be sure that the differences between these two solutions are a consequence of the fact that the two solutions correspond to different spacetimes.

Figure 4.9 displays radial profiles of the angular momentum along the equatorial plane, together with the corresponding profiles of the potential, for our three choices of l_0 and for $\alpha = 0.5$. From left to right each panel corresponds to one of the three different models of KBHsSHs we are considering, namely models I, IV and VII. The radial coordinate used in these plots (and in all figures in the paper) is the perimeteral radius R, related to the Boyer-Lindquist radial coordinate r according to $R = e^{F_2} r$ (see Paper I for details on the geometrical meaning of this coordinate).

It can be seen that for the three spacetimes, the profiles of $l_{\rm eq}(R)$ for criteria 1 and 2 are very similar. The deviations from the Kerr black hole case can be observed in the Keplerian angular momentum profile: in the first column, $l_{\rm K}(R)$ looks very similar to that of a rapidly rotating Kerr BH; some small deviations are visible in the profile plotted in the second column; finally, in the third column, a significant deviation from what should be expected from any Kerr BH is noticeable. The second row of Fig. 4.9 depicts the potential distribution at the equatorial plane, $W_{\rm eq}(R)$. It becomes apparent that a very small variation in the value of l_0 affects significantly the value of $W_{\rm cusp}$ (e.g. the bottom left panel shows that, when comparing the profiles from criteria 1 and 2, a difference between the values of l_0 of about $\sim 1\%$, yields a large difference in the value of $\Delta W_{\rm max} = W_{\rm c} - W_{\rm cusp}$ such that $\Delta W_{\rm max,1} = 2\Delta W_{\rm max,2}$).

To compute the potential at the equatorial plane we rewrite Eq. (4.18) as

$$W_{\rm eq}(r) = -\int_r^{+\infty} \left(\frac{\partial \ln |u_{t,\rm in}|(r)}{\partial r} - \frac{\Omega_{\rm eq} \frac{dl}{dr}}{1 - l_{\rm eq}\Omega_{\rm eq}} \right) dr \,, \tag{4.29}$$

where we have used that $W_{\rm eq}(r) \to 0$ when $r \to \infty$ and u_t can be written as

$$u_t = -\sqrt{\frac{g_{t\phi}^2 - g_{tt} g_{t\phi}}{g_{\phi\phi} + 2 g_{t\phi} l + g_{tt} l^2}}. \tag{4.30}$$

Then, to obtain the values of l_0 we require, we choose the following procedure. First, we start by considering a constant distribution of angular momentum (i.e. $\alpha = 0$) and $l_0 = l_{\rm mb}$ where $l_{\rm mb} = l_{\rm K}(r_{\rm mb})$ and $r_{\rm mb}$ is the radius of the marginally bound orbit. Notice that this choice of the parameters corresponds to the cases we considered in Gimeno-Soler et al. 2019 (and implies that $W_{\rm cusp} = 0$)

and that we obtain $l_{\rm mb}$ and $r_{\rm mb}$ computing the minimum of Eq.(8) in Paper I. We also need to compute $l_{\rm ms}$ and $r_{\rm ms}$ as the minimum of the Keplerian angular momentum (Eq. (4.7)). In this way, Eq. (4.18) amounts to evaluate $W = \ln|u_t|$ and we only need to obtain the minimum of $W(r, \pi/2)$. The location of this minimum corresponds to the center of the disk $r_{\rm c}$ and the value of the potential there is $W_{\rm c,1}$ ($r_{\rm c}$ also corresponds to the largest solution of $l_{\rm K}(r) = l_0$). Once we have the value of $W_{\rm c,1}$ for $\alpha = 0$, we can compute the required quantities to build the three distributions of angular momentum we need. For the first case we only need to find the value of $r_{\rm in}$ that fulfills the condition

$$W(r_{\rm in}, \pi/2) = 0.5 W_{\rm c,1}. \tag{4.31}$$

For the second case, we iteratively solve the following equation for l_0

$$W_{\rm cusp}(l_0) - W_{\rm c}(l_0) = 0.5 W_{\rm c,1}\,, \tag{4.32}$$

taking into account that l_0 must be in the interval $l_{\rm K}(r_{\rm ms}) < l_0 < l_{\rm K}(r_{\rm mb})$ so $W_{\rm cusp} < 0$. And in the third case, we solve

$$W_{\rm c}(l_0) = 0.5 W_{\rm c,1}\,, \tag{4.33}$$

in the same way as in the second case, but taking into account that $l_0 > l_{\rm K}(r_{\rm mb})$, so that $W_{\rm cusp} > 0$.

To obtain the values of l_0 for $\alpha \neq 0$ we only have to take into account that the potential is defined by the integral Eq. (4.29). As we do not have an easy way to compute $W_{\rm c,1}$ (i.e. to compute a value for l_0 such that the condition $W_{\rm cusp} = 0$ is guaranteed), we have to solve iteratively the following equation for l_0

$$W_{\rm eq}(r_{\rm in}; l_0) = 0\,, \tag{4.34}$$

where the left-hand side of the equation is an integral and we know that, for $\alpha > 0$, the value of l_0 corresponding to this case will always be between $l_{\rm K}(r_{\rm ms}) < l_0 < l_{\rm K}(r_{\rm mb})$. With this, we can obtain the value of $W_{\rm c,1}$ for any $\alpha \neq 0$ and following the aforementioned three steps and taking into account that now the potential is defined by the integral (4.29), we can compute all angular momentum and potential distributions at the equatorial plane that we require. It is worth to mention that the value of $W_{\rm c,1}$ is very sensitive to small changes in l_0, due to the fact that the potential is very steep around the maximum, so we solve equations (4.31), (4.32), (4.33) and (4.34) using the bisection method with a tolerance that ensures that the computed values of l_0 fulfill $|(\Delta W_{\rm c} - 0.5 W_{\rm c,1})/-(0.5 W_{\rm c,1})| < 10^{-8}$ for all the cases we have considered. The integral (4.29) is solved using the trapezoidal rule with a radial grid 100

times denser than our regular grid (see below), to ensure the correct finding of $r_{\rm cusp}$, $r_{\rm in}$ and $r_{\rm c}$.

4.6.2 Angular momentum and potential outside the equatorial plane

To extend the angular momentum and the potential distribution to the region outside the equatorial plane we need to solve Eq. (4.10). As we use a numerical grid, it is inconvenient to solve the curves starting from the equatorial plane, as in general the von Zeipel cylinders will not pass through the points in the grid. Instead, we run through all the (r, θ) points in our grid and, for each point, we solve Eq. (4.10) to obtain the crossing point of the corresponding von Zeipel cylinder in the equatorial plane, $(r_0, \pi/2)$. To improve the accuracy of the procedure, we interpolate the function $l_{\rm eq}(r)$ with a third-order spline and we solve Eq. (4.10) with the bisection method and a tolerance of $\sim 10^{-8}$. A sample of the geometry of these cylinders is shown in Fig. 4.10 for the first criterion for the angular momentum at the equatorial plane and $\alpha = 0.5$. To obtain the potential we follow Daigne and Font 2004 and use the fact that the specific angular momentum is constant along the von Zeipel cylinders to recast Eq. (4.18) as

$$W(r,\theta) = W_{\rm eq}(r_0) + \ln\left[\frac{-u_t(r,\theta)}{-u_t(r_0,\pi/2)}\right], \tag{4.35}$$

which yields the potential everywhere.

4.6.3 Building the magnetized disk

To build the disk we follow the same procedure as in Paper I. First, we compute the polytropic constant K by solving

$$W - W_{\rm in} + \ln\left(1 + \frac{\Gamma K}{\Gamma - 1}\rho_{\rm c}^{\Gamma-1}\right) + \frac{q}{q-1}\frac{K\rho_{\rm c}^{\Gamma}}{\beta_{\rm m_c}\left(\rho_{\rm c} + \frac{K\Gamma\rho_{\rm c}^{\Gamma}}{\Gamma-1}\right)} = 0\,, \tag{4.36}$$

which is Eq. (4.17) evaluated at the center of the disk $r_{\rm c}$. Once K is computed we can obtain the remaining relevant quantities at the center, namely $p_{\rm c}$, $p_{\rm m,c}$ and $h_{\rm c}$ along with the polytropic constant of the magnetic EoS $K_{\rm m}$. Then, to compute the distribution of the rest-mass density $\rho(r, \theta)$, we only have to solve

$$W - W_{\rm in} + \ln\left(1 + \frac{\Gamma K}{\Gamma - 1}\rho^{\Gamma-1}\right)$$

$$+\frac{q}{q-1}K_{\rm m}\left(\mathcal{L}\left(\rho+\frac{K\Gamma\rho^{\Gamma}}{\Gamma-1}\right)\right)^{q-1}=0\,, \quad (4.37)$$

if $W(r,\theta)<0$. For $W(r,\theta)>0$ we set $\rho=p=p_{\rm m}=0$. Note that Eqs.(4.36) and (4.37) are both trascendental equations, and must be solved numerically. As in Gimeno-Soler et al. 2019 we solve these equations using a non-uniform (r,θ) grid with a typical domain given by $[r_{\rm H},199.2]\times[0,\pi/2]$ and a typical number of points $N_r\times N_\theta=2500\times300$. Those numbers are only illustrative as the actual values depend on the horizon radius $r_{\rm H}$ and on the specific model. The spacetime metric data on this grid is interpolated from the original data obtained by Herdeiro and Radu 2015a. The original grid in Herdeiro and Radu 2015a is a uniform $(x,\,\theta)$ grid (where x is a compactified radial coordinate) with a domain $[0,1]\times[0,\pi/2]$ and a number of points of $N_x\times N_\theta=251\times30$ [2].

[2] In particular, the three spacetimes which are presented here, are publicly available in *http://gravitation.web.ua.pt/node/416*

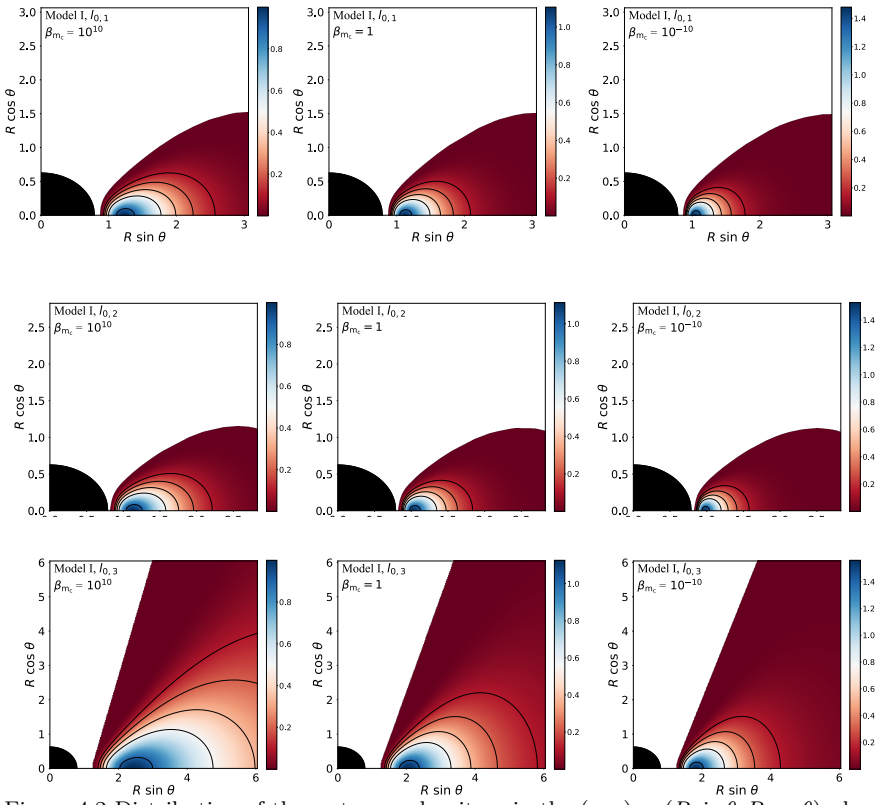

Figure 4.2 Distribution of the rest-mass density ρ in the $(x, y) = (R\sin\theta, R\cos\theta)$ plane (in terms of the perimeteral coordinate R) for spacetime I and $\alpha = 0.5$. From top to bottom the rows correspond to different values of the constant part of the specific angular momentum l_0, namely $l_{0,1}$, $l_{0,2}$ and $l_{0,3}$. From left to right, the columns correspond to different values of the magnetization parameter at the center $\beta_{\mathrm{m,c}}$, namely 10^{10}, 1 and 10^{-10}. The black quarter-circle in the bottom-left corner of each plot marks the position of the black hole. The black curves represent rest-mass density isocontours, corresponding to the values $\rho = \rho_{\max}/x$, where $x = \{10, 5, 3, 2, 1.1\}$.

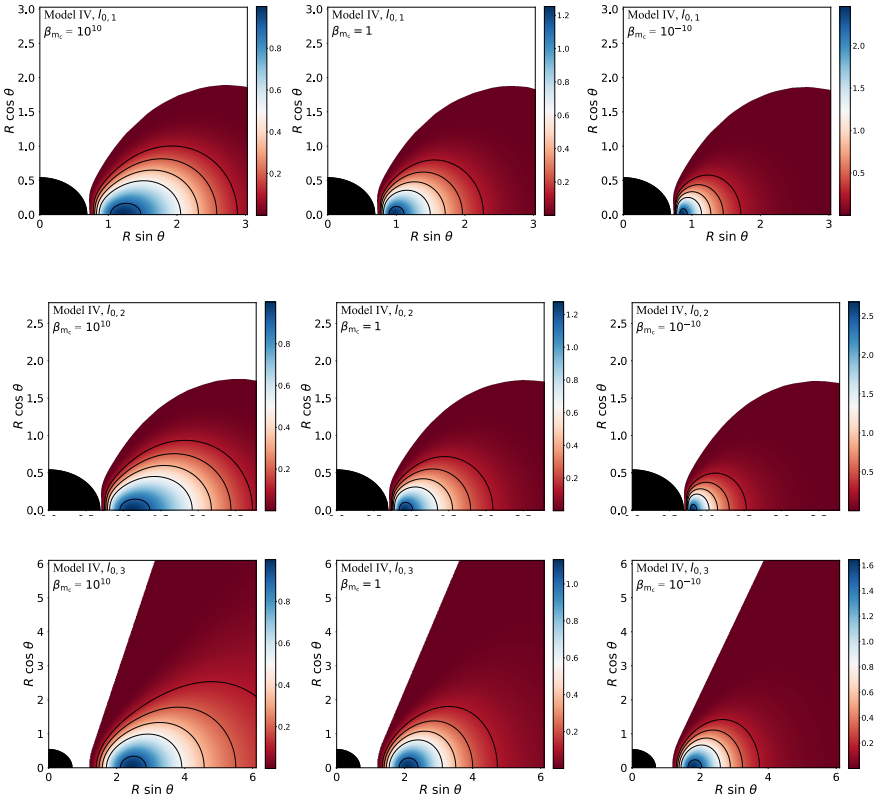

Figure 4.3 Same as Fig. 4.2 but for spacetime IV.

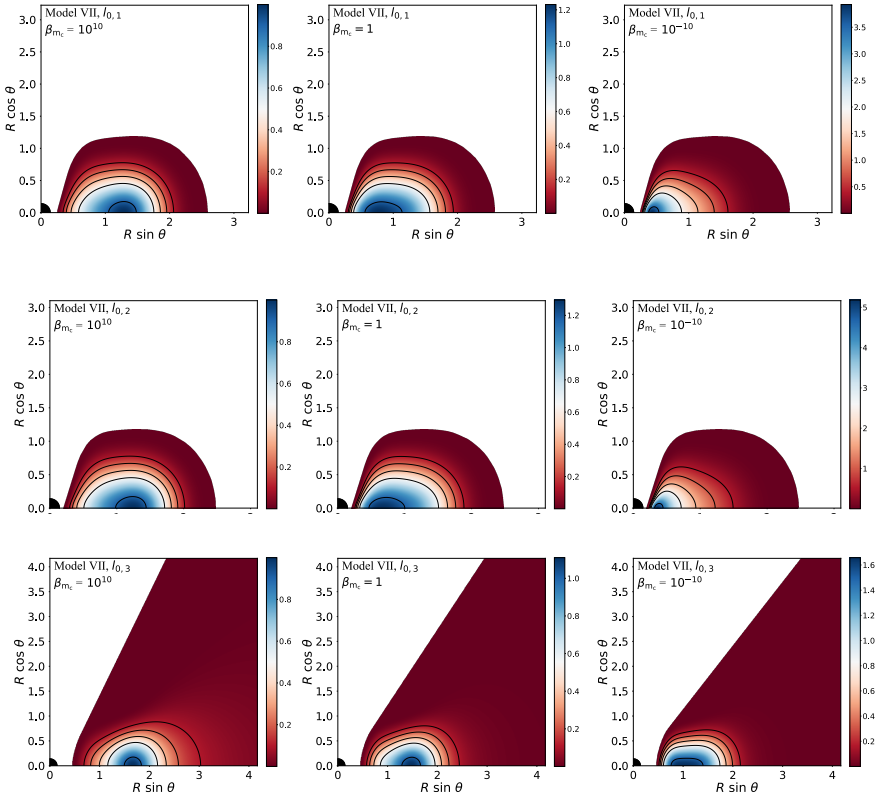

Figure 4.4 Same as Fig. 4.2 but for spacetime VII

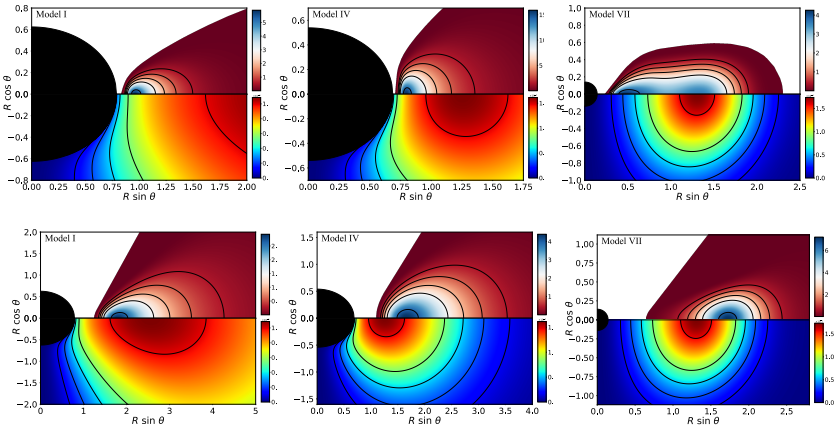

Figure 4.5 Distribution of the gravitational energy density of the matter ρ_{T} (top half of each panel) and of the scalar field ρ_{SF} (bottom half of each panel) for $\alpha = 0.75$, $\beta_{\mathrm{m,c}} = 10^{-10}$, and $l_0 = l_{0,2}$ (top row) and $l_0 = l_{0,3}$ (bottom row). Spacetimes I, IV and VII are shown in the left, middle and right columns, respectively. Note that the spatial scale is not the same for all plots.

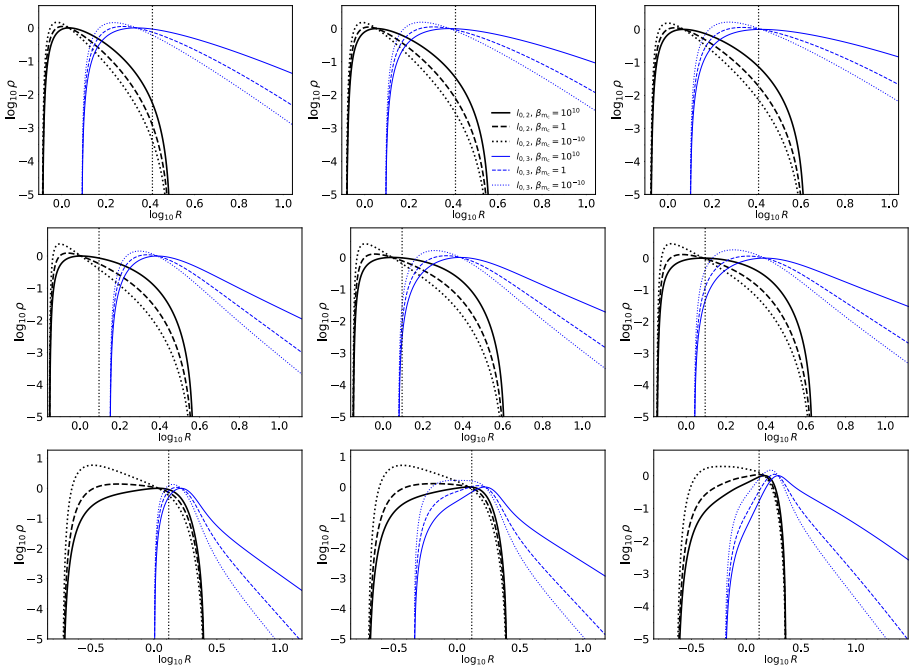

Figure 4.6 Radial profiles of the logarithm of the rest-mass density at the equatorial plane. From top to bottom, the rows correspond to the three different spacetimes we are considering, namely Models, I, IV and VII. From left to right, the columns correspond to different values of the exponent of the angular momentum distribution α, namely 0, 0.5 and 0.75. In each panel, black and blue curves correspond to models with the constant part of the angular momentum distribution l_0 computed following the criterion 2 and 3, respectively. The solid, dashed and dotted lines correspond to different values of the magnetization parameter at the center of the disk $\beta_{\rm m,c}$, namely 10^{10}, 1, 10^{-10}. (See legend in the top-central panel.) The vertical black dotted lines denote the location of the maximum of the gravitational energy density of the scalar field $\rho_{\rm SF,max}$.

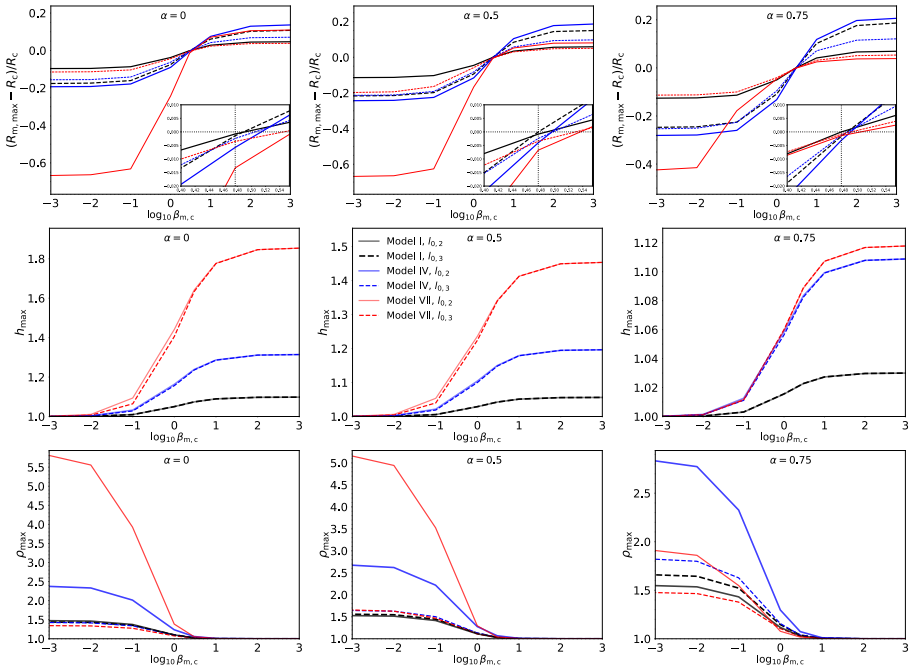

Figure 4.7 Effects of the magnetization on the values of the relative variation of the maximum of the magnetic pressure $(R_{\rm m,max} - R_{\rm c})/R_{\rm c}$ (top panels), the maximum value of the specific enthalpy $h_{\rm max}$ (central panels) and the maximum value of the rest-mass density (bottom panels). From left to right, the columns correspond to different values of the exponent of the angular momentum distribution α, indicated in the plots. In all the panels, black, blue and red lines correspond to the three KBHsSH spacetimes we are considering, namely I, IV and VII. Solid and dashed lines correspond to either criterion 2 or 3 employed to compute l_0, respectively. (See legend in the central plot.) The top panels also display an inset of the region around $\beta_{\rm m,c} = 3$. The horizontal and vertical dotted lines correspond to $R_{\rm m,max} = R_{\rm c}$ and $\beta_{\rm m,c} = 3$ respectively. Note that in this figure we include additional results for values of $\beta_{\rm m,c}$ that are not present in the tables, namely $\beta_{\rm m,c} = \{10^3, 10^2, 10, 3, 10^{-1}, 10^{-2}, 10^{-3}\}$.

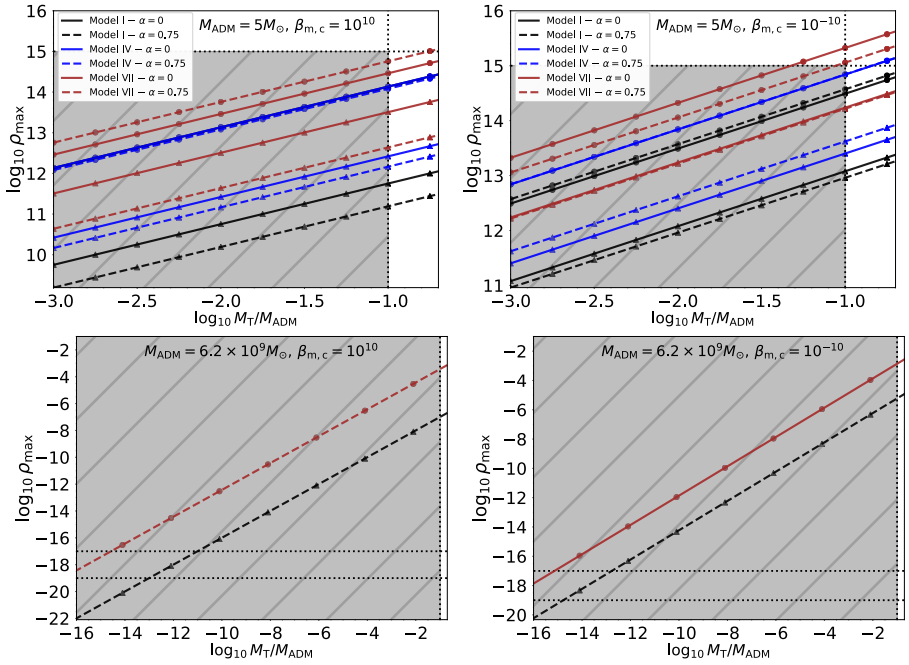

Figure 4.8 Dependence of the logarithm of the maximum of the rest-mass density $\rho_{\rm max}$ in cgs units as a function of the logarithm of the mass of the accretion disk in units of the ADM mass of the spacetime $M_{\rm T}/M_{\rm ADM}$. The top panels show cases with $M_{\rm ADM} = 5M_\odot$ and for the bottom panels $M_{\rm ADM} = 6.2 \times 10^9 M_\odot$. The left column shows nonmagnetized disks ($\beta_{\rm m,c} = 10^3$) and the right column shows highly magnetized disks ($\beta_{\rm m,c} = 10^{-3}$). In the top panels, we show a subset of our parameter space. In particular we show, for our three KBHsSH spacetimes I, IV and VII (black, blue and brown lines, respectively), two values of the exponent $\alpha = 0, 0.75$ (solid and dashed lines respectively) and two ways of prescribing l_0, namely criteria 2 and 3 (circle and triangle markers, respectively). The shaded region of each plot shows the region where our results are physically acceptable. The vertical and horizontal black dotted lines represent $M_{\rm T}/M_{\rm ADM} = 0.1$ and $\rho_{\rm max} = 10^{15}{\rm gcm}^{-3}$ respectively.

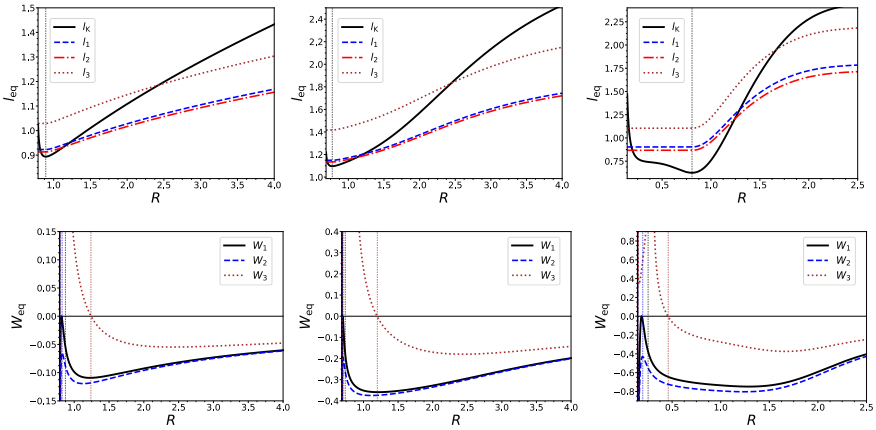

Figure 4.9 Radial distributions of the angular momentum and of the potential at the equatorial plane for $\alpha = 0.5$. Each column corresponds to our three KBHsSH spacetimes (I, IV and VII from left to right). In the first row we show the distribution of angular momentum at the equatorial plane for the three different criteria discussed in Section III.A (namely, a blue dashed line for criterion 1, a red dash-dotted line for criterion 2 and a brown dotted line for criterion 3). The Keplerian angular momentum is also shown in a solid black line. The location of $r_{\rm ms}$ is displayed with a vertical dotted black line. In the second row we show the potential profiles corresponding to each angular momentum distribution displayed in the first row. They are shown by a solid black line, a blue dashed line and a brown dotted line, for each of the three criteria. The vertical dotted lines indicate the location of $r_{\rm in}$ for each case. Note that all the panels use the perimeteral radius R.

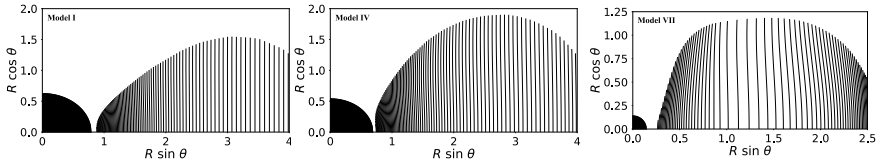

Figure 4.10 Structure of the von Zeipel cylinders (i.e. the surfaces of constant angular velocity Ω that correspond to surfaces of constant specific angular momentum [Daigne and Font 2004]) for the three KBHsSH spacetimes we consider. The particular angular momentum distribution used in this figure corresponds to l_0 computed using criterion 1 in Section III.A and $\alpha = 0.5$. Note that the cylinders are only shown in the region occupied by the disks.

Chapter 5

Magnetized discs and photon rings around Yukawa-like black holes

This chapter is based on the following publication: A. Cruz-Osorio, S. Gimeno-Soler, J. A. Font, M. De Laurentis & S. Mendoza. Magnetized discs and photon rings around Yukawa-like black holes, *Physical Review D* 103, 124009 (2021), DOI: 10.1103/PhysRevD.103.124009.

5.1 Introduction

Astrophysical systems comprising a rotating black hole surrounded by an accretion thick disc of plasma are recognized as natural end results of highly dynamical events involving compact objects in a general-relativistic regime. Stellar-origin systems are produced in mergers of compact binaries comprising either a black hole and a neutron star or two neutron stars, as well as in the gravitational collapse of massive stars (“failed" supernovae) [Woosley 1993, Baiotti and Rezzolla 2017]. Mergers of compact binaries have been dramatically disclosed in recent times thanks to the LIGO-Virgo observations of gravitational waves from GW170817 and the scores of multiwavelength electromagnetic observations that followed [Abbott et al. 2017b, Abbott et al. 2017]. Additionally, black hole-disc systems are used to explain astrophysical phenomenology of supermassive black holes in active galactic nuclei [Shakura and Sunyaev 1973, Rees 1984]. Major

observational advances of the strong-gravity region of such systems have recently been accomplished through the ground-breaking first image of the M87 black hole by the Event Horizon Telescope [Event Horizon Telescope Collaboration et al. 2019a].

Theoretical models describing the morphology of stationary thick discs around black holes in general relativity were first developed in the seminal papers of Fishbone and Moncrief [1976] and Kozlowski, Jaroszynski, and Abramowicz [1978] for isentropic and barotropic discs respectively, assuming a constant distribution of angular momentum. The modeling has gradually improved through the elapsing decades [see e.g. Abramowicz and Fragile 2013, for a review]. Proposals to construct the initial data for magnetized discs with weak magnetic fields exploring different configurations were put forward and evolved by various authors, e.g. advection-dominated accretion flows (ADAF) [Narayan and Yi 1994, Yuan and Narayan 2014], standard and normal evolution (SANE) flows with poloidal magnetic field [Narayan et al. 2012, Sądowski et al. 2013] – for a comparison between codes for SANE evolutions see [Porth et al. 2019] –, and magnetically arrested dominated (MAD) flows [Narayan, Igumenshchev, and Abramowicz 2003, De Villiers and Hawley 2003b, Tchekhovskoy, Narayan, and McKinney 2011, McKinney, Tchekhovskoy, and Blandford 2012]. Self-consistent solutions for magnetized thick discs with toroidal distributions of the magnetic field were obtained by Komissarov [2006] for constant angular momentum discs. This solution was extended to the nonconstant angular momentum case by Montero et al. [2007] (see also [Gimeno-Soler and Font 2017]) and by Pimentel, Lora-Clavijo, and Gonzalez [2018] and Pimentel, Lora-Clavijo, and González [2018] who incorporated magnetic polarization. Recently, equilibrium solutions of self-gravitating magnetized discs in general relativity have been reported by Mach et al. [2019], building on a procedure introduced by Shibata [2007] for unmagnetized tori (see also Stergioulas [2011a]). Numerical evolution of those solutions have been used to study the development of possible dynamical instabilities in the discs. These studies include the runaway instability [Abramowicz, Calvani, and Nobili 1983], the Papaloizou-Pringle instability [Papaloizou and Pringle 1984]), the magneto-rotational instability [Balbus and Hawley 1991] as well as the formation of jets and outflows [see e.g. Hawley 1991, Font and Daigne 2002, De Villiers and Hawley 2003b, Gammie, McKinney, and Tóth 2003, Rezzolla, Zanotti, and Font 2003, Daigne and Font 2004, Zanotti et al. 2005, Fragile et al. 2007, Montero, Font, and Shibata 2010, Kiuchi et al. 2011, Korobkin et al. 2011, McKinney, Tchekhovskoy, and Blandford 2012, Korobkin et al. 2013, Wielgus et al. 2015, Mewes et al. 2016, Fragile and Sądowski 2017,

Bugli et al. 2018, Witzany and Jefremov 2018, Cruz-Osorio, Gimeno-Soler, and Font 2020]).

All of those studies have been performed within the framework of general relativity in which astrophysical black holes are described by the Schwarzschild or Kerr solutions. However, other types of black hole solutions have been obtained in extended theories of gravity. The observational capabilities offered by the Event Horizon Telescope, targeted to measure black hole shadows and associated strong-field lensing patterns from accretion discs around black holes, allows to test the validity of the black hole solutions of general relativity. As a recent example Mizuno et al. [2018] used the parametrized Einstein-Maxwell-dilaton-axion gravity solutions of García, Galtsov, and Kechkin [1995] and Konoplya, Rezzolla, and Zhidenko [2016] to compare the shadows from a Kerr black hole and a dilaton one, offering a proof of concept for the feasibility of such tests. More recently, the shadow of a boson star -surfaceless black hole mimicker- was also studied in Olivares et al. [2020], where considering realistic astronomical observing conditions shows that is possible to distinguish between Kerr black holes and nonrotating boson stars. The dynamics of charged particles around quasi-Schwarzschild and quasi-Kerr black holes, and particle motion around modified black holes, have been recently investigated in Lin et al. [2015], Narzilloev et al. [2021], and Narzilloev et al. [2019]. Motivated by those works here we explore the consequences of a simple extended model of gravity that at "zeroth" perturbation order reproduces the standard Schwarzschild spacetime geometry of general relativity, but greatly differs from it when additional terms are taken into account. This is done using a pure metric $f(R)$ theory of gravity [Capozziello and Faraoni 2010, Capozziello and De Laurentis 2010, Capozziello and de Laurentis 2011, Nojiri, Odintsov, and Oikonomou 2017, Harko and Lobo 2018] by the introduction of a Yukawa-like potential following the proposal of De Martino, Lazkoz, and De Laurentis [2018] and De Laurentis, De Martino, and Lazkoz [2018]. As an astrophysical application, in this article we explore two directions: (1) building stationary solutions of magnetized thick discs with a self-consistent toroidal magnetic field around a Yukawa-like black hole and (2) computing the photon ring size in both general relativity and in our extended theory of choice. The two solutions are compared with the aim of exploring whether the extended $f(R)$ theory involving a Yukawa-like potential can still be valid with current observations. Previous attempts to construct accretion discs around black holes in $f(R)$ theories of gravity can be found in Pérez, Romero, and Perez Bergliaffa [2013] and Alipour, Khesali, and Nozari [2016] for thin and thick discs, respectively.

This paper is organized as follows: In Sec. 5.2 we summarize the problem setup, describing the black hole space-time in $f(R)$ gravity and the procedure to build the disc solution. Stationary models of thick discs varying the space-time parameters and the disc magnetization are presented in Sec. 5.3. This section also discusses the dependence of the photon ring size on the space-time parameters Finally Sec. 5.4 summarizes our conclusions. Unless stated otherwise we use geometrized units in which the light speed, Newton's constant, and the mass of the black hole are equal to one, $c = G = M = 1$, the Kerr metric has the signature $(-,+,+,+)$, and the $1/4\pi$ factor in the MHD equations is assumed to be one.

5.2 Setup

The immediate generalization of the Einstein equations is done by allowing the Ricci scalar R in the gravitational action to be a general analytical function $f(R)$ [see e.g. Sotiriou and Faraoni 2010, Capozziello and Faraoni 2010, Capozziello and De Laurentis 2010, Capozziello and de Laurentis 2011, Nojiri, Odintsov, and Oikonomou 2017, Harko and Lobo 2018], with the matter action written in its usual form [see e.g. Landau and Lifshitz 2013, Mendoza and Silva 2020]. The field equations in this pure metric construction are then obtained by the null variations of the whole action, i.e. the sum of the gravitational and matter actions, with respect to the space-time metric. The obtained field equations turn out to be fourth-order differential equations for the metric and therefore, finding solutions of a well-posed particular problem constitute a much harder task. By construction, when $f(R) = R$, the Einstein field equations are recovered and the differential field equations are of second order in the metric.

5.2.1 Spherically symmetric black hole space-time in a pure metric static $f(R)$ model

In this article we consider a static spherically symmetric space-time. The field equations are obtained by the a specific choice of an $f(R)$ function. In order to provide a general scenario, Capozziello, Stabile, and Troisi [2007] showed that it was possible to find a weak-field limit solution that can be satisfied for all analytic $f(R)$ functions (see also Capozziello and de Laurentis [2011] and references therein). The idea is to expand in a Taylor series the function $f(R)$ and keep terms up to order $1/c^2$ in the field equations. The resulting field equations at that order of approximation have a Yukawa-like potential

solution and, as shown by De Laurentis, De Martino, and Lazkoz [2018] at that perturbation order, the general solution can be written as [see also De Martino et al. 2014, De Martino, Lazkoz, and De Laurentis 2018]:

$$ds^2 = -\left[1+\Phi(r)\right]dt^2 + \left[1-\Phi(r)\right]dr^2 + r^2 d\tilde{\Omega}^2\,, \tag{5.1}$$

with

$$\Phi(r) \quad = \quad -\frac{2M\left(\delta e^{-\frac{r}{\lambda}}+1\right)}{r(\delta+1)}\,. \tag{5.2}$$

This Yukawa-like black hole (YBH) solution constitutes a generalization of the Schwarzschild space-time for all analytic $f(R)$ functions in the post-Newtonian limit [see e.g. Will 2018]. In the previous two equations $d\tilde{\Omega}^2 \equiv d\theta^2 + \sin^2\theta d\phi^2$ is the angular displacement and $\Phi(r)$ is a Yukawa-like potential. Mathematically, the constant parameters λ and δ are related to the coefficients of the Taylor expansion of the function $f(R)$ about a fixed R_0. In fact $\lambda := \sqrt{-6f_0''/f_0'}$ and $\delta := f_0' - 1$, where $[\,]' := \mathrm{d}[\,]/\mathrm{d}R$. As such, when $f(R) = R$, the gravitational action becomes the Hilbert action of general relativity and so $\delta = 0$ which leads to the Newtonian potential $\phi(r) = -M/r$ for a point mass source and equation (5.1) converges to the Schwarzschild exterior solution.

The parameter λ is a length scale which can in principle be adjusted depending on the spatial scale of the particular astrophysical system (see below). Moreover, δ is the parameter of the theory and governs the strength of the Yukawa-like potential (general relativity and therefore Newton's potential is recovered when $\delta = 0$). The event horizon of the YBH is computed in the same way as for the Schwarzschild black hole, solving the condition $\mathrm{g_{tt}(r)} = 0$, where the surface of infinite redshift and the event horizon coincide. Since Yukawa's potential has a nonlinear dependence on the radial coordinate we obtain a transcendental equation for $\mathrm{r_{EH}}$. Hence, we use a Newton-Raphson root-finder to compute the event horizon.

For our YBH solution the angular velocity of Keplerian circular orbits around the black hole reads

$$\Omega_{\mathrm{K}}^2(r) = \frac{M\delta e^{-r/\lambda}}{r^2\lambda(\delta+1)} - \frac{\Phi}{2r^2}\,. \tag{5.3}$$

For circular orbits, we can write the angular velocity and the specific angular momentum in terms of the nonzero components of the 4-velocity u^μ, namely $\Omega = u^\phi/u^t$ and $l = -u_\phi/u_t$. Using this the expression for the Keplerian specific

angular momentum can be written as

$$l_{\rm K} = \frac{\pm r^2}{1+\Phi}\sqrt{\frac{M\delta e^{-r/\lambda}}{r^2\lambda(\delta+1)} - \frac{\Phi}{2r^2}}. \tag{5.4}$$

We also define the specific bound angular momentum function $l_{\rm b}(r)$ which corresponds to the specific angular momentum of a marginally bound orbit at a certain radius r and can be written in our case as

$$l_{\rm b}^2(r) = -\frac{r^2\Phi}{1+\Phi}. \tag{5.5}$$

If we consider prograde (retrograde) motion, finding the minimum (maximum) of the function $l_{\rm b}(r)$ gives the location of the innermost marginally bound circular orbit $r_{\rm mb}$ and the value of the specific angular momentum there ($l_{\rm b}(r_{\rm mb}) = l_{\rm mb}$). It is also worth noticing that at said point, the Keplerian angular momentum is equal to $l_{\rm mb}$ as well (i.e. $l_{\rm K}(r_{\rm mb}) = l_{\rm mb}$).

5.2.2 Procedure to build equilibrium magnetized thick discs

We build sequences of equilibrium thick discs endowed with a toroidal magnetic field in YBH space-time following the procedure first presented in Komissarov [2006] and generalized by Montero et al. [2007] and Gimeno-Soler and Font [2017]. For simplicity we assume that the plasma in the disc obeys a constant distribution of specific angular momentum $l = l_{\rm K}(r_{\rm mb})$ given by the Keplerian angular momentum equation (5.4), evaluated at $r_{\rm mb}$. The fundamental equation to describe a non-self-gravitating equilibrium torus around a black hole is obtained by applying the projection tensor $h^{\alpha}_{\ \beta} = \delta^{\alpha}_{\ \beta} + u^{\alpha}u_{\beta}$ to the conservation law of the energy-momentum tensor [Gimeno-Soler and Font 2017]. This equation reads

$$\partial_i(\ln|u_t|) - \frac{\Omega\partial_i l}{1-l\Omega} + \frac{\partial_i p}{\rho h} + \frac{\partial_i\left[\mathcal{L}b^2\right]}{2\mathcal{L}\rho h} = 0\,, \tag{5.6}$$

where $i = r, \theta$. To obtain the previous equation we have assumed that the thermodynamical relationship between the rest-mass density ρ and the thermal pressure p is given by a barotropic equation of state (EoS), $\rho = \rho(p)$. In particular, we choose a polytropic EoS such as $p = K\rho^{\Gamma}$ and an EoS for the magnetic pressure $p_{\rm m} \equiv b^2/2$ such as $p_{\rm m} = K_{\rm m}\mathcal{L}^{q-1}(\rho h)^q$, where K, K_m, q and Γ are constants and $\mathcal{L} \equiv g_{t\phi}^2 - g_{tt}g_{\phi\phi}$. Moreover, h and b^2 in Eq. (5.6) are the enthalpy and the modulus (squared) of the magnetic field 4-vector. Using this relations we can rewrite Eq. (5.6) as

$$\mathcal{W} - \mathcal{W}_{\rm in} + \ln\left(1 + \frac{K\Gamma}{\Gamma-1}\rho^{\Gamma-1}\right) +$$

$$\frac{qK_{\rm m}}{q-1}\left[\mathcal{L}\left(\rho+\frac{K\Gamma\rho^{\Gamma}}{\Gamma-1}\right)\right]^{q-1}=0, \tag{5.7}$$

where $\mathcal{W}=\ln|u_t|$ is the (gravitational plus centrifugal) potential. To solve Eq. (5.7) we fix $q=\Gamma=4/3$, the density at the center of the disc $\rho_{\rm c}=1$, the specific angular momentum $l=l_{\rm mb}$ and we fill 80% of the potential gap $\Delta\mathcal{W}\equiv\mathcal{W}_{\rm in}-\mathcal{W}_{\rm cusp}$, where subindices 'in' and 'cusp' indicate that the potential is calculated at the inner edge of the disc or at the cusp (see below). Therefore, in our models the discs will always be inside their corresponding Roche lobes ($\Delta\mathcal{W}<0$). Models are built using a numerical (r,θ) grid in a domain $r\in[r_{\rm EH},r_{\rm out}]$, whose specific values are reported in Table 5.1. The number of zones in our base grid is 252×256 in r and θ, respectively.

5.3 Results

5.3.1 YBH parameters

Before constructing the YBH-disc solutions we explore suitable values of the freely specifiable parameters of the theory, λ and δ. This serves the purpose of understanding the intrinsic properties of the space-time and offers the possibility of comparing our findings with the analysis of De Martino, Lazkoz, and De Laurentis [2018] and De Laurentis, De Martino, and Lazkoz [2018]. We consider three length scales, $\lambda=10$, 60, and 1000 in geometrized units. In physical units and for the case of M87 the first case corresponds to the scale of the black hole photon ring shadow, $\lambda_{\rm phys}(10)\sim3.11\times10^{-3}$ pc (23μas), the second one to the size of the inner core of the jet, $\lambda_{\rm phys}(60)\sim1.866\times10^{-2}$ pc (230μas), and the third case to the large scale jet of M87, $\lambda_{\rm phys}(10^3)\sim3.11\times10^{-1}$ pc (3.8mas). Similarly, for the galactic center SgrA* the corresponding values are $\lambda_{\rm phys}(10)\sim1.985\times10^{-6}$ pc (50μas), $\lambda_{\rm phys}(60)\sim1.191\times10^{-5}$ pc (300μas), and $\lambda_{\rm phys}(10^3)\sim1.985\times10^{-4}$ pc (5mas)[1]. For each value of λ we use 14 values of δ. We focus our attention in the case $\delta<0$ which is where more noticeable changes with respect to general relativity are observed. Taking into account these considerations, we build 294 magnetized accretion discs around YBHs varying the space-time parameters δ and λ and the strength of the toroidal magnetic field at the center of the tori, $\beta_{\rm c}$.

[1]To estimate the length scales in μas we assume the following black hole masses and distances to the source: $\mathrm{M_{M87}}=(6.2\pm0.7)\times10^9$ $\mathrm{M_\odot}$ and $\mathrm{D}=16.8\pm0.8$ Mpc for M87 [Event Horizon Telescope Collaboration et al. 2019a], and $\mathrm{M_{SgrA*}}=(4.148\pm0.014)\times10^6$ $\mathrm{M_\odot}$ and $\mathrm{D}=8.178$ Mpc for the galactic center SgrA* [Gravity Collaboration et al. 2019].

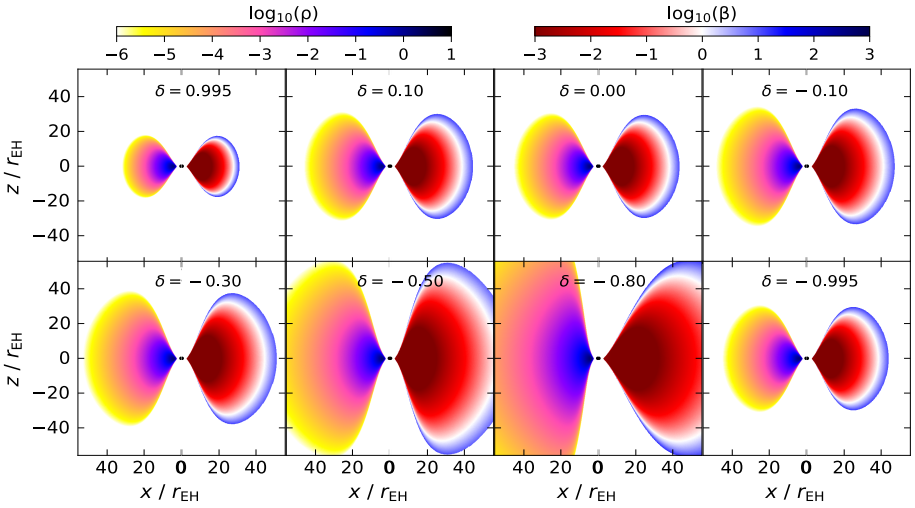

Figure 5.1 Logarithm of the rest-mass density (left half portion of each panel) and magnetization parameter (right half) for an illustrative sample of tori around YBHs with $\lambda = 60$ and different values of δ. All tori are built assuming high magnetization, using a central magnetization parameter of $\beta_c = 10^{-3}$. Each box covers a spatial domain $[-50\ r_{\rm EH}, 50\ r_{\rm EH}]$ in the $x - z$ plane. Note that each solution has a different length scale if expressed in conventional black hole mass M units, due to the dependence of $r_{\rm EH}$ with δ (see Table 5.1 for details).

Note that the choices $\delta < 0$ are to be taken with care since they may produce modifications around a Schwarzschild space-time with $M < 0$ [see e.g Townsend 1997]. For the purpose of this article, we have selected models for which $\Phi(r) < 0$ in order to avoid a negative mass Schwarzschild-like spherical solution.

5.3.2 Tori geometry

Table 5.1 reports the values of selected geometrical quantities of the discs for a subset of representative models (parametrized by δ) for all three values of λ. We note that those quantities are only related to the space-time and hence do not depend on the magnetization parameter of the discs. Varying parameter $\delta \in [-1, 1]$ yields YBHs with different event horizon radii $r_{\rm EH}$. We find that the event horizon size increases for negative values of δ and small values of λ reaching $r_{\rm EH} = 400M$ for $\lambda = 10$ and 60. On the other hand, for $\lambda = 1000$ the variation of $r_{\rm EH}$ with negative δ is not too pronounced, staying at $r_{\rm EH} = 2$ for most models and reaching $r_{\rm EH} = 3.32$ for $\delta = -0.995$. For positive δ values, the values of $r_{\rm EH}$ we obtain are comparable to the event horizon size of a slowly rotating black hole with $r_{\rm EH} = 1.83$ and 1.97 (for $\lambda = 10$ and 60) corresponding to Kerr black holes with spin parameters $a = 0.558$, and 0.243, respectively.

Moreover, for positive δ and $\lambda = 1000$ no changes are observed with respect to the event horizon radius of a nonrotating black hole in general relativity.

Table 5.1 also reports the radius of the marginally bound orbit $r_{\rm mb}$ and its corresponding specific angular momentum $l_{\rm mb}$. For all λ, these two quantities show a weak dependence on δ except for extreme values very close to $\delta = -1$. Additional disc radii reported in Table 5.1 are the location of the cusp, $r_{\rm cusp}$, the center of the disc, $r_{\rm c}$, and the inner and outer edges of the disc, $r_{\rm in}$, $r_{\rm out}$, respectively. The latter are computed assuming the discs fill 80% of the gap of the potential $\Delta\mathcal{W}$ (i.e. of their Roche lobes). The center of the disc is defined as the minimum of $\mathcal{W}$. The orbital period of the disc, $t_{\rm orb}$, reported in the last column of Table 5.1 is measured at the center of the disc. It is found that all characteristic quantities defining the torus size, $r_{\rm cusp}$, $r_{\rm c}$, $r_{\rm in}$, and $r_{\rm out}$, only show a strong dependence on the YBH parameters as $\delta \to -1$. For all models those quantities increase fairly slowly (or barely increase at all) as δ goes from positive to negative values, except for $\delta = -0.995$ where the increment is significantly larger.

The gap of the potential, $\Delta\mathcal{W}$, also reported in Table 5.1, defines the regions where the equilibrium plasma is located around the black hole. In particular, the surface of the magnetized disc is defined as the equipotential surface with $\mathcal{W} = \mathcal{W}_{\rm in}$ and the solution of the thermodynamical quantities (see Eq. (5.7)) also depends on this gap. In general relativity ($\delta = 0$) this value is $\Delta\mathcal{W} = 0.043$, irrespective of λ. The largest deviations found are $\Delta\mathcal{W} = 0.112$ (for $\delta = -0.7$), 0.176 (for $\delta = -0.9$), and 0.277 (for $\delta = -0.995$), respectively.

Figure 5.1 shows the two-dimensional morphology of a representative sample of models. We plot the rest-mass density (left side of each panel) and the magnetization parameter (right side of each panel) of the tori, the two quantities in logarithmic scale. Results are shown for a YBH space-time with $\lambda = 60$ and for different values of δ and considering a magnetization parameter at the center of the disc of $\beta_{\rm c} = 10^{-3}$. Therefore, the examples shown in Fig. 5.1 correspond to highly magnetized tori. For clarity in the comparison we rescale the spatial domain $(r\cos\theta,\ r\sin\theta)$ by the event horizon size of each YBH (the specific values are reported in Table 5.1) showing a domain $[-50\ r_{\rm EH}, 50\ r_{\rm EH}]$ in the $x - z$ plane.

As δ increases from 0 toward $\delta = 1$, the size of the disc decreases while $r_{\rm EH}$ is kept essentially constant, slightly changing from 2.0 to 1.97 (see Table 5.1). The most noticeable modifications are visible, however, only for the largest values. For $\delta = 0.995$ the disc is about 40% smaller than in general relativity. On the other hand, as δ decreases from 0 toward $\delta = -1$, the size of the discs becomes

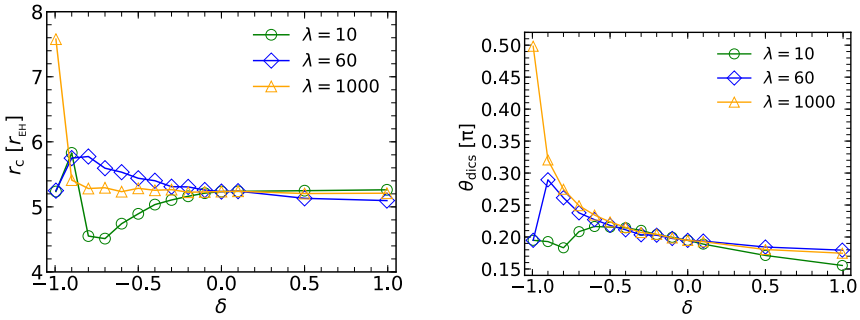

Figure 5.2 Dependence on δ of the position of the center of the disc r_c in units of r_{EH} (top) and of the angular thickness of the disc measured with respect to the x-axis at r_c (bottom). Note that the dependence of both quantities on δ does not change with the magnetic field strength.

gradually larger. The largest value in Fig. 5.1 corresponds to the $\delta = -0.995$ case. Note that the apparent smaller size of this model as compared e.g. with the $\delta = -0.8$ case is because the domain plotted in the figure is expressed in units of r_{EH} which is 2.3 for the latter and about 400 for the former. Despite these significant modifications in the geometrical size, the distribution of the density and of the magnetization in the torus seem only weakly affected by the changes in δ. For the most negative values of δ further extended low-density layers are obtained as well as high-density regions along the symmetry axis of the black hole. Similarly, the angular thickness of the disc also increases.

Fig. 5.1 shows that the inner edge of each torus is at the same distance of the YBH horizon since we are using as unit of distance the event horizon size. The same occurs for the location of the cusp of the potential, as confirmed by the values reported in Table 5.1. Nevertheless, we notice differences in the location of the center of the discs r_c and of their outer edge r_{out}. The top plot in Fig. 5.2 displays the position of the center of the tori in units of the event horizon radii of the corresponding YBH as function of δ and for all three values of λ. Since the center of the disc is defined as the location of the minimum of the potential, it does not depend on the magnetic field strength. We observe noticeable changes in the position of the disc center for negative values of δ. For the case $\lambda = 60$, r_c increases monotonically with r_{EH} as $\delta \to -1$, up to $\delta = -0.8$ where $r_{in} \approx 5.8 r_{EH}$. For $\delta = -0.995$, r_c decreases to about $5.2 r_{EH}$. Note, however, that in terms of the YBH mass, the radial position of the center of the disc always increases monotonically (see Table 5.1).

The bottom plot of Figure 5.2 shows the corresponding angular thickness - expressed in radians - between the surface of the tori, defined by the equipotential

surface, and the x-axis as a function of δ. In the Schwarzschild case, $r_{\rm c} \sim 5.3\, r_{\rm EH}$ and the angular thickness is $\theta_{\rm disc} \sim \pi/5$. Therefore, for negative values of δ more elongated discs with higher angular thickness are obtained, as shown in the bottom plot of Fig. 5.2.

The dependence we have just described is affected by the value of the length scale parameter λ. The corresponding results for $\lambda = 10$ and 1000 are also plotted in Fig. 5.2. For $\lambda = 10$, $r_{\rm c}$ decreases monotonically with $r_{\rm EH}$ as $\delta \to -1$, up to $\delta \approx -0.8$. For even more negative values of δ, $r_{\rm c}$ increases. The discs are in general smaller than in the $\lambda = 60$ case and their angular sizes, which depend weakly with δ, are also smaller. Finally, for $\lambda = 1000$ both $r_{\rm c}$ and $\theta_{\rm disc}$ increase monotonically with $r_{\rm EH}$ as $\delta \to -1$. The largest discs with the highest angular thicknesss are found for this value of λ. It is relevant to note that for $\lambda = 0$, both the top and the bottom panels of Fig. 5.2 would show flat curves, since in that case, the modification induced by the parameter δ would only act as a correction of the mass parameter $M \to M/(\delta + 1)$ that cannot induce any change in the morphology of the disk. However, when $\lambda \neq 0$, it can be seen that we can define an effective mass function $M(r)$ such as

$$M(r) = \frac{M(\delta e^{-r/\lambda} + 1)}{\delta + 1}\,. \tag{5.8}$$

Then, the effective mass $M(r)$ seen by the disk is not a constant, and is different from the asymptotic mass as seen by an observer at $r \to \infty$ which is $M(r \to \infty) = M/(\delta + 1)$. These two facts are the reason of the deviations from the morphology expected for a Schwarzschild BH.

The range of variation of $r_{\rm out}$ with δ in our models is also significant, as reported in Table 5.1. For $\lambda = 10$, $r_{\rm out} \sim 21 - 70\ r_{\rm EH}$, for $\lambda = 60$, $r_{\rm out} \sim 35 - 114\ r_{\rm EH}$ and for $\lambda = 1000$, $r_{\rm out} \sim 47 - 1100\ r_{\rm EH}$. This effect is a consequence of the particular value of the gravitational-centrifugal potential gap for each model (which is a nonlinear function of the Yukawa-like potential), which increases as we move from positive to negative values of δ, modifying the Roche lobes of each YBH solutions and the morphology and thermodynamics of the equilibrium torus. Such behavior depends directly on the Yukawa-like potential; for values of λ comparable with the radial extent of the disk the exponential function in Eq. (5.1) has an important contribution on the space-time. On the other hand, for large values of λ the exponential part goes to zero and the potential mostly depends on $1/(\delta + 1)$, consistent with the geometry and the thermodynamics of the magnetized discs (see Figs. 5.2, 5.4, 5.5).

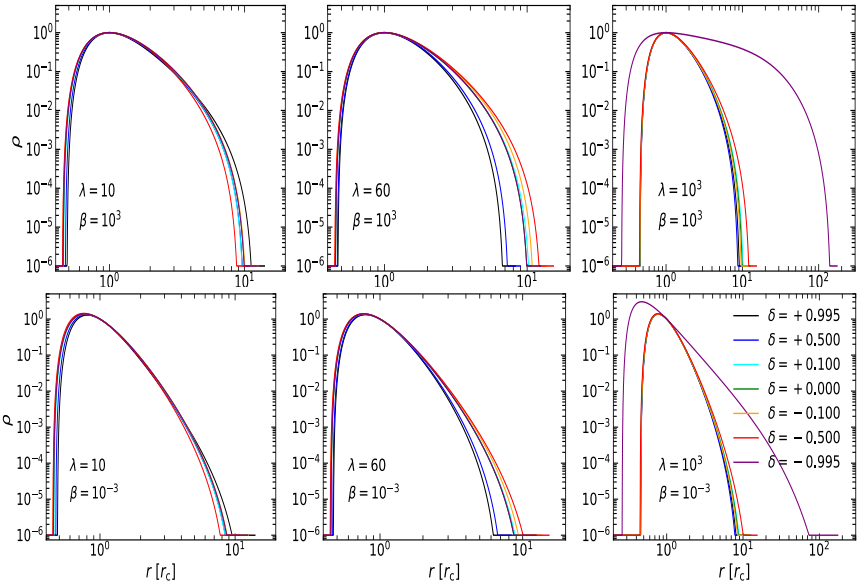

Figure 5.3 Radial profiles of the rest-mass density of the magnetized discs in logarithmic scale at the equatorial plane. The left panels correspond to the YBH space-time with $\lambda = 10$, the middle panels to $\lambda = 60$ and the right panels to $\lambda = 10^3$. The top panels show low magnetized discs and the bottom ones display highly magnetized cases. In each plot seven values for δ are shown. The radial coordinate is in units of the center of the disc to facilitate the comparison.

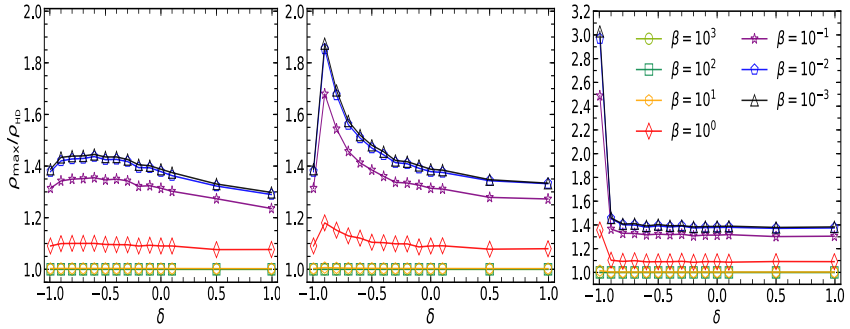

Figure 5.4 Maximum of the rest-mass density normalized by the corresponding value for a nonmagnetized disc $\rho_{\rm HD}$ (see Table 5.1), for $\lambda = 10$ (left), $\lambda = 60$ (middle), and $\lambda = 10^3$ (right). The maximum density increases with the magnetization, in agreement with the Schwarzschild black hole case. The largest increments are found for $\delta < 0$.

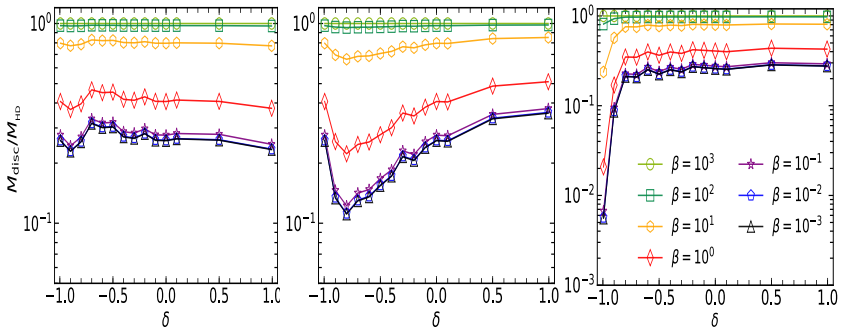

Figure 5.5 Disc mass as a function of δ normalized by the mass of an unmagnetized disc, $M_{\rm HD}$ (see Table 5.2), for different magnetizations. From left to right the panels correspond to $\lambda = 10$, $\lambda = 60$, and $\lambda = 10^3$, respectively. The disc mass decreases when the magnitude of the magnetic field increases. The least massive torus is obtained for $\lambda = 10^3$ and $\delta \to -1$.

5.3.3 Tori thermodynamics

The differences found in the geometry of the discs are accompanied by quantitative differences in the physical magnitudes characterizing the matter content of our models and their thermodynamics. Figure 5.3 shows radial profiles along the equatorial plane ($\theta = \pi/2$) of the rest-mass density in logarithmic scale for two values of the magnetization parameter and for all values of parameters λ and δ. The profiles are shown for both an unmagnetized disc ($\beta = 10^3$) and a highly magnetized one ($\beta = 10^{-3}$). For YBH space-time, the maximum of the rest-mass density increases for high magnetized discs and its location shifts toward the inner edge of the torus. This is in agreement with what is found for the case of Schwarzschild space-time [Gimeno-Soler et al. 2019]. However, the deviations are not large and they only become significant for $\delta = -0.995$. For some of the models, the form of the YBH space-time allows us to build discs which are almost filled by high-density regions (e.g. model with $\lambda = 10^3$, $\delta = -0.995$ and $\beta = 10^3$).

Table 5.2 reports, for all of our models, the values of the maximum of the rest-mass density and of the baryon mass of the disc, defined as

$$M_{\rm disc} = \int \sqrt{\gamma} W \rho d^3x \,, \tag{5.9}$$

where W is the Lorentz factor. This table allows to quantify the effects on these two quantities of the parameters δ and λ that characterize the YBH spectime and to find the dependence on the magnetic-field strength, from unmagnetized to highly magnetized discs. We assume that the mass of the disc is 10% of the mass

of the black hole for the unmagnetized case, $M_{\rm HD} = 0.1M$, fixing the rest-mass density, $\rho_{\rm HD}$. The highest value of $M_{\rm disc}$ is attained for the unmagnetized model ($\beta = 10^3$) and the mass of the tori decreases monotonically as the magnetization increases.

Figures 5.4 and 5.5 show the maximum of the rest-mass density and of the baryon mass of the disc as a function of δ, normalized by $\rho_{\rm HD}$ and $M_{\rm HD}$, respectively. Both quantities do not show a strong dependence on δ, irrespective of the value of λ, except for values of δ close to -1, where the largest deviations are found. The increase in $\rho_{\rm max}$ is monotonic with the increase of the disc magnetization, and it is similar for all three values of λ. Except for $\delta \to -1$ the maximum value of the density is fairly constant and about 1.4 $\rho_{\rm HD}$ which is the value found for tori around a Schwarzschild black hole by Gimeno-Soler et al. [2019]. Only when $\delta \to -1$ higher values of the rest-mass density are found, namely $\sim 1.54, 1.9, 3.0$ $\rho_{\rm HD}$ for $\lambda = 10, 60, 1000$ respectively. In those cases, the total baryon mass of the discs decreases to about $\sim M_{\rm HD}/3$, $M_{\rm HD}/10$ and $M_{\rm HD}/100$ when the strength of the magnetic field increase.

5.3.4 Constraining the YBH parameters with the photon ring size

The Event Horizon Telescope observations of the black hole shadow in M87 [Event Horizon Telescope Collaboration et al. 2019a, Event Horizon Telescope Collaboration et al. 2019c] and the forthcoming observations of SgrA* provide a laboratory to test general relativity and modified theories of gravity by using the shadow properties. In particular, the fundamental property M87's shadow revealed in EHT observations is the photon ring. This is the geometrical region in which space-time bends light in such a way that photons must follow circular orbits. For an observer at infinity, the photon ring defines the apparent size of the shadow, i.e. the shadow size, that only depends on the gravity of space-time. We turn now to analyze how the shadow size of our YBH solution differs from that of a Schwarzschild black hole, constraining the parameters of the space-time with the size of the photon ring. To this aim we solve the geodesic equations for photon (null) trajectories in the YBH space-time given by Eq. (5.1) following the procedure developed by Hioki and Maeda [2009] and Hou et al. [2018]. We neglect any contribution from the emissivities and absorptivities of the magnetized torus (i.e. we do not consider the spectral content of the light) because for our stationary models we assume that the emission from the photon ring is brighter than in the disc, but the disc is sufficiently illuminated so that a

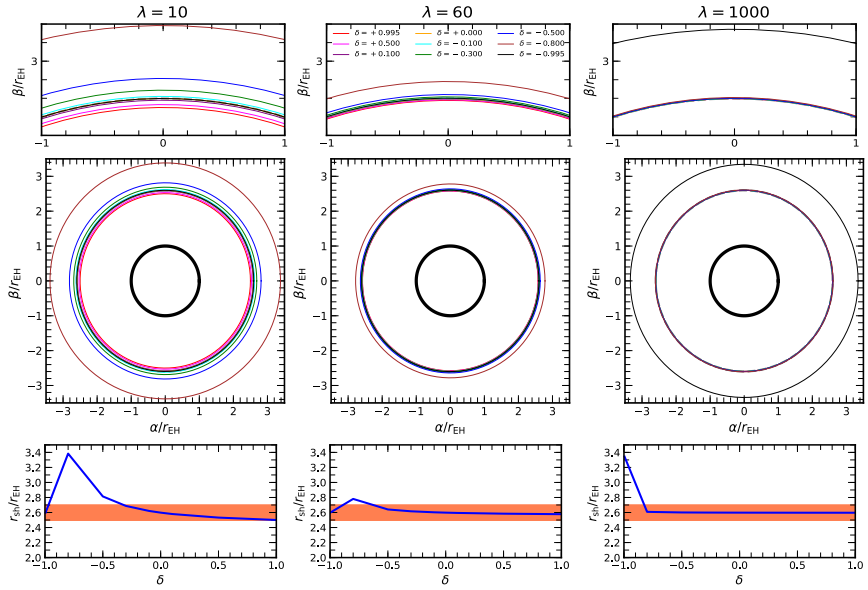

Figure 5.6 Photon ring size (shadow size) of different YBH space-times with varying δ parameter and length scales λ. The full rings are displayed in celestial coordinates (α, β) normalized by the event horizon size in the middle panels, while a closeup is shown in the top panels. The shadow radius as a function of δ is shown in the bottom panels (blue curves), where the orange regions indicate the range of the shadow size for maximally rotating Kerr black holes. The dashed gray lines correspond to the Schwarzschild black hole shadow radius, $r_{sh} = 3\sqrt{3}r_g$ [Johannsen and Psaltis 2010] and the black line is the radius of the event horizon. An observer view angle $i^o = \pi/2$ at infinity is assumed.

photon ring is visible. A detailed assessment of the shadows based on numerical evolutions of our YBH-torus systems will be presented elsewhere. The apparent shape of the YBH shadow is computed by introducing the celestial coordinates (α, β) assuming a source located at infinity and a viewing angle $\mathrm{i^o} = \pi/2$. Such coordinates measure apparent angular distances of the image on the celestial sphere. The shadow of the black hole is defined by a bright ring at the radius of the lensed photon sphere or photon ring [Event Horizon Telescope Collaboration et al. 2019b]. For a Kerr black hole at different viewing angles such radius varies between $\mathrm{r_{sh}} \sim 3\sqrt{3}\mathrm{r_g} \pm 4\%$ [Johannsen and Psaltis 2010], where $3\sqrt{3}r_g$ is the photon ring of the Schwarzschild black hole, and r_g is the gravitational radius. The $\pm 4\%$ limits in the variation of the size of the Schwarzschild black hole shadow correspond to the maximally rotating Kerr black hole cases (with Kerr dimensionless spin parameter $a = \pm 1$).

Figure 5.6 shows the shadow size at a viewing angle $\mathrm{i^o} = \pi/2$ for the YBH space-times listed in Table 5.1. Each column corresponds to one of our three length scales $\lambda = 10, 60$, and 10^3. In the middle panels we show the complete shape of the photon rings in celestial coordinates, normalized by the event horizon of the black hole, for representative values of the δ parameter. In the top panels we show a close-up of the upper region of the ring while the bottom panels display the radius of the photon ring r_{sh} as a function of δ. The orange regions in these plots are the shadow sizes estimated from general relativity for Kerr black holes. Almost all of our models are consistent with Event Horizon Telescope observations [Event Horizon Telescope Collaboration et al. 2019b]. The largest deviations are obtained for the most negative values of δ, irrespective of λ, albeit for $\lambda = 60$ the variations are the smallest. On the other hand, for positive values of δ the photon ring size only increases slowly with δ for the two lowest values of λ we consider.

To obtain a better understanding of the dependence of the shadow size on δ and λ we finish our analysis by exploring 10^4 space-time models varying both parameters. The results are displayed in Fig. 5.7 which shows the shadow radius normalized by the event horizon radius as a function of δ and λ. The blue isocontour corresponds to a family of YBH with the same photon ring size as the Schwarzschild black hole. The red iscontours are the bounds for $3\sqrt{3}r_g \pm 4\%$. All YBH photon rings between these two isocontours are consistent with general relativity Kerr black hole solutions. Photon rings of YBH which are not allowed in this range can be neglected (white regions in the figure). Figure 5.7 shows that YBH with $\delta > 0$ and $\lambda < 50$ generate small photon rings, whereas large photon rings are produced for $\delta < 0$ for all values of λ. Irrespective of

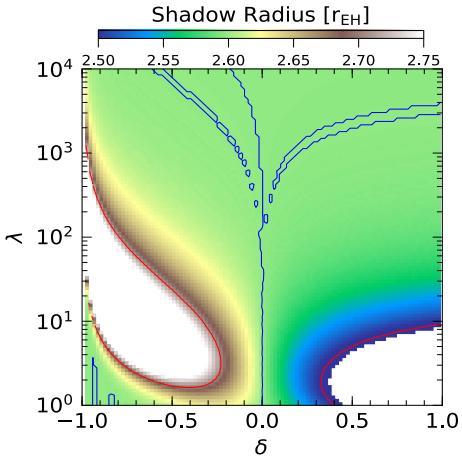

Figure 5.7 Shadow radius of the YBH as function of δ and λ, normalized by the event horizon. The blue contour corresponds to shadow size for Schwarzschild black hole $r_{sh} \sim 3\sqrt{3}$, in r_g radius units and red contours to $r_{sh} \pm 4\%$.

the sign of δ we observe nonlinear correlations between the shadow size and the δ parameter. In particular, at small scales, for $\lambda < 20$, the effects of the Yukawa-like gravitational potential are strong, leading to a high variability of the photon ring size - from minimum to maximum - when the δ parameter decreases from $\delta \sim 0.3$ to $\delta \sim -0.25$. This is expected since light bending is more noticeable in stronger gravity regimes. Correspondingly, for asymptotic values $\lambda \to \infty$ the YBH photon rings tend asymptotically to the Schwarzschild photon ring.

Applying the δ parameter constriction to the supermassive black holes of M87 and the galactic center ($\lambda \sim 60$) we find that astrophysically accepted values for δ would fall in the range $-0.75 < \delta < 1.0$. For our stationary accretion disc solutions this implies that we can neglect very thick torus with large angular thickness, $\theta_{disc} > 0.26\pi$, for which the location of the center is $r_c > 6r_{EH}$ and have large event horizon, $r_{EH} \sim 400M$. The maximum densities in YBH-torus systems compatible with the constrained range of δ are in agreement with the values found in general relativity [Gimeno-Soler et al. 2019] with small deviations $\sim \pm 0.2$.

5.4 Summary

We have presented stationary solutions of geometrically thick discs (or tori) with constant angular momentum and endowed with a self-consistent toroidal

magnetic field distribution surrounding a nonrotating black hole in $f(R)$-gravity. The particular $f(R)$-gravity model we have employed introduces a Yukawa-like modification to the Newtonian potential, encoded in a single parameter δ and whose specific values affect the disc configurations compared to the general relativistic case. We have built models for different magnetic field strengths, from low magnetized discs (essentially hydrodynamic) to highly magnetized tori. This has been achieved by adjusting the magnetization parameter β, i.e., the ratio of thermal pressure to magnetic pressure, in the range $\log_{10}\beta \in \{-3, 3\}$. Our stationary solutions have been obtained numerically, employing the approach discussed in detail in Gimeno-Soler et al. [2019].

The characteristics of our solutions have been quantified by analyzing the central density of the discs, their baryonic mass, their geometrical size and angular thickness, as well as the effects of the deviations of the YBH metric from the Schwarzschild metric. We have found that in the general relativistic limit ($\delta = 0$) our models reproduce our previous results for a Schwarzschild black hole [Gimeno-Soler and Font 2017, Gimeno-Soler et al. 2019]. For small values of the δ parameter, corresponding to $\sim 10\%$ deviations from general relativity, we have found small geometrical variations in the models with respect to the general relativistic results, namely $\sim 2\%$ in the event horizon size, a $\sim 5\%$ shift in the location of the inner edge and center of the disc, and $\sim 10\%$ variation in the location of the outer edge. We note that our results are consistent with the shift in the periastron advance of about 10% reported by De Laurentis, De Martino, and Lazkoz [2018].

Our analysis for $|\delta| > 0.1$ has revealed notable changes in the black hole solutions, particularly in the limit $\delta \to -1$. Those modifications of the gravitational potential have a large direct impact in the torus solution. We have found that the influence of the magnetic field in the disc properties becomes stronger in this case. In particular we have observed an increment of the YBH event horizon of about four orders of magnitude with respect to the event horizon of a Schwarzschild black hole, a $\sim 10\%$ increase of $r_{\rm c}(r_{\rm EH})$ and three orders of magnitude increase of the locations of the outer edge of the disc, $r_{\rm out}$.

The impact of the strength of the toroidal magnetic field in the morphology of the discs follows the same trend of previous analysis for nonrotating black holes in general relativity [Gimeno-Soler and Font 2017, Gimeno-Soler et al. 2019]. The maximum density for our most highly magnetized disc is $\sim 1.4\ \rho_{\rm HD}$ and the total mass of the disc is $\sim 0.25\ M_{\rm HD}$. The variation in these two quantities is less than 10% for small deviations from general relativity. For $|\delta| > 0.1$ the increment in the maximum density is a factor two with respect to general relativity and

the disc mass decreases one order of magnitude. In addition, negative values of the YBH parameter δ influence the angular size of the discs, which become more elongated along the z-axis. This may affect the angular size of outflows and jets that might form when evolving these magnetized discs in the alternative theory of gravity discussed here.

Finally, we have analyzed the differences between the YBH space-time and the Schwarzschild space-time by computing the size of the photon ring produced by a source located at infinity. This has allowed us to constrain the parameters δ and λ of the YBH space-time when applying our approach to the supermassive black holes of M87 and SgrA*. The variations in the photon ring reported in this work, even for small deviations from general relativity, might be measurable in upcoming observations of the galactic center by the Event Horizon Telescope Collaboration.

Even though the variations we have found in our YBH-disc models are less than 10% for realistic deviations of general relativity, namely $\delta = \pm 0.1$, nonlinear time evolution of these initial data might still disclose potential differences in observable quantities like jet power or mass accretion rates, as well as in the time-dependent morphology of the photon ring produced by a turbulent, illuminating disc. Those results will be presented elsewhere.

Table 5.1 Summary of space-time and disc properties- in geometrized units - for our three values of the length scale λ and some representative values of δ. From left to right the columns report the radii of the event horizon $r_{\rm EH}$, of the marginally bound orbit $r_{\rm mb}$, of the cusp of the gravitational potential $r_{\rm cusp}$, of the inner edge of the disc $r_{\rm in}$, of the center of the disc $r_{\rm c}$, and of the outer edge of the disc $r_{\rm out}$, as well as the specific angular momentum $l_{\rm mb}$ at $r_{\rm mb}$, the gap of the potential $\Delta\mathcal{W}$, the angular velocity Ω, and the orbital period $t_{\rm orb}$ at the center of the disc.

δ	$r_{\rm EH}$	$r_{\rm mb}$	$r_{\rm cusp}$	$r_{\rm in}$	$r_{\rm c}$	$r_{\rm out}$	$l_{\rm mb}$	$\Delta\mathcal{W}$	Ω	$t_{\rm orb}$
					$\lambda = 10$					
+0.995	1.83	3.98	3.97	4.70	9.63	120.97	3.39	0.022	0.0313	32.0
+0.500	1.97	3.98	3.98	4.74	10.32	102.83	3.88	0.039	0.0306	33.6
+0.100	1.89	3.96	3.96	4.67	9.92	99.30	3.58	0.028	0.0298	32.7
+0.000	2.00	4.00	4.00	4.67	10.47	108.52	4.00	0.043	0.0295	33.9
−0.100	2.04	4.03	4.03	4.80	10.63	111.28	4.15	0.048	0.0293	34.1
−0.300	2.17	4.16	4.15	4.95	11.08	116.95	4.61	0.062	0.0288	34.7
−0.500	2.43	4.50	4.51	5.35	11.89	107.87	5.57	0.081	0.0282	35.5
−0.800	5.28	9.91	9.90	11.59	24.03	269.63	15.50	0.099	0.0165	60.7
−0.995	400.0	800.0	800.0	952.0	2094.4	21704.8	800.0	0.043	0.0001	6777.7
					$\lambda = 60$					
+0.995	1.97	4.00	4.01	4.67	10.04	69.45	3.87	0.036	0.0314	31.9
+0.500	1.98	4.00	4.01	4.67	10.16	76.27	3.91	0.038	0.0308	32.4
+0.100	1.99	4.00	3.99	4.72	10.43	111.80	3.98	0.043	0.0297	33.7
+0.000	2.00	4.00	4.00	4.67	10.47	108.52	4.00	0.043	0.0295	33.9
−0.100	2.01	4.00	3.99	4.67	10.57	120.04	4.03	0.045	0.0291	34.3
−0.300	2.03	4.01	4.01	4.77	10.78	130.68	4.11	0.048	0.0283	35.3
−0.500	2.07	4.02	4.02	4.78	11.26	182.45	4.27	0.057	0.0267	37.5
−0.800	2.30	4.22	4.21	5.06	13.28	262.41	5.20	0.099	0.0215	46.4
−0.995	399.0	800.0	799.9	952.0	2094.4	21708.8	800.0	0.043	0.0001	6777.7
					$\lambda = 1000$					
+0.995	2.00	4.00	4.00	4.76	10.42	98.48	3.99	0.042	0.0297	33.6
+0.500	2.00	4.00	4.01	4.76	10.41	94.07	3.99	0.042	0.0298	33.6
+0.100	2.00	4.00	3.99	4.76	10.48	111.68	4.00	0.043	0.0295	33.9
+0.000	2.00	4.00	4.00	4.76	10.47	108.52	4.00	0.043	0.0295	33.9
−0.100	2.00	4.00	4.00	4.76	10.46	104.90	4.00	0.043	0.0296	33.8
−0.300	2.00	4.00	3.99	4.76	10.53	123.53	4.01	0.044	0.0293	34.2
−0.500	2.00	4.00	3.99	4.76	10.57	135.08	4.02	0.045	0.0291	34.4
−0.800	2.02	4.00	4.01	4.76	10.67	147.41	4.06	0.046	0.0287	34.8
−0.995	3.32	5.50	5.51	6.60	25.16	3671.75	9.80	0.277	0.0082	122.5

Table 5.2 Maximum values of the rest-mass density $\rho_{\max}$ and of the baryon mass of the disc $M_{\rm disc}$ as a function of the magnetization of the plasma β. The quantities are shown for all values of the YBH space-time parameters δ and λ. We assume that the baryon mass is $M_{\rm disc} = 0.1M$ in the purely hydrodynamical case ($\beta = 10^3$).

δ	$\beta = 10^3$	$\beta = 10^2$	$\beta = 10^1$	$\beta = 10^0$	$\beta = 10^{-1}$	$\beta = 10^{-2}$	$\beta = 10^{-3}$
				$\boldsymbol{\rho_{\max}}$			
				$\boldsymbol{\lambda = 10}$			
$+0.995$	3.32×10^{-5}	3.32×10^{-5}	3.33×10^{-5}	3.57×10^{-5}	4.10×10^{-5}	4.28×10^{-5}	4.31×10^{-5}
$+0.500$	2.97×10^{-5}	2.97×10^{-5}	2.98×10^{-5}	3.20×10^{-5}	3.78×10^{-5}	3.93×10^{-5}	3.95×10^{-5}
$+0.100$	2.26×10^{-5}	42.26×10^{-5}	2.27×10^{-5}	2.46×10^{-5}	2.94×10^{-5}	3.08×10^{-5}	3.10×10^{-5}
$+0.000$	2.00×10^{-5}	2.00×10^{-5}	2.00×10^{-5}	2.18×10^{-5}	2.62×10^{-5}	2.75×10^{-5}	2.77×10^{-5}
-0.100	1.83×10^{-5}	1.83×10^{-5}	1.83×10^{-5}	2.00×10^{-5}	2.42×10^{-5}	2.55×10^{-5}	2.56×10^{-5}
-0.500	1.43×10^{-5}	1.43×10^{-5}	1.43×10^{-5}	1.56×10^{-5}	1.92×10^{-5}	2.03×10^{-5}	2.05×10^{-5}
-0.995	2.45×10^{-12}	2.45×10^{-12}	2.50×10^{-12}	2.72×10^{-12}	3.28×10^{-12}	3.44×10^{-12}	3.46×10^{-12}
				$\boldsymbol{\lambda = 60}$			
$+0.995$	4.20×10^{-5}	4.20×10^{-5}	4.21×10^{-5}	4.53×10^{-5}	5.34×10^{-5}	5.59×10^{-5}	5.60×10^{-5}
$+0.500$	3.53×10^{-5}	3.53×10^{-5}	3.54×10^{-5}	3.80×10^{-5}	4.51×10^{-5}	4.74×10^{-5}	4.75×10^{-5}
$+0.100$	2.02×10^{-5}	2.02×10^{-5}	2.03×10^{-5}	2.20×10^{-5}	2.65×10^{-5}	2.78×10^{-5}	2.08×10^{-5}
$+0.000$	2.00×10^{-5}	2.00×10^{-5}	2.00×10^{-5}	2.18×10^{-5}	2.62×10^{-5}	2.75×10^{-5}	2.77×10^{-5}
-0.100	1.67×10^{-5}	1.67×10^{-5}	1.68×10^{-5}	1.81×10^{-5}	2.21×10^{-5}	2.32×10^{-5}	2.34×10^{-5}
-0.500	6.00×10^{-6}	6.00×10^{-6}	6.02×10^{-6}	6.62×10^{-6}	8.30×10^{-6}	8.81×10^{-6}	8.88×10^{-6}
-0.995	2.49×10^{-12}	2.49×10^{-12}	2.50×10^{-12}	2.72×10^{-12}	3.28×10^{-12}	3.44×10^{-12}	3.46×10^{-12}
				$\boldsymbol{\lambda = 1000}$			
$+0.995$	2.25×10^{-5}	2.25×10^{-5}	2.26×10^{-5}	2.46×10^{-5}	2.94×10^{-5}	3.10×10^{-5}	3.12×10^{-5}
$+0.500$	2.38×10^{-5}	2.38×10^{-5}	2.39×10^{-5}	2.60×10^{-5}	3.10×10^{-5}	3.27×10^{-5}	3.29×10^{-5}
$+0.100$	1.93×10^{-5}	1.93×10^{-5}	1.94×10^{-5}	2.10×10^{-5}	2.54×10^{-5}	2.66×10^{-5}	2.68×10^{-5}
$+0.000$	2.00×10^{-5}	2.00×10^{-5}	2.00×10^{-5}	2.18×10^{-5}	2.62×10^{-5}	2.75×10^{-5}	2.77×10^{-5}
-0.100	2.08×10^{-5}	2.08×10^{-5}	2.08×10^{-5}	2.27×10^{-5}	2.73×10^{-5}	2.86×10^{-5}	2.88×10^{-5}
-0.500	1.54×10^{-5}	1.54×10^{-5}	1.54×10^{-5}	1.68×10^{-5}	2.03×10^{-5}	2.14×10^{-5}	2.16×10^{-5}
-0.995	5.66×10^{-10}	5.67×10^{-10}	5.75×10^{-10}	7.69×10^{-10}	1.41×10^{-9}	1.68×10^{-9}	1.72×10^{-9}
				$\boldsymbol{M_{\rm disc} = \int \sqrt{\gamma} W \rho d^3 x}$			
				$\boldsymbol{\lambda = 10}$			
$+0.995$	1.00×10^{-1}	9.72×10^{-2}	7.73×10^{-2}	3.76×10^{-2}	2.48×10^{-2}	2.35×10^{-2}	2.34×10^{-2}
$+0.500$	1.00×10^{-1}	9.76×10^{-2}	7.97×10^{-2}	4.07×10^{-2}	2.79×10^{-2}	2.62×10^{-2}	2.61×10^{-2}
$+0.100$	1.00×10^{-1}	9.76×10^{-2}	8.00×10^{-2}	4.14×10^{-2}	2.81×10^{-2}	2.65×10^{-2}	2.64×10^{-2}
$+0.000$	1.00×10^{-1}	9.76×10^{-2}	7.97×10^{-2}	4.07×10^{-2}	2.76×10^{-2}	2.60×10^{-2}	2.59×10^{-2}
-0.100	1.00×10^{-1}	9.76×10^{-2}	7.97×10^{-2}	4.08×10^{-2}	2.77×10^{-2}	2.62×10^{-2}	2.60×10^{-2}
-0.500	1.00×10^{-1}	9.79×10^{-2}	8.23×10^{-2}	4.53×10^{-2}	3.20×10^{-2}	3.05×10^{-2}	3.03×10^{-2}
-0.995	1.00×10^{-1}	9.76×10^{-2}	7.97×10^{-2}	4.07×10^{-2}	2.76×10^{-2}	2.60×10^{-2}	2.59×10^{-2}
				$\boldsymbol{\lambda = 60}$			
$+0.995$	1.00×10^{-1}	9.83×10^{-2}	8.51×10^{-2}	5.11×10^{-2}	3.75×10^{-2}	3.59×10^{-2}	3.56×10^{-2}
$+0.500$	1.00×10^{-1}	9.82×10^{-2}	8.40×10^{-2}	4.86×10^{-2}	3.51×10^{-2}	3.36×10^{-2}	3.33×10^{-2}
$+0.100$	1.00×10^{-1}	9.75×10^{-2}	7.95×10^{-2}	4.05×10^{-2}	2.74×10^{-2}	2.58×10^{-2}	2.57×10^{-2}
$+0.000$	1.00×10^{-1}	9.76×10^{-2}	7.97×10^{-2}	4.07×10^{-2}	2.76×10^{-2}	2.60×10^{-2}	2.59×10^{-2}
-0.100	1.00×10^{-1}	9.74×10^{-2}	7.82×10^{-2}	3.81×10^{-2}	2.56×10^{-2}	2.40×10^{-2}	2.39×10^{-2}
-0.500	1.00×10^{-1}	9.62×10^{-2}	7.08×10^{-2}	2.78×10^{-2}	1.67×10^{-2}	1.55×10^{-2}	1.54×10^{-2}
-0.995	1.00×10^{-1}	9.76×10^{-2}	7.97×10^{-2}	4.07×10^{-2}	2.76×10^{-2}	2.60×10^{-2}	2.59×10^{-2}
				$\boldsymbol{\lambda = 1000}$			
$+0.995$	1.00×10^{-1}	9.77×10^{-2}	8.08×10^{-2}	4.27×10^{-2}	2.93×10^{-2}	2.78×10^{-2}	2.76×10^{-2}
$+0.500$	1.00×10^{-1}	9.78×10^{-2}	8.14×10^{-2}	4.37×10^{-2}	3.01×10^{-2}	2.86×10^{-2}	2.85×10^{-2}
$+0.100$	1.00×10^{-1}	9.75×10^{-2}	7.93×10^{-2}	4.00×10^{-2}	2.72×10^{-2}	2.55×10^{-2}	2.54×10^{-2}
$+0.000$	1.00×10^{-1}	9.76×10^{-2}	7.97×10^{-2}	4.07×10^{-2}	2.76×10^{-2}	2.60×10^{-2}	2.59×10^{-2}
-0.100	1.00×10^{-1}	9.76×10^{-2}	8.01×10^{-2}	4.14×10^{-2}	2.83×10^{-2}	2.66×10^{-2}	2.65×10^{-2}
-0.500	1.00×10^{-1}	9.72×10^{-2}	7.70×10^{-2}	3.65×10^{-2}	2.40×10^{-2}	2.26×10^{-2}	2.25×10^{-2}
-0.995	1.00×10^{-1}	8.17×10^{-2}	2.38×10^{-2}	2.08×10^{-3}	6.69×10^{-4}	5.68×10^{-4}	5.58×10^{-4}

Chapter 6

Self-gravitating magnetized tori around black holes in general relativity

This chapter is based on the following publication: P. Mach, S. Gimeno-Soler, J. A. Font, A. Odrzywołek & M. Piróg. Self-gravitating magnetized tori around black holes in general relativity, *Physical Review D* 99, 104063 (2019), DOI: 10.1103/PhysRevD.99.104063.

6.1 Introduction

Compact accretion disks (or tori) around black holes are astrophysical transient systems that can form in a number of situations. Examples include the core-collapse of massive stars Woosley and Bloom 2006, the merger of compact binaries consisting of either two neutron stars or a black hole and a neutron star (see e.g. Baiotti and Rezzolla 2017 and references therein), and the gravitational collapse of a supermassive star Rees 1984, Shibata and Shapiro 2002. Observations of the formation and evolution of black hole–torus systems are challenging, either using neutrino, electromagnetic or gravitational-wave approaches. Since the recent breakthrough observation of gravitational waves from a binary neutron star (BNS) merger by Advanced LIGO and Virgo Abbott et al. 2017b, Abbott et al. 2017 one may hope that this cosmic messenger may offer the best possibility of observing black hole–torus systems in the near future.

Numerical relativity is the best approach to study the dynamical formation of black hole–torus systems from *ab-initio* simulations. Long-term simulations of BNS mergers that include the late inspiral of the two neutron stars and account for the relevant physics (i.e. relativistic gravity, general-relativistic magnetohydrodynamics (GRMHD), and neutrino transport) are in general fairly expensive. Therefore, building equilibrium initial data of black hole–torus systems is highly motivated, as it allows to carry out follow-up studies of the last stages of the merger in a less expensive way and in a more controlled environment, sidestepping the computation of the late inspiral and early merger phase. Equilibrium models must therefore be as faithful as possible to the end-products of the numerical evolutions, increasing their realism as new physical ingredients are incorporated (see Abramowicz and Fragile 2013 and references therein). Numerical works have shown that the mass of the tori may be large enough to render necessary to account for the disk self-gravity in order to properly describe its dynamics. This is particularly true for the case of unequal-mass BNS mergers Baiotti and Rezzolla 2017, Rezzolla et al. 2010. Motivated by these results, we present in this paper new families of self-gravitating disks around black holes.

A few authors have previously investigated this issue Nishida and Eriguchi 1994, Ansorg and Petroff 2005, Shibata 2007, Stergioulas 2011b. In their seminal work, Nishida and Eriguchi Nishida and Eriguchi 1994 computed self-gravitating toroids around stars and black holes using Komatsu-Eriguchi-Hachisu's (KEH) self-consistent-field method Komatsu, Eriguchi, and Hachisu 1989a, Komatsu, Eriguchi, and Hachisu 1989b. Elliptic-type field equations were converted into integral equations using Green's functions. Later on, Ansorg and Petroff Ansorg and Petroff 2005 built solutions of black holes surrounded by uniformly rotating rings of constant density using the same approach as Nishida and Eriguchi 1994, but solving the equations with a highly accurate multi-domain, pseudo-spectral method. A similar strategy was followed by Stergioulas Stergioulas 2011b to construct general-relativistic models of self-gravitating, constant angular momentum tori around black holes with KEH's self-consistent-field method. An important ingredient of this approach was the use of a compactified radial coordinate, which improved the enforcement of the boundary conditions asymptotically. Among all previous studies, the most relevant one for our work is that of Shibata Shibata 2007, since we follow very closely his procedure. Shibata's work departs from the other three approaches in that it builds self-gravitating tori around rotating black holes adopting the so-called puncture framework to describe the spacetime of a rotating black hole, and hence avoiding potential numerical issues when

dealing with the curvature singularity at the origin. The models reported by Shibata 2007 are purely hydrodynamical (i.e. with no magnetic field), and they are characterized by the constant angular momentum. (Non-constant angular momentum tori were considered in Kiuchi et al. 2011 albeit around non-rotating black holes.) On the contrary, the models presented in this paper incorporate a toroidal distribution of the magnetic field, a physically motivated Keplerian rotation law Karkowski et al. 2018a, Karkowski et al. 2018b and rotating black holes.

In addition to self-gravity, our disks also incorporate magnetic fields, within the ideal GRMHD approach. To the best of our knowledge, equilibrium sequences of self-gravitating and magnetised disks around black holes in general relativity have not yet been reported in the literature. (Notice, however, that Appendix A of Shibata 2007 outlines the procedure to build a self-gravitating magnetised disk with a toroidal magnetic field, but no examples are provided.) There exist a number of previous works where equilibrium solutions of magnetised disks around black holes have been built Komissarov 2006, Montero et al. 2007, Gimeno-Soler and Font 2017 but, to the best of our knowledge, all of them are restricted to the test-fluid approximation (i.e. neglecting self-gravity). Komissarov Komissarov 2006 first presented a general procedure to build magnetised "Polish doughnuts" (constant angular momentum tori) using a barotropic equation of state and the assumption that the specific enthalpy of the fluid is close to unity. This restrictive condition on the thermodynamics was relaxed in the work of Montero et al. Montero et al. 2007, who also performed dynamical evolutions of those tori. More recently, Gimeno-Soler and Font Gimeno-Soler and Font 2017 built new sequences of equilibrium magnetised tori around Kerr black holes assuming a form of the angular momentum distribution proposed in Qian et al. 2009 that departs from the constant case of Komissarov 2006 and from which the equipotential surfaces can be easily computed.

The study of the stability of equilibrium solutions of accretion tori under perturbations has received considerable numerical attention (see Abramowicz and Fragile 2013 for a review). In particular, constant angular momentum disks have been found to be generically unstable. On the other hand, in most BNS merger simulations the final black hole–torus system does not manifest signs of dynamical instabilities on short dynamical timescales (see [Baiotti and Rezzolla 2017] and references therein). Specifically, the simulations of Rezzolla et al. 2010 indicate that the angular velocity Ω of tori formed from unequal-mass BNS mergers follows Keplerian profiles, $\Omega \propto r^{-3/2}$, where r denotes the distance from the rotation axis, which explains the scaling of the

specific angular momentum as $r^{1/2}$. This provides firm evidence that tori produced self-consistently are dynamically stable. However, despite their non-constant angular momentum profiles make them stable against the development of the so-called runaway instability [Abramowicz, Calvani, and Nobili 1983, Font and Daigne 2002, Montero, Font, and Shibata 2010], on longer timescales non-axisymmetric instabilities (e.g. the Papaloizou-Pringle instability (PPI) [Papaloizou and Pringle 1984]) set in [Korobkin et al. 2011, Kiuchi et al. 2011, Mewes et al. 2016, Mewes et al. 2016]. Recently Bugli et al. Bugli et al. 2018 studied the development of the PPI in tori threaded by weak toroidal magnetic fields and how this instability may be affected by the concurrent development of the magnetorotational instability (MRI). Their simulations, within the test-fluid limit, showed that the magnetic fields provide local viscous stresses through turbulence and global angular momentum transport, leading to the suppression of large-scale PPI modes. The self-gravitating, magnetised tori we built in the present work may thus be used in the future to investigate the generality of the findings of Bugli et al. 2018 beyond the test-fluid limit.

The paper is organised as follows: in Sec. 6.2 we discuss the mathematical aspects of our procedure, presenting the Euler-Bernoulli equations, the Einstein equations, and the Keplerian rotation law. The masses and angular momentum of the black hole–torus spacetime are discussed in Sec. 6.3. Section 6.4 briefly describes our numerical method and the results are discussed in Sec. 6.5. Finally, Sec. 6.6 gives a summary of this work. In the Appendix we provide expressions for the Kerr metric in quasi-isotropic coordinates. We use geometric units with $G = c = 1$, where G is Newton's constant and c is the speed of light, and assume the signature of the metric $(-,+,+,+)$. Spacetime dimensions are labeled with Greek indices, $\mu = 0, 1, 2, 3$, while Latin indices are used to denote spatial dimensions, $i = 1, 2, 3$.

6.2 Equations

We start by deriving the equations describing stationary, axially symmetric, self-gravitating, magnetised toroids rotating around black holes. The black hole (which can be spinning) is included in the system using the puncture method. The torus is described in terms of ideal GRMHD; we restrict ourselves to toroidal magnetic fields and barotropic equations of state. In specific numerical examples discussed in Sec. 6.5 we assume polytropic fluids and a Keplerian rotation law introduced recently in Karkowski et al. 2018a, Karkowski et al. 2018b.

As mentioned in the introduction the formulation presented in this paper is based on the approach to modeling stationary perfect-fluid disks around black holes derived originally in Shibata 2007 for the case with no magnetic fields. In particular, in the derivation of the equations we follow closely the steps taken in Shibata 2007. Because the terms connected with the magnetic field appear irregularly in many of the equations, we repeat the corresponding calculations also in this paper. The magnetic field enters the description of stationary disks in two places: in the stationary Euler equation and in the "source terms" of the Einstein equations.

Within the framework of ideal GRMHD the energy-momentum tensor has the form

$$T_{\mu\nu} = (\rho h + b^2)u_\mu u_\nu + \left(p + \frac{1}{2}b^2\right) g_{\mu\nu} - b_\mu b_\nu, \tag{6.1}$$

where ρ is the baryonic density, h is the specific enthalpy, p is the (thermal) pressure, u^μ denotes components of the four-velocity of the fluid, and b^μ is the four-vector of the magnetic field. We denote $b^2 = b_\mu b^\mu$. Note that the quantity $p_{\rm mag} = \frac{1}{2}b^2$ plays the role of a magnetic pressure. It is assumed that

$$b_\mu u^\mu = 0. \tag{6.2}$$

In this case the dual of the Faraday tensor relative to an observer with four-velocity u^μ, ${}^*F^{\mu\nu} = b^\mu u^\nu - b^\nu u^\mu$, satisfies $\nabla_\mu {}^*F^{\mu\nu} = 0$.

We will work in spherical coordinates (t, r, θ, φ). It is convenient to start with a general, stationary and axially symmetric metric of the form

$$g = g_{tt}dt^2 + 2g_{t\varphi}dtd\varphi + g_{rr}dr^2 + g_{\theta\theta}d\theta^2 + g_{\varphi\varphi}d\varphi^2, \tag{6.3}$$

where the metric potentials g_{tt}, $g_{t\varphi}$, g_{rr}, $g_{\theta\theta}$, $g_{\varphi\varphi}$ depend on r and θ only. We consider an axially symmetric, stationary configuration with $u^r = u^\theta = b^r = b^\theta = 0$. It follows from Eq. (6.2) that

$$b_t = -\frac{u^\varphi}{u^t} b_\varphi = -\Omega b_\varphi, \tag{6.4}$$

where $\Omega = u^\varphi/u^t$. Note that the normalization of the four-velocity $u_\mu u^\mu = -1$ yields

$$g_{tt} + 2g_{t\varphi}\Omega + g_{\varphi\varphi}\Omega^2 = -\frac{1}{(u^t)^2}. \tag{6.5}$$

It can be easily shown that

$$b_\varphi^2 = -(u^t)^2 \mathcal{L} b^2, \tag{6.6}$$

where $\mathcal{L} = g_{\varphi\varphi}g_{tt} - g_{t\varphi}^2$.

6.2.1 Euler-Bernoulli equation

The way of deriving the Euler-Bernoulli equation (or the first integral of the Euler equations) for the ideal GRMHD energy-momentum tensor is described in Appendix A of Shibata 2007. The computation of the four-divergence

$$\nabla_\mu T^\mu{}_\nu = \frac{1}{\sqrt{-g}}\partial_\mu\left(\sqrt{-g}T^\mu{}_\nu\right) - \frac{1}{2}(\partial_\nu g_{\alpha\beta})T^{\alpha\beta} = 0 \tag{6.7}$$

yields

$$\partial_\nu\left(p + \frac{1}{2}b^2\right) - \frac{1}{2}(\partial_\nu g_{\alpha\beta})\left[(\rho h + b^2)u^\alpha u^\beta - b^\alpha b^\beta\right] = 0. \tag{6.8}$$

The above equation is trivially satisfied for $\nu = t$ and $\nu = \varphi$. Nontrivial information is contained in Eq. (6.8) for $\nu = r, \theta$. Following Shibata 2007, one can show that

$$\frac{1}{2}u^\alpha u^\beta \partial_\nu g_{\alpha\beta} = \frac{\partial_\nu u^t}{u^t} - u^t u_\varphi \partial_\nu \Omega \tag{6.9}$$

and

$$\frac{1}{2}b^\alpha b^\beta \partial_\nu g_{\alpha\beta} = b^2\left(\frac{\partial_\nu u^t}{u^t} + \frac{\partial_\nu \mathcal{L}}{2\mathcal{L}} - u^t u_\varphi \partial_\nu \Omega\right). \tag{6.10}$$

Combining the above expressions one gets

$$\rho h\left(u^t u_\varphi \partial_\nu \Omega - \frac{\partial_\nu u^t}{u^t}\right) + \partial_\nu p + \frac{\partial_\nu(b^2\mathcal{L})}{2\mathcal{L}} = 0, \tag{6.11}$$

or, dividing by ρh,

$$u^t u_\varphi \partial_\nu \Omega - \frac{\partial_\nu u^t}{u^t} + \frac{\partial_\nu h}{h} + \frac{\partial_\nu(b^2\mathcal{L})}{2\rho h\mathcal{L}} = 0, \tag{6.12}$$

where we have used the fact that $dh = dp/\rho$. Therefore, it is possible to search for a solution in the form

$$\int u^t u_\varphi d\Omega + \ln\left(\frac{h}{u^t}\right) + \int \frac{d(b^2\mathcal{L})}{2\rho h\mathcal{L}} = C, \tag{6.13}$$

which is Eq. (A11) of Shibata 2007 (note a misprint in the last term of the equation given in Shibata 2007). The above equation is also equivalent to Eq. (11) of Gimeno-Soler and Font 2017. We define the angular momentum per unit inertial mass ρh as $j = u^t u_\varphi$ and write

$$\int j(\Omega) d\Omega + \ln\left(\frac{h}{u^t}\right) + \int \frac{d(b^2\mathcal{L})}{2\rho h\mathcal{L}} = C. \tag{6.14}$$

This stays in agreement with the purely hydrodynamical case, where a functional relation $j = j(\Omega)$ (the rotation law) is an integrability condition of the Euler equations. Here we assume that $j = j(\Omega)$. It follows that also $b^2\mathcal{L}$ must be a function of $\rho h\mathcal{L}$. Further details of the Euler-Bernoulli equation, as well as

the specific choices regarding the equation of state, the rotation law, and the prescription of the magnetic field will be discussed in Sec. 6.2.3.

6.2.2 Einstein equations

Following Shibata 2007 we derive the set of equations corresponding to a stationary black hole–torus spacetime from the standard $3+1$ formulation of the Einstein equations. The 3+1 metric reads

$$g = (-\alpha^2 + \beta_i\beta^i)dt^2 + 2\beta_i dx^i dt + \gamma_{ij}dx^i dx^j, \tag{6.15}$$

where α is the lapse function, β_i is the shift vector, and γ_{ij} denote the components of the spatial metric. The vector normal to a surface of constant time Σ_t is given by

$$n^\mu = \frac{1}{\alpha}(1, -\beta^r, -\beta^\theta, -\beta^\varphi), \quad n_\mu = (-\alpha, 0, 0, 0). \tag{6.16}$$

The Einstein constraint equations read

$$D_j(K^{ij} - \gamma^{ij}K) = 8\pi j^i \tag{6.17}$$

and

$$\frac{1}{2}\left(R + K^2 - K_{ij}K^{ij}\right) = 8\pi\rho_{\rm H}, \tag{6.18}$$

where D_i and R denote, respectively, the covariant derivative and the scalar curvature with respect to the metric γ_{ij}, induced on the slices Σ_t. The extrinsic curvature K_{ij} of a slice Σ_t is defined by

$$K_{ij} = -\frac{1}{2\alpha}\left(\partial_t\gamma_{ij} - \mathcal{L}_\beta\gamma_{ij}\right), \tag{6.19}$$

where the Lie derivative of the three-metric is given by

$$\mathcal{L}_\beta\gamma_{ij} = \beta^k\partial_k\gamma_{ij} + \gamma_{ik}\partial_j\beta^k + \gamma_{kj}\partial_i\beta^k. \tag{6.20}$$

We denote $K = \gamma^{ij}K_{ij}$ and use a standard convention that spatial indices are raised and lowered using the induced metric γ_{ij}. The source terms $\rho_{\rm H}$ and j^i are defined as

$$\rho_{\rm H} = n^\mu n^\nu T_{\mu\nu}, \quad j_i = -P^\alpha{}_i\, n^\beta T_{\alpha\beta}, \tag{6.21}$$

where $P^\mu{}_\nu = \delta^\mu{}_\nu + n^\mu n_\nu$ is the spatial projection operator. The evolution equation for the extrinsic curvature K_{ij} is

$$\begin{aligned}\partial_t K_{ij} - \mathcal{L}_\beta K_{ij} \;=\; & -D_iD_j\alpha + \alpha\left(R_{ij} + KK_{ij} - 2K_{ik}K^k{}_j\right) \\ & +4\pi\alpha\left[\gamma_{ij}(S - \rho_{\rm H}) - 2S_{ij}\right].\end{aligned} \tag{6.22}$$

Here R_{ij} is the Ricci tensor with respect to the metric γ_{ij}. The tensor S_{ij} is defined as

$$S_{ij} = P^{\mu}{}_{i} P^{\nu}{}_{j} T_{\mu\nu}, \tag{6.23}$$

and $S = \gamma^{ij} S_{ij}$.

We start by computing the source terms $\rho_{\rm H}$, j_i, S_{ij} and S. Assuming the energy momentum-tensor (6.1), one gets

$$\rho_{\rm H} = \alpha^2 \rho h (u^t)^2 - p + \frac{1}{2} b^2, \tag{6.24}$$

$$S_{ij} = (\rho h + b^2) u_i u_j + \left(p + \frac{1}{2} b^2 \right) \gamma_{ij} - b_i b_j, \tag{6.25}$$

$$S = \rho h \left[\alpha^2 (u^t)^2 - 1 \right] + 3p + \frac{1}{2} b^2. \tag{6.26}$$

Finally, the only nonvanishing component of j_i is

$$j_\varphi = \alpha \rho h u^t u_\varphi. \tag{6.27}$$

Note that there is no explicit magnetic contribution to j_φ. All these formulas can be obtained quite generally, assuming the metric of the form (6.3) and the conditions $u^r = u^\theta = b^r = b^\theta = 0$.

As in Shibata 2007 we assume from now on a metric in quasi-isotropic form:

$$\begin{aligned} g = & -\alpha^2 dt^2 + \psi^4 e^{2q} (dr^2 + r^2 d\theta^2) + \\ & \psi^4 r^2 \sin^2\theta (\beta dt + d\varphi)^2. \end{aligned} \tag{6.28}$$

Thus, we need to provide equations for the four metric potentials appearing in Eq. (6.28), α, β, ψ, and q, or, as we shall see, suitable combinations of these quantities (as in Shibata 2007). In Eq. (6.28) $\beta_\varphi = \psi^4 r^2 \beta \sin^2\theta$, $\beta \equiv \beta^\varphi$, and α denotes the lapse function [as in Eq. (6.15)]. Since $\partial_t \gamma_{ij} = 0$ and $\beta^k \partial_k \gamma_{ij} = 0$, we get

$$K_{ij} = \frac{1}{2\alpha} \left(\gamma_{ik} \partial_j \beta^k + \gamma_{kj} \partial_i \beta^k \right), \tag{6.29}$$

and $K = \gamma^{ik} K_{ik} = 0$, i.e., we are in fact working in a maximal slicing. Therefore, the momentum constraint (6.17) can be written as

$$D_j K^j{}_l = 8\pi j_l. \tag{6.30}$$

The only nonvanishing components of K_{ij} read

$$K_{\varphi r} = K_{r\varphi} = \frac{1}{2\alpha} \psi^4 r^2 \sin^2\theta \partial_r \beta, \tag{6.31}$$

$$K_{\varphi\theta} = K_{\theta\varphi} = \frac{1}{2\alpha} \psi^4 r^2 \sin^2\theta \partial_\theta \beta. \tag{6.32}$$

To compute the momentum constraint we use a standard formula for symmetric tensors K_{ij}:

$$D_j K^j{}_l = \frac{1}{\sqrt{\gamma}}\partial_j\left(\sqrt{\gamma}K^j{}_l\right) - \frac{1}{2}(\partial_l\gamma_{ik})K^{ik}, \tag{6.33}$$

where $\gamma = \det(\gamma_{ij})$. Assuming the metric of the form (6.28) one obtains $\sqrt{\gamma} = \psi^6 r^2 \sin\theta e^{2q}$. The only nontrivial component of Eqs. (6.30) is obtained for $l = \varphi$,

$$\begin{aligned} &\frac{1}{r^2}\partial_r\left(\psi^2 r^2 K_{r\varphi}\right) + \\ &\frac{1}{r^2\sin\theta}\partial_\theta\left(\psi^2\sin\theta K_{\theta\varphi}\right) &= 8\pi\psi^6 e^{2q} j_\varphi. \end{aligned} \tag{6.34}$$

Following Shibata 2007 the shift vector β can be now split into two parts, $\beta = \beta_{\rm K} + \beta_{\rm T}$, where subindex K indicates the Kerr metric and subindex T the torus. We require that

$$K_{r\varphi} = K_{\varphi r} = \frac{H_{\rm E}\sin^2\theta}{\psi^2 r^2} + \frac{1}{2\alpha}\psi^4 r^2\sin^2\theta\partial_r\beta_{\rm T}, \tag{6.35}$$

$$K_{\theta\varphi} = K_{\varphi\theta} = \frac{H_{\rm F}\sin\theta}{\psi^2 r} + \frac{1}{2\alpha}\psi^4 r^2\sin^2\theta\partial_\theta\beta_{\rm T}, \tag{6.36}$$

and assume $H_{\rm E}$ and $H_{\rm F}$ corresponding to the Kerr metric (see Appendix A). More precisely, we choose $H_{\rm E}$ and $H_{\rm F}$ so that for the Kerr metric written in the form (6.28) one has

$$K_{r\varphi} = K_{\varphi r} = \frac{H_{\rm E}\sin^2\theta}{\psi^2 r^2}, \tag{6.37}$$

$$K_{\theta\varphi} = K_{\varphi\theta} = \frac{H_{\rm F}\sin\theta}{\psi^2 r}. \tag{6.38}$$

These functions satisfy the momentum constraint of the form

$$r\sin^3\theta\partial_r H_{\rm E} + \partial_\theta(H_{\rm F}\sin^2\theta) = 0. \tag{6.39}$$

If a self-gravitating torus is present, we compute $\beta_{\rm K}$ from the relation

$$\partial_r\beta_{\rm K} = \frac{2H_{\rm E}\alpha}{r^4\psi^6}, \tag{6.40}$$

which does not yield the Kerr form, as the conformal factor ψ contains a contribution from the torus.

Inserting the expressions for $K_{r\varphi}$ and $K_{\theta\varphi}$ into Eq. (6.34) we obtain, after some algebra, an elliptic-type equation for $\beta_{\rm T}$

$$\begin{aligned}\Delta\beta_{\rm T} + \frac{\alpha}{\psi^6 r^2}(\partial_r\beta_{\rm T})\partial_r\left(\frac{\psi^6 r^2}{\alpha}\right) + \\ \frac{\alpha}{\psi^6 r^2\sin^2\theta}(\partial_\theta\beta_{\rm T})\partial_\theta\left(\frac{\psi^6\sin^2\theta}{\alpha}\right) &= \frac{16\pi\alpha e^{2q}j_\varphi}{r^2\sin^2\theta},\end{aligned} \tag{6.41}$$

where Δ denotes the flat Laplacian operator in spherical coordinates. Again, as in Shibata 2007 we replace the lapse function α by the combination $\Phi = \alpha\psi$ and rewrite the previous equation as

$$\begin{aligned}\Delta\beta_{\rm T} + \left(\frac{2}{r} + \frac{7\partial_r\psi}{\psi} - \frac{\partial_r\Phi}{\Phi}\right)\partial_r\beta_{\rm T} + \\ \frac{1}{r^2}\left(2\cot\theta + \frac{7\partial_\theta\psi}{\psi} - \frac{\partial_\theta\Phi}{\Phi}\right)\partial_\theta\beta_{\rm T} &= \frac{16\pi\alpha e^{2q}j_\varphi}{r^2\sin^2\theta},\end{aligned} \tag{6.42}$$

which is the same as Eq. (20) of Shibata 2007.

The equation for the conformal factor follows from the Hamiltonian constraint, Eq. (6.18), which for metric (6.28) reads

$$R - K_{ij}K^{ij} = 16\pi\rho_{\rm H}. \tag{6.43}$$

It can be easily shown that

$$K_{ij}K^{ij} = \frac{2A^2}{\psi^{12}e^{2q}}, \tag{6.44}$$

where we use the short-hand notation

$$A^2 = \frac{(\psi^2 K_{r\varphi})^2}{r^2\sin^2\theta} + \frac{(\psi^2 K_{\theta\varphi})^2}{r^4\sin^2\theta}. \tag{6.45}$$

The Ricci scalar can be computed as

$$R = -\frac{8}{\psi^5 e^{2q}}\Delta\psi + \frac{1}{\psi^4}\tilde{R}, \tag{6.46}$$

where

$$\tilde{R} = -2e^{-2q}\left(\partial_{rr}q + \frac{1}{r}\partial_r q + \frac{1}{r^2}\partial_{\theta\theta}q\right). \tag{6.47}$$

This allows us to write the Hamiltonian constraint (6.18) in the form (Eq. (19) of Shibata 2007)

$$\Delta\psi = \frac{1}{8}\psi e^{2q}\tilde{R} - \frac{1}{4}\frac{A^2}{\psi^7} - 2\pi\psi^5 e^{2q}\rho_{\rm H}. \tag{6.48}$$

The next equation follows from the general evolution equation for K. It can be obtained by computing the trace of Eq. (6.22):

$$\begin{aligned} \partial_t K - \mathcal{L}_\beta K &= -\gamma^{ij} D_i D_j \alpha + \alpha(R + K^2) + \\ &\quad 4\pi\alpha(S - 3\rho_{\rm H}). \end{aligned} \tag{6.49}$$

Using the Hamiltonian constraint, this equation can also be written as

$$\partial_t K - \mathcal{L}_\beta K = -\gamma^{ij} D_i D_j \alpha + \alpha K_{ij} K^{ij} + 4\pi\alpha(S + \rho_{\rm H}). \tag{6.50}$$

Since

$$-\gamma^{ij} D_i D_j \alpha = -\frac{1}{\psi^5 e^{2q}}\Delta\Phi + \frac{\Phi}{\psi^6 e^{2q}}\Delta\psi, \tag{6.51}$$

we obtain an elliptic-type equation for Φ

$$\Delta\Phi = \frac{\Phi}{\psi}\Delta\psi + \frac{2\Phi A^2}{\psi^8} + 4\pi\Phi e^{2q}\psi^4(\rho_{\rm H} + S), \tag{6.52}$$

or, in terms of $\tilde{R}$,

$$\Delta\Phi = \frac{1}{8}\Phi e^{2q}\tilde{R} + \frac{7\Phi A^2}{4\psi^8} + 2\pi\Phi e^{2q}\psi^4(2S + \rho_{\rm H}), \tag{6.53}$$

which is Eq. (18) of Shibata 2007.

The last equation (for the potential q) is obtained from Eq. (6.22). We define

$$\begin{aligned} I_{ij} &= \partial_t K_{ij} = \mathcal{L}_\beta K_{ij} - D_i D_j \alpha + \\ &\quad \alpha\left(R_{ij} + K K_{ij} - 2K_{ik}K^k{}_j\right) + \\ &\quad 4\pi\alpha\left[\gamma_{ij}(S - \rho_{\rm H}) - 2S_{ij}\right] = 0. \end{aligned} \tag{6.54}$$

Consider the equation

$$I_{rr} + \frac{1}{r^2} I_{\theta\theta} - \frac{3e^{2q}}{r^2 \sin^2\theta} I_{\varphi\varphi} = 0. \tag{6.55}$$

It yields, in particular, the term

$$-\frac{4\pi}{r^2}\left(r^2 S_{rr} + S_{\theta\theta} - \frac{3e^{2q}}{\sin^2\theta} S_{\varphi\varphi} + e^{2q} r^2 \psi^4 S\right) =$$

$$-8\pi e^{2q}\psi^4\left(p-\frac{\rho h u_\varphi^2}{\psi^4 r^2\sin^2\theta}+\frac{3}{2}b^2\right), \tag{6.56}$$

and the equation

$$\begin{aligned}\left(\partial_{rr}+\frac{1}{r}\partial_r+\frac{1}{r^2}\partial_{\theta\theta}\right)q=&\\ -8\pi e^{2q}\psi^4&\left(p-\frac{\rho h u_\varphi^2}{\psi^4 r^2\sin^2\theta}+\frac{3}{2}b^2\right)+\frac{3A^2}{\psi^8}\\ +2&\left(\frac{1}{r}\partial_r+\frac{\cot\theta}{r^2}\partial_\theta\right)\ln(\Phi\psi)\\ +\frac{4}{\Phi\psi}&\left(\partial_r\Phi\partial_r\psi+\frac{1}{r^2}\partial_\theta\Phi\partial_\theta\psi\right).\end{aligned} \tag{6.57}$$

This allows us to compute $\tilde{R}$. The result can be combined with Eq. (6.48), yielding a new form of the elliptic equation for the conformal factor ψ

$$\begin{aligned}\Delta\psi \;=\;& -2\pi e^{2q}\psi^5\left(\rho_{\rm H}-p-\frac{3}{2}b^2+\frac{\rho h u_\varphi^2}{\psi^4 r^2\sin^2\theta}\right)-\frac{A^2}{\psi^7}\\ &-\frac{1}{2}\psi\left(\frac{1}{r}\partial_r+\frac{\cot\theta}{r^2}\partial_\theta\right)\ln(\Phi\psi)\\ &-\frac{1}{\Phi}\left(\partial_r\Phi\partial_r\psi+\frac{1}{r^2}\partial_\theta\Phi\partial_\theta\psi\right),\end{aligned} \tag{6.58}$$

which corresponds to Eq. (30) of Shibata 2007. A direct calculation then gives

$$\left(\Delta+\frac{1}{r}\partial_r+\frac{\cot\theta}{r^2}\partial_\theta\right)(\Phi\psi)=16\pi\Phi\psi^5 e^{2q}\left(p+\frac{1}{2}b^2\right), \tag{6.59}$$

which generalizes Eq. (31) of Shibata 2007.

From the technical point of view, the black hole is introduced by specifying suitable boundary conditions. This can be done in an elegant manner by adapting the above equation to the "puncture" form (see Brandt and Brügmann 1997, Krivan and Price 1998). Assuming that the puncture is located at $r=0$, we define

$$\psi=\left(1+\frac{r_{\rm s}}{r}\right)e^{\phi},\quad \Phi=\left(1-\frac{r_{\rm s}}{r}\right)e^{-\phi}B, \tag{6.60}$$

where $r_{\rm s}=\frac{1}{2}\sqrt{m^2-a^2}$ is a radius of a coordinate sphere corresponding to the black hole horizon. Parameters m and a are chosen in such a way that in the Kerr spacetime with the asymptotic mass m and the spin parameter a the event horizon would be located at $r=r_{\rm s}$.

The above definitions lead to the following equations for the functions ϕ, B, $\beta_{\rm T}$, and q:

$$\left[\partial_{rr}+\frac{1}{r}\partial_r+\frac{1}{r^2}\partial_{\theta\theta}\right]q = S_q, \tag{6.61a}$$

$$\left[\partial_{rr}+\frac{2r}{r^2-r_{\rm s}^2}\partial_r+\frac{1}{r^2}\partial_{\theta\theta}+\frac{\cot\theta}{r^2}\partial_\theta\right]\phi = S_\phi, \tag{6.61b}$$

$$\left[\partial_{rr}+\frac{3r^2+r_{\rm s}^2}{r(r^2-r_{\rm s}^2)}\partial_r+\frac{1}{r^2}\partial_{\theta\theta}+\frac{2\cot\theta}{r^2}\partial_\theta\right]B = S_B, \tag{6.61c}$$

$$\left[\partial_{rr}+\frac{4r^2-8r_{\rm s}r+2r_{\rm s}^2}{r(r^2-r_{\rm s}^2)}\partial_r+\frac{1}{r^2}\partial_{\theta\theta}+\frac{3\cot\theta}{r^2}\partial_\theta\right]\beta_{\rm T} = S_{\beta_{\rm T}}, \tag{6.61d}$$

where

$$\begin{aligned} S_q &= -8\pi e^{2q}\left(\psi^4 p-\frac{\rho h u_\phi^2}{r^2\sin^2\theta}+\frac{3}{2}\psi^4 b^2\right)+\frac{3A^2}{\psi^8} \\ &\quad +2\left[\frac{r-r_{\rm s}}{r(r+r_{\rm s})}\partial_r+\frac{\cot\theta}{r^2}\partial_\theta\right]\tilde{b}+\left[\frac{8r_{\rm s}}{r^2-r_{\rm s}^2}+4\partial_r(\tilde{b}-\phi)\right]\partial_r\phi \\ &\quad +\frac{4}{r^2}\partial_\theta\phi\partial_\theta(\tilde{b}-\phi), \end{aligned} \tag{6.62a}$$

$$\begin{aligned} S_\phi &= -2\pi e^{2q}\psi^4\left[\rho_{\rm H}-p+\frac{\rho h u_\phi^2}{\psi^4 r^2\sin^2\theta}-\frac{3}{2}b^2\right]-\frac{A^2}{\psi^8} \\ &\quad -\partial_r\phi\partial_r\tilde{b}-\frac{1}{r^2}\partial_\theta\phi\partial_\theta\tilde{b}-\frac{1}{2}\left[\frac{r-r_{\rm s}}{r(r+r_{\rm s})}\partial_r\tilde{b}+\frac{\cot\theta}{r^2}\partial_\theta\tilde{b}\right], \end{aligned} \tag{6.62b}$$

$$S_B = 16\pi B e^{2q}\psi^4\left(p+\frac{1}{2}b^2\right), \tag{6.62c}$$

$$\begin{aligned} S_{\beta_{\rm T}} &= \frac{16\pi\alpha e^{2q}j_\varphi}{r^2\sin^2\theta}-8\partial_r\phi\partial_r\beta_{\rm T}+\partial_r\tilde{b}\partial_r\beta_{\rm T} \\ &\quad -8\frac{\partial_\theta\phi\partial_\theta\beta_{\rm T}}{r^2}+\frac{\partial_\theta\tilde{b}\partial_\theta\beta_{\rm T}}{r^2}, \end{aligned} \tag{6.62d}$$

which replace Eqs. (44–47) of Shibata 2007 when a toroidal magnetic field is present in the disk. In the above formulas we denoted $B=e^{\tilde{b}}$. Equation (6.40) can be written as

$$\partial_r\beta_{\rm K}=2H_{\rm E}Be^{-8\phi}\frac{(r-r_{\rm s})r^2}{(r+r_{\rm s})^7}. \tag{6.63}$$

Notice that it does not yield the Kerr form, as there are contributions from the torus in both B and ϕ.

In our numerical approach we assume equatorial symmetry and solve equations (6.61), (6.62) and (6.63) in the domain defined by $r\in(r_{\rm s},r_\infty)$, $\theta\in(0,\pi/2)$. Here r_∞ is large, but finite.

The boundary conditions at $r = r_{\rm s}$ read

$$\partial_r q = \partial_r \phi = \partial_r B = \partial_r \beta_{\rm T} = 0. \tag{6.64}$$

It can be shown that Eq. (6.61d) requires a more stringent condition, which we set as $\beta_{\rm T} = O[(r - r_{\rm s})^4]$, or equivalently, $\beta_{\rm T} = \partial_r \beta_{\rm T} = \partial_{rr} \beta_{\rm T} = \partial_{rrr} \beta_{\rm T} = 0$ at $r = r_{\rm s}$. In this choice, reflecting a freedom of fixing the splitting $\beta = \beta_{\rm T} + \beta_{\rm K}$, we follow Shibata 2007; this choice has consequences in the definition of the angular momentum of the black hole (cf. Sec. 6.3).

With the above boundary conditions, the two-surface $r = r_{\rm s}$ embedded in a hypersurface of constant time Σ_t becomes a Marginally Outer Trapped Surface (MOTS) or the so-called apparent horizon. This can be easily demonstrated as follows. A MOTS is defined as a two-surface $\mathcal{S}$ embedded in Σ_t on which the scalar expansion of the outgoing null geodesics

$$\theta_+ = H - K_{ij} m^i m^j + K \tag{6.65}$$

vanishes. Here $H = D_i m^i$ denotes the mean curvature of the surface $\mathcal{S}$, and m^i is a unit vector tangent to Σ_t and normal to $\mathcal{S}$. For the two-surface $r = r_{\rm s}$, the components of the three-vector m^i are given by $m^i = (m^r, m^\theta, m^\varphi) = (\psi^{-2} e^{-q}, 0, 0)$. Consequently, at $r = r_{\rm s}$,

$$\theta_+ = H = \frac{1}{\psi^6 e^{2q} r^2} \partial_r \left(\psi^4 e^q r^2 \right), \tag{6.66}$$

since both terms $K_{ij} m^i m^j$ and K vanish. Using Eq. (6.60), one can show that

$$\theta_+ = H = \frac{1}{4} e^{-2\phi - q} \left(4 \partial_r \phi + \partial_r q \right), \tag{6.67}$$

at $r = r_{\rm s}$. It is now clear that the boundary conditions assumed at $r = r_{\rm s}$ imply that $\theta_+ = H = 0$. Note that the surface $r = r_{\rm s}$ is not only an apparent horizon, but it is also a minimal surface.

At the axis $\theta = 0$ we assume regularity conditions $\partial_\theta \phi = \partial_\theta B = \partial_\theta \beta_{\rm T} = 0$. Local flatness implies that $q = 0$ at $\theta = 0$. At the equator, we require symmetry conditions $\partial_\theta q = \partial_\theta \phi = \partial_\theta B = \partial_\theta \beta_{\rm T} = 0$.

The asymptotic expansions of q, ϕ, B, and $\beta_{\rm T}$ are discussed in Sec. 6.3. They are used to impose boundary conditions at $r = r_\infty$. Further details on the numerical implementation of the boundary and asymptotic conditions can be found in Karkowski et al. 2018b.

6.2.3 Details of the Euler-Bernoulli equation

We next discuss details of the Euler-Bernoulli equation, Eq. (6.14). The following three components have to be specified in order to obtain a solution: the equation of state, the rotation law $j = j(\Omega)$, and a prescription of the distribution of the magnetic field.

We assume the Keplerian rotation law derived in Karkowski et al. 2018a, Karkowski et al. 2018b, i.e.,

$$j(\Omega) = -\frac{1}{2}\frac{d}{d\Omega}\ln\left\{1 - \left[a^2\Omega^2 + 3w^{\frac{4}{3}}\Omega^{\frac{2}{3}}(1 - a\Omega)^{\frac{4}{3}}\right]\right\}. \tag{6.68}$$

This is an exact formula that characterizes the motion of circular geodesics at the equatorial plane of the Kerr spacetime, in which case $w^2 = m$, where m is the Kerr mass. For self-gravitating tori $w^2 \neq m$, in general. In the Newtonian limit rotation law (6.68) yields the standard Keplerian prescription of the angular velocity $\Omega = w/(r\sin\theta)^{\frac{3}{2}}$. It also agrees (for $a = 0$) with the post-Newtonian Keplerian prescription proposed in Mach and Malec 2015. The advantage of using this rotation law is that it allows one to obtain numerical solutions in a wide range of the parameters describing the torus Karkowski et al. 2018a, Karkowski et al. 2018b.

The angular velocity Ω can be obtained by solving the relation $j(\Omega) = u^t u_\varphi$ for Ω. In more explicit terms this relation reads

$$j(\Omega)\left(-g_{tt} - 2g_{t\varphi}\Omega - g_{\varphi\varphi}\Omega^2\right) = g_{\varphi\varphi}\Omega + g_{t\varphi} \tag{6.69}$$

or

$$j(\Omega)\left[\alpha^2 - \psi^4 r^2\sin^2\theta(\Omega + \beta)^2\right] = \psi^4 r^2\sin^2\theta(\Omega + \beta), \tag{6.70}$$

where $j(\Omega)$ is given by Eq. (6.68). We assume a convention with $\Omega > 0$. This can correspond both to a torus corotating with the black hole, if $a > 0$, or counterrotating, for $a < 0$.

The specification of the magnetic term

$$\int \frac{d(b^2\mathcal{L})}{2\rho h\mathcal{L}} = \int \frac{d(b^2|\mathcal{L}|)}{2\rho h|\mathcal{L}|}, \tag{6.71}$$

with $\mathcal{L} = -\alpha^2\psi^4 r^2\sin^2\theta$, is somewhat more arbitrary, in the sense that there seem to be no physical "hints" concerning its prescription. Assuming a functional relation of the form $b^2|\mathcal{L}| = f(x)$, where $x = \rho h|\mathcal{L}|$ (note that this functional relation fulfills the general relativistic version of the von Zeipel condition for a

purely toroidal magnetic field Zanotti and Pugliese 2015), we obtain

$$\int \frac{d(b^2|\mathcal{L}|)}{2\rho h|\mathcal{L}|} = \int \frac{f'(x)dx}{2x}. \tag{6.72}$$

Suppose that we would like to get

$$\int \frac{f'(x)dx}{2x} = \ln(1 + C_1 x)^n, \tag{6.73}$$

where C_1 and n are constants. This yields

$$f'(x) = \frac{2nC_1 x}{1 + C_1 x}, \tag{6.74}$$

and a solution of the form

$$f(x) = 2n\left[x - \frac{1}{C_1}\ln(1 + C_1 x)\right] + C_2. \tag{6.75}$$

For $x = 0$ we get $f(x = 0) = C_2$. Consequently, we set $C_2 = 0$. This ensures that the magnetic field vanishes for vanishing ρ. We have, finally

$$\int \frac{d(b^2\mathcal{L})}{2\rho h\mathcal{L}} = \ln\left[\left(1 + C_1\alpha^2\psi^4 r^2 \sin^2\theta\rho h\right)^n\right]. \tag{6.76}$$

We assume the above prescription of the magnetic field in this paper.

Equation (6.5) with the metric terms of Eq. (6.28) yields

$$\frac{1}{u^t} = \sqrt{\alpha^2 - \psi^4 r^2 \sin^2\theta(\Omega + \beta)^2}. \tag{6.77}$$

The Euler-Bernoulli Eq. (6.14) can be now written in the form

$$\begin{aligned} & h\left(1 + C_1\alpha^2\psi^4 r^2 \sin^2\theta\rho h\right)^n \\ & \quad \times\sqrt{\alpha^2 - \psi^4 r^2 \sin^2\theta(\Omega + \beta)^2} \\ & \quad \times\left\{1 - \left[a^2\Omega^2 + 3w^{\frac{4}{3}}\Omega^{\frac{2}{3}}(1 - a\Omega)^{\frac{4}{3}}\right]\right\}^{-\frac{1}{2}} = C'. \end{aligned} \tag{6.78}$$

In this paper we work with the polytropic equation of state of the form $p = K\rho^\gamma$. This yields the expression for the specific enthalpy

$$h = 1 + \frac{K\gamma}{\gamma - 1}\rho^{\gamma - 1}. \tag{6.79}$$

Note that the magnetic distribution was chosen in such a way that in the limit $\rho \to 0$, the Euler-Bernoulli equation has the same form as in the absence

of the magnetic field, i.e.,

$$\frac{\sqrt{\alpha^2 - \psi^4 r^2 \sin^2\theta(\Omega+\beta)^2}}{\sqrt{1-\left[a^2\Omega^2 + 3w^{\frac{4}{3}}\Omega^{\frac{2}{3}}(1-a\Omega)^{\frac{4}{3}}\right]}} = C'. \tag{6.80}$$

In our numerical procedure this form is used to establish the constants w and C', assuming that the torus is characterized by some fixed equatorial coordinate radii r_1 and r_2.

An important numerical aspect concerns the specification of the polytropic constant K of the equation of state. It is adjusted during the numerical iterative procedure so that the maximum value of the density ρ within the torus is fixed at an a priori prescribed value (see Sec. 6.4 for an exact discussion of this point).

We note that another possibility of setting up the details of the Euler-Bernoulli equation is to assume the rotation law of the form $\tilde{j} = hu_\varphi = \tilde{j}(\Omega)$. This is, for instance, the choice used in Shibata 2007. The Euler-Bernoulli equation is then given by Eq. (A10) of Shibata 2007. Such a formulation would suggest a different profile of b^2, given for instance by Eq. (A14) of Shibata 2007.

6.3 Masses and angular momenta

The asymptotic Arnowitt-Deser-Misner mass can be computed as Shibata 2007

$$M_{\rm ADM} = \sqrt{m^2 - a^2} + M_1, \tag{6.81}$$

where

$$M_1 = -2\int_{r_{\rm s}}^{\infty} dr \int_0^{\pi/2} d\theta (r^2 - r_{\rm s}^2)\sin\theta S_\phi, \tag{6.82}$$

and m is the Kerr mass. Defining the mass of the black hole is less straightforward. The central black hole is surrounded by a minimal two-surface located at $r = r_{\rm s}$ in the puncture method, on a fixed hypersurface of constant time. There is a collection of quantities that can be used to characterize the geometry of the horizon $r = r_{\rm s}$. The area of the horizon is given by

$$A_{\rm H} = 4\pi \int_0^{\pi/2} \psi^4 e^q r^2 \sin\theta d\theta, \tag{6.83}$$

where the integral is evaluated at $r = r_{\rm s}$. One can also define (at $r = r_{\rm s}$) $\Omega_{\rm H} = -\beta = -\beta_{\rm K} = \text{const}$, and the surface gravity $\kappa = \partial_r \alpha \psi^{-2} e^{-q} = \text{const}$. It can be easily shown that $\kappa = Be^{-4\phi-q}/8r_{\rm s}$. The angular momentum of the

black hole can be defined as (see below)

$$J_{\rm H} = \frac{1}{4}\int_0^{\pi/2} d\theta \left(\frac{r^4 \sin^3\theta \psi^6 \partial_r \beta}{\alpha}\right)_{r=r_{\rm s}}. \tag{6.84}$$

A mass defined at $r = r_{\rm s}$ as

$$M_{\rm H} = \int_0^{\pi/2} \psi^2 r^2 \partial_r \alpha \sin\theta d\theta + 2\Omega_{\rm H} J_{\rm H}, \tag{6.85}$$

obeys the Smarr formula

$$M_{\rm H} = \frac{\kappa}{4\pi} A_{\rm H} + 2\Omega_{\rm H} J_{\rm H}. \tag{6.86}$$

The mass of the black hole used in this paper is defined differently. Following Shibata 2007 we adopt Christodoulou's formula Christodoulou 1970. We define first the so-called irreducible mass

$$M_{\rm irr} = \sqrt{\frac{A_{\rm H}}{16\pi}}. \tag{6.87}$$

Then the mass of the black hole is defined as

$$M_{\rm BH} = M_{\rm irr}\sqrt{1 + \frac{J_{\rm H}^2}{4M_{\rm irr}^4}}. \tag{6.88}$$

From the ADM mass and the black hole mass we can define the torus mass as $M_{\rm T} = M_{\rm ADM} - M_{\rm BH}$, as was done in Karkowski et al. 2018a, Karkowski et al. 2018b. There is, however, another possibility for the mass measure of the torus:

$$M_{\rm T} = 8\pi \int_{r_{\rm s}}^{\infty} dr \int_0^{\pi/2} d\theta r^2 \sin\theta \alpha \psi^6 e^{2q} \left(-T^t_{\ t} + \frac{1}{2} T^{\mu}_{\ \mu}\right). \tag{6.89}$$

It satisfies the relation

$$M_{\rm H} + M_{\rm T} = \sqrt{m^2 - a^2} + M_1 = M_{\rm ADM}. \tag{6.90}$$

We use this relation as a test of the accuracy of our numerical solutions. A direct computation yields

$$-T^t_{\ t} + \frac{1}{2} T^{\mu}_{\ \mu} = -\rho h u^t u_t - \frac{1}{2}\rho h + p + \frac{1}{2} b^2. \tag{6.91}$$

In the numerical code, we compute the above quantity as

$$-T^t_{\ t} + \frac{1}{2}T^\mu_{\ \mu} = -\frac{1}{2}\rho h + 2p + \rho_{\rm H} - \beta\rho h u^t u_\varphi. \tag{6.92}$$

Correspondingly, the angular momentum of the torus is defined as

$$\begin{aligned} J_1 &= \int \sqrt{-g} T^t_{\ \varphi}\, d^3x \\ &= 4\pi \int_{r_{\rm s}}^{\infty} dr \int_0^{\pi/2} d\theta r^2 \sin\theta \alpha \psi^6 e^{2q} \rho h u^t u_\varphi. \end{aligned} \tag{6.93}$$

This is a standard definition corresponding to the Killing vector $\eta^\mu = (0,0,0,1)$, and the conservation law $\eta^\nu \nabla_\mu T^\mu_{\ \nu} = \nabla_\mu (T^\mu_{\ \nu}\, \eta^\nu) = 0$ Bardeen 1973. Note that $T^t_{\ \varphi} = (\rho h + b^2) u^t u_\varphi - b^t b_\varphi = \rho h u^t u_\varphi$, i.e., the contributions from the magnetic terms cancel. The total, asymptotic angular momentum reads $J = J_{\rm H} + J_1$.

The value of the angular momentum $J_{\rm H}$ depends on the assumed boundary conditions for $\beta_{\rm T}$. In our case $\beta_{\rm T} = \partial_r \beta_{\rm T} = \partial_{rr} \beta_{\rm T} = \partial_{rrr} \beta_{\rm T} = 0$ at $r = r_{\rm s}$, and consequently $J_{\rm H} = am$.

The mass M_1 and the angular momentum J_1 are related to the asymptotic behaviour of the metric functions ϕ and $\beta_{\rm T}$, namely,

$$\phi \sim \frac{M_1}{2r}, \quad \beta_{\rm T} \sim -\frac{2J_1}{r^3}, \tag{6.94}$$

as $r \to \infty$. The asymptotic behaviour of the two remaining functions B and q is given by

$$B \sim 1 - \frac{B_1}{r^2}, \quad q \sim \frac{q_1 \sin^2\theta}{r^2}, \tag{6.95}$$

where

$$B_1 = \frac{2}{\pi} \int_{r_{\rm s}}^{\infty} dr \frac{(r^2 - r_{\rm s}^2)^2}{r} \int_0^{\pi/2} d\theta \sin^2\theta S_B, \tag{6.96}$$

and

$$\begin{aligned} q_1 &= \frac{2}{\pi} \int_{r_2}^{\infty} dr r^3 \int_0^{\pi/2} d\theta \cos(2\theta) S_q \\ &\quad - \frac{4r_{\rm s}^2}{\pi} \int_0^{\pi/2} d\theta \cos(2\theta) q(r_{\rm s}, \theta). \end{aligned} \tag{6.97}$$

We use the above asymptotic expansions to set the boundary conditions at the outer boundary of the numerical grid, i.e., at $r = r_\infty$.

Table 6.1 Parameters of the numerical solutions. In all cases we assumed the polytropic exponent $\gamma = 4/3$, the magnetisation law parameter $n = 1$, and the black hole mass parameter $m = 1$. From left to right the columns report: the black hole spin parameter a, the coordinate inner radius of the disk r_1, the circumferential inner radius of the disk $r_{\mathrm{C},1}$, the coordinate outer radius of the disk r_2, the circumferential outer radius of the disk $r_{\mathrm{C},2}$, the maximum rest-mass density within the disk $\rho_{\max}$, the parameter C_1 appearing in the magnetisation law, the total ADM mass m_{ADM}, the mass of the black hole m_{BH}, the angular momentum of the disk J_1, and the magnetisation parameter β_{mag}.

No.	a	r_1	$r_{\mathrm{C},1}$	r_2	$r_{\mathrm{C},2}$	$\rho_{\max}$	C_1	m_{ADM}	m_{BH}	J_1	β_{mag}
1a	-0.5	8.0	9.2	35.3	36.7	5×10^{-5}	0	1.33	1.01	1.7	∞
1b	-0.5	8.0	9.2	35.3	36.7	5×10^{-5}	0.01	1.34	1.01	1.75	30.5
1c	-0.5	8.0	9.3	35.3	36.8	5×10^{-5}	0.1	1.40	1.01	2.08	3.49
1d	-0.5	8.0	9.4	35.3	36.9	5×10^{-5}	1	1.51	1.02	2.65	0.21
1e	-0.5	8.0	9.4	35.3	36.9	5×10^{-5}	1.3	1.50	1.02	2.58	5.3×10^{-2}
1f	-0.5	8.0	9.3	35.3	36.9	5×10^{-5}	1.42	1.49	1.02	2.54	1.3×10^{-3}
2a	0	8.1	9.3	35.1	36.5	5×10^{-5}	0	1.33	1.02	1.64	∞
2b	0	8.1	9.3	35.1	36.5	5×10^{-5}	0.01	1.34	1.02	1.69	29.4
2c	0	8.1	9.3	35.1	36.5	5×10^{-5}	0.1	1.40	1.02	2.02	3.37
2d	0	8.1	9.4	35.1	36.7	5×10^{-5}	1	1.52	1.03	2.61	0.19
2e	0	8.1	9.4	35.1	36.7	5×10^{-5}	1.3	1.51	1.03	2.55	3.0×10^{-2}
2f	0	8.1	9.4	35.1	36.7	5×10^{-5}	1.37	1.50	1.03	2.52	5.8×10^{-4}
3a	0.9	3.0	4.4	20.0	21.7	3.5×10^{-4}	0	1.52	1.00	2.04	∞
3b	0.9	3.0	4.4	20.0	21.7	3.5×10^{-4}	0.01	1.52	1.00	2.05	75.8
3c	0.9	3.0	4.4	20.0	21.7	3.5×10^{-4}	0.1	1.55	1.00	2.17	8.38
3d	0.9	3.0	4.4	20.0	21.7	3.5×10^{-4}	1	1.57	1.01	2.23	0.96
3e	0.9	3.0	4.4	20.0	21.6	3.5×10^{-4}	2	1.47	1.00	1.79	0.26
3f	0.9	3.0	4.4	20.0	21.5	3.5×10^{-4}	2.74	1.39	1.00	1.45	5.88×10^{-4}
4a	0.99	0.8	2.41	20.1	21.9	1.5×10^{-3}	0	1.70	1.00	2.31	∞
4b	0.99	0.8	2.41	20.1	21.9	1.5×10^{-3}	0.01	1.70	1.00	2.30	805.5
4c	0.99	0.8	2.40	20.1	21.9	1.5×10^{-3}	0.1	1.68	1.00	2.24	80.3
4d	0.99	0.8	2.38	20.1	21.7	1.5×10^{-3}	1	1.51	1.00	1.64	7.72
4e	0.99	0.8	2.35	20.1	21.5	1.5×10^{-3}	2	1.32	1.00	1.01	3.07
4f	0.99	0.8	2.33	20.1	21.3	1.5×10^{-3}	3	1.17	1.00	0.52	1.31
4g	0.99	0.8	2.32	20.1	21.3	1.5×10^{-3}	4	1.08	1.00	0.24	0.39
4h	0.99	0.8	2.32	20.1	21.2	1.5×10^{-3}	4.5	1.05	1.00	0.17	0.11
4i	0.99	0.8	2.32	20.1	21.2	1.5×10^{-3}	4.7	1.05	1.00	0.15	2.28×10^{-2}

6.4 Numerical method

To construct our models of self-gravitating, magnetised tori around rotating black holes we need to solve numerically the equations derived in Sec. 6.2. The metric functions are described by Eq. (6.63) and Eqs. (6.61) with the source terms given by Eqs. (6.62). The angular velocity Ω must satisfy Eq. (6.70) with $j(\Omega)$ given by Eq. (6.68). The distribution of the enthalpy h, rest-mass density, and the pressure p are obtained from Eq. (6.78) and from the polytropic relation (6.79). The quantity A^2 appearing in expressions (6.62) is defined by (6.45) where $K_{r\varphi}$ and $K_{\theta\varphi}$ should be computed according to formulas (6.35) and (6.36).

The numerical code used to obtain the solutions presented in this paper is a modification of the code described and tested in Karkowski et al. 2018b to which the interested reader is addressed for details. It is an iterative method, where in each Newton-Raphson iteration one solves Eq. (6.70) for the angular velocity Ω, Eq. (6.78) for the density ρ (or the specific enthalpy h), and then Eqs. (6.61) for the metric functions. The latter are solved with 2nd-order finite differences. We take advantage of the banded matrix structure of the resulting linear equations and use LAPACK Anderson et al. 1999. The changes introduced with respect to the version of the code described in Karkowski et al. 2018b are only related to the presence of the magnetic field. While the inclusion of the magnetic terms in Eqs. (6.61) is straightforward, solving Eq. (6.78) with the magnetic terms is more troublesome. To describe it we need to discuss details connected with the treatment of Eqs. (6.70) and (6.78).

Each iteration is started with a Newton-Raphson procedure that gives the values of constants w and C', assuming that the inner and outer equatorial radii of the disk (r_1 and r_2, respectively) are fixed. This procedure solves Eqs. (6.70) and (6.80) at points $(r, \theta) = (r_1, \pi/2), (r_2, \pi/2)$. These are four equations for the four unknowns w, C', $\Omega_1 = \Omega(r_1, \pi/2)$, $\Omega_2 = \Omega(r_2, \pi/2)$; in this step we assume that the metric functions are known from the previous iteration, or from the initial guess. In the next step we compute the values of Ω in a region which is large enough to contain the disk, but smaller than the domain covered by the numerical grid. In this way we can avoid problems with finding solutions to Eq. (6.70) in the vicinity of the symmetry axis $\theta = 0$. Equation (6.70) is also solved with a Newton-Raphson scheme. The next stage consists in solving Eq. (6.78) for the specific enthalpy h, also by a Newton-Raphson procedure. The problem that one encounters here (which is absent in the purely hydrodynamical case) is that Eq. (6.78) contains a density term ρ, and in order to obtain a

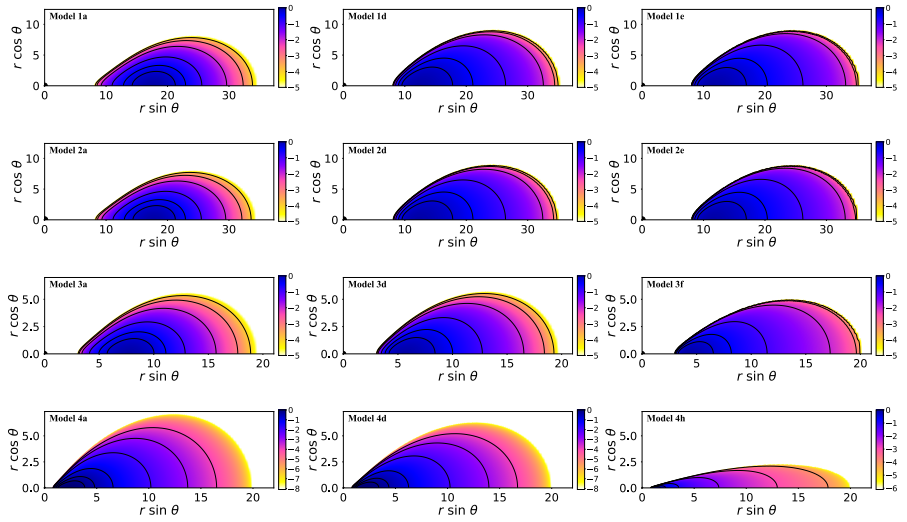

Figure 6.1 Morphology of the disks: distribution of the logarithm of the rest-mass density for selected models of our sample (see Table 6.1). The effects of the magnetisation increase from left to right; the leftmost column depicts disks with no magnetic field.

solution for h one has to specify the value of the polytropic constant K. On the other hand, in Karkowski et al. 2018b we found that the possibility of obtaining a convergent solution increases considerably if the solution is parameterized by a maximum value of the rest-mass density $\rho_{\max}$ within the disk. In the purely hydrodynamical case the value of the polytropic constant is then adjusted at each iteration so that the maximum value of the specific enthalpy h obtained from Eq. (6.78) (with no magnetic terms) corresponds to the maximum of ρ equal to an a priori prescribed value $\rho_{\max}$. This approach is not straightforward in the present GRMHD case. Therefore, we instead take the value of the polytropic constant K inherited from the previous iteration, solve Eq. (6.78) for h, and then assume a value of K so that the maximum in the specific enthalpy h corresponds to the maximum in ρ equal to $\rho_{\max}$. This approach leads to convergent solutions.

All stationary solutions of self-gravitating, magnetised disks obtained in this work have been computed on a numerical grid with approximately 800 nodes in the radial direction and 200 nodes in the angular direction. Specifically, the nodes in the grid are distributed according to

$$r_i = r_{\rm s} + \frac{f^{i-1} - 1}{f - 1}\Delta r, \quad i = 1, \ldots, N_r, \tag{6.98}$$

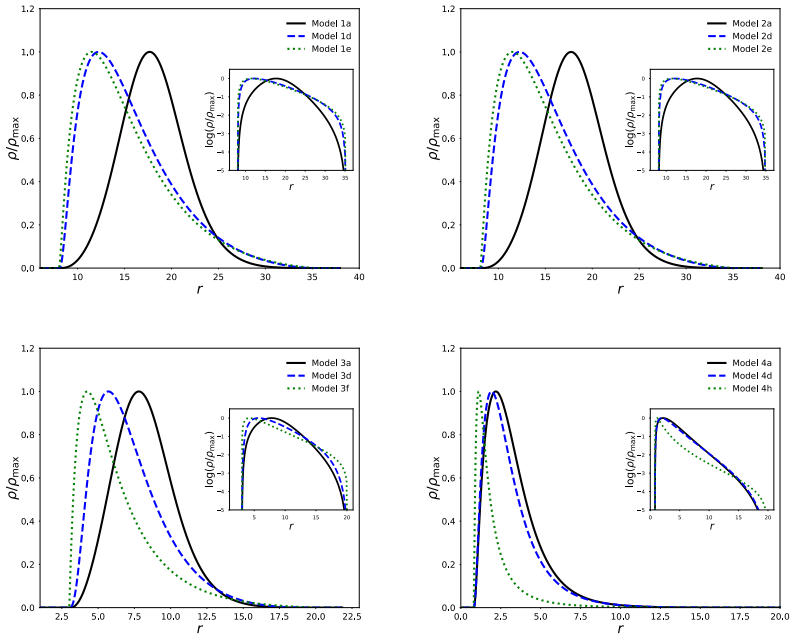

Figure 6.2 Radial profiles of the rest-mass density at the equatorial plane for the same subset of models plotted in Fig. 6.1. The insets show the same profiles in the logarithmic scale, to better account for the low-density regions.

in the radial direction, and

$$\theta_j = \begin{cases} 0, & j = 1, \\ \arccos\left[1 + \left(\frac{3}{2} - j\right)\Delta\mu\right], & j = 2, N_\theta - 1, \\ \frac{\pi}{2}, & j = N_\theta, \end{cases} \tag{6.99}$$

where $\Delta\mu = 1/(N_\theta - 2)$, in the angular direction. We choose, in particular, $\Delta r = r_\mathrm{s}/50$, $f = 1.01$, $N_r = 800$, $N_\theta = 200$. The above grid specification is similar to the one used in Shibata 2007.

The number of iterations required to obtain a solution depends mainly on the resolution of the grid, but also on the parameters of the solution Karkowski et al. 2018b. Obtaining the solutions collected in Table 6.1 required typically $\sim 10^4$ to $\sim 2 \times 10^4$ interations. Highly magnetised disks denoted in Table 6.1 as 4e–4i are exceptional, and required up to $\sim 10^5$ iterations.

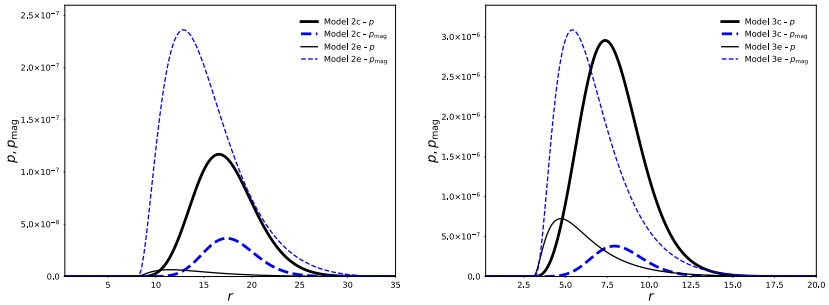

Figure 6.3 Comparison of the thermal pressure p (solid black lines) and the magnetic pressure $p_{\rm mag} = \frac{1}{2}b^2$ (dashed blue lines) at the equatorial plane.

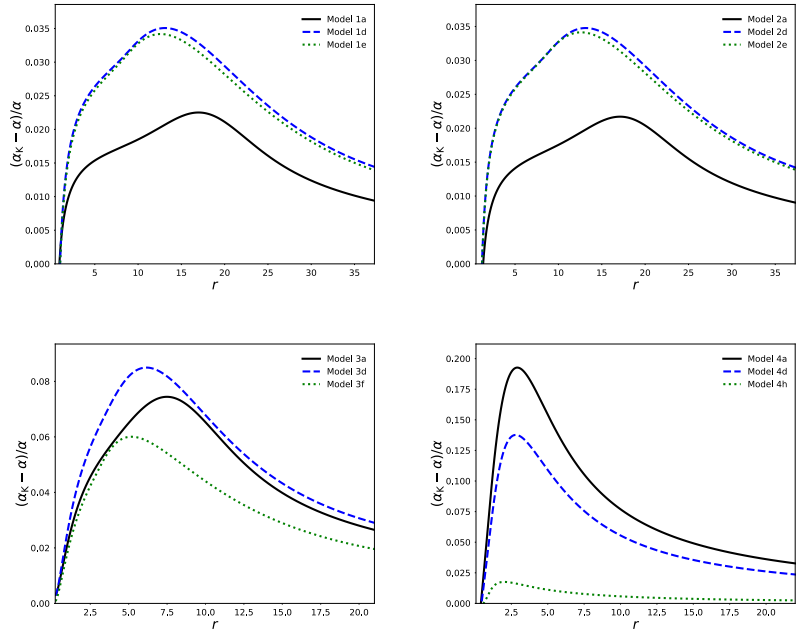

Figure 6.4 Radial profiles of the deviation of the lapse function α with respect to its value for an isolated Kerr black hole with mass $m_{\rm ADM}$ and spin a. The models displayed are the same subset of models plotted in Fig. 6.1.

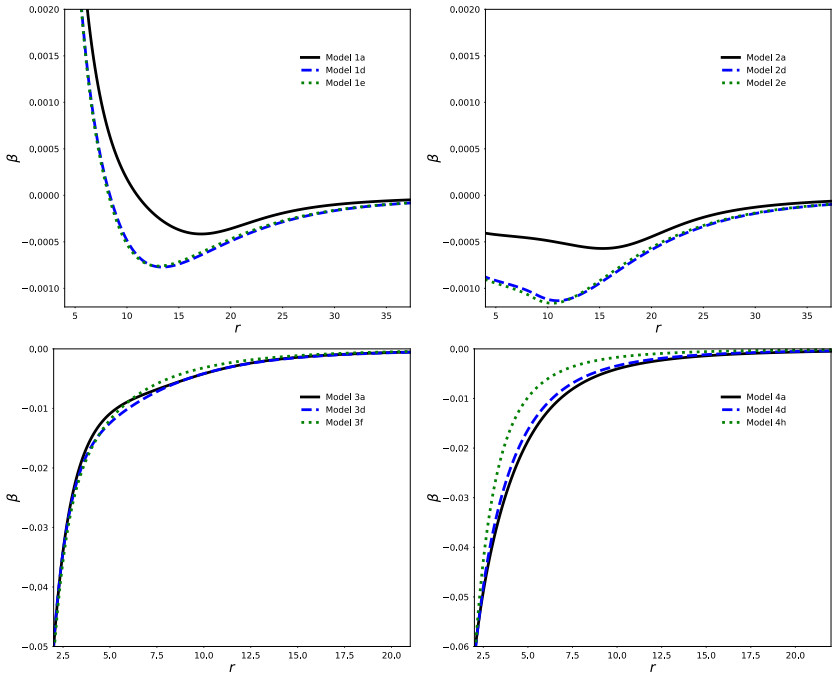

Figure 6.5 Radial profiles of the shift vector component β at the equatorial plane. The models displayed are the same subset of models plotted in Fig. 6.1.

6.5 Results

The numerical solutions are specified by the following set of parameters: the black hole mass and angular momentum parameters, m and a, the inner and outer radii of the disk r_1, r_2, the polytropic exponent of the equation of state γ, the maximum rest-mass density within the disk $\rho_{\max}$, and the constants C_1 and n that characterize the prescription of the magnetic field. We note that this parameterization does not specify solutions uniquely. In fact, even in the case with no magnetic field one can observe a bifurcation: two solutions corresponding to different asymptotic masses can be obtained for fixed m, a, r_1, r_2, γ, and $\rho_{\max}$. Usually, one of these solutions corresponds to a case with the mass of the torus much larger than the mass of the central black hole *private communication.* This effect is interesting per se, and it will be the subject of a separate study.

The values r_1 and r_2 refer to coordinate radii of the torus. The simplest way of obtaining a geometrical size measure would be to use the circumferential radius $r_{\rm C}$ related to r at the equatorial plane by the coordinate transformation $r_{\rm C} = \psi^2 r$. In the following, by $r_{\rm C,1}$ and $r_{\rm C,2}$ we will denote the circumferential radii corresponding to coordinate radii r_1 and r_2, respectively. It should be kept in mind that in the strong gravitational-field regime the relation between r and $r_{\rm C}$ may be not monotonic. In fact, numerical solutions representing self-gravitating tori with a maximum of $r_{\rm C}$ occurring within the torus, and not at its outer edge, were computed in Labranche, Petroff, and Ansorg 2007.

We measure the impact of the magnetic field by computing a magnetisation parameter $\beta_{\rm mag}$ defined as

$$\beta_{\rm mag} = \frac{p}{p_{\rm mag}} = \frac{2p}{b^2}, \tag{6.100}$$

and evaluated at the maximum of the thermal pressure p.

We have computed a sample of numerical solutions. Their parameters are reported in Table 6.1. This table also provides the values of a handful of quantities that can be used to characterize the solutions: the total ADM mass $m_{\rm ADM}$, the mass of the black hole $m_{\rm BH}$, the angular momentum of the torus J_1, the circumferential inner and outer radii of the torus $r_{\rm C,1}$, $r_{\rm C,2}$, and the magnetisation parameter $\beta_{\rm mag}$. In all our numerical examples we set $m = 1$. This can be viewed as fixing the system of units; in practice, setting $m = 1$ yields $m_{\rm BH} \approx 1$. Table 6.1 is divided into parts which group models with the same values of a, r_1, r_2, $\rho_{\max}$ but different values of C_1. In particular, each group corresponds to a different value of a; we chose specifically $a = -0.5$, 0, 0.9, and 0.99. A negative value of a means counterrotation, i.e. we adhere to a

convention with $\Omega > 0$. For simplicity, we fix in all our solutions the value of the polytropic exponent to $\gamma = 4/3$ and the parameter n of the magnetisation law to $n = 1$. Except for the models with the fastest spinning black hole ($a = 0.99$), in all investigated cases we were able to obtain solutions with the magnetisation parameter $\beta_{\rm mag}$ ranging from ∞ (no magnetic field) to the level of the order of 10^{-3} to 10^{-4} (i.e. highly magnetised models). The case with ($a = 0.99$) listed in Table 6.1 is exceptional: the tori characterized by small values of $\beta_{\rm mag}$ are fairly light. Moreover, a large number of numerical iterations ($\sim 10^5$) is required in order to converge to a solution.

It is not unreasonable to assume that stable solutions should have r_1 larger than the location of the Innermost Stable Circular Orbit (ISCO). Because of the self-gravity of the torus, the location of the ISCO deviates from the value characteristic for the Kerr spacetime with a given mass m and spin parameter a. Nevertheless, the Kerr values can be still used to get a rough estimate of the location of the ISCO. For $m = 1$ and $a = -0.5$, the circumferential radius of the ISCO in the Kerr spacetime is $r_{\rm C,ISCO} = 7.57$. For $m = 1$ and $a = 0, 0.9$ and 0.99, we obtain, respectively, $r_{\rm C,ISCO} = 6, 2.63$, and 2.11. Of course, given a numerical solution, the true location of the ISCO can also be computed, for instance using the formalism described in Shibata and Sasaki 1998. We have actually checked that the solutions listed in Table 6.1 satisfy the condition $r_{\rm C,1} > r_{\rm C,ISCO}$. A detailed analysis of the influence of the self-gravitating torus on the location of the ISCO will be given elsewhere.

From the inspection of all solutions listed in Table 6.1 we conclude that the configurations with smaller values of $\beta_{\rm mag}$ (relatively stronger magnetic fields) tend to have the maxima of the density shifted towards smaller radii. This behavior is illustrated in Fig. 6.1, which depicts the morphology of a subset of models by plotting the logarithm of their rest-mass density ρ in the meridional half-plane. Figure 6.2, in which we plot radial profiles of the density at the equatorial plane, shows this trend in a more clear way. For clarity, Fig. 6.2 displays the profiles both in linear and logarithmic scales (the latter in the insets). We note that the shift of the maximum of the density towards smaller radii in magnetised disks has already been observed in the test-fluid models built in Gimeno-Soler and Font 2017.

On the other hand, the analysis of the solutions with different values of the constant C_1 appearing in Eq. (6.78) shows that the larger C_1 the smaller the thermal pressure p, even in cases in which the maximum of the baryonic density ρ is fixed. In general we also observe an increase of the absolute values of the magnetic pressure $p_{\rm mag} = \frac{1}{2}b^2$. Both factors lead to a rapid decrease of the

magnetisation parameter $\beta_{\rm mag}$. In some sense, with an increase of C_1, the role of the (gradient of the) thermal pressure in counter-balancing gravity is taken over by the magnetic pressure. This effect is illustrated in Fig. 6.3 for models 2c, 2e, 3c and 3e. Note that in both cases the maximum of the largest of the two pressures (thermal or magnetic) is about two orders of magnitude smaller than the maximum of the rest-mass density.

The presence of a magnetic field affects the total ADM mass of the system (mainly by influencing the mass of the torus) in a nontrivial way. Although a direct contribution of the terms related with the magnetic field to the mass, as computed e.g. from Eq. (6.89), is small, the magnetic field changes the total mass of the system by affecting the distribution of the rest-mass density within the disk. The nature of the changes of the ADM mass with an increasing magnetic field contribution depends on the spin of the black hole and on the distance between the black hole and the torus (mainly on the location of the inner edge of the torus r_1). Disentangling these two factors is difficult, since the location of the ISCO depends predominantly on the spin of the black hole, and we want our models to satisfy the condition $r_{\rm C,ISCO} < r_{\rm C,1}$. The dependence of the ADM mass with the black hole spin in the examples collected in Table 6.1 is as follows: for $a = -0.5$ the ADM mass grows with increasing C_1, for $a = 0$ and $a = 0.9$ the behaviour of the ADM mass is not monotonic with C_1, and for $a = 0.99$ the ADM mass decreases with increasing C_1. In the latter case this effect is strong. The ADM mass drops from $m_{\rm ADM} = 1.70$ for $C_1 = 0$ (no magnetic field) to $m_{\rm ADM} = 1.05$ for $C_1 = 4.7$ (magnetisation parameter $\beta_{\rm mag} = 2.28 \times 10^{-2}$).

The importance of the effects of the disk self-gravity can be estimated by plotting the deviation of the lapse function at the equatorial plane with respect to its value for an isolated Kerr black hole, $(\alpha_{\rm K} - \alpha)/\alpha$ (here $\alpha_{\rm K}$ is computed using Eq. (6.107)). These radial profiles are plotted in Fig. 6.4 for the same subset of models depicted in Fig. 6.1. We observe a correlation of the maximum deviations with the rest-mass density $\rho_{\rm max}$ of the models, the deviations being larger the larger the value of $\rho_{\rm max}$, namely 20% for model 4a, 8.5% for model 3d and 3.5% for models 1d and 2d. Furthermore, it can be seen that, as expected, the deviation grows if the fraction of the mass stored at the torus is greater. This fraction can be easily inferred from Table 6.1.

A close inspection of plots in Figs. 6.2 and 6.4 reveals a somewhat unexpected similarity of certain features of models 1a–1f and 2a–2f. These two families of models are characterized by the same values of coordinate radii r_1 and r_2, and the same maximal densities $\rho_{\rm max}$, but they differ in the assumed values of the black hole spin parameter ($a = -0.5$ and $a = 0$, respectively). The

plots of the rest-mass density shown in Fig. 6.2 and corresponding to models belonging to both families are nearly indistinguishable from one another. One can also hardly spot any difference between models 1a–1f and 2a–2f in the plots of the differences between the lapse functions (the actual lapse and the lapse corresponding to the Kerr metric) shown in Fig. 6.4. However, both classes of models are actually different. The differences stand out clearly in the plots of the shift vector β shown in Fig. 6.5. Of course, the absolute values of the lapse function characterizing the models belonging to both classes are also different.

6.6 Summary

We have presented general-relativistic models of stationary, axisymmetric, self-gravitating, magnetised disks (or tori) rotating around spinning black holes. They have been obtained by solving numerically the coupled system of the Einstein equations and the equations of ideal GRMHD. The mathematical formulation of our approach has closely followed the work of Shibata Shibata 2007, who built purely hydrodynamical self-gravitating, constant angular momentum tori around black holes in the puncture framework. The inclusion of magnetic fields represents the first new ingredient of our approach. On the other hand, building on previous studies of configurations with no magnetic field Karkowski et al. 2018a, Karkowski et al. 2018b, Kulczycki, Mach, and Malec 2019, we have constructed our magnetised models assuming a Keplerian rotation law in the disks, which departs from the constant angular momentum disks reported by Shibata 2007. The use of the Keplerian rotation law is the second new ingredient of our procedure. We have focused on toroidal distributions of the magnetic field and presented a large set of models corresponding to a wide range of values of the magnetisation parameter, starting with weakly magnetised disks and ending at configurations in which the magnetic pressure dominates over the thermal one.

The impact of the magnetic field on the disk structure is mainly related to the magnetic pressure. In all investigated models, we have observed a shift of the location of the maximum of the rest-mass density towards the central black hole. The impact of the magnetisation on the total mass of the system (or the mass of the disk) depends on the black hole spin and on the geometry of the disk. It is possible to obtain classes of solutions in which the mass of the torus decreases with the decreasing magnetisation parameter, but the converse can also be true.

All our solutions have been obtained for the polytropic equation of state with the polytropic exponent $\gamma = 4/3$, and for a specific choice of the magnetisation law. These choices can, of course, have an impact on the obtained results. Furthermore, the values of the ratio of the black-hole mass to the total mass of the system reported in this paper were kept within a reasonable range: the obtained disks are massive enough so that the effects connected with the self-gravity become important. On the other hand, in this work we have not considered disks with masses exceeding the mass of the central black hole. It is known that allowing for sufficiently large disk masses can lead to the occurrence of several general-relativistic effects, characteristic of the strong gravitational-field regime. In Ansorg and Petroff 2006 Ansorg and Petroff showed that a perfect fluid torus rotating (rigidly) around a black hole can create its own ergoregion, disconnected from the ergoregion of the black hole. (This effect is also present in more exotic objects, for instance the scalar hairy black holes described in Herdeiro and Radu 2015a, for which the scalar field has a toroidal distribution.) In Labranche, Petroff, and Ansorg 2007 Labranche, Petroff, and Ansorg gave examples of perfect fluid tori (with no central object) in which the circumferential radius attains its maximum inside the torus, and not at its outer edge. We expect these effects to be present also within our formulation.

The results presented in this paper can be extended in several directions. On the one hand we plan to investigate the influence of the self-gravity of the torus on the location of the ISCO of a rotating black hole. In addition, we will also study the non-linear stability properties of our solutions through numerical-relativity simulations in a dynamical spacetime setup. There are a number of instabilities that may affect the disks, such as the runaway, the Papaloizou-Pringle and the magneto-rotational instabilities. In particular, the development of the PPI in tori threaded by toroidal magnetic fields may be significantly affected by the concurrent development of the MRI, as shown recently by Bugli et al. 2018 for non-self-gravitating disks. The self-gravitating, magnetised tori we have built in this work can be used to investigate the generality of those findings beyond the test-fluid limit.

The presented solutions, and models of self-gravitating magnetised disks in general, should be also relevant to the ongoing attempts to estimate the amount of angular momentum within a given volume. This is an interesting area of research within mathematical relativity Dain and Gabach-Clement 2018, Khuri and Xie 2017. Recent works focusing on such estimates for stationary Keplerian self-gravitating disks around black holes include Kulczycki, Mach, and Malec 2019, Karkowski et al. 2016.

6.7 Appendix: Kerr metric in quasi-isotropic coordinates

For completeness, we express the Kerr metric in the quasi-isotropic coordinates of the form (6.28) Shibata 2007, Brandt and Seidel 1995.

Define

$$r_{\rm K} = r\left(1+\frac{m}{r}+\frac{m^2-a^2}{4r^2}\right), \tag{6.101}$$

$$\Delta_{\rm K} = r_{\rm K}^2 - 2r_{\rm K} + a^2, \tag{6.102}$$

$$\Sigma_{\rm K} = r_{\rm K}^2 + a^2\cos^2\theta. \tag{6.103}$$

The Kerr metric can be expressed as

$$g = -\alpha_{\rm K}^2 dt^2 + \psi^4 e^{2q_{\rm K}}(dr_{\rm K}^2 + r_{\rm K}^2 d\theta^2) + \psi_{\rm K}^4 r_{\rm K}^2 \sin^2\theta(\beta_{\rm K}dt + d\varphi)^2, \tag{6.104}$$

where

$$\psi_{\rm K} = \frac{1}{\sqrt{r}}\left(r_{\rm K}^2 + a^2 + 2ma^2\frac{r_{\rm K}\sin^2\theta}{\Sigma_{\rm K}}\right)^{1/4}, \tag{6.105}$$

$$\beta_{\rm K} = -\frac{2mar_{\rm K}}{(r_{\rm K}^2+a^2)\Sigma_{\rm K} + 2ma^2 r_{\rm K}\sin^2\theta}, \tag{6.106}$$

$$\alpha_{\rm K} = \left[\frac{\Sigma_{\rm K}\Delta_{\rm K}}{(r_{\rm K}^2+a^2)\Sigma_{\rm K} + 2ma^2 r_{\rm K}}\sin^2\theta\right]^{1/2}, \tag{6.107}$$

$$e^{q_{\rm K}} = \frac{\Sigma_{\rm K}}{\sqrt{(r_{\rm K}^2+a^2)\Sigma_{\rm K} + 2ma^2 r_{\rm K}\sin^2\theta}}. \tag{6.108}$$

The functions $H_{\rm E}$ and $H_{\rm F}$ corresponding to the Kerr metric read

$$H_{\rm E} = \frac{ma\left[(r_{\rm K}^2-a^2)\Sigma_{\rm K} + 2r_{\rm K}^2(r_{\rm K}^2+a^2)\right]}{\Sigma_{\rm K}^2}, \tag{6.109}$$

$$H_{\rm F} = -\frac{2ma^3 r_{\rm K}\sqrt{\Delta_{\rm K}}\cos\theta\sin^2\theta}{\Sigma_{\rm K}^2}. \tag{6.110}$$

Chapter 7

Stationary models of magnetized viscous tori around a Schwarzschild black hole

This chapter is based on the following publication: S. Lahiri, S. Gimeno-Soler, J. A. Font & A. Mus Mejías. Stationary models of magnetized viscous tori around a Schwarzschild black hole, *Physical Review D* 103, 0044034 (2021), DOI: 10.1103/PhysRevD.103.0044034.

7.1 Introduction

One of the outstanding predictions of general relativity is the existence of black holes. By their very nature, black holes can only be observed by the gravitational effects they produce in their environment. An accretion disk embedded in the geometry of a black hole provides a natural framework for its indirect detection through the study of the gravitational influence it exerts on the disk. As a result of the black hole's gravity, the mass of an orbiting disk is pulled inwards resulting into an inward flow of its matter and the outward transport of angular momentum, a process accompanied by the conversion of gravitational energy into radiation and heat. This is one of the most efficient processes of energy release

in the cosmos and it operates in systems as diverse as proto-planetary disks, X-ray binaries, gamma-ray bursts, active galactic nuclei, and quasars [Frank, King, and Raine 2002].

Models of accretion disks around black holes are abundant in the scientific literature (see [Abramowicz and Fragile 2013] and references therein). Among the various proposals, geometrically thick disks or tori (also referred to as "Polish doughnuts") are the simplest, relativistic, stationary configurations describing an ideal fluid orbiting around a rotating black hole under the assumption that the specific angular momentum of the disk is constant [Fishbone and Moncrief 1976, Abramowicz, Jaroszynski, and Sikora 1978, Kozlowski, Jaroszynski, and Abramowicz 1978]. Extensions of the original model to incorporate additional effects such as non-constant distributions of angular momentum, magnetic fields, or self-gravity, have also been put forward [Font and Daigne 2002, Daigne and Font 2004, Ansorg and Petroff 2005, Komissarov 2006, Montero et al. 2007, Shibata 2007, Qian et al. 2009, Stergioulas 2011b, Gimeno-Soler and Font 2017, Pimentel, Lora-Clavijo, and Gonzalez 2018, Mach et al. 2019].

In all stationary models the accretion torus is assumed to be composed of an ideal fluid and the effects of dissipation are neglected. However, the contribution of dissipative fluxes might not exactly vanish in an accretion disk, especially if it undergoes differential rotation, thus giving rise to shear viscous effects. It is well known that viscosity and magnetic fields play a key role in accretion disks to account for angular momentum transport, in particular through the magneto-rotational instability [Balbus and Hawley 1991]. In this paper we discuss stationary models of magnetized viscous tori, assuming a toroidal distribution of the field and the presence of shear stresses.

The conservation laws of relativistic hydrodynamics of a non-ideal fluid involving dissipative effects like viscosity, developed by Landau-Lifschitz and Eckart, do not give rise to hyperbolic equations of motion [Romatschke 2010]. Moreover, the corresponding equilibrium states are unstable under linear perturbations [Hiscock and Lindblom 1985]. The pathological nature of the conservation laws is attributed to the existence of first-order gradients of hydrodynamical variables in the dissipative flux quantities. This limitation can be circumvented by including second-order gradients, a formalism first developed by Müller [Muller 1967] in the non-relativistic setup and later extended by Israel and Stewart [Israel 1976] for relativistic non-ideal fluids. The resulting conservation laws are hyperbolic and stable [Rezzolla and Zanotti 2013].

Assuming that the shear viscosity is small and instils perturbative effects in the disk fluid, stationary solutions of constant angular momentum *unmagnetized*

tori in the Schwarszchild geometry were first presented in Lahiri and Lämmerzahl [2019]. This work showed that stationary models of viscous thick disks can only be constructed in the context of general relativistic causal approach by using the gradient expansion scheme [Lahiri 2020]. The imprints of the shear viscosity and of the curvature of the Schwarzschild geometry are clearly present on the isopressure surfaces of the tori. In particular, the location of the cusps of such surfaces is different from those predicted with an ideal fluid model [Font and Daigne 2002]. In the present paper the purely hydrodynamical solutions presented in Lahiri and Lämmerzahl [2019] are extended by incorporating toroidal magnetic fields in the stationary solutions of the tori. Our new solutions are built using the second-order gradient expansion scheme in the Eckart frame description [Lahiri 2020], which keeps the same spirit of the Israel-Stewart formalism and gives rise to hyperbolic equations of motion, hence preserving causality. Furthermore, we also adopt the test-fluid approximation, neglecting the self-gravity of the disk. As we show below, in our formalism the general form of the shear viscosity tensor contains additional curvature terms (as one of many second-order gradients) and, as a result, the curvature of the Schwarzschild geometry directly influences the isopressure surfaces, as in the hydrodynamical case considered in Lahiri and Lämmerzahl [2019]. The presence and strength of a toroidal magnetic field brings forth some quantitatative differences with respect to the unmagnetized case, as we discuss below.

The paper is organised as follows: Section 7.2 presents the mathematical framework of our approach introducing, in particular, the perturbation equations that characterize the stationary solutions. Those solutions are built following the procedure described in Section 7.3. Our results are discussed in Section 7.4. Finally Section 7.5 summarizes our findings. Throughout the paper we use natural units where $c = G = 1$. Greek indices in mathematical quantities run from 0 to 4 and Latin indices are purely spatial.

7.2 Framework

7.2.1 Basic equations

Our framework assumes that the spacetime geometry is that of a Schwarzschild black hole of mass M and that the disk is not self-gravitating, it has a constant distribution of specific angular momentum, and that the magnetic field only has a toroidal component. We neglect possible effects of heat flow and bulk viscosity and we further assume that the shear viscosity is small enough so as to act as a

perturbation to the matter configuration. Therefore, the radial velocity of the flow vanishes and the fluid particles describe circular orbits.

The Schwarzchild spacetime is described by the metric

$$ds^2 = -\left(1 - \frac{2M}{r}\right) dt^2 + \left(1 - \frac{2M}{r}\right)^{-1} dr^2 + r^2 d\Omega^2 \,, \tag{7.1}$$

where $d\Omega^2 = d\theta^2 + \sin^2\theta d\phi^2$. Since the fluid particles follow circular orbits their four-velocity u^μ, subject to the normalization condition $u^\alpha u_\alpha = -1$, is given by

$$u^\mu = (u^t, 0, 0, u^\phi) \,, \tag{7.2}$$

where $u^\mu \equiv u^\mu(r, \theta)$, with $\mu = t, \phi$. The specific angular momentum l and the angular velocity Ω are given by

$$l(r,\theta) = -\frac{u_\phi}{u_t}, \quad \Omega(r,\theta) = \frac{u^\phi}{u^t} \,, \tag{7.3}$$

so that the following relationship holds between both quantities

$$l(r,\theta) = -\frac{g_{\phi\phi}}{g_{tt}}\Omega(r,\theta) = \frac{r\sin\theta}{(1 - \frac{2M}{r})}\Omega(r,\theta) \,. \tag{7.4}$$

In our study we consider the Eckart frame for addressing viscous hydrodynamics which is a common choice of reference frame in relativistic astrophysics [Romatschke 2010]. The energy-momentum tensor of viscous matter in the presence of a magnetic field is given by

$$T^{\mu\nu} = (w + b^2)u^\mu u^\nu + \left(p + \frac{1}{2}b^2\right) g^{\mu\nu} - b^\mu b^\nu + \pi^{\mu\nu} \,. \tag{7.5}$$

In this expression, the enthalpy density is given by $w = e + p$, where p is the fluid pressure and e is the total energy, and $\pi^{\mu\nu}$ is the shear viscosity tensor. The dual of the Faraday tensor relative to an observer with four-velocity u^μ is [Anile 2005],

$${}^*F^{\mu\nu} = b^\mu u^\nu - b^\nu u^\mu \,, \tag{7.6}$$

where b^μ is the magnetic field in that frame, which obeys the relation $b^2 = b^\alpha b_\alpha$ and yields to the conservation law $\nabla_\nu {}^*F^{\mu\nu} = 0$, where ∇_ν is the covariant derivative. In the fluid frame $b^\mu = (0, \mathbf{B})$ where $\mathbf{B}$ denotes the three-vector of the magnetic field which satisfies the condition $u^\alpha b_\alpha = 0$. Since the magnetic

field distribution is purely toroidal, it follows that

$$b^r = b^\theta = 0, \qquad b^\mu = (b^t, 0, 0, b^\phi)\,. \tag{7.7}$$

From the condition $u^\alpha b_\alpha = 0$ we obtain

$$b^t = l b^\phi, \qquad b_t = -\Omega b_\phi\,, \tag{7.8}$$

and

$$b^2 = (1 - \Omega l) b^\phi b_\phi = 2 p_m\,, \tag{7.9}$$

where the magnetic pressure is defined as $p_m \equiv b^2/2$.

As mentioned before we consider a second-order theory of viscous hydrodynamics constructed using the gradient expansion scheme which ensures the causality of propagation speeds in the Eckart frame. In this scheme the shear viscosity tensor is expressed in terms of a causality-preserving term and additional curvature terms which will help investigate the influence of curvature contributions on our system. As a result, the general form of the shear viscosity tensor can be expressed as [Lahiri 2020],

$$\begin{aligned} \pi^{\mu\nu} &= -2\eta\sigma^{\mu\nu} - \tau_2^{<} D(-2\eta\sigma^{\mu\nu})^{>} + \kappa_1 R^{<\mu\nu>} \\ &\quad + \kappa_2 u_\alpha u_\beta R^{\alpha<\mu\nu>\beta}\,, \end{aligned} \tag{7.10}$$

with the definition $D \equiv u^\alpha \nabla_\alpha$. Here $R^{\alpha\beta\gamma\delta}$ and $R^{\alpha\beta}$ are the Riemann tensor and the Ricci tensor, respectively, η is the shear viscosity coefficient and τ_2, κ_1 and κ_2 are the second-order transport coefficients. Moreover, the angular brackets in the previous equation indicate traceless symmetric combinations. The remaining quantities appearing in Eq. (7.10) are defined as

$$\begin{aligned} \sigma^{\mu\nu} &= \triangle^{\mu\alpha}\triangle^{\nu\beta}\left(\frac{\nabla_\alpha u_\beta + \nabla_\beta u_\alpha}{2}\right) - \frac{1}{3}\triangle^{\mu\nu}\triangle^{\alpha\beta}\nabla_\alpha u_\beta\,, \\ {}^{<}D\sigma^{\mu\nu>} &= \triangle^{\mu\alpha}\triangle^{\nu\beta}\left(\frac{D\sigma_{\alpha\beta} + D\sigma_{\beta\alpha}}{2}\right) - \frac{1}{3}\triangle^{\mu\nu}\triangle^{\alpha\beta}D\sigma_{\alpha\beta}\,, \\ R^{<\mu\nu>} &= \triangle^{\mu\alpha}\triangle^{\nu\beta}\left(\frac{R_{\alpha\beta} + R_{\beta\alpha}}{2}\right) - \frac{1}{3}\triangle^{\mu\nu}\triangle^{\alpha\beta}R_{\alpha\beta}\,, \\ R^{\alpha<\mu\nu>\beta} &= \left[\triangle^{\mu\rho}\triangle^{\nu\sigma}\left(\frac{R^\alpha_{\rho\sigma\gamma} + R^\alpha_{\sigma\rho\gamma}}{2}\right) - \frac{1}{3}\triangle^{\mu\nu}\triangle^{\rho\sigma}R^\alpha_{\rho\sigma\gamma}\right] g^{\beta\gamma}\,, \end{aligned}$$

where the projection tensor is given by $\triangle^{\mu\nu} = g^{\mu\nu} + u^\mu u^\nu$. Using Eq. (7.5), the momentum conservation equation $\triangle_{\mu\nu}\nabla_\lambda T^{\lambda\nu} = 0$ can be written as

$$(e + p)a_\mu \quad + \quad \triangle^\rho_\mu \nabla_\rho\, p + \frac{\partial_\mu(\mathcal{L}b^2)}{2\mathcal{L}} + g_{\mu\rho}\pi^{\rho\nu}a_\nu$$

$$+ \quad \triangle_{\mu\gamma}\triangle_{\kappa\tau}\nabla^{\tau}\pi^{\gamma\kappa} = 0\,, \tag{7.11}$$

which is the general form of the momentum conservation equation in the presence of a magnetic field. The four-acceleration is given by $a^{\mu} = u^{\rho}\nabla_{\rho}u^{\mu} = Du^{\mu}$ and $\mathcal{L} \equiv -g_{tt}g_{\phi\phi}$.

7.2.2 Perturbation of the magnetized torus

Since we consider disks with constant specific angular momentum distributions we take $l(r) \equiv l_0$. We further assume that the internal energy density, ε, is very small and, therefore, the total energy is approximately equal to the rest-mass density i,e. $e = \rho(1+\varepsilon) \approx \rho$. For the Schwarzschild black hole, the term $R^{<\mu\nu>} = 0$ and therefore it does not contribute to the shear viscosity tensor. We also assume that the shear viscosity is small in the sense that the coefficients η and κ_2 can be considered as perturbations in the disk fluid. These two coefficients will be assumed to be constant and to act as perturbations with the perturbation parameter λ as follows,

$$\eta = \lambda m_1, \qquad\qquad \kappa_2 = \lambda m_2\,. \tag{7.12}$$

The shear viscosity perturbation in the disk fluid generates linear perturbations in the energy density, pressure, and magnetic field. Up to linear order, we can express each of these quantities as follows:

$$e(r,\theta) = e_{(0)}(r,\theta) + \lambda e_{(1)}(r,\theta)\,, \tag{7.13}$$

$$p(r,\theta) = p_{(0)}(r,\theta) + \lambda p_{(1)}(r,\theta)\,, \tag{7.14}$$

$$b^{t}(r,\theta) = b^{t}_{(0)}(r,\theta) + \lambda b^{t}_{(1)}(r,\theta)\,, \tag{7.15}$$

$$b^{\phi}(r,\theta) = b^{\phi}_{(0)}(r,\theta) + \lambda b^{\phi}_{(1)}(r,\theta)\,, \tag{7.16}$$

where, as usual, index (0) denotes background quantities and index (1) quantities at linear perturbation order. By using Eqs. (7.9) and (7.16) the magnetic pressure at both zeroth order and first order reads

$$p^{(0)}_{m} = \frac{1}{2}(1-\Omega l)\, b^{\phi}_{(0)} b^{(0)}_{(\phi)}\,, \tag{7.17}$$

$$p^{(1)}_{m} = \frac{1}{2}\left[b^{\phi}_{(0)}\left(l b^{(1)}_{t} + b^{(1)}_{\phi}\right) + b^{(0)}_{\phi}\left(b^{\phi}_{(1)} - \Omega b^{t}_{(1)}\right)\right]\,. \tag{7.18}$$

Defining the magnetization parameter as $\beta_m \equiv p/p_m$, the zeroth-order and first-order changes in this parameter can be written as follows

$$\beta^{(0)}_{m} = \frac{p_{(0)}}{p^{(0)}_{m}}\,, \tag{7.19}$$

and

$$\beta_m^{(1)} = \frac{p_{(1)}}{p_m^{(0)}} - \beta_m^{(0)} \frac{p_m^{(1)}}{p_m^{(0)}} \,. \tag{7.20}$$

From the momentum conservation equation (7.11) we see that there are four unknown quantities to be determined, namely, $p_{(1)}, e_{(1)}, b_t^{(1)}$ and $b_\phi^{(1)}$. However, the variables $p_{(1)}$ and $e_{(1)}$ are not independent under the assumption of a barotropic equation of state. Following Komissarov [2006] and Gimeno-Soler and Font [2017] we take the same polytropic index γ for the equations of state corresponding to both the fluid pressure p and the magnetic pressure p_m, given by,

$$p = Ke^\gamma, \tag{7.21}$$

and

$$p_m = K_m \mathcal{L}^{\gamma-1} e^\gamma. \tag{7.22}$$

Now, expanding up to linear order one can write the equations of state at zeroth order and first order as

$$p_{(0)} = Ke_{(0)}^\gamma, \qquad p_{(1)} = \gamma K e_{(0)}^{\gamma-1} e_{(1)} \,, \tag{7.23}$$

$$p_m^{(0)} = K_m \mathcal{L}^{\gamma-1} e_{(0)}^\gamma, \quad p_m^{(1)} = \gamma K_m \mathcal{L}^{\gamma-1} e_{(0)}^{\gamma-1} e_{(1)} \,. \tag{7.24}$$

From the above relations, we find that $p_{(0)}$, $p_{(1)}$, $p_m^{(0)}$ and $p_m^{(1)}$ are related by

$$p_{(1)} = p_{(0)} \frac{\gamma e_{(1)}}{e_{(0)}} \,, \tag{7.25}$$

$$p_m^{(1)} = p_m^{(0)} \frac{\gamma e_{(1)}}{e_{(0)}}. \tag{7.26}$$

Using the last two equations we obtain the following condition

$$\frac{p_{(1)}}{p_m^{(1)}} = \frac{p_{(0)}}{p_m^{(0)}} \,. \tag{7.27}$$

Substituting Eqs.(7.25) and (7.26) in Eq. (7.20) leads to

$$\begin{aligned} \beta_m^{(1)} &= \frac{\gamma p_{(0)} e_{(1)}}{e_{(0)} p_m^{(0)}} - \beta_m^{(0)} \frac{\gamma e_{(1)}}{e_{(0)}} \\ &= \beta_m^{(0)} \frac{\gamma e_{(1)}}{e_{(0)}} - \beta_m^{(0)} \frac{\gamma e_{(1)}}{e_{(0)}} = 0 \,, \end{aligned} \tag{7.28}$$

which shows that the linear corrections $p_{(1)}$ and $p_m^{(1)}$ do not affect the value of the magnetization parameter in the disk.

Moreover, from the orthogonality relation $u^\alpha b_\alpha = 0$ we obtain

$$b^t_{(0)} = l b^\phi_{(0)}, \qquad b^t_{(1)} = l b^\phi_{(1)}\,, \tag{7.29}$$

which imply that $b^\phi_{(1)}$ and $b^t_{(1)}$ are not independent variables. Using the relations, $b^2 = (1 - l\Omega) b^\phi b_\phi$ and $b^2 = 2p_m$, the zeroth-order and first-order terms of the magnetic field read

$$b^\phi_{(0)} = \sqrt{\frac{2\beta_m}{p_{(0)}(1 - l\Omega) g_{\phi\phi}}}\,, \tag{7.30}$$

$$b^\phi_{(1)} = \frac{p_{(1)}}{\beta_m}\sqrt{\frac{p_{(0)}}{2\beta_m(1 - \Omega l) g_{\phi\phi}}}\,, \tag{7.31}$$

where we have also used Eq. (7.29). Hence, the variables $p_m^{(1)}, b^t_{(1)}$ and $b^\phi_{(1)}$ are all related to $p_{(1)}$. The pressure correction $p_{(1)}$ is determined by solving the momentum conservation law given by Eq. (7.11) with a constant angular momentum distribution $l = l_0$. Using Eq. (7.31) and expanding Eq. (7.11) up to linear order in the variables $p_{(1)}$, $e_{(1)}$ and $b_{(1)}$, the fluid pressure correction equation can be expressed as

$$\begin{aligned}(e_{(1)} + p_{(1)}) a_\mu + \triangle^\rho_\mu \nabla_\rho p_{(1)} + \frac{\partial_\mu\left[\frac{\mathcal{L}}{\beta_m} p_{(1)}\right]}{\mathcal{L}} \\ + g_{\mu\rho}\pi^{\rho\nu} a_\nu + \triangle_{\mu\gamma}\triangle_{\kappa\tau}\nabla^\tau \pi^{\gamma\kappa} = 0\,,\end{aligned} \tag{7.32}$$

where $e_{(1)}$ is related to $p_{(1)}$ by Eq. (7.25). Once $p_{(1)}$ is determined by solving the above equation, we can also determine the impact of the shear viscosity on the magnetic pressure $p_m^{(1)}$ through Eq. (7.26).

Let us now for simplicity take the black hole mass $M = 1$ in the rest of our calculations. Both the temporal and azimuthal components of Eq. (7.32) lead to

$$\frac{2\eta l_0 r\left[r(r-3)\sin^4\theta - l_0^2(1-2/r)^2(r - 3\sin^2\theta)\right]}{\sin^6\theta\sqrt{r-2}\left(r^3 + l_0^2(2-r)\csc^2\theta\right)^{5/2}} = 0\,.$$

For $\eta \neq 0$, the above equation in the equatorial plane reduces to

$$r^3 - l_0^2(r-2)^2 = 0\,. \tag{7.33}$$

Correspondingly, the radial and angular components of (7.32) are, respectively,

$$\frac{(\tau_2 m_1) l_0^2 (r-3)}{2r^2 \sin^6\theta \left(r^3 + l_0^2(2-r)\csc^2\theta\right)^3}\left[r^3\cos 4\theta(10r-21) + \cos 2\theta\left\{4r^3(2r^2-14r+21) - 8l_0^2(r-3)(r-2)\right\} - r^3(2r-7)(4r-9) - 8l_0^2(r-2)(r^2-3r+3)\right] + m_2\frac{3r^6 + r^6\cos 4\theta + 2r^3\cos 2\theta\left\{l_0^2(r-2)(5r-14) - 2r^3\right\} - 2r^3 l_0^2(r-2)(5r-14)}{4r^5\sin^4\theta\left(r^3 + l_0^2(2-r)\csc^2\theta\right)^2} - \frac{-4l_0^4(r-2)^3}{4r^5\sin^4\theta\left(r^3 + l_0^2(2-r)\csc^2\theta\right)^2} + \left(1 + \frac{1}{\beta_m}\right)\frac{(r-2)}{r}\frac{\partial p_{(1)}}{\partial r} + \left[\frac{2(r-1)}{r^2\beta_m} + \frac{\left\{r^3 - l_0^2(2-r)^2\csc^2\theta\right\}\left(\gamma K + e_{(0)}^{1-\gamma}\right)}{\gamma K r^2\left(r^3 + l_0^2(2-r)\csc^2\theta\right)}\right] p_{(1)} = 0\,, \quad (7.34)$$

$$\tau_2 m_1 \frac{4l_0^2\cot\theta\left\{r^3(4r-9)\sin^2\theta + (r-2)\left(2l_0^2(4r-9) - r l_0^2(r-2)\csc^2\theta - 2r^4\right)\right\}}{r^2\sin^4\theta\left(r^3 + l_0^2(2-r)\csc^2\theta\right)^3} + m_2\frac{2l_0^2(r-2)\cot\theta\left(2r^3\sin^2\theta + l_0^2(r-2)\right)}{r^3\sin^4\theta\left(r^3 + l_0^2(2-r)\csc^2\theta\right)^2} + \left(1 + \frac{1}{\beta_m}\right)\frac{\partial p_{(1)}}{\partial\theta} + \left[\frac{2\cot\theta}{\beta_m} - \frac{(r-2)l_0^2\cot\theta\left(\gamma K + e_{(0)}^{1-\gamma}\right)}{\gamma K\sin^2\theta\left(r^3 + l_0^2(2-r)\csc^2\theta\right)}\right] p_{(1)} = 0\,. \quad (7.35)$$

In the limit $\beta_m \to \infty$, Eqs. (7.34) and (7.35) reduce to the corresponding equations obtained in Lahiri and Lämmerzahl [2019] for a purely hydrodynamical viscous thick disk. Substituting $p_{(1)}$ from Eq. (7.35) in Eq. (7.34) we obtain the following equation:

$$2l_0^2\cot\theta\left(\tilde{A} + \frac{\tilde{B}k_1}{C}\right)(\tau_2 m_1) + \frac{1}{2}\cot\theta\left(\tilde{f}_1 - \frac{\tilde{f}_2 k_1}{C}\right)m_2 + \sin^6\theta\left[r^3 + l_0^2(2-r)\csc^2\theta\right]^3\frac{(1+\beta_m)}{\beta_m}\left[r(r-2)\cot\theta\frac{\partial p_{(1)}}{\partial r} - \frac{4k_1}{C}\frac{\partial p_{(1)}}{\partial\theta}\right] = 0\,, \quad (7.36)$$

with the definitions

$$\tilde{A} = -2(r-3)\left[r^3(10r-21)\cos 4\theta + \cos 2\theta\left\{4r^3(2r^2-14r+21) - 8l_0^2(r-3)(r-2)\right\} - r^3(2r-7)(4r-9) - 8l_0^2(r-2)(r^2-3r+3)\right]\,,$$

$$\tilde{B} = 4\left[2rl_0^2(r-2)^2 - \sin^2\theta\left\{r^3(2r-3) + 4l_0^2(4r-9)(r-2) - r^3\cos 2\theta(4r-9)\right\}\right]\,,$$

$$k_1 = \left[-2\beta_m\sin^2\theta\left(r^3 + l_0^2(2-r)\csc^2\theta\right)e_{(0)} + K\gamma e_{(0)}^{\gamma}\left\{8l_0^2(1+\beta_m) + 2r^2 l_0^2(\beta_m+2) - 2r^4 - r^3(\beta_m-2) - 4l_0^2 r(3+\beta_m) + r^3\cos 2\theta(2r+\beta_m-2)\right\}\right]\,,$$

$$C = (r-2)l_0^2\beta_m e_{(0)} + K\gamma e_{(0)}^{\gamma}\left[l_0^3(r-2)(2+\beta_m) - 2r^3\sin^2\theta\right]\,,$$

$$\tilde{f}_1 = \Bigg[10r^6 - 6r^3 l_0^2(5r-12)(r-2) + 32 l_0^4 (r-3)(r-2)^2 + 16 r l_0^6 \left(1-\frac{2}{r}\right)^4 + \cos 2\theta \left\{8(5r-12)r^3 l_0^2 - 15 r^6 - 32 l_0^4 (r-3)(r-2)^2\right\}\Bigg] ,$$

$$\tilde{f}_2 = 4r^3 \left(1-\frac{2}{r}\right)\left[3r^6 - 2r^3 l_0^2 (r-2) + 4 l_0^4 (r-2)^2 + 2r^3 \cos 2\theta (2r^3 - (r-2) l_0^2) + r^6 \cos 4\theta\right] .$$

We must solve Eq. (7.36) once the values of the parameters m_1, τ_2, l_0 and β_m are selected and using the appropriate boundary conditions. Eq. (7.28) shows that $\beta_m^{(1)} = 0$. Therefore, the magnetization parameter can be completely expressed in terms of the zeroth-order magnetic pressure and fluid pressure, and is given by $\beta_m(r,\theta) = p_{(0)}/p_m^{(0)}$. Using Eqs. (7.21) and (7.22) we can further express

$$\beta_m(r,\theta) = \frac{K}{K_m \mathcal{L}^{\gamma-1}(r,\theta)} . \tag{7.37}$$

In addition, we can define the magnetization parameter at the center of the disk as $\beta_{m,c} \equiv \beta_m(r_c, \pi/2)$ and write it as

$$\beta_{m,c} = \frac{K}{K_m \mathcal{L}^{\gamma-1}(r_c,\pi/2)} . \tag{7.38}$$

Then, the magnetization parameter can be expressed as

$$\beta_m(r,\theta) = \beta_{m,c}\left(\frac{\mathcal{L}(r_c,\pi/2)}{\mathcal{L}(r,\theta)}\right)^{\gamma-1} , \tag{7.39}$$

which, for the Schwarzschild metric, reads

$$\beta_m(r,\theta) = \beta_{m,c}\left(\frac{r_c(r_c-2)}{r(r-2)\sin^2\theta}\right)^{\gamma-1} , \tag{7.40}$$

where r_c, $\beta_{m,c}$ and K are constant parameters. Let us compute r_c for a given angular momentum l_0. This can be determined by finding the extrema of the effective (gravitational plus centrifugal) potential W, as the center of the disk is located at a minimum of the potential (see, e.g. [Font and Daigne 2002] for details). In the Schwarzschild geometry, the total potential $W(r,\theta)$ for constant angular momentum distributions is be defined as,

$$W(r,\theta) = \frac{1}{2}\ln\frac{r^2(r-2)\sin^2\theta}{r^3\sin^2\theta - l_0^2(r-2)} . \tag{7.41}$$

At the equatorial plane, taking $\partial_r W = 0$ leads, after some algebra, to

$$r^3 - l_0^2(r-2)^2 = 0 . \tag{7.42}$$

The largest root of the above equation corresponds to the disk center, r_c. In the absence of dissipative terms, the relativistic momentum conservation equation, with our choices of equation of state, can be expressed as follows [Gimeno-Soler and Font 2017]

$$W - W_{\rm s} + \frac{\gamma}{\gamma - 1}\left(\frac{p_{(0)}}{e_{(0)}} + \frac{p_m^{(0)}}{e_{(0)}}\right) = 0\,, \tag{7.43}$$

which can further be rewritten as

$$W - W_{\rm s} + \frac{\gamma K e_{(0)}^{\gamma-1}}{\gamma - 1}\left(1 + \frac{1}{\beta_m(r,\theta)}\right)\,, \tag{7.44}$$

where $W_{\rm s}$ is the potential at the surface of the disk, i.e. the surface for which $p_{(0)} = p_m^{(0)} = e_{(0)} = 0$. From the above expression, the zeroth-order energy density can be obtained and it reads as

$$e_{(0)} = \left(\frac{1}{K}\right)^{\frac{1}{\gamma-1}}\left(\frac{\gamma(1+\beta_m(r,\theta))}{(1-\gamma)\beta_m(r,\theta)(W - W_{\rm s})}\right)^{\frac{1}{1-\gamma}}\,, \tag{7.45}$$

and the zeroth-order pressure, in terms of $\beta_{m,c}, r_c$ and $W_{\rm s}$, becomes

$$p_{(0)} = K^{\frac{1}{\gamma-1}}\left(\frac{\gamma\left(1+\beta_{m,c}\left(\frac{r_c(r_c-2)}{r(r-2)\sin^2\theta}\right)^{\gamma-1}\right)}{(1-\gamma)\beta_{m,c}\left(\frac{r_c(r_c-2)}{r(r-2)\sin^2\theta}\right)^{\gamma-1}(W - W_{\rm s})}\right)^{\frac{\gamma}{1-\gamma}}\,, \tag{7.46}$$

which corresponds to the fluid pressure of the magnetized ideal fluid. From this equation it follows that for the term inside the parenthesis to be positive, we require that $W - W_{\rm s} < 0$. On the contrary, if $W - W_{\rm s} > 0$, the pressure (and the energy density) should vanish, which indicates regions outside the disk.

Table 7.1 Location of $r_{\rm cusp}$ and the magnitudes of pressure $p_{(0),\rm cusp}$ at $r_{\rm cusp}$ in an ideal fluid magnetized disk with two different choices of magnetization parameter $\beta_{m,c}$.

	$W_{\rm s} = -0.039$		$W_{\rm s} = -0.040$		$W_{\rm s} = -0.041$	
$\beta_{\rm m,c}$	$r_{\rm cusp}$	$p_{(0),\rm cusp}$	$r_{\rm cusp}$	$p_{(0),\rm cusp}$	$r_{\rm cusp}$	$p_{(0),\rm cusp}$
10^{3}	4.576	1.041×10^{-4}	4.576	3.556×10^{-5}	4.576	3.700×10^{-6}
10^{-3}	4.644	1.229×10^{-6}	4.617	4.252×10^{-7}	4.591	4.480×10^{-8}

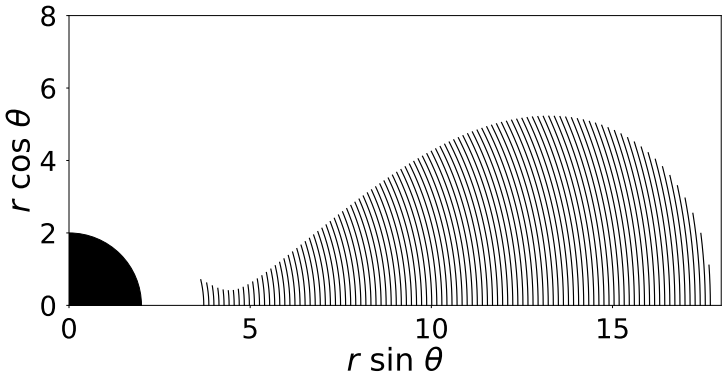

Figure 7.1 Characteristic curves computed for $W_{\rm s} = -0.039$ (i.e. the solutions of Eq. (7.57).). For visualization purposes we only show a sample of 101 curves instead of the complete set of 703 curves we have computed. The black circle represents the black hole.

7.3 Methodology

7.3.1 Formalism

We solve Eq. (7.36) with the domain of definition set by the conditions $W(r,\theta) \leq W_{\rm s}$, $r_{\rm in} \leq r \leq r_{\rm out}$ where $r_{\rm in}$ and $r_{\rm out}$ are the inner and the outer boundary of the disk at the equatorial plane. As in this work we are considering disks slightly overflowing their Roche lobe (i.e. $W_{\rm s} \gtrsim W(r_{\rm cusp}, \pi/2)$ where $r_{\rm cusp}$ corresponds to the location of the self-crossing point of the critical equipotential surface) it is important to note that the disks do not possess an inner edge (i.e. the outermost equipotential surface is attached to the event horizon of the black hole) and thus our choice of $r_{\rm in}$ is arbitrary. Here, we choose the value of $r_{\rm in}$ such that $r_{\rm in} \lesssim r_{\rm cusp}$ so we can study the cusp region, and exclude the region closest to the black hole, as it is irrelevant for our study (the reason will become clear in Section 7.4). In addition, we exclude the funnel region along the symmetry axis ($\theta = 0$) by further restricting our domain by only considering the region containing equipotential surfaces that cross the equatorial plane at least once. As our system has axisymmetry and reflection symmetry with respect to the equatorial plane, we can further restrict our domain to $0 < \theta < \pi/2$.

Eq. (7.36) can be rewritten in a more compact form as

$$\vec{\alpha}(r,\theta) \cdot \vec{\nabla}_{(r,\theta)} p_{(1)} - \tilde{c}(r,\theta) = 0, \tag{7.47}$$

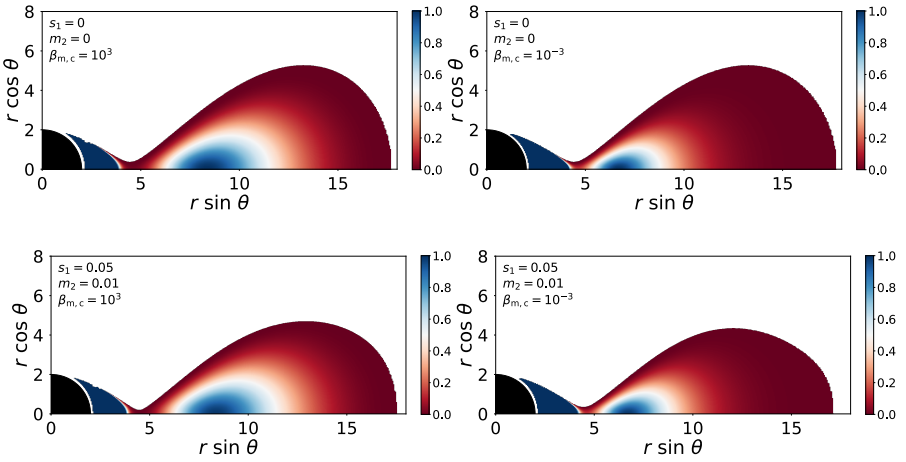

Figure 7.2 Comparison of the full disk structure for $W_s = -0.039$. The top row shows inviscid solutions and the bottom row shows viscous solutions for $s_1 = 0.05$ and $m_2 = 0.01$. The left panels correspond to non-magnetized disks ($\beta_{m,c} = 10^3$) and the right panels to highly-magnetized disks ($\beta_{m,c} = 10^{-3}$). In all figures the colour gradient refers to the distributions of the total fluid pressure. Furthermore, in the four cases the pressure has been normalized to the corresponding value of $p_{(0),max}$. The morphology of the disks remains essentially the same for all cases, the only noticeable difference being a small decrease in size at the very low pressure region for the viscous cases. Note that, for visualization purposes we have extended our original domain of integration ($r_{in} = 2.1$ instead of the original $r_{in} = 3.7$) so that it is apparent that the inner region of the disk is attached to the event horizon of the black hole.

with the following definitions

$$\begin{aligned}
\alpha_r(r,\theta) &= \sin^6\theta \left[r^3 + l_0^2(2-r)\csc^2\theta\right]^3 \frac{(1+\beta_m)}{\beta_m}\left(r(r-2)\cot\theta\right), \\
\alpha_\theta(r,\theta) &= r\sin^6\theta \left[r^3 + l_0^2(2-r)\csc^2\theta\right]^3 \frac{(1+\beta_m)}{\beta_m}\left(-\frac{4k_1}{C}\right), \\
\tilde{c}(r,\theta) &= -2l_0^2\cot\theta\left(\tilde{A} + \frac{\tilde{B}k_1}{C}\right)(\tau_2 m_1) - \frac{m_2}{2}\cot\theta\left(\tilde{f}_1 - \frac{\tilde{f}_2 k_1}{C}\right).
\end{aligned} \tag{7.48}$$

Close examination of the coefficients in Eq. (7.48) reveals that, at the equatorial plane ($\theta = \pi/2$), Eq. (7.47) is simply

$$\frac{\partial p_{(1)}}{\partial\theta} = 0. \tag{7.49}$$

Eq. (7.49) has two relevant consequences for our solution. The first one is that surfaces of constant $p_{(1)}$ are orthogonal to the equatorial plane (a consequence of the reflection symmetry of the problem). The second one is that one cannot extract information of the distribution of $p_{(1)}$ at the equatorial plane directly from Eq. (7.47) at $\theta = \pi/2$. To know the values of $p_{(1)}$ at the equatorial plane we must look for the solution $p_{(1)}(r,\theta)$ when $\theta \to \pi/2$ i.e. a point that belongs to the

domain of the θ coordinate. Thus, to maximize the accuracy of the solution is convenient to solve Eq. (7.47) in Cartesian coordinates, as the distance between the last point of our domain and the equatorial plane will remain the same. Then, we can rewrite this equation as

$$\vec{\alpha}'(x,y)\cdot\vec{\nabla}_{(x,y)}p_{(1)} - c'(x,y) = 0, \tag{7.50}$$

in which we used the change of coordinates defined by $x = r\sin\theta$, $y = r\cos\theta$, and the new expressions for the coefficients

$$\begin{aligned}
\alpha'_x(x(r,\theta),y(r,\theta)) &= \alpha_r(r,\theta)\sin\theta + \alpha_\theta(r,\theta)\cos\theta\,,\\
\alpha'_y(x(r,\theta),y(r,\theta)) &= \alpha_r(r,\theta)\cos\theta - \alpha_\theta(r,\theta)\sin\theta\,,\\
c'(x(r,\theta),y(r,\theta)) &= \tilde{c}(r,\theta)\,,
\end{aligned} \tag{7.51}$$

where α'_x and α'_y are the x and y components of the vector of coefficients $\vec{\alpha}'(x,y)$. Taking into account that $\alpha'_y(x,y) \neq 0$ in our domain, we can redefine all the coefficients as

$$\begin{aligned}
a(x,y) &= \alpha'_x(x,y)/\alpha'_y(x,y)\,,\\
b(x,y) &= 1\,,\\
c(x,y) &= c'(x,y)/\alpha'_y(x,y)\,.
\end{aligned} \tag{7.52}$$

Therefore, the final form of the partial differential equation (PDE) we want to solve reads

$$a(x,y)\frac{\partial p_{(1)}}{\partial x} + \frac{\partial p_{(1)}}{\partial y} - c(x,y) = 0\,. \tag{7.53}$$

To solve Eq. (7.53) we use the so-called method of characteristics, in which we can reduce a PDE to a set of ordinary differential equations (ODEs), one for each initial value defined at the boundary of the domain. The final form of the characteristic equations is

$$\frac{dx}{dt} = a(x,y)\,, \tag{7.54}$$

$$\frac{dy}{dt} = 1\,, \tag{7.55}$$

$$\frac{dp_{(1)}}{dt} = c(x,y)\,. \tag{7.56}$$

To solve this system, we start from a point (x_0,y_0) in the boundary of the domain (i.e. $\{(x_0,y_0)\,/\,W(x_0,y_0) = W_\mathrm{s}\}$). Then, we can integrate the system of ODEs as follows: first, the solution of Eq. (7.55) is trivially $y(t) = t + y_0$. Using this result, we can rewrite Eq. (7.54) as

$$\frac{dx}{dy} = a(x,y)\,. \tag{7.57}$$

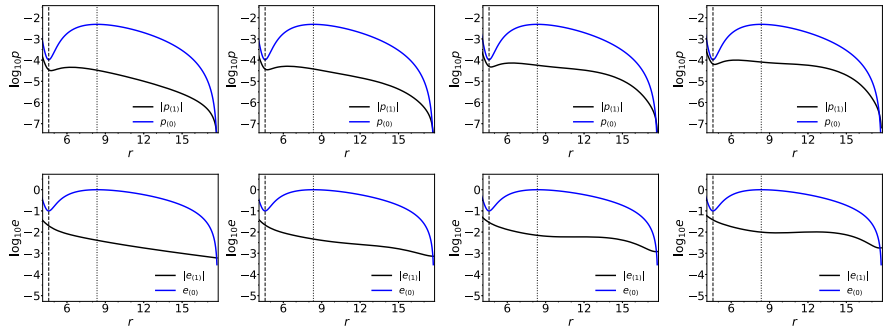

Figure 7.3 Radial plots of $\log p_{(0)}$ and $\log |p_{(1)}|$ (top row) and $\log e_{(0)}$ and $\log |e_{(1)}|$ (bottom row) at the equatorial plane for $W_{\rm s} = -0.039$, $s_1 = 0.05$, $\beta_{\rm m,c} = 10^3$ and $m_2 = (0, 0.001, 0.005, 0.01)$. Each column corresponds to an increasing value of m_2. The vertical dashed line represents the location of the self-crossing pressure isocontour $r_{\rm cusp}$ and the vertical dotted line represents the location of the maximum of the pressure $r_{\rm max}$, which coincides to the center of the disk $r_{\rm c}$ for non-magnetized disks.

We can integrate numerically this equation starting from the selected point (x_0, y_0). The solution of this equation $(x(y))$ will give us a characteristic curve of the problem, i.e. a curve along which the solution of our PDE coincides with the solution of the ODE. To finish the procedure, we take Eq. (7.56) and rewrite it in the same way as the previous one.

$$\frac{dp_{(1)}}{dy} = c(x(y), y)\,. \tag{7.58}$$

Then, we can integrate $p_{(1)}$

$$p_{(1)}(y) = \int_{y_0}^{y} c(x(y), y)dy + p_{(1)_0}\,, \tag{7.59}$$

where we have used that $p_{(1)}(x_0, y_0) = p_{(1)_0}$. It is easy to see that we can recover $p_{(1)}(x, y)$ by using both Eq. (7.59) and the expression for the characteristic curve $x(y)$. Repeating this three-step procedure over a sufficiently large and well-chosen sample of initial points will give us a mapping of the domain and hence, the solution of the PDE for the whole domain.

7.3.2 Numerical implementation

The numerical implementation of the procedure we have just described is as follows: First, we start by defining N_x equally spaced points in the open interval (at the equatorial plane) $(r_{\rm in}, r_{\rm out})$, where $r_{\rm in} = 3.7$ and $r_{\rm out}$ is the only solution of the equation $W(r, \pi/2) - W_{\rm s} = 0$ and its value is $r_{\rm out} = 17.76$. In this work

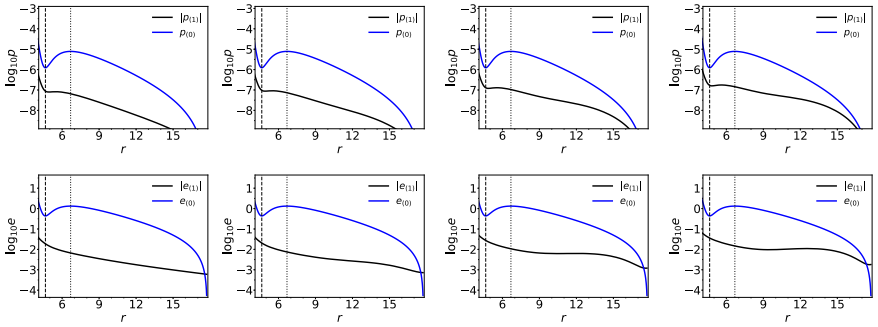

Figure 7.4 Same as Fig. 7.3 but for $\beta_{\rm m,c} = 10^{-3}$.

we fix $N_x = 703$ which corresponds to a distance between points $\Delta x = 0.02$. Starting from this set of points we integrate Eq. (7.57) using the fourth-order Runge-Kutta method with $W(x, y) > W_{\rm s}$ as the terminating condition of the integration and an integration step $h = 10^{-3}$. As a result of the previous step we obtain a set of points belonging to the boundary of the domain and a set of characteristic curves $\{x(y)_i \ / \ i = [1, N_x]\}$ that start at the boundary and end at the equatorial plane. An example of the distribution of the characteristic curves for the case $W_{\rm s} = -0.039$ is depicted in Fig. 7.1. Now, we can integrate Eq. (7.59) along the characteristics, starting from the boundary $(x_0, y_0)_i$. To do this we use the same fourth-order Runge-Kutta solver as before (which in this case reduces to Simpson's rule) and the initial condition $p_{(0)_0} = 0$.

7.4 Results

The primary motivation of this paper is to determine possible changes in the morphology of geometrically thick magnetized disks in the presence of shear viscosity as compared to the inviscid case. We use a simple setup where stationary viscous disks with constant angular momentum distributions are built around a Schwarzschild black hole. The shear viscosity is assumed to only induce perturbative effects on the fluid so that the fluid in the disk can still move in circular orbits. The analysis of isopressure and isodensity surfaces of our constrained system provides evidences showing that the shear viscous and curvature effects in the stationary disk models are only tractable using the causal approach.

Stationary magnetized tori are constructed for a set of values of the parameters τ_2, m_1, m_2 and the magnetization parameter at the center of the disk,

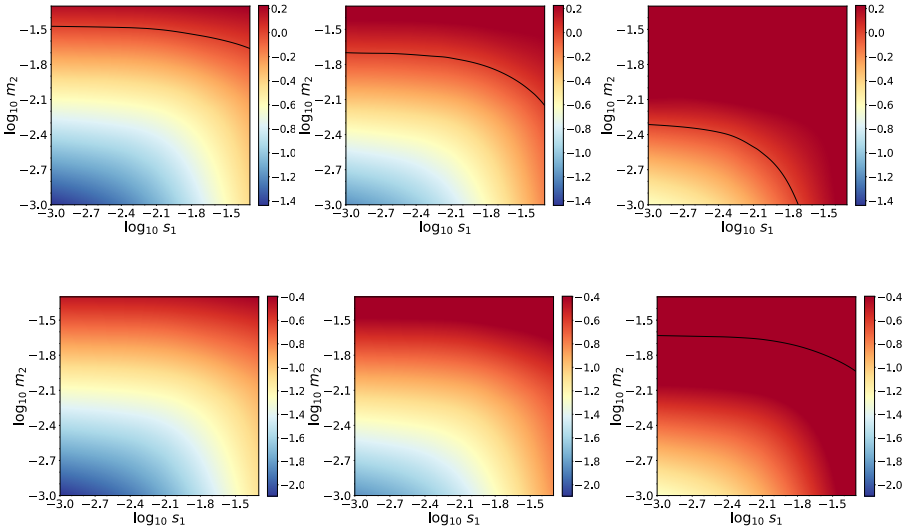

Figure 7.5 Two dimensional plots for $\log_{10}|\Delta p_{\rm cusp}|$. The first row corresponds to the models with $\beta_{\rm m,c} = 10^3$ and the second row correspond to the models with $\beta_{\rm m,c} = 10^{-3}$. The columns correspond, from left to right, to the three different values of $W_{\rm s}$ we have considered, namely -0.039, -0.040 and -0.041. The black contour appearing in some of the plots corresponds to $\log_{10}|\Delta p_{\rm cusp}| = 0$.

$\beta_{m,c}$ (Note that, to build the solutions, we have to fix the polytropic exponent γ and the value of the zeroth-order correction to the energy density at the center $e_{(0),c} = e_{(0)}(r_{\rm c}, \pi/2)$. In particular, we have chosen $\gamma = 5/3$ and $e_{(0),c} = 1$). For convenience, we define a new parameter $s_1 = \tau_2\, m_1$ and set $\tau_2 = 1$ without loss of generality. We consider two values of the magnetization parameter at the center of the disk, namely $\beta_{m,c} = 10^3$ (low magnetization, almost a purely hydrodynamical model) and $\beta_{m,c} = 10^{-3}$ (high magnetization) which are sufficient to bring out the effects of a toroidal magnetic field on the viscous disk.

The corrections to the pressure $p_{(1)}$ and to the energy density $e_{(1)}$ for a given choice of parameters are determined by solving Eq. (7.36) numerically, using the method of characteristics as described in the previous section. Our results reveal that the effects of the shear viscosity are particularly noticeable only fairly close to the cusp of the disks. The large-scale morphology of the torus remains essentially unaltered irrespective of the values of the parameters s_1 and m_2. This can be immediately concluded from figure 7.2 which displays the distribution of the pressure in the entire domain for a set of illustrative stationary models. Note that the physical solution is attached to the black hole, even though in the figure there is a gap between the disk and the event horizon.

This is due to the fact that Eq. (7.53) is singular at the event horizon, so the solution cannot be extended to it. Figures 7.3 and 7.4 display radial plots at the equatorial plane showing the zeroth-order and first-order corrections of the pressure and of the energy density, corresponding to the low and high value of the magnetization parameter, respectively. We note that, contrary to purely hydrodynamical disks, for magnetized tori the location of the center of the disk $r_{\rm c}$ does not exactly coincide with the location of the maximum of the pressure but it is slightly shifted towards the black hole [Gimeno-Soler and Font 2017]. This can be observed for the highly magnetized case in figure 7.4. For both low and high values of $\beta_{m,c}$ the corrections $p_{(1)}$ and $e_{(1)}$ near the cusp remain small in comparison to their respective equilibrium values $p_{(0)}$ and $e_{(0)}$. As one moves away from the cusp and approaches the outer edge of the disk, the difference between $p_{(0)}$ and $p_{(1)}$ diminishes. This trend is most prominent for low magnetized disk as shown in figure 7.3. In addition, by increasing the value of m_2, i,e. the curvature effects (while keeping m_1 fixed), the difference between $p_{(0)}$ and $p_{(1)}$ also decreases near the cusp, until a value is reached for which $p_{(1)}/p_{(0)} \sim \mathcal{O}(1)$ and $e_{(1)}/e_{(0)} \sim \mathcal{O}(1)$ and neither m_1 nor m_2 can further be increased. Under these conditions we are no longer in the regime of validity of near-equilibrium hydrodynamics where gradients are small. Since we are not addressing the non-equilibrium sector, our analysis can set an upper limit on the contributions of curvature and shear viscosity on stationary solutions of magnetized viscous disks before far-from-equilibrium effects set in.

The change in pressure $\triangle p_{\rm cusp}$ at the newly formed cusp $\triangle r_{\rm cusp}$ of the magnetized disk in the presence of shear viscosity, as compared to the inviscid case, is determined in the following way,

$$\triangle r_{\rm cusp} = \frac{r_{\rm cusp,new} - r_{\rm cusp}}{r_{\rm cusp}}\,, \tag{7.60}$$

$$\triangle p_{\rm cusp} = \frac{p_{\rm t,cusp} - p_{(0),\rm cusp}}{p_{(0),\rm cusp}}\,, \tag{7.61}$$

where $p_{\rm t} = p_{(0)} + p_{(1)}$ and $r_{\rm cusp,new}$ is the new location of the cusp due to shear viscosity effects. Both $p_{\rm t}$ and $r_{\rm cusp,new}$ therefore contain all contributions from shear viscosity and spacetime curvature for various choices of input parameters m_1, m_2. The new position of the cusp at the equatorial plane corresponds to the location of the minimum of the total pressure $p_{\rm t}(r)$. We compute it by fitting the values of $p_{\rm t}$ using a third-order order spline interpolation. The values of $r_{\rm cusp,new}$ and $p_t(r_{\rm cusp,new})$ are obtained at the same time using this technique.

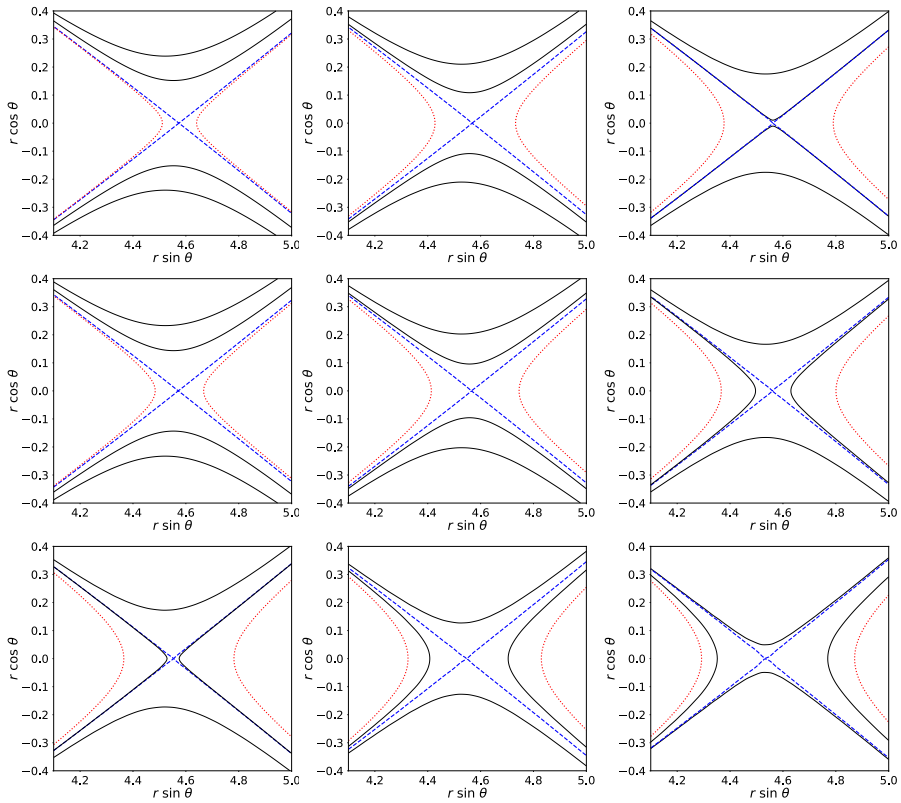

Figure 7.6 Isocontours of $p_{(\mathrm{t})} = p_{(0)} + p_{(1)}$ in the cusp region for $W_{\mathrm{s}} = -0.039$ and $\beta_{\mathrm{m,c}} = 10^3$. From top to bottom the rows correspond to $m_2 = (0, 0.005, 0.01)$. From left to right the columns correspond to $s_1 = (0.005, 0.01, 0.05)$. Red isocontours correspond to cusp-generating constant pressure surfaces without viscosity and blue isocontours depict newly-formed self-intersecting constant pressure surfaces when viscosity and curvature effects are present. The two black isocontours correspond to the values $p_{\mathrm{t}} = 2p_{0,\mathrm{cusp}}/3$ and $p_{\mathrm{t}} = p_{0,\mathrm{cusp}}/3$.

For completeness, the locations of r_{cusp} and $p_{(0),\mathrm{cusp}}$ for an inviscid magnetized disk are reported in Table 7.1.

The allowed values of parameters s_1 and m_2 are reported in Table 7.2 for all of our magnetized disk models. The range of variation of these parameters is $s_1 = (0.001, 0.005, 0.01, 0.05)$ and $m_2 = (0, 0.001, 0.005, 0.01, 0.05)$. Forbidden values of s_1 and m_2 appear when $|\triangle p_{\mathrm{cusp}}| \gtrsim \mathcal{O}(1)$ (marked in boldface in Table 7.2) implying $p_{(1)}/p_{(0)} \sim \mathcal{O}(1)$. As s_1 (or m_1) and m_2 increase and the potential gap $\triangle W_{\mathrm{s}}$ decreases from $\triangle W_{\mathrm{s}} > 0$ to $\triangle W_{\mathrm{s}} \approx 0$, the condition $p_{(1)}/p_{(0)} \sim \mathcal{O}(1)$ is more frequently satisfied.

A more concrete estimation of the allowed values of the parameters s_1 and m_2 with $\beta_{m,c}$ can be obtained from the 2D plot of $|\triangle p_{\mathrm{cusp}}|$ shown in figure 7.5.

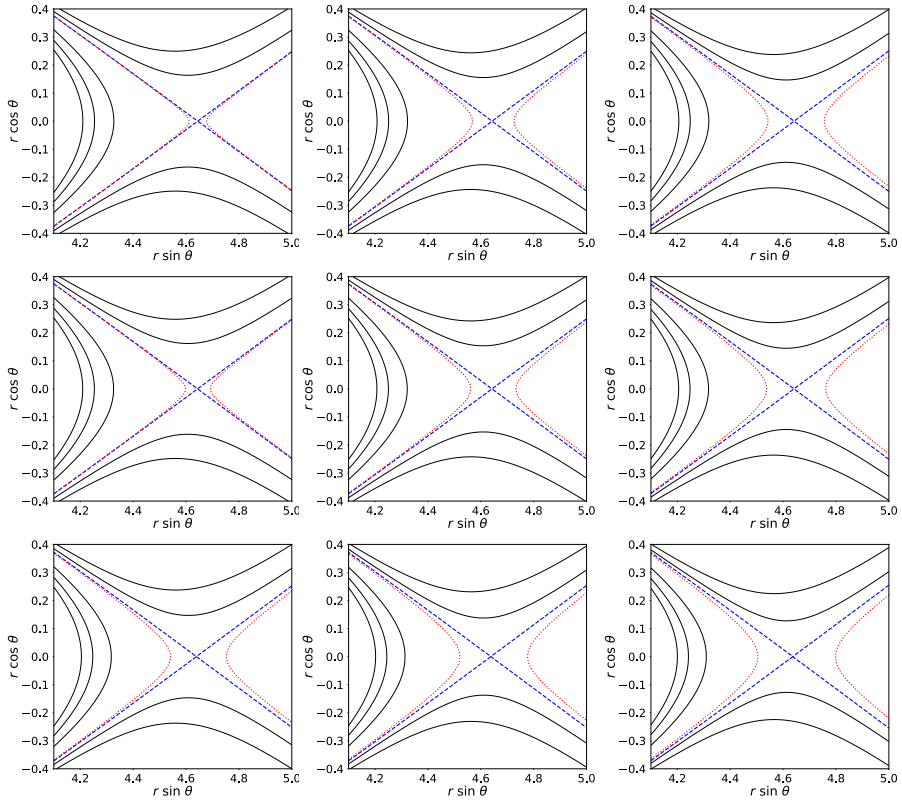

Figure 7.7 Same as Fig. 7.6 but for $\beta_{\rm m,c} = 10^{-3}$. The three black isocontours in the left part of all plots represent values of the total pressure equal to $p_{{\rm t}_i} = (p_{(0),\rm max} i - p_{(0),\rm cusp})/4$ for $i = 1, 2, 3$, where $p_{(0),\rm max}$ is the value of $p_{(0)}$ at the maximum of the pressure.

The black contour depicted in some of the plots in this figure indicates a cut-off value of s_1 and m_2 corresponding to $\log_{10} |\Delta p_{\rm cusp}| = 0$. For low magnetized viscous disks ($\beta_{m,c} = 10^3$, top panels), we find that the allowed values of s_1 and m_2 are large for $\Delta W_{\rm s} > 0$ and that the permitted parameter space of (s_1, m_2) appreciably decreases as the potential gap $\Delta W_{\rm s} \to 0$. This indicates that stationary magnetized disks with $\Delta W_{\rm s} \approx 0$ do not allow for large shear viscosity and curvature effects in comparison to $\Delta W_{\rm s} > 0$. On the other hand, for highly magnetized disks ($\beta_{m,c} = 10^{-3}$, bottom panels), stationary viscous models can be constructed over the entire choice of the parameter space and in the considered regions of the potential gap i.e. $\Delta W_{\rm s} > 0$ and $\Delta W_{\rm s} \approx 0$. Therefore, in order not to be in conflict with the adopted perturbative approach, our stationary models are restricted up to maximum values of $m_1 = s_1 = 0.05$ and $m_2 = 0.05$. Table 7.2 also shows that the changes in the location of the

cusp positions are small for small values of s_1 and m_2. This behaviour remains the same for both low and high values of magnetization as well as for $\triangle W_\mathrm{s} > 0$ and $\triangle W_\mathrm{s} \approx 0$.

Isocontours of the total pressure p_t of our stationary viscous tori are shown in figures 7.6 and 7.7 for low and high values of the central magnetization parameter, respectively. These figures concentrate on the regions close to the cusp of the disks since it is in those regions where the effects of the shear viscosity are most manifest. The self-intersecting contours of p_t possessing a cusp are depicted by the blue dashed curves in the figures for the values of s_1 and m_2 indicated in the captions. The red isocontours correspond to surfaces of constant pressure of magnetized ideal fluid disks which would self-intersect, had there been no dissipative effects in the disk. For a given value of s_1 and W_s we observe that when m_2 increases (from the top row to the bottom panels) the location of the newly formed cusp moves towards the black hole. At the same time the thickness of the cusp region in the disk also diminishes. This can be observed by looking at the change of location of the black isocontours located above and below the cusp region in figures 7.6 and 7.7. These two iscontours correspond to the values of the total pressure $p_\mathrm{t} = 2p_{0,\mathrm{cusp}}/3$ and $p_\mathrm{t} = p_{0,\mathrm{cusp}}/3$. In particular, in Fig. 7.6 it can be seen that, in the bottom row and in the right column, the isocontour corresponding to $p_\mathrm{t} = 2p_{0,\mathrm{cusp}}/3$, changes its position (from above and below the cusp, to the left and right of the cusp). This means that, for these cases, $p_{\mathrm{t,cusp}} < 2p_{0,\mathrm{cusp}}/3$. In addition, the isocontour corresponding to $p_\mathrm{t} = p_{0,\mathrm{cusp}}/3$ also moves significantly closer to the self-crossing surface. Therefore, within our framework based on causal relativistic hydrodynamics, the role of shear viscosity triggered by the curvature of the Schwarzschild black hole spacetime is apparent through a noticeable rearrangement of the constant pressure surfaces of magnetized viscous disks when compared to the purely inviscid case [Lahiri and Lämmerzahl 2019]. In addition, the comparison of figures 7.6 and 7.7 shows that as the strength of the magnetic field increases the shift of the location of the cusp towards the black hole also increases. This might have implications on the dynamical stability of constant angular momentum thick disks, mitigating the development of the so-called runaway instability that affects inviscid constant angular momentum tori [Abramowicz, Calvani, and Nobili 1983, Font and Daigne 2002].

7.5 Summary

We have discussed stationary solutions of magnetized, viscous thick accretion disks around a Schwarzschild black hole, neglecting the self-gravity of the tori and assuming that they are endowed with a toroidal magnetic field and obey a constant angular momentum law. Our study has focused on the role of the spacetime curvature in the shear viscosity tensor and in the effects viscosity may have on the stationary solutions. This work is a generalization of a previous study for purely hydrodynamical disks presented in Lahiri and Lämmerzahl [2019].

Following Lahiri and Lämmerzahl [2019] we have considered a simple framework to encapsulate the quantitative effects of the shear viscosity (neglecting any contributions of the heat flow) and the curvature of the background geometry. In this setup, both the shear viscosity and the curvature have perturbative influences on the fluid, thereby allowing the fluid particles in the disk to undergo circular orbits. In particular, the magnetic field distribution, the fluid pressure and the energy density (related to the pressure by a barotropic equation of state) are perturbatively modified due to dissipative effects. Our framework is based on causal relativistic hydrodynamics and uses the gradient expansion scheme up to second order such that the governing equations of motion of the fluid in the Eckart frame are hyperbolic. Within this approach the curvature of the background geometry, in which the accretion disk is situated, naturally appears in the equations of motion. In analogy with what was found in Lahiri and Lämmerzahl [2019] for unmagnetized tori, the present work also shows that the viscosity and the curvature of the Schwarzschild black hole play some role on the morphology of magnetized tori.

The stationary models have been constructed by numerically solving the general relativistic momentum conservation equation using the method of characteristics. By varying the parameters m_1 and m_2 with two different choices of magnetization, we have studied the radial profiles of $p_{(0)}$ and $p_{(1)}$ to identify regions of the disk where shear viscosity and curvature are mostly casting their effects. Our results have revealed that the effects are most prominent near the cusp of the disk, which helped us focus our analysis on two regions of the potential gap, namely $\triangle W_{\rm s} > 0$ and $\triangle W_{\rm s} \approx 0$. Moreover, our study has allowed us to constrain the range of validity of the second-order transport coefficients m_1 and m_2 (after setting $\tau_2 = 1$). The allowed parameter space can be derived from figure 7.5 and from Table 7.2, where the bold-lettered values of $\triangle p_{\rm cusp}$ for a given value of $W_{\rm s}$ mark the breakdown of the perturbative approach. Furthermore,

the computations of $\triangle r_{\rm cusp}$ pinpoint the exact modification in the position of the cusp due to the shear viscosity and curvature effects.

The obtained isopressure contours of $p_{\rm t}$ corresponding to $\triangle W_{\rm s} > 0$ further divulge the cumulative effects of the viscosity and curvature on the magnetized disk. The self-intersection of these isopressure contours indicate new locations of the cusp as well as the formation of a new $p_{\rm cusp}$. We have found that for each magnetization and $\triangle W_{\rm s}$ considered, the location of cusps moves towards the black hole as parameter m_2 increases. Moreover, for higher magnetized disks the shift is even larger. Therefore, the combined effects of shear viscosity and spacetime curvature might help mitigate, or even suppress, the development of the runaway instability in constant angular momentum tori [Abramowicz, Calvani, and Nobili 1983, Font and Daigne 2002], a conclusion that is at par with the assumptions of our setup.

The present work is a small step towards constructing stationary models of viscous magnetized tori based on a causal approach for relativistic hydrodynamics. Despite our simplistic approach we have shown here that the morphology of geometrically thick accretion disks is non-trivially affected by viscosity and curvature. These effects, though small, should not be neglected. In particular, they could potentially alter the radiation profiles of magnetized accretion tori. As an example Vincent et al. [2015] discussed magnetised Polish doughnuts using Kommissarov's approach [Komissarov 2006] including radiation. However, they did not treat dissipation or shear stresses from first principles as in the current work but used, instead, an ad-hoc parameterisation to allow the gas to be non-ideal. It would be interesting to employ the second-order gradient approximation scheme discussed here to determine the temperature dependence in magnetized viscous tori from first principles and then examine the associated radiation spectra as the spectral properties are directly influenced by hydrodynamic and thermodynamic structures of the disks. Likewise, the intensity and emission lines of viscous magnetized tori are expected to show imprints of shear viscosity and curvature [Vincent et al. 2015, Straub et al. 2012]. Similarly, another system worth analysing would be a thick disk with advection dominated flows, as discussed by Ghanbari, Abbassi, and Ghasemnezhad [2009], since the viscous heating rate might be modified when using the present form of the shear viscosity tensor. Investigating these various possibilities will be the target of future studies.

Finally, to actually observe the consequences of dissipative flux quantities in detail, a more realistic construction is required. That would involve taking into account the contributions of the heat flux and of the radial velocity of the fluid.

Ultimately, considering dissipative flux quantities to behave as perturbations is an assumption that should also be relaxed.

Table 7.2 Values of $\Delta p_{\rm cusp}$ and $\Delta r_{\rm cusp}$ corresponding to different choices of s_1, m_2 and $\beta_{m,c}$. The considered values of $W_{\rm s}$ are respectively -0.039, -0.040 and -0.041. Bold-faced values of $\Delta p_{\rm cusp}$ are employed to indicate the regions when $p_{(1)} \gtrsim p_{(0)}$, such that $p_{(1)}$ cannot be treated as a perturbation for a given value of $W_{\rm s}$ and $\beta_{m,c}$.

			$W_{\rm s} = -0.039$		$W_{\rm s} = -0.040$		$W_{\rm s} = -0.041$	
s_1	m_2	$\beta_{\rm m,c}$	$\Delta r_{\rm cusp}$	$\Delta p_{\rm cusp}$	$\Delta r_{\rm cusp}$	$\Delta p_{\rm cusp}$	$\Delta r_{\rm cusp}$	$\Delta p_{\rm cusp}$
0.001	0	10^{3}	-9.71×10^{-5}	-6.66×10^{-3}	-1.10×10^{-4}	-1.20×10^{-2}	-1.05×10^{-4}	-4.40×10^{-2}
0.001	0	10^{-3}	-2.45×10^{-5}	-1.43×10^{-3}	-2.95×10^{-5}	-2.61×10^{-3}	-4.38×10^{-5}	-9.71×10^{-3}
0.001	0.001	10^{3}	-3.27×10^{-4}	-3.64×10^{-2}	-3.95×10^{-4}	-6.55×10^{-2}	-2.33×10^{-4}	-0.241
0.001	0.001	10^{-3}	-8.55×10^{-5}	-7.99×10^{-3}	-1.10×10^{-4}	-1.45×10^{-2}	-1.68×10^{-4}	-5.35×10^{-2}
0.001	0.005	10^{3}	-1.35×10^{-3}	-0.156	-1.97×10^{-3}	-0.281	-7.03×10^{-4}	**-1.03**
0.001	0.005	10^{-3}	-3.27×10^{-4}	-3.43×10^{-2}	-4.72×10^{-4}	-6.20×10^{-2}	-6.97×10^{-4}	-0.229
0.001	0.01	10^{3}	-2.65×10^{-3}	-0.306	-3.62×10^{-3}	-0.552	-1.32×10^{-2}	**-1.92**
0.001	0.01	10^{-3}	-6.19×10^{-4}	-6.71×10^{-2}	-9.97×10^{-4}	-0.122	-1.35×10^{-3}	-0.449
0.001	0.05	10^{3}	-2.48×10^{-2}	**-1.48**	-4.72×10^{-2}	**-2.03**	-7.06×10^{-2}	**-2.33**
0.001	0.05	10^{-3}	-2.58×10^{-3}	-0.331	-3.74×10^{-3}	-0.602	-1.66×10^{-2}	**-2.02**
0.005	0	10^{3}	-5.00×10^{-4}	-3.34×10^{-2}	-5.99×10^{-4}	-6.00×10^{-2}	-5.10×10^{-4}	-0.220
0.005	0	10^{-3}	-1.22×10^{-4}	-7.16×10^{-3}	-1.51×10^{-4}	-1.31×10^{-2}	-2.23×10^{-4}	-4.86×10^{-2}
0.005	0.001	10^{3}	-7.46×10^{-4}	-6.32×10^{-2}	-9.51×10^{-4}	-0.114	-6.29×10^{-4}	-0.417
0.005	0.001	10^{-3}	-1.83×10^{-4}	-1.37×10^{-2}	-2.36×10^{-4}	-2.49×10^{-2}	-3.51×10^{-4}	-9.25×10^{-2}
0.005	0.005	10^{3}	-1.80×10^{-3}	-0.183	-2.56×10^{-3}	-0.330	-4.66×10^{-3}	**-1.20**
0.005	0.005	10^{-3}	-4.23×10^{-4}	-4.00×10^{-2}	-6.15×10^{-4}	-7.25×10^{-2}	-8.86×10^{-4}	-0.268
0.005	0.01	10^{3}	-3.03×10^{-3}	-0.333	-3.98×10^{-3}	-0.601	-1.71×10^{-2}	**-2.01**
0.005	0.01	10^{-3}	-7.12×10^{-4}	-7.22×10^{-2}	-1.15×10^{-3}	-0.132	-1.51×10^{-3}	-0.488
0.005	0.05	10^{3}	-2.52×10^{-2}	**-1.50**	-4.77×10^{-2}	**-2.06**	-7.12×10^{-2}	**-2.34**
0.005	0.05	10^{-3}	-2.66×10^{-3}	-0.337	-3.79×10^{-3}	-0.613	-1.75×10^{-2}	**-2.04**
0.01	0	10^{3}	-1.03×10^{-3}	-6.69×10^{-2}	-1.30×10^{-3}	-0.120	-1.03×10^{-3}	-0.441
0.01	0	10^{-3}	-2.44×10^{-4}	-1.43×10^{-2}	-3.10×10^{-4}	-2.61×10^{-2}	-4.53×10^{-4}	-9.73×10^{-2}
0.01	0.001	10^{3}	-1.29×10^{-3}	-9.68×10^{-2}	-1.70×10^{-3}	-0.174	-1.17×10^{-3}	-0.638
0.01	0.001	10^{-3}	-3.04×10^{-4}	-2.09×10^{-2}	-4.01×10^{-4}	-3.80×10^{-2}	-5.86×10^{-4}	-0.141
0.01	0.005	10^{3}	-2.33×10^{-3}	-0.217	-3.18×10^{-3}	-0.391	-8.24×10^{-3}	**-1.41**
0.01	0.005	10^{-3}	-5.41×10^{-4}	-4.72×10^{-2}	-7.98×10^{-4}	-8.57×10^{-2}	-1.12×10^{-3}	-0.317
0.01	0.01	10^{3}	-3.47×10^{-3}	-0.367	-4.43×10^{-3}	-0.662	-2.18×10^{-2}	**-2.07**
0.01	0.01	10^{-3}	-8.26×10^{-4}	-8.01×10^{-2}	-1.34×10^{-3}	-0.145	-1.71×10^{-3}	-0.538
0.01	0.05	10^{3}	-2.56×10^{-2}	**-1.53**	-4.85×10^{-2}	**-2.09**	-7.22×10^{-2}	**-2.33**
0.01	0.05	10^{-3}	-2.77×10^{-3}	-0.344	-3.85×10^{-3}	-0.626	-1.86×10^{-2}	**-2.05**
0.05	0	10^{3}	-4.92×10^{-3}	-0.340	-6.10×10^{-3}	-0.613	-2.58×10^{-2}	**-1.87**
0.05	0	10^{-3}	-1.18×10^{-3}	-7.19×10^{-2}	-1.73×10^{-3}	-0.132	-2.15×10^{-3}	-0.491
0.05	0.001	10^{3}	-5.13×10^{-3}	-0.370	-6.44×10^{-3}	-0.668	-2.89×10^{-2}	**-1.91**
0.05	0.001	10^{-3}	-1.23×10^{-3}	-7.85×10^{-2}	-1.83×10^{-3}	-0.144	-2.24×10^{-3}	-0.535
0.05	0.005	10^{3}	-6.12×10^{-3}	-0.491	-9.70×10^{-3}	-0.887	-4.04×10^{-2}	**-1.95**
0.05	0.005	10^{-3}	-1.44×10^{-3}	-0.105	-2.22×10^{-3}	-0.192	-2.56×10^{-3}	-0.711
0.05	0.01	10^{3}	-9.44×10^{-3}	-0.645	-1.54×10^{-2}	**-1.15**	-4.62×10^{-2}	**-2.16**
0.05	0.01	10^{-3}	-1.69×10^{-3}	-0.138	-2.64×10^{-3}	-0.252	-2.90×10^{-3}	-0.931
0.05	0.05	10^{3}	-4.12×10^{-2}	**-1.68**	-6.28×10^{-2}	**-2.01**	-8.08×10^{-2}	**-2.20**
0.05	0.05	10^{-3}	-3.79×10^{-3}	-0.403	-4.28×10^{-3}	-0.733	-2.61×10^{-2}	**-2.13**

Chapter 8

Non-linear evolutions of magnetised thick discs around black holes: dependence on the initial data

This chapter is based on the following publication: A. Cruz-Osorio, S. Gimeno-Soler & J. A. Font. Non-linear evolutions of magnetized thick discs around black holes: dependence on the initial data, *MNRAS* 492, 5730-5742 (2020), DOI: 10.1093/mnras/staa216.

8.1 Introduction

Astrophysical systems consisting of stellar mass black holes surrounded by thick discs (or tori) are broadly regarded as natural end results of catastrophic events involving compact objects. To a significant extent, our theoretical understanding of the formation of those systems has been built from ever more accurate numerical simulations. Two distinctive examples that keep receiving major numerical attention are binary mergers formed by either two neutron stars or by a black hole and a neutron star. Numerical work has shown that those types of mergers may quite generically lead to rotating black holes surrounded

by geometrically thick accretion discs (see, e.g. [Shibata and Taniguchi 2011b, Baiotti and Rezzolla 2017] and references therein).

Likewise, understanding the long-term dynamics of black hole-torus systems also requires to perform time-dependent numerical simulations. Most studies have made use of a rather simplistic model in which the specific angular momentum of the disc is assumed to be constant. In a purely hydrodynamical context this model is commonly refereed to as a 'Polish doughnut', after the seminal work by Abramowicz, Jaroszynski, and Sikora [1978] (but see also [Fishbone and Moncrief 1976]). The extension to the MHD regime of a constant angular momentum disc endowed with a toroidal magnetic field was achieved by Komissarov [2006] (see also [Gimeno-Soler and Font 2017] for the non-constant angular momentum case and [Pimentel, Lora-Clavijo, and Gonzalez 2018, Pimentel, Lora-Clavijo, and González 2018] for models including magnetic polarisation). Polish doughnuts have been extensively used to study instabilities of accretion flows onto black holes (e.g. the runaway instability [Abramowicz, Calvani, and Nobili 1983] and the Papaloizou-Pringle instability (PPI) [Papaloizou and Pringle 1984]) and the formation of jets and outflows (see e.g. [Font and Daigne 2002, De Villiers and Hawley 2003b, Daigne and Font 2004, Fragile et al. 2007, Dexter and Fragile 2011, Dexter, McKinney, and Agol 2012, McKinney, Tchekhovskoy, and Blandford 2012, McKinney et al. 2014, Wielgus et al. 2015, Fragile and Sądowski 2017, Bugli et al. 2018, Witzany and Jefremov 2018, Janiuk et al. 2018]). In all of these works the self-gravity of the fluid/MHD is neglected in the construction of the equilibrium configurations and in the subsequent time evolutions. Equilibrium solutions of self-gravitating tori around black holes, for which the initial data satisfy the constraint equations of the coupled Euler-Einstein system, have been obtained in the purely hydrodynamical constant angular momentum case by Shibata [2007] (see also [Mach et al. 2019] for the magnetised non-constant angular momentum case) and by Stergioulas [2011b] (see [Korobkin et al. 2011, Mewes et al. 2016] for numerical relativity simulations of those solutions). Moreover, Shibata and Sekiguchi [2012] obtained solutions of self-gravitating and magnetised tori accounting for the coupled system of radiation, general relativistic MHD and the Einstein equations.

The way the magnetic field is accounted for in the equilibrium solutions is, for most approaches in the literature, essentially arbitrary, i.e., its influence on the disc morphology is not treated in a self-consistent fashion. As a result, the initial distribution and strength of the magnetic field in the torus may impact the subsequent time evolution and lead to potential inaccuracies. Early attempts, e.g. [Koide, Shibata, and Kudoh 1999], were based on equilibrium

hydrodynamical solutions of a disc around a black hole which was arbitrarily seeded by a uniform magnetic field in the direction perpendicular to the disc. In most recent approaches, the magnetic field distribution is derived from an 'ad hoc' guess for the vector potential. This allows to study both poloidal and toroidal configurations of the magnetic field and sets the framework to study the growth of the magneto-rotational instability (MRI), the redistribution of the angular momentum and the accretion mechanism itself [De Villiers and Hawley 2003a, De Villiers and Hawley 2003b, Gammie, McKinney, and Tóth 2003, Anninos, Fragile, and Salmonson 2005, Noble et al. 2006, McKinney and Blandford 2009, Hawley, Guan, and Krolik 2011, McKinney, Tchekhovskoy, and Blandford 2012, Shiokawa et al. 2012, Sorathia, Krolik, and Hawley 2013, Penna, Kulkarni, and Narayan 2013, Foucart et al. 2016, Anninos et al. 2017, Porth et al. 2017, Mizuta et al. 2018]. Similar configurations have been used in recent MHD simulations in general relativity of mini-discs in binary black hole mergers [Bowen et al. 2018], neutrino-cooled thick accretion discs [Siegel and Metzger 2017, Siegel and Metzger 2018], or to compute the shadows around the black holes of SgrA^* [Chan et al. 2015] or M87* [Event Horizon Telescope Collaboration et al. 2019a, Event Horizon Telescope Collaboration et al. 2019c].

In this paper we study whether the way the initial magnetic field distribution in a thick disc is built has an impact on the long-term dynamics of the system and, if so, how significant.

To this aim we build magnetised Polish doughnuts around rotating black holes, neglecting the self-gravity of the discs and using three different approaches to account for the magnetic field, namely: i) a purely hydrodynamical solution (see e.g. [Abramowicz, Jaroszynski, and Sikora 1978, Font and Daigne 2002, Daigne and Font 2004]) in which an 'ad hoc' toroidal magnetic field is seeded afterwards; ii) the self-consistent solution from Komissarov [2006], in which the distribution of the rest-mass density of the disc is coupled to the toroidal magnetic field through the equation of state for the magnetic pressure; this approach assumes that the fluid is thermodynamically non-relativistic; and iii) the self-consistent approach of Komissarov [2006] but dropping the assumption of a thermodynamically non-relativistic fluid, as done in Montero et al. [2007] and Gimeno-Soler et al. [2019]. Using these three approaches we build initial data and compare their non-linear dynamical evolutions by means of axisymmetric numerical simulations, finding interesting differences. Our study has been limited to axisymmetry to reduce the computational cost involved in the simulations, since we are interested in the long-term dynamics of the discs, which are evolved up to 100 orbital periods. We note that the first approach has been employed

in some general relativistic magneto-hydrodynamics (GRMHD) simulations of magnetised thick discs (e.g. Gammie, McKinney, and Tóth [2003], Noble et al. [2006], Shiokawa et al. [2012], Porth et al. [2017], Mizuta et al. [2018], and Bowen et al. [2018]) albeit for poloidal configurations of the magnetic field which are MRI unstable.

All configurations considered in this paper are purely toroidal. Currently, our self-consistent approach to build stationary magnetised discs around black holes can only accommodate toroidal magnetic fields. We plan to extend our approach to poloidal magnetic fields in the future and, if possible, perform a similar comparison with the ad hoc poloidal magnetic field configurations employed in the literature.

The paper is organised as follows: In Section 8.2 we summarise the problem setup, i.e. the equations of general relativistic MHD and the numerical code. Section 8.3 describes the three types of approaches we follow to construct the initial data for magnetised tori. The results of the time evolutions and the comparison among the three approaches are presented in Section 8.4. Finally Section 8.5 summarises our conclusions. Unless stated otherwise we use geometrised units in which the light speed, Newton's constant, and the mass of the black hole are equal to one, $c = G = M = 1$, the Kerr metric has the signature $(-,+,+,+)$, and the $1/4\pi$ factor in the MHD equations is assumed to be one.

8.2 Setup

To describe the Kerr black hole spacetime we use horizon-penetrating Kerr-Schild coordinates with a logarithmic radial coordinate. In the 3+1 decomposition the line element and metric potentials are written as

$$\begin{aligned}
ds^2 &= -(\alpha^2 - \beta_i\beta^i)dt^2 + 2\beta_i dx^i dt + \gamma_{ij}dx^i dx^j, \qquad (8.1)\\
\alpha &= \left(1 + 2Me^R/\varrho^2\right)^{-1/2},\\
\beta^R &= e^R \frac{2M}{\varrho^2}\left(1 + 2Me^R/\varrho^2\right)^{-1},\\
\gamma_{RR} &= \left(1 + 2Me^R/\varrho^2\right)e^{2R}, \qquad \gamma_{\theta\theta} = \varrho^2,\\
\gamma_{R\phi} &= -ae^R\left(1 + 2Me^R/\varrho^2\right)\sin^2\theta,\\
\gamma_{\phi\phi} &= \sin^2\theta\,[\,\varrho^2 + a^2\left(1 + 2Me^R/\varrho^2\right)\sin^2\theta]
\end{aligned}$$

where M stands for mass of the black hole and $a = J/M$ is the rescaled angular momentum of the black hole. Note that, in the above expressions the lapse function α, the shift vector β^i and the three-metric components γ_{ij}

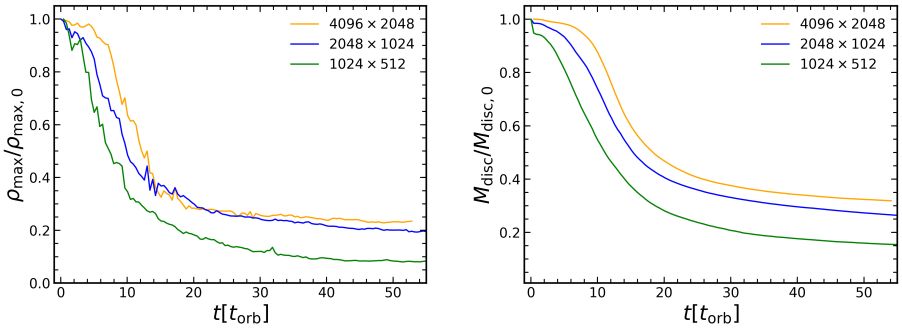

Figure 8.1 Grid resolution comparison: evolution of the maximum rest-mass density normalised by the initial value (left) and of the mass of the disc (right) for model KMρ-D. The time is given in units of the orbital period at the centre of the disc and the effective number of zones employed in each simulation are indicated in the legend. For all grid resolutions, the density maximum and the mass of the disc gradually decrease as a result of accretion until they reach constant asymptotic values. With the standard base grid used in our simulations, the final values of the two quantities are underestimated by about 10%.

are written using a modified Kerr-Schild coordinate such as $r = e^R$ (and then $\varrho^2 \equiv e^{2R} + a^2 \cos^2\theta$).

The general relativistic ideal MHD (GRMHD) evolution equations are obtained from the baryon number conservation, the local conservation of the energy-momentum tensor $T^{\mu\nu}$ and the Maxwell equations

$$\nabla_\mu(\rho u^\mu) = 0\,, \tag{8.2}$$

$$\nabla_\mu T^{\mu\nu} = 0\,, \tag{8.3}$$

$$\nabla_\mu {}^*F^{\mu\nu} = 0\,, \tag{8.4}$$

where ρ is the rest-mass density, and $F^{\mu\nu}$ and ${}^*F^{\mu\nu} = b^\mu u^\nu - b^\nu u^\mu$ are the Faraday tensor and its dual with respect to an observer with four-velocity u^μ, respectively. The energy-momentum tensor for a magnetised perfect fluid can be written as

$$T^{\mu\nu} = \rho h_{\rm tot} u^\mu u^\nu + p_{\rm tot} g^{\mu\nu} - b^\mu b^\nu, \tag{8.5}$$

where $h_{\rm tot} = 1 + \epsilon + p/\rho + b^2/\rho$ is the total specific enthalpy, $p_{\rm tot} = p + p_{\rm m}$ is the total pressure and $p_{\rm m} = b^2/2$ can be seen as the magnetic field contribution to the total pressure, and $b^2 = b_\mu b^\mu$ is the square of the magnetic field four-vector. Given the spacetime metric we can write the GRMHD equations in flux-conservative form, in the so-called Valencia formulation [for details see Antón et al. 2006, Porth et al. 2017].

The numerical simulations reported in this paper are performed in axisymmetry using the `BHAC` code [Porth et al. 2017]. This code solves the GRMHD equations with a third-order Runge-Kutta method of lines [Shu and Osher 1988] together with high-resolution shock-capturing algorithms. We use the HLLE two-wave flux formula [Harten, Lax, and Leer 1983, Einfeldt 1988] and a modified five-order WENO-Z cell reconstruction scheme [Acker, B. de R. Borges, and Costa 2016]. We note that modern extensions of HLLE such as the five-wave HLLD method [Mignone, Ugliano, and Bodo 2009, Matsumoto, Miyoshi, and Takasao 2019], where the complete fan of waves is considered, are not yet implemented in `BHAC`. The preservation of the no magnetic monopoles constriction is achieved by using the flux constrained transport method [for more details see Olivares Sánchez, Porth, and Mizuno 2018]. Primitive variables are recovered using the inversion technique 2DW from Noble et al. [2006]. The density and the pressure of the atmosphere outside of the magnetised tori used in our simulations are $\rho_{\rm atm} = \rho_0 r^{-3/2}$ and $p_{\rm atm} = p_0 r^{-5/2}$ where $\rho_0 = 10^{-5}$ and $p_0 = 10^{-7}$ as used in Noble et al. [2006]. In addition, the magnetic field is set to zero if $\rho \leq \rho_{\rm atm}$.

Both to build the initial data and in the time-dependent simulations we use a numerical (r, θ) grid with three refinement levels in a domain $r \in [0.5M, 1000M]$. Outflow boundary conditions are applied in the radial direction and reflecting boundary conditions in the angular direction. We use three levels of octree adaptive mesh refinement in the base grid with 512×256 zones in $r \times \theta$, respectively. The error estimator formula from Lohner [1987] is applied to the rest-mass density and magnetic field with a tolerance of 0.1. This error is monitored every 1000 time iterations, changing the grid resolution when necessary. Our two finer grids have thus 1024×512 and 2048×1024 zones, respectively. Test runs with a factor 2 coarser and finer grids have been carried out for validation purposes, as displayed in Fig. 8.1. This figure shows the time evolution for over 50 orbital periods of the (normalised) mass of one of our accretion discs and of the maximum of the rest-mass density. For this grid comparison we employ a representative highly magnetised model of our sample (namely, case D of model `KM`ρ; see below). We explore three effective resolutions, with 1024×512, 2048×1024 and 4096×2048 cells, respectively. In the two quantities plotted in Fig. 8.1 we can see that, as a result of accretion on to the black hole, the density maximum and the mass of the disc gradually decrease until they reach constant asymptotic values. While the particular final values are sensitive to the resolution employed, the actual trend is similar for all resolutions. From this figure we conclude that, with our standard base grid, the final values of the maximum density and of the mass of the disc are underestimated by about

10%. Keeping this in mind, and considering that employing a high-resolution grid with 4096×2048 zones would be highly time-consuming (even in axisymmetry) for our long-term evolutions extending up to about 100 orbital periods, we use the standard base grid in all results discussed in this paper.

8.3 Initial data for magnetised thick discs

Since the standard procedure to build a stationary accretion disc around a Kerr black hole is well known, we will only sketch it here skipping most details. The interested reader is addressed to Abramowicz, Jaroszynski, and Sikora [1978], Komissarov [2006], and Montero et al. [2007] for details.

We begin by assuming a stationary and axisymmetric fluid field in a Kerr background. Also, we consider a purely toroidal magnetic field (i.e. $b^r = b^\theta = 0$). By contracting the conservation law for the energy-momentum tensor with the projection tensor $h^\alpha_{\ \beta} = \delta^\alpha_{\ \beta} + u^\alpha u_\beta$ and following Komissarov [2006], we can rewrite the conservation law in terms of the specific angular momentum $l = -u_\phi/u_t$ and of the angular velocity $\Omega = u^\phi/u^t$, to obtain

$$\partial_i(\ln|u_t|) - \frac{\Omega\partial_i l}{1-l\Omega} + \frac{\partial_i p}{\rho h} + \frac{\partial_i(\mathcal{L}b^2)}{2\mathcal{L}\rho h} = 0\,, \tag{8.6}$$

where $i = r, \theta$ and $\mathcal{L} \equiv g_{t\phi}^2 - g_{tt}g_{\phi\phi}$. It is also useful to introduce the definition of total (gravitational plus centrifugal) potential [Abramowicz, Jaroszynski, and Sikora 1978] as

$$W = \ln|u_t| - \int_l^{l_\infty} \frac{\Omega\partial_i l}{1-l\Omega}. \tag{8.7}$$

From this point on, and as we previously mentioned, we take three different approaches to integrate Eq. (8.6) which are discussed next.

8.3.1 Non-magnetised torus plus toroidal magnetic field

Following the procedure described by Font and Daigne [2002] we can construct a non-magnetised torus and subsequently seed it with a magnetic field. We denote the corresponding model as `MFD`. To do this, we simply need to take $b = 0$ in Eq. (8.6). Then, assuming a constant distribution of angular momentum and a barotropic equation of state (EoS) $\rho = \rho(p)$ we can rewrite Eq. (8.6) as

$$\mathrm{d}\left(\ln|u_t| + \int_0^p \frac{\mathrm{d}p}{\rho h}\right) = 0\,. \tag{8.8}$$

At the inner edge of the disc we assume $u_t = u_{t_{\rm in}}$ and $p = 0$, and we can rewrite the above equation as

$$W - W_{\rm in} + \int_0^p \frac{{\rm d}p}{\rho h} = 0 \tag{8.9}$$

where we have used the definition of the potential, Eq. (8.7). Using a polytropic EoS $p = K\rho^\Gamma$, with K and Γ constants, and the definition of the specific enthalpy, we can integrate Eq. (8.9)

$$W_{\rm in} - W = \ln \frac{h}{h_{\rm in}}\,, \tag{8.10}$$

which can be rewritten as

$$h = h_{\rm in} e^{\Delta W}\,, \tag{8.11}$$

where $\Delta W = W_{\rm in} - W$. Then, we can write the expressions for the rest-mass density and the fluid pressure

$$\rho = \left(\frac{\Gamma - 1}{\Gamma}\frac{(h_{\rm in}e^{\Delta W} - 1)}{K}\right)^{1/(\Gamma-1)}\,, \tag{8.12}$$

$$p = \left(\frac{\Gamma - 1}{\Gamma}\frac{(h_{\rm in}e^{\Delta W} - 1)}{K^{1/\Gamma}}\right)^{\Gamma/(\Gamma-1)}\,. \tag{8.13}$$

To complete the model, following Porth et al. [2017] we add an 'ad hoc' toroidal magnetic field in the following way: we choose a value for the magnetisation parameter $\beta_{\rm m} = p/p_{\rm m}$ and insert Eq. (8.13) in its definition to arrive at

$$p_{\rm m} = \frac{1}{\beta_{\rm m}}\left(\frac{\Gamma - 1}{\Gamma}\frac{(h_{\rm in}e^{\Delta W} - 1)}{K^{1/\Gamma}}\right)^{\Gamma/(\Gamma-1)}\,, \tag{8.14}$$

which provides the magnetic pressure in this approach. Note that, in this model, the ratio between the pressure p and the magnetic pressure $p_{\rm m}$ (i.e., $\beta_{\rm m}$) remains constant throughout the disc. To obtain the non-zero components of the magnetic field, we use

$$b^\phi = \sqrt{\frac{2p_{\rm m}}{\mathcal{A}}}, \tag{8.15}$$

$$b^t = l b^\phi, \tag{8.16}$$

where $\mathcal{A} \equiv g_{\phi\phi} + 2l g_{t\phi} + l^2 g_{tt}$.

8.3.2 Magnetised torus plus relativistic fluid

Our second approach follows the procedure described in Montero et al. [2007] which takes into account the magnetic field from the beginning to construct the

disc in a self-consistent way. We denote this model as `KM`ρ. First, we choose a barotropic EoS $\rho = \rho(p)$ of the same form as before

$$p = K\rho^{\Gamma}\,, \tag{8.17}$$

and we introduce the magnetic pressure, $p_{\rm m} = b^2/2$, and the following quantities: $w = \rho h$, , $\tilde{w} = \mathcal{L}w$ and $\tilde{p}_{\rm m} = \mathcal{L}p_{\rm m}$. We can write a similar equation to Eq. (8.17) for the magnetic pressure

$$\tilde{p}_{\rm m} = K_{\rm m}\tilde{w}^{q}\,, \tag{8.18}$$

where K_m and q are constants. In terms of the magnetic pressure, this equation reads

$$p_{\rm m} = K_{\rm m}\mathcal{L}^{q-1}w^{q}\,. \tag{8.19}$$

This particular choices of EoS for the fluid pressure and the magnetic pressure fulfill the general relativistic version of the von Zeipel theorem for a toroidal magnetic field [von Zeipel 1924, Zanotti and Pugliese 2015]. This allows us to integrate Eq. (8.6)

$$\ln|u_t| - \int_0^l \frac{\Omega {\rm d}l}{1-\Omega l} + \int_0^p \frac{{\rm d}p}{\rho h} + \int_0^{\tilde{p}_{\rm m}} \frac{{\rm d}\tilde{p}_{\rm m}}{\tilde{w}} = \text{const.} \tag{8.20}$$

Following the same reasoning as in the previous section, we can find the constant of integration as

$$\text{const.} = \ln|u_t| - \int_{l_{\rm in}}^{l} \frac{\Omega {\rm d}l}{1-\Omega l}. \tag{8.21}$$

If we insert in this expression the definition of the total potential Eq. (8.7) we can rewrite the previous expression as

$$W - W_{\rm in} = \int_0^p \frac{{\rm d}p}{\rho h} + \int_0^{\tilde{p}_{\rm m}} \frac{{\rm d}\tilde{p}_{\rm m}}{\tilde{w}}. \tag{8.22}$$

Substituting the EoS and taking into account that our fluid is ideal and isentropic, we can integrate Eq. (8.22) as

$$W - W_{\rm in} + \ln\left(\frac{h}{h_{\rm in}}\right) + \frac{q}{q-1}K_{\rm m}(\mathcal{L}w)^{q-1} = 0\,, \tag{8.23}$$

where we have used that $p_{\rm in} = p_{\rm m,in} = \rho_{\rm in} = 0$. We can rewrite this equation in terms of the rest-mass density ρ

$$\begin{aligned} &W - W_{\rm in} + \ln\left(1 + \frac{K\Gamma}{\Gamma-1}\rho^{\Gamma-1}\right) + \\ &\frac{q}{q-1}K_{\rm m}\left[\mathcal{L}\left(\rho + \frac{K\Gamma\rho^{\Gamma}}{\Gamma-1}\right)\right]^{q-1} = 0. \end{aligned} \tag{8.24}$$

Table 8.1 Summary of some relevant quantities of our different models, namely: the magnetisation parameter at the centre of the disc $\beta_{\rm m,c}$, the location of the maximum of the rest-mass density $r_{\rm max}$, the radial location of the outer boundary of the disc at the equatorial plane $r_{\rm out}$ (the inner boundary is at $r_{\rm in}$=1.25 for all discs), the maximum of the rest-mass density of the initial data $\rho_{\rm max,0}$ (adjusted for a disc initial mass of $M = 0.1M_{\rm BH}$), the mass of the disc at the initial time $M_{\rm disc,0}$, the maximum of the rest-mass density at the end of our simulation $\rho_{\rm max,F}$, and the final mass of the disc $M_{\rm disc,F}$.

Model	$\beta_{\rm m,c}$	$r_{\rm max}$	$r_{\rm out}$	$\rho_{\rm max,0}$	$M_{\rm disc,0}$	$\rho_{\rm max,F}$	$M_{\rm disc,F}$
`MFD-A`	10^{3}	1.99	209.0	4.47×10^{-4}	0.1000	7.78×10^{-4}	0.0737
`MFD-B`	10^{1}	1.99	209.0	4.47×10^{-4}	0.1000	4.66×10^{-4}	0.0744
`MFD-C`	10^{-1}	1.99	209.0	4.47×10^{-4}	0.1000	3.01×10^{-5}	0.0084
`MFD-D`	10^{-3}	1.99	209.0	4.47×10^{-4}	0.1000	4.47×10^{-9}	0.0000
`KMh-A`	10^{3}	1.99	37.40	1.71×10^{-3}	0.1000	1.51×10^{-3}	0.0911
`KMh-B`	10^{1}	1.92	36.41	1.71×10^{-3}	0.0643	1.33×10^{-3}	0.0592
`KMh-C`	10^{-1}	1.57	28.97	2.99×10^{-3}	0.0234	7.31×10^{-4}	0.0078
`KMh-D`	10^{-3}	1.54	28.21	3.41×10^{-3}	0.0237	5.07×10^{-4}	0.0054
`KM`ρ`-A`	10^{3}	1.99	37.40	1.84×10^{-3}	0.100	2.12×10^{-3}	0.0902
`KM`ρ`-B`	10^{1}	1.92	36.41	1.83×10^{-3}	0.071	1.69×10^{-3}	0.0656
`KM`ρ`-C`	10^{-1}	1.57	28.97	3.25×10^{-3}	0.025	8.37×10^{-4}	0.0083
`KM`ρ`-D`	10^{-3}	1.54	28.21	3.63×10^{-3}	0.025	5.57×10^{-4}	0.0058

We should note that Eq. (8.23) is equivalent to Eq. (8.11) in the previous section for a non-magnetised flow ($K_{\rm m} = 0$). Also, it is important to note that Eq. (8.24) is a trascendental equation and must be solved numerically.

8.3.3 Magnetised torus plus non-relativistic fluid

We describe next our third procedure to build a magnetised torus. This one is based on the approach introduced by Komissarov [2006]. This solution is obtained by assuming the rest-mass density ρ to be almost equal to the fluid enthalpy $\rho \simeq w$ (i.e. $h \simeq 1$). This approximation means that the fluid is non-relativistic from a thermodynamical point of view. We denote the corresponding disc model as `KM`h.

Since $\rho \simeq w$, we rewrite Eq. (8.17) as $p = Kw^{\Gamma}$. Substituting this into the definition of the specific enthalpy h and taking the first-order Taylor series expansion of the logarithm around $h \simeq 1$ of Eq. (8.23) yields

$$W - W_{\rm in} + \frac{K\Gamma}{\Gamma-1}w^{\Gamma-1} + \frac{q}{q-1}K_{\rm m}(\mathcal{L}w)^{q-1} = 0\,, \tag{8.25}$$

which is the equation for w obtained by Komissarov [2006] and it can be solved algebraically.

It is interesting to make a few remarks concerning the validity of the approximation. First of all, we can neglect the magnetic field (i.e. $K_{\rm m} \to 0$) to obtain the non-magnetised fluid approximation. In this case, we can see that the specific enthalpy can be written as

$$h = 1 + |\Delta W|. \tag{8.26}$$

This result can be considered as the first-order Taylor series approximation of Eq. (8.11). Then, this shows that, for a non-magnetised flow, $h \simeq 1$ is valid only for small values of $|\Delta W|$. This is not a source of concern as the upper bound[1] for $|\Delta W|$ goes from $|\Delta W| \simeq 0.0431$ for a Schwarzschild black hole ($a = 0$) to $|\Delta W| = \frac{1}{2}\ln 3 \simeq 0.549$ for a extremal Kerr black hole ($a = 1$) [Abramowicz, Jaroszynski, and Sikora 1978]. Conversely, for a strongly magnetised disc, $p_{\rm m} \gg p$, it is easy to see that no approximation is done, and this also could be seen as $h \to 1$ when $K \to 0$. This shows that the non-relativistic fluid approximation is always valid for strong enough magnetised flows (irrespective of the value of the total potential well $|\Delta W|$).

8.3.4 Parameters and construction of the discs

In order to build the discs we have to choose a suitable set of parameters for each one of the three approaches. For the `MFD` model (and following [Font and Daigne 2002]) we fix the specific enthalpy at the inner edge of the disc as $h_{\rm in} = 1$ and the polytropic constant as $K = 1.5 \times 10^{20}$cgs. The free parameters for this approach are the adiabatic exponent Γ, the radial coordinate of the inner edge of the disc $r_{\rm in}$ (and thus, the total potential at the inner edge of the disc $W_{\rm in}$), and the specific angular momentum l. For the `KM`ρ model, we fix the rest-mass density at the centre $\rho_{\rm c}$ as $\rho_{\rm c} = 1$ and we also set the exponent of the magnetic pressure EoS equal to the exponent of the fluid pressure EoS, $q = \Gamma$. The free parameters for this approach are then Γ, $r_{\rm in}$, l, and the magnetisation parameter at the centre of the disc, $\beta_{\rm m,c}$. Finally, for the `KM`h model, we proceed as for the `KM`ρ model but fixing the fluid enthalpy at the centre, $w_{\rm c} = 1$.

For the sake of simplifying the comparison between the three approaches, we fix most of the parameters that characterise the discs and only vary the value of the magnetisation parameter. Therefore, our discs are described by the following set of parameters: the polytropic exponent, which is set to $\Gamma = 4/3$, the constant specific angular momentum, which is set to the value of the Keplerian angular momentum at the marginally bound orbit $l = l_{\rm K}(r_{\rm mb}) = 2.2$, the

[1] The upper bound of $|\Delta W|$ is achieved for a Keplerian angular momentum at the radius of the marginally bound orbit, $l = l_{\rm K}(r_{\rm mb})$ and $r_{\rm in} = r_{\rm mb}$ (this implies $W_{\rm in} = 0$).

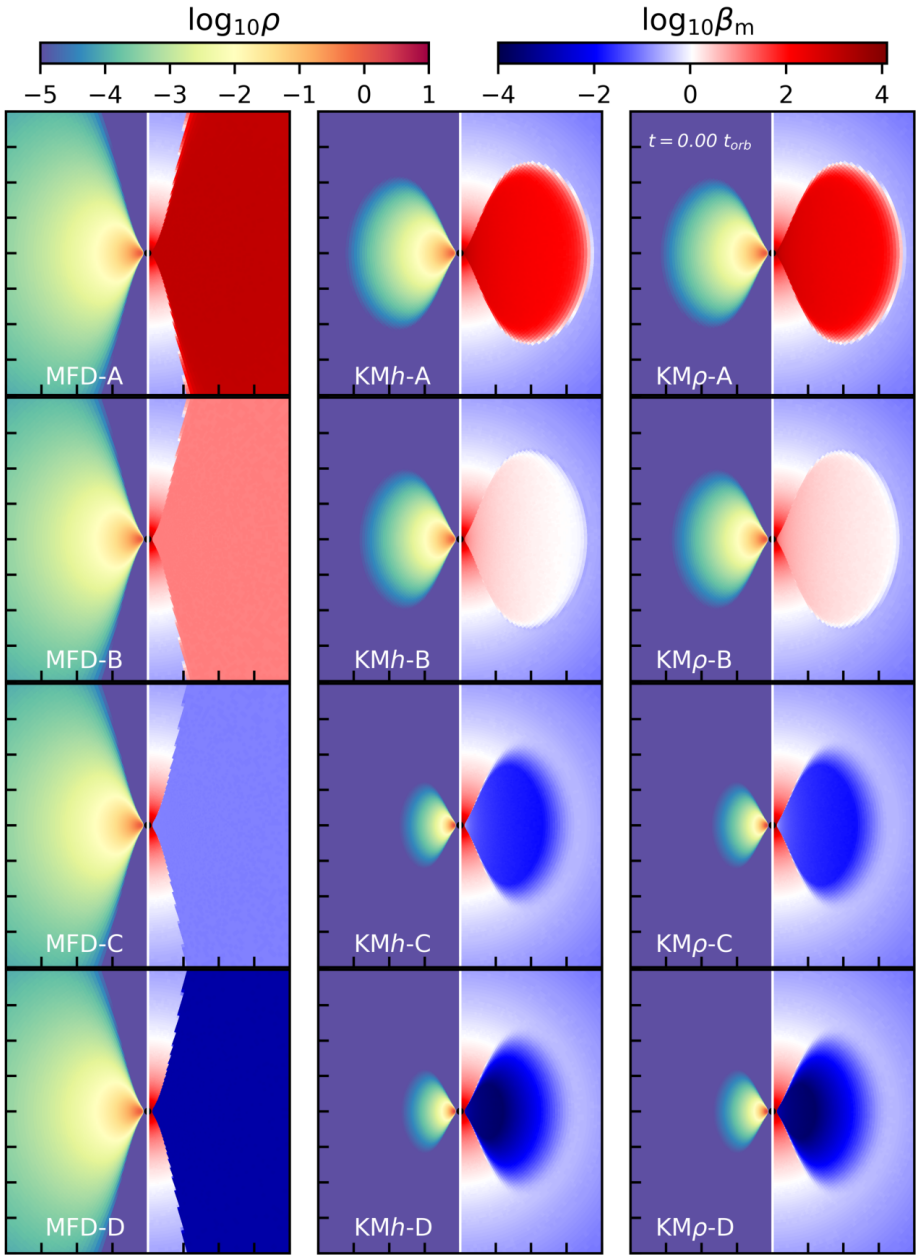

Figure 8.2 Initial morphology of the rest-mass density (left side of each panel) and magnetisation parameter $\beta_{\rm m}$ (right side of each panel) for our sample of magnetised tori around a Kerr black hole with spin $a = 0.99$ (black circle). From left to right, the columns correspond to models built following the `MFD`, `KM`h, and `KM`ρ approaches, respectively. From top to bottom, the rows correspond to models with different values of the magnetisation parameter $\beta_{\rm m,c}$, namely 10^{3}, 10^{1}, 10^{-1}, and 10^{-3}. The domain plotted on each panel corresponds to $(x, z) \in [-40M, 40M] \times [-40M, 40M]$. For models `KM`$h$ and `KM`ρ the discs are smaller and the maximum of the density is further inward the lower the value of $\beta_{\rm m,c}$. Models `MFD` do not show such dependence as they are purely hydrodynamical initially.

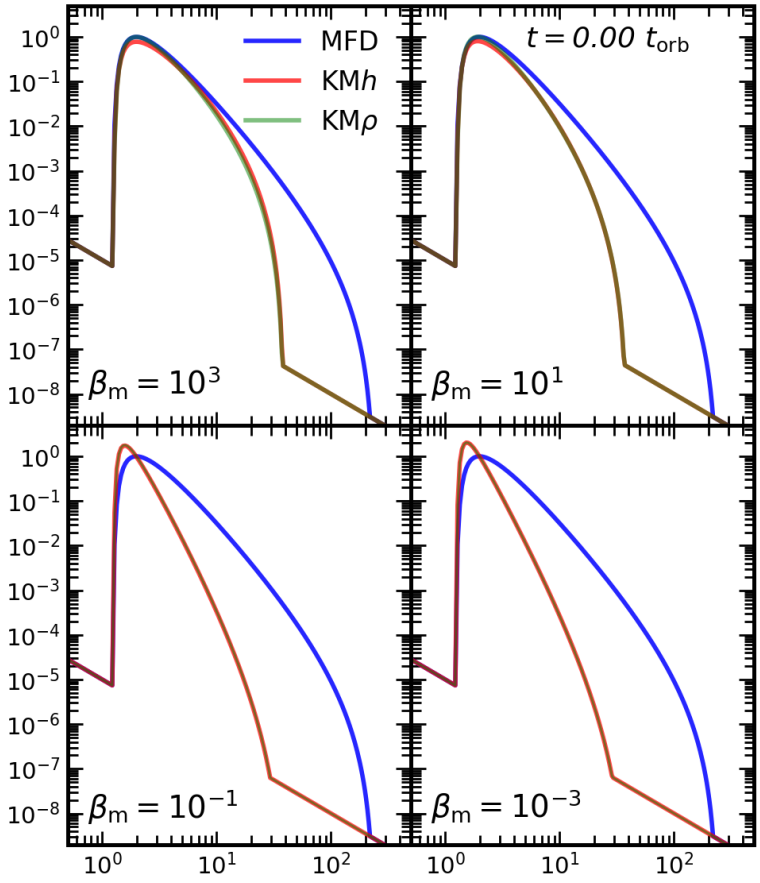

Figure 8.3 Radial profiles of the rest-mass density at the equatorial plane at the initial time for the four values of the magnetisation parameter considered, indicated in the legends. Blue, red and green lines correspond to approaches `MFD`, `KM`h and `KM`ρ to build the initial data, respectively. The radial extent of the `MFD` discs does not depend on $\beta_{\rm m}$ and is significantly larger than that of the two other approaches that incorporate the magnetic field in a self-consistent way. `KM`h and `KM`ρ discs are hardly distinguishable, becoming practically identical in the most highly magnetised cases (the red and green lines overlap in the bottom panels).

radial coordinate of the inner edge of the disc, which is chosen to be such that $W_{\rm in} = 0.1W_{\rm c}$ and leads to $r_{\rm in} = 1.25$ (then, the potential gap is set to $\Delta W = 0.222$), the black hole spin, set to $a = 0.99$, the radius of the cusp, $r_{\rm cusp} = 1.21$, and the radius of the centre of the disc, $r_{\rm c} = 1.99$. We furthermore introduce a dynamical timescale given by the orbital period measured at the centre of the tori, $t_{\rm orb} = 23.86$. In total we build and evolve 12 equilibrium models, corresponding to the three ways to construct the initial data for magnetised tori, namely `MFD`, `KM`h, and `KM`ρ, and four different values of the magnetisation parameter at the centre of the disc, $\beta_{\rm m,c} = 10^3, 10, 10^{-1}$, and 10^{-3}, cases A, B, C and D, respectively. Case A corresponds to a weakly magnetised disc (i.e., nearly purely hydrodynamical) and case D is a highly magnetised torus, while the other two are intermediate cases. Numerical values for some relevant quantities characterising the 12 disc models are reported in Table 1. In order to test the dynamics of the tori, we apply a 4% perturbation on the thermal pressure, namely we use $p = p(1 + 0.04\chi_r)$, where $\chi_r = (2r_i - 1)$ and r_i is a random number. We note that, while the discs do not completely fill their corresponding Roche lobe, the addition of this perturbation is enough to trigger accretion.

8.4 Results

8.4.1 Initial data

We start by discussing the initial data of the 12 disc models we are going to evolve. These models are depicted in Figs. 8.2 to 8.5, which display the 2D morphology of the discs (Fig. 8.2) and the radial profiles of selected quantities on the equatorial plane (Figs. 8.3 to 8.5).

Fig. 8.2 shows the logarithm of the rest-mass density and the logarithm of the magnetisation parameter for our sample of 12 initial models. Each row of this figure corresponds to a different value of the magnetisation parameter at the centre of the disc and each column indicates one of the three approaches we use to construct the magnetised discs. We note that, despite the atmosphere has no magnetic field, in order to plot the magnetisation $\beta_{\rm m} = p/p_{\rm m}$ we need to select a non-zero value of the magnetic pressure (namely, $p_{\rm m} = 10^{-10}$). This explains the spherical distribution of the magnetisation parameter visible outside the discs in figure 8.2 (and in Fig. 8.6 below).

For models `MFD-A` to `MFD-D` (left panel of the first column), the rest-mass density and all thermodynamical quantities are identical due to the fact that the

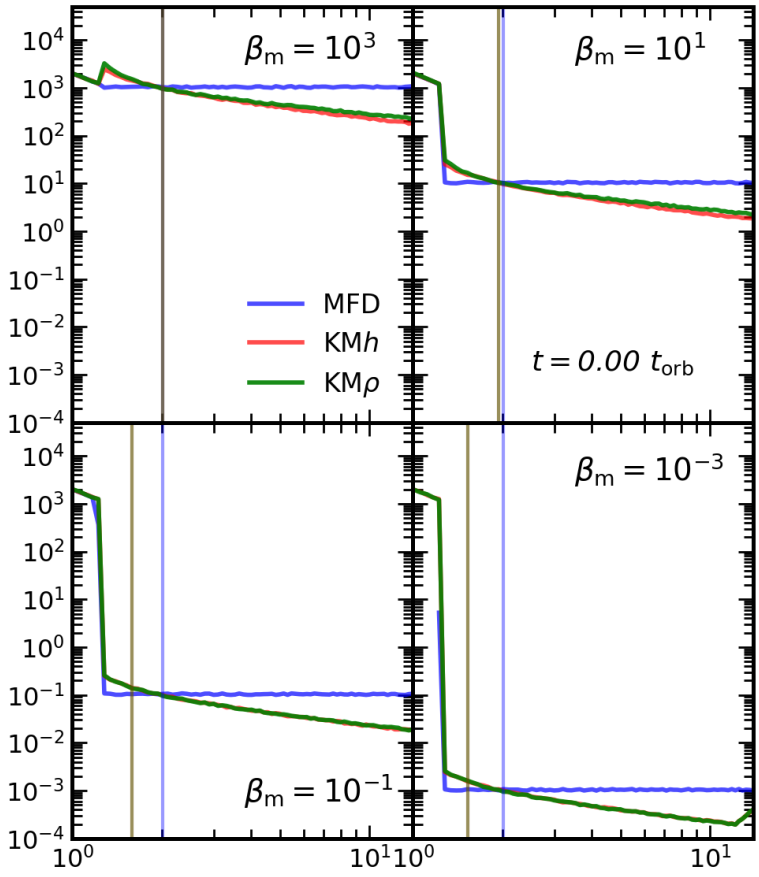

Figure 8.4 Radial profiles of the disc magnetisation at the equatorial plane at the initial time for the four values of the magnetisation parameter considered, indicated in the legends. Blue, red and green lines correspond to approaches `MFD`, `KM`h and `KM`ρ, respectively. Whereas for `MFD` discs, $\beta_{\rm m}$ is constant along the disc, for approaches `KM`h and `KM`ρ the magnetisation parameter distribution follows Eq. (8.27) and Eq. (8.28), respectively. The vertical lines indicate the location of the maximum of the rest-mass density for each disc using the same color code. Beyond this maximum, `KM`h and `KM`ρ discs are significantly more magnetised than `MFD` discs.

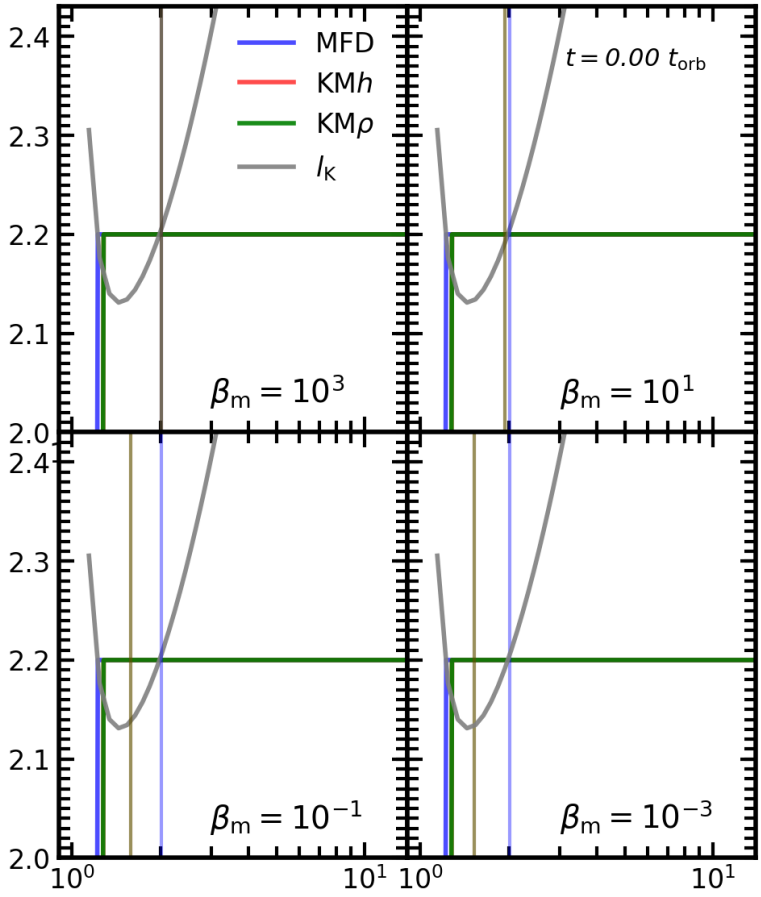

Figure 8.5 Radial profiles of the specific angular momentum at the equatorial plane at the initial time for the four values of the magnetisation parameter considered, indicated in the legends. Blue, red and green lines correspond to approaches `MFD`, `KM`h and `KM`ρ, respectively, and the vertical lines show the location of the maximum of the rest-mass density for each disc using the same color code. The specific angular momentum is initially constant and equal for all models, by construction. With respect to the Keplerian angular momentum profile, depicted by the grey line, all discs are composed of an inner super-Keplerian region, $[r_{\rm in}, r_{\rm c})$, and an outer sub-Keplerian region, $(r_{\rm c}, r_{\rm out}]$.

initial data for these models are purely hydrodynamical at first (i.e., at $t = 0$, the fluid pressure and the magnetic pressure distributions do not *see* each other and the interaction between them is introduced from the first timestep onward). By contrast, the morphology of models KMh and KMρ (middle and right columns) changes for varying values of $\beta_{\rm m,c}$. In particular, the size of the disc is smaller for lower values of the magnetisation parameter (i.e. a stronger magnetic field) at the centre $\beta_{\rm m,c}$, and the location of the maximum of the density moves towards the inner edge of the disc. This can be better observed in Fig. 8.3, where we plot the logarithm of the rest-mass density versus the logarithm of the radial coordinate at the equatorial plane. The radial location of the outer boundary of the discs along the equatorial plane is reported in Table 1. We note that the maximum of the rest-mass density for models KMh-A and KMh-B is less than one. The reason is because, in this approach, we set $w_{\rm c} = 1$, and then $\rho_{\rm c} = w_{\rm c}/h_{\rm c}$. It follows from Eq. (8.26) that $\rho_{\rm c} = 1/(1 - |W_{\rm c} - W_{\rm in}|) < 1$. The interested reader is addressed to Gimeno-Soler and Font [2017] and Gimeno-Soler et al. [2019] for an extensive discussion on the morphology of magnetised discs for different degrees of magnetisation.

In Fig. 8.4 we show the 1D initial profiles of the magnetisation at the equatorial plane for each procedure and also the location of the maximum of the rest-mass density, indicated by the vertical lines. For the purely hydrodynamical solutions MFD the location of this maximum is at the centre of the disc (vertical blue line). As it can be seen, the behaviour of $\beta_{\rm m}$ is different for the models MFD on the one hand and for the models KMh and KMρ on the other hand. This is expected, as the method to build the magnetic field is different. In particular, as we mentioned before, for the MFD approach $\beta_{\rm m}$ is constant throughout the disc, and for the KMh and KMρ cases $\beta_{\rm m}$ decreases with increasing radial coordinate. This fact can be easily explained when $\beta_{\rm m}$ is written as

$$\beta_{\rm m} = \frac{K}{K_{\rm m}\mathcal{L}^{\Gamma-1}}\,, \tag{8.27}$$

for the KMh models, and as

$$\beta_{\rm m} = \frac{K}{K_{\rm m}h^{\Gamma}\mathcal{L}^{\Gamma-1}}\,, \tag{8.28}$$

for the KMρ models. The presence of the specific enthalpy h in equation (8.28) also explains the differences observed between the cases A and B for models KMh and KMρ. Additionally, in Fig. 8.5 we show the initial radial profiles at the equatorial plane of the specific angular momentum, the Keplerian angular momentum and the location of the maximum of the rest-mass density (indicated with blue, red and green vertical lines for models MFD, KMh and KMρ respectively).

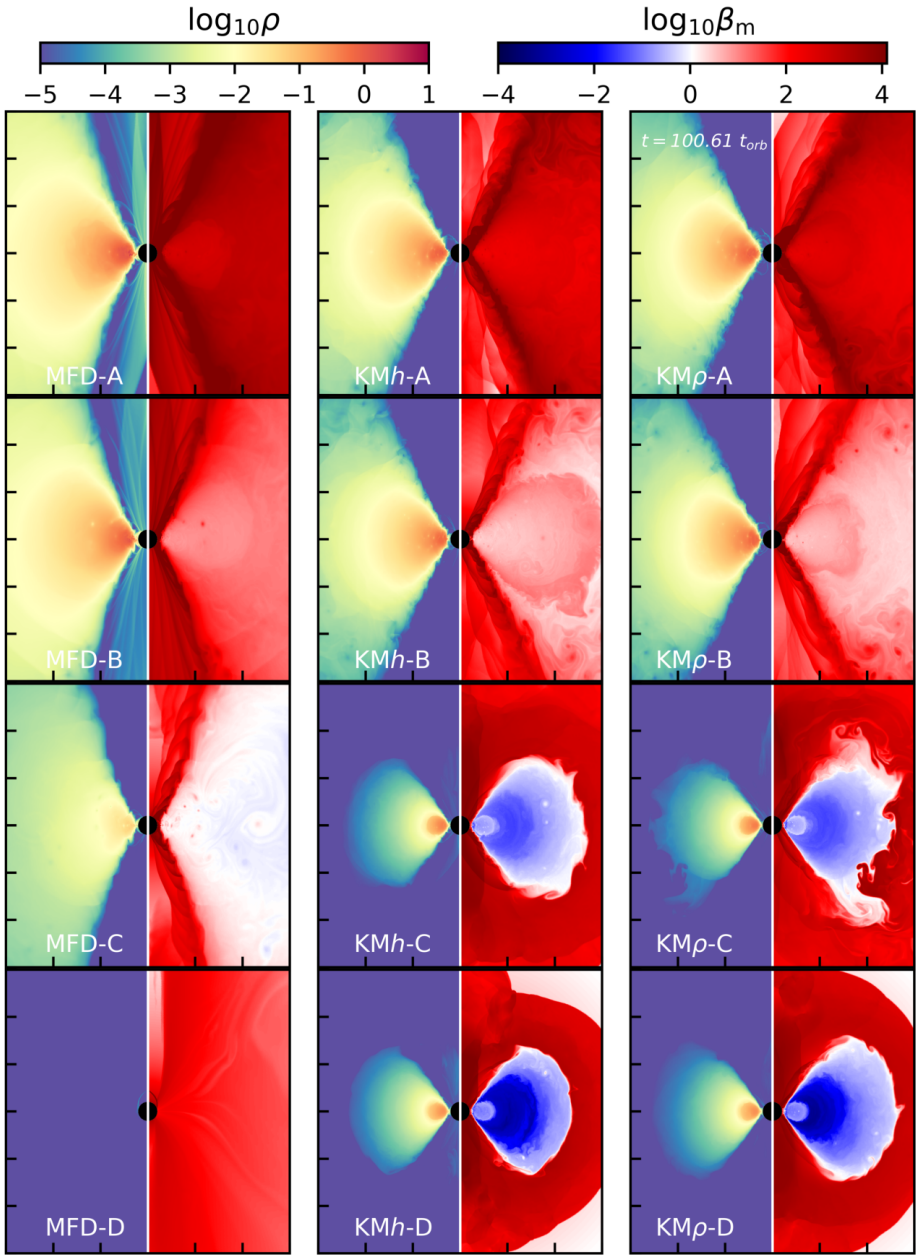

Figure 8.6 Final morphology (at $t \sim 100t_{\rm orb}$) of the rest-mass density (left side of each panel) and magnetisation parameter $\beta_{\rm m}$ (right side of each panel) for our sample of magnetised tori around a Kerr black hole with spin $a = 0.99$. From left to right, the columns correspond to models built following the `MFD`, `KMh`, and `KM`ρ approaches, respectively. From top to bottom, the rows correspond to models with different values of the magnetisation parameter $\beta_{\rm m,c}$, namely 10^3, 10^1, 10^{-1}, and 10^{-3}. The domain plotted on each panel corresponds to $(x, z) \in [-15M, 15M] \times [-15M, 15M]$. For low magnetisation values ($\beta_{\rm m,c} = 10^3$ and 10), the final rest-mass density distribution of the discs is similar for the three approaches but the `MFD` discs become less magnetised than the other two. However, for high magnetisation values the `MFD` discs are significantly perturbed to even become completely disrupted for $\beta_{\rm m,c} = 10^{-3}$. `KMh`, and `KM`$\rho$ discs remain stable throughout although they become significantly smaller compared to their original size, due to accretion.

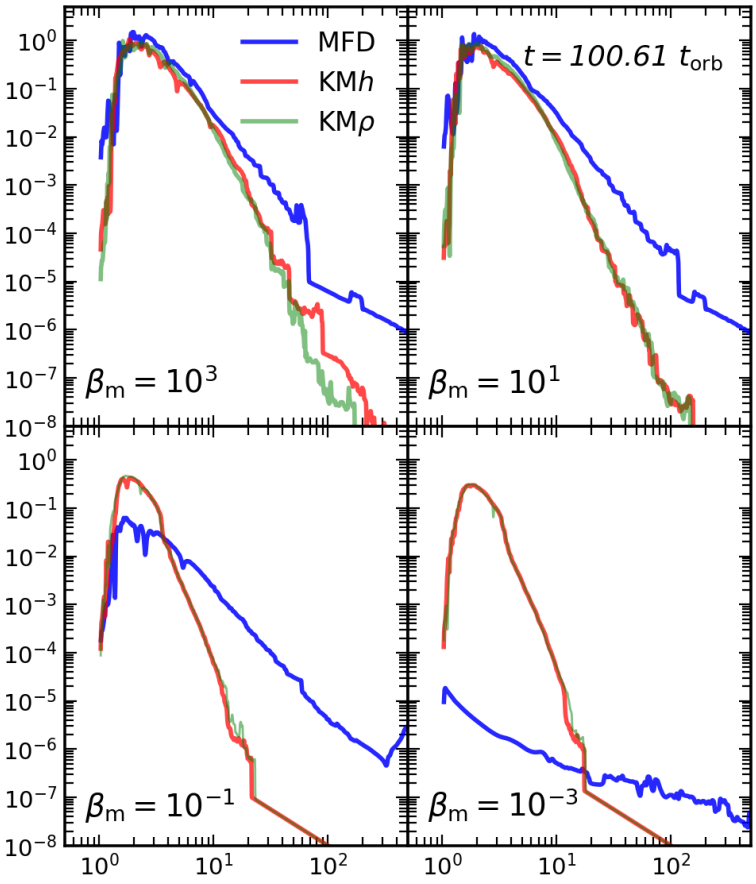

Figure 8.7 Radial profiles of the rest-mass density at the equatorial plane at the end of the evolution ($100.61 t_{\rm orb}$) for the four values of the magnetisation parameter considered, indicated in the legends. Blue, red and green lines correspond to approaches `MFD`, `KM`h and `KM`ρ, respectively. Comparing with the initial profiles (Fig. 8.3) the general shape of the discs is preserved during the evolution, except for model `MFD-D` (blue line at the bottom-right panels) where the disc is destroyed. The agreement between approaches `KM`h and `KM`ρ is also maintained.

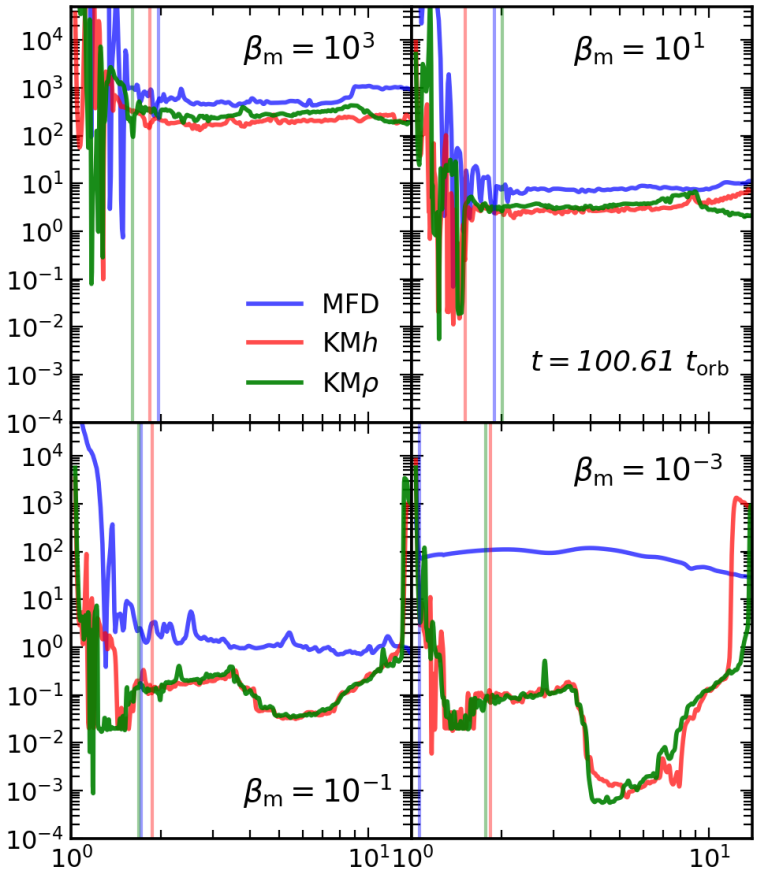

Figure 8.8 Radial profiles of the disc magnetisation at the equatorial plane at the end of the evolution ($100.61 t_{orb}$) for the four values of the magnetisation parameter considered, indicated in the legends. Blue, red and green lines correspond to approaches `MFD`, `KM`h and `KM`ρ, respectively, and the vertical lines show the location of the maximum of the rest-mass density for each disc using the same color code. For weakly magnetised disks (top panels) the magnetisation is roughly constant along the disc and its value only increases slightly with respect to its initial value (cf. Fig. 8.4. For strongly magnetised disks (bottom panels), and for approaches `KM`h and `KM`ρ, we observe the development of a highly magnetised envelope surrounding the high-density central region of the disc.

By construction, the specific angular momentum is initially constant and we can observe that, with respect to the Keplerian angular momentum, the disc is divided into two regions: A first super-Keplerian region, spanning the interval $[r_{\rm in}, r_{\rm c})$ and a second sub-Keplerian region at $(r_{\rm c}, r_{\rm out}]$.

8.4.2 Late time morphology

We evolve the initial data for about 100 orbital periods in order to find out whether noticeable long-term differences appear in the discs, both with respect to the initial data and among them, due to the way the magnetic field is set up in the three approaches. The results of the simulations are depicted in Figs. 8.6 to 8.9. In addition, Figs. 8.10 and 8.11 show the time evolution of the fraction of the initial total mass that remains in the disc and the time evolution of the rest-mass density at the centre of the disc normalised by its value at the initial time, respectively.

The late time 2D morphology of the discs is shown in Fig. 8.6. As in Fig. 8.2, the columns correspond to the three different models (namely `MFD`, `KM`h and `KM`ρ), the rows correspond to the four values of the magnetisation parameter that we have considered (namely 10^3, 10, 10^{-1}, 10^{-3}). Likewise, the left half of each panel of Fig. 8.6 displays the logarithm of the rest-mass density whereas the right half displays the magnetisation parameter in logarithmic scale.

The perturbation of the initial data triggers accretion of the material of the discs on to the black hole. Figure 8.6 shows that for the lowest magnetisation we have considered ($\beta_{\rm m,c} = 10^3$), the rest-mass density distribution of the discs after the evolution is very similar for the three approaches. In particular, the only perceptible difference is that the disc built using the `MFD` approach is slightly bigger. Regarding the evolution of the magnetisation, we can see that after 100 orbital periods the discs have undergone a redistribution of their magnetic field, with the appearance of a slightly more magnetised toroidal region (with respect to the initial data values) which coincides with the most dense region of the disc. We note that the disc built with the `MFD` approach is the less magnetised of the three approaches.

This trend continues when we observe the second row of Fig. 8.6 (which corresponds to $\beta_{\rm m,c} = 10$). In this case, the differences between the `MFD` and the `KM` approaches are more apparent: the discs are smaller and more magnetised in both `KM` cases when compared to the `MFD` disc. Nevertheless, the morphology of the three discs is still quite similar.

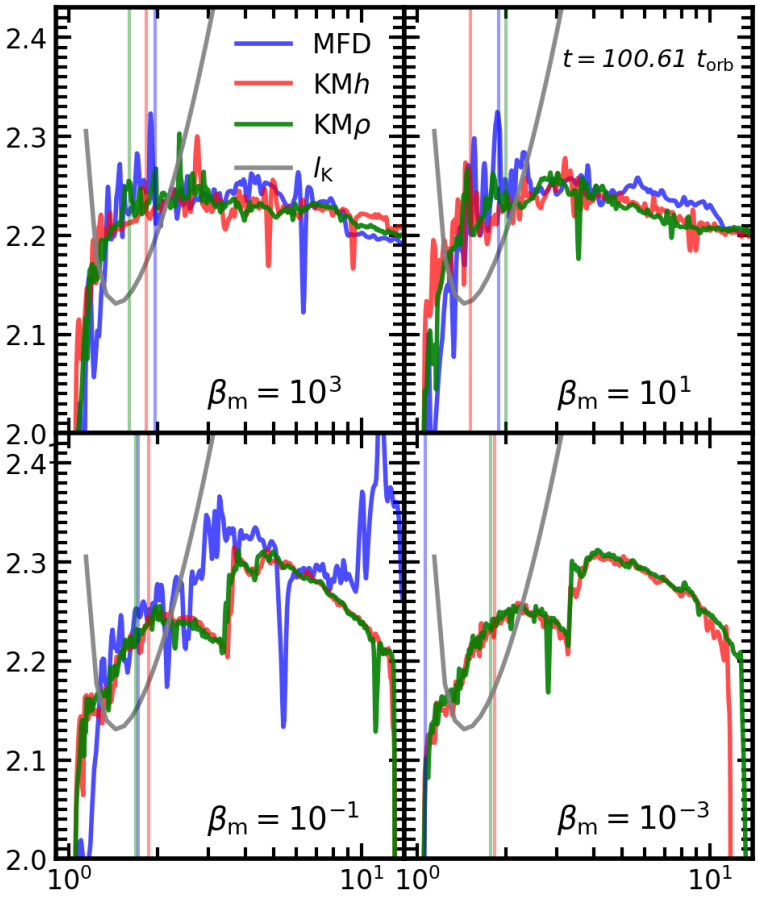

Figure 8.9 Radial profiles of the specific angular momentum at the equatorial plane at the end of the evolution ($100.61 t_{\rm orb}$) for the four values of the magnetisation parameter considered, indicated in the legends. Blue, red and green lines correspond to approaches `MFD`, `KM`h and `KM`ρ, respectively, and the vertical lines show the location of the maximum of the rest-mass density for each disc using the same color code. The Keplerian angular momentum is depicted with a grey line. The comparison with the initial profile (cf. Fig. 8.5) shows that the angular momentum drops in the inner regions of the discs for all models and increases slightly above 2.2 in the rest. The increase is larger for strongly magnetised discs (bottom panels) where an external envelope with a higher value of the angular momentum forms, coinciding with the highly magnetised region observed in Fig. 8.8.

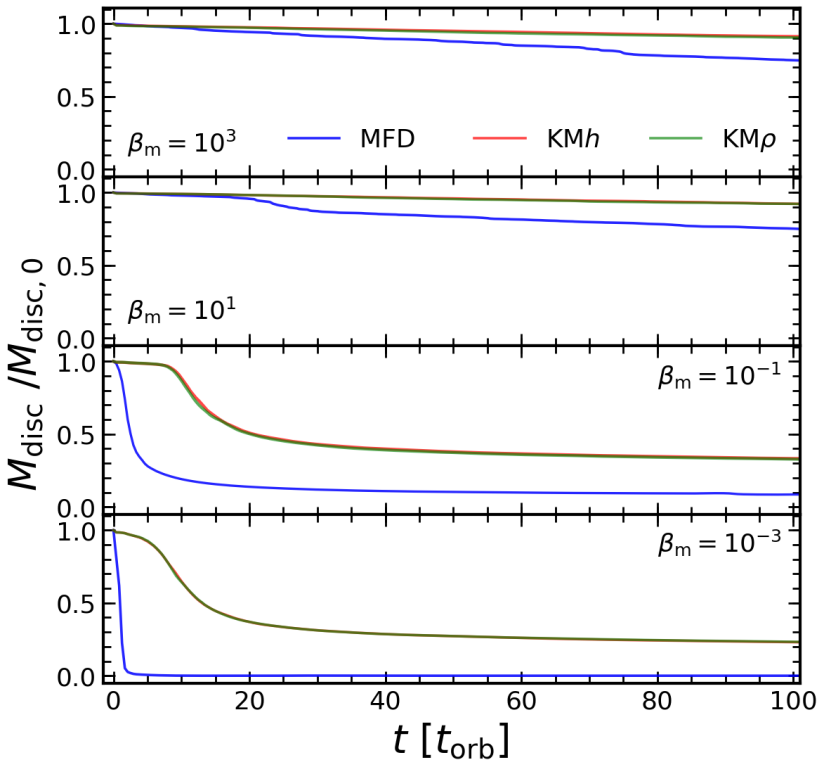

Figure 8.10 Evolution of the mass of the disc in units of its initial value. From top to bottom, the panels correspond to $\beta_m = 10^3$, 10, 10^{-1}, and 10^{-3}. Models `MFD`, `KM`h and `KM`ρ are shown in blue, red and green lines, respectively, in each panel. The initial perturbation triggers the accretion of mass on to the black hole for all models. The effect is more pronounced and rapid as the magnetisation is increased, especially for the `MFD` discs, where mass is also expelled, for which the final mass drops to a $\sim 10\%$ value of the initial mass for $\beta_m = 10^{-1}$ and to negligible values for $\beta_m = 10^{-3}$.

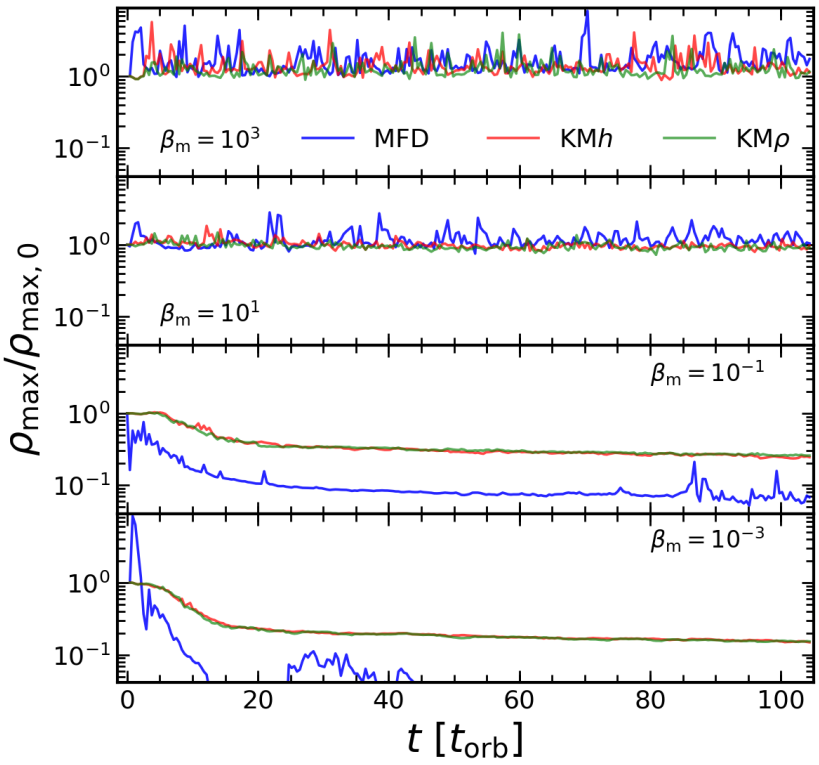

Figure 8.11 Evolution of the maximum of the rest-mass density at the equatorial plane normalized by its maximum at the initial time. From top to bottom, the panels correspond to $\beta_{\rm m} = 10^3$, 10, 10^{-1}, and 10^{-3}. Models `MFD`, `KM`h and `KM`ρ are shown in blue, red and green lines, respectively, in each panel. The maximum rest-mass density stays close to its initial value for the less magnetised models but drops as the magnetisation is increased, especially for the `MFD` discs.

So far, we have compared low magnetised models, so it is expected that the discrepancy between the different approaches should be small. In particular, the addition of the magnetic field for the low-magnetised `MFD` models introduces only a small perturbation of the fluid pressure (the magnetic pressure). However, when the magnetisation parameter goes below $\beta_{\rm m} = 1$, the magnetic pressure becomes larger than the fluid pressure and it is not longer possible for it to be considered as a small perturbation.

In the third row of Fig. 8.6 we consider discs with a magnetisation parameter of $\beta_{\rm m,c} = 10^{-1}$, Here, we start to see the limits of the `MFD` approach. As we can observe, the outcome of the evolution is now very different for the `MFD` and the `KM`h and `KM`ρ approaches. In the first case, the disc is significantly bigger, the maximum rest-mass density is significantly lower and it is less magnetised than its `KM` counterparts. This is caused by the introduction of the magnetic field as a perturbation of the pressure; in this case, the (overall) perturbation is large enough to further intensify the accretion of a significant part of the disc (hence the drop of the maximum of the rest-mass density). Nevertheless, for this value of the magnetisation parameter the shape of the disc is not yet drastically altered.

Finally, in the last row of Fig. 8.6, we show the outcome of the evolution of the highest magnetised discs we have considered in this work. In this case, after 100 orbital periods, the disc built using approach `MFD` has entirely disappeared. The reason is because, as discussed before, the 'ad hoc' magnetic field is introduced as a perturbation of the pressure, but compared to the previous case it is now 100 times bigger (as $\beta_{\rm m} = 10^{-3}$). Therefore, the magnetisation is sufficiently large to disrupt the disc in such a way that by the end of the simulation the disc material has been either accreted by the black hole or expelled away, leaving behind a low-magnetised remnant hardly distinguishable from the atmosphere.

It is worth now to describe the 2D morphology of the discs at $t \sim 100 t_{\rm orb}$ for both `KM` models and magnetisations $\beta_{\rm m,c} = 10^{-1}$ and $\beta_{\rm m} = 10^{-3}$. For these two cases, it is apparent that the final disc is significantly smaller when compared to its intial state. Also, it can be seen that the value of the maximum rest-mass density is also smaller. This is due to the initial perturbation we applied in the pressure. As these highly-magnetised discs have the location of the maximum of the rest-mass density $r_{\rm max}$ closer to the inner edge of the disc (and hence, closer to the black hole), a perturbation can trigger the accretion of a greater amount of matter in an easier way. The magnetisation distribution of these discs is also different. The central, highest density region ends up becoming less magnetised than at the start of the simulation, whereas the external, less dense layers of the

disc are endowed with a stronger magnetic field than at the initial time. Besides this, we can also see that the two KM approaches yield almost the same outcome after the evolution. This is expected, as they coincide when $\beta_{\rm m} \to 0$.

In Figs. 8.7, 8.8 and 8.9 we show radial slices along the equatorial plane of the rest-mass density, the magnetisation parameter, and the specific angular momentum, respectively. The rest-mass density plots show that for low magnetisation (high values of $\beta_{\rm m}$) the radial profiles at the end of the evolution closely resemble those at $t = 0$, irrespective of the prescription employed to account for the magnetic field. In particular, the peak values and location of the density remain roughly the same of the initial values. (The differences in the location of the density maxima can be appreciated best by comparing the radial position of the vertical lines in Fig. 8.8 with their counterparts in Fig. 8.4. Note that the radial scale is logarithmic.) The most important difference is the formation of a more extended, low-density, envelope for large radii for the three models. However, for the two most highly magnetized models, the late time radial profiles of the density show important differences with the initial profiles. As we also observed in Fig. 8.6, while approaches KMh and KMρ still show disc-like profiles (albeit smaller and the peak density has decreased to $\sim 3 \times 10^{-1}$ for models C and to $\sim 2 \times 10^{-1}$ for models D by $t \sim 100\, t_{\rm orb}$), the MFD-C model rest-mass profile is more similar to the ones found in less magnetised models but it has suffered a heavy mass loss, with a maximum density at $t \sim 100\, t_{\rm orb}$ of $\rho_{\rm max} \sim 7 \times 10^{-2}$, and the MFD-D model has completely vanished, leaving behind only a very low density remnant far from the central black hole. It is also worth noting that, for the two most highly magnetized models, the location of the maximum of the rest-mass density $r_{\rm max}$ has barely drifted away from the black hole.

The inspection of Fig. 8.8 and the comparison with Fig. 8.4 reveals that the magnetisation parameter along the disc decreases for weakly magnetised models (A and B) but grows for the stronger magnetised cases (C and D). This suggests a value of $\beta_{\rm m,c} \sim 1$ for which the magnetisation of the disc is constant during the evolution. The mechanism responsible for the redistribution of the magnetisation is, most likely, the radial compression and expansion that the discs suffer during the evolution. Radial compression of the magnetic field lines lead, in turn, to the local amplification of the magnetic field. On the one hand, for models A and B (and MFD-C), Fig. 8.7 shows that, even though the morphology of the discs does not change significantly, the central parts become a little more compact by the end of the evolution. The infall of matter into those central regions produces the corresponding local amplification of the magnetic field (as

observed in Fig. 8.6). On the other hand, for the two most magnetised models `C` and `D`, the dynamics leads to the appearance of two distinct regions in the disc (best visible for $\beta_{\rm m} = 10^{-3}$; see also Fig. 8.6): a central less magnetised region surrounded by a region where the magnetic field has been slightly amplified.

Radial profiles of the final angular momentum along the equatorial plane are depicted in Fig. 8.9. This figure reveals a redistribution of the specific angular momentum along the disc. For cases `A` and `B` (and case `MFD-C`), and irrespective of the approach used to incorporate the magnetic field, the specific angular momentum increases slightly in the central region of the disc but overall stays roughly constant. However, for the `KM` models `C` and `D` we end up with a different configuration: a lower l region near the inner edge of the disc as in the previous cases, a second high-density region with $l > 2.2$ containing a local maximum of the specific angular momentum, and a third low-density region, also with $l > 2.2$, which contains the absolute maximum of the specific angular momentum. In any event, the specific angular momentum does not change much during the evolution (at most $\pm \sim 5\%$). Moreover, it can be seen that the initial structure (an inner super-Keplerian region and an outer sub-Keplerian region) is preserved during the evolution.

The change in the location of the maximum of the rest-mass density for models `KM`h`-C/D` and `KM`ρ`-C/D` is worth a further comment. The fact that a non-constant angular momentum region develops during the evolution of these models and that the inner region of the discs lose part of their magnetisation are the reason of said drift in $r_{\rm max}$. That can be seen in the central panel of Fig. (6) shown in Gimeno-Soler and Font [2017], where the authors plot $r_{\rm max}$ vs. $\log_{10}\beta_{\rm m,c}$ for a Kerr black hole with spin parameter $a = 0.99$ and for three different non-constant angular momentum distributions (the black line in that figure represents our `KM`h models). As it can be seen in Gimeno-Soler and Font [2017], the drop of the magnetisation would not be enough to achieve the values of $r_{\rm max}$ we observe here; we would need a change in the specific angular-momentum distribution as well.

In Fig. 8.10 and Fig. 8.11 we show the time evolution of the mass of the discs and of the maximum of the rest-mass density (normalised by the initial values). The disc mass is computed using

$$m = \int \sqrt{\gamma} W \rho \, d^3x \,. \tag{8.29}$$

The values of these two quantities, at the initial and final times, are reported in Table 1. We find that, for the three approaches and the lowest magnetised models (i.e., `A` and `B`), the maximum of the rest-mass density is oscillating, but

remains close to its initial value. With respect to the fraction of the mass in the disc, we see that the initial perturbation triggers the accretion of a very small fraction of the total mass for the KM models ($> 90\%$ of the mass survives after an evolution of $t \sim 100\, t_{\rm orb}$). A bit less (about a 75% of the total mass) survives for models MFD-A and MFD-B,which we attribute to the presence of an additional source of perturbation due to the inconsistent incorporation of the magnetic field on top of purely hydrodynamic initial data.

By increasing the magnetisation, these trends become more acute. For models KMh-C and KMρ-C the maximum of the rest-mass density drops to a $\sim 15\%$ fraction of $\rho_{\rm max,0}$ and the total mass of the disc drops to $\sim 33\%$ of the initial mass. The change is more dramatic for the model MFD-C, where the final density is a $\sim 7\%$ fraction of $\rho_{\rm max,0}$ and the final mass is a $\sim 10\%$ fraction of the initial mass. Again, this is due to the perturbation introduced by the magnetic field being too large. Lastly, for the highest magnetised case, the discs in models KMh-D and KMρ-D lose even more matter: the maximum of the rest-mass density is a $\sim 15\%$ of its initial value and the final mass is around $\sim 23\%$ of the initial mass. By recalling the results from our resolution tests in Fig. 8.1 we note that, at our fiducial resolution, we are overestimating the mass loss for the highly-magnetised KM models by about 10%. For the MFD-D model, Figs. 8.10 and 8.11 reveal that the disc is rapidly destroyed at the beginning of the evolution, as the total mass drops to negligible values during the first orbital periods. The maximum of the rest-mass density also vanishes but at a different rate, as the code keeps track of the matter that is being expelled away.

8.5 Discussion

In this paper we have built equilibrium solutions of magnetised thick discs around a highly spinning Kerr black hole ($a = 0.99$). The study has considered non-self-gravitating, polytropic, constant angular momentum discs endowed with a purely toroidal magnetic field. The initial data have been constructed considering three different approaches. In two of them, which we labelled KMh and KMρ, the magnetic field has been incorporated in a consistent way in the solution, and they differ by the fluid being relativistic or otherwise from a thermodynamical point of view. In the third approach (MFD) the magnetic field has been incorporated as an 'ad hoc' perturbation on to an otherwise purely hydrodynamical solution. This straightforward last approach has also been adopted by previous works (e.g. Gammie, McKinney, and Tóth [2003], Noble et al. [2006], Shiokawa et al. [2012], Porth et al. [2017], Mizuta et al. [2018],

Bowen et al. [2018], and Event Horizon Telescope Collaboration et al. [2019c]). However, those studies are based on poloidal magnetic field setups, which lead to MRI unstable evolutions. Hence, our findings for toroidal distributions should not necessarily be taken at face value for other types of field setups.

The initial data have been perturbed and evolved up to a final time of about 100 orbital periods using the `BHAC` code [Porth et al. 2017] which solves the non-linear GRMHD equations. We have analysed the stability properties of the initial data under a small perturbation that triggers the accretion of mass and angular momentum on to the black hole. The various outcomes of the different prescriptions used to account for the magnetic field have been compared for increasingly larger values of the disc magnetisation. We have explored, in particular, four representative values of the magnetisation parameter $\beta_{\rm m}$ spanning from almost hydrodynamical discs to very strongly magnetised tori.

Notable differences have been found in the long-term evolutions of the initial data. Most importantly, our study has revealed that highly magnetised discs (namely, $\beta_{\rm m} = 10^{-3}$) are unstable, and hence prone to be accreted or expelled, unless the initial data incorporate the magnetic field in a self-consistent way. Only for weak magnetic fields, the long-term evolution of the models is unaffected by the way the magnetic field is incorporated in the initial data. We note, in particular, that in the simulations by the EHT Collaboration, despite the magnetic field is not consistently built in, the values of the magnetisation parameter are sufficiently small ($\beta_{\rm m} = 10^2$) not to artificially affect the stability of the discs. In our *consistent* approaches the evolution leads to the formation of smaller *mini-discs* with weaker magnetisation when compared to the initial state, surrounded by a highly magnetised, low density envelope. In general we find that the disc angular momentum increases during the evolution with respect to the initial constant value and the discs become smaller and stripped of any external material for increasing values of the magnetisation. This is in agreement with previous results from Wielgus et al. [2015], who found that magnetised discs ($\beta_{\rm m} = 0.1$, 1.0) are stable to axisymmetric perturbation, although those simulations are fairly short, extending only $t \sim 4t_{\rm orb}$. Our simulations are also consistent with those of Montero et al. [2007] (again, significantly shorter) where the frequencies of quasi-periodic oscillations of the discs were computed from a quasi-stable configuration for weakly and mildly magnetised discs.

Two obvious limitations of this work have to do with our simplifying assumptions. Firstly, a constant specific angular momentum distribution is simplistic and unrealistic. And secondly, a purely toroidal magnetic field distribution is very unlikely to exist in a realistic astrophysical scenario (see [Ioka and Sasaki

2003] for a discussion on this topic). Therefore, we could extend this study in two directions, namely i) considering non-constant angular momentum distributions, and ii) considering poloidal magnetic field distributions (to this end, we first have to construct *consistent* initial data). Finally, we note that the similarities we have found in the evolutions of approaches `KM`h and `KM`ρ are expected due to the small deviation of the value $h \simeq 1$ for a potential gap of $|\Delta W| = 0.2216$. However, other types of compact objects might provide larger potential gaps (e.g., the Kerr black holes with scalar hair described in Gimeno-Soler et al. [2019] achieve values of $|\Delta W| > 1$). For this reason, we could expect to find differences in the evolution between approaches `KM`h and `KM`ρ for such central objects even for low magnetised discs. This study will be reported elsewhere.

Chapter 9

Conclusions and outlook

In this thesis I have focused on improving our knowledge of the physical properties of equilibrium configurations of magnetized fluids around compact objects in general relativity. In particular, new prescriptions to build initial data of magnetized accretion disks around compact objects have been obtained. Those solutions can be used as initial data to perform numerical simulations in dynamical situations. Indeed, extending the classes of available initial data for accretion disk simulations in different directions (accommodating, e.g. diverse magnetic field configurations, angular momentum distributions, and types of spacetimes where the fluid resides) is a timely topic. Current astronomical facilities are providing unprecedented opportunities to start testing our theories about spacetime and the true nature of black holes in the strong-field regime, e.g. through gravitational-wave astronomy [Abbott et al. 2019, Abbott et al. 2020b, Abbott et al. 2021a] and precision astrometry of stars around the supermassive BH at the center of our galaxy [Do et al. 2019, Gravity Collaboration et al. 2019]. Moreover, the physics of accretion flows in the vicinity of compact objects is now within experimental reach through the radio observations of the supermassive BH at the core of the M87 galaxy [Event Horizon Telescope Collaboration et al. 2019a]. Numerical simulations that cover a wide range of the parameter space of the problem are badly required to correctly infer the physical properties of such BH-torus systems from the observational data. Those opportunities have been a motivation to the work reported here.

In Chapter 2 we extended the Komissarov solution of a magnetized, thick accretion disk (a magnetized 'Polish doughnut') to the case of nonconstant angular momentum distributions. In this study we described the behaviour of magnetized accretion disks under changes of the magnetization parameter

for different black hole spin parameters and angular momentum distribution. We also characterized some properties of the equilibrium solutions that are independent of the Kerr parameter and the angular momentum distribution considered.

The topic of Chapter 3 considered a different type of compact object known as a Kerr black hole with scalar hair [Herdeiro and Radu 2014b]. This is a generalization of the Kerr BH of general relativity (but still within GR) that takes into account the presence of an ultralight complex scalar field that is synchronized to the BH horizon. Here, we first focused on constant angular momentum disks and the morphological and thermodynamical features that were introduced by the presence of the scalar field. An extension of this study, discussed in Chapter 4, considered non-constant angular momentum disks. As a whole, these two works revealed the peculiar morphological and thermodynamical features of some of the solutions (in particular when the scalar field stores most of the mass and angular momentum of the system). We note that the non-linear time evolution of these models is still required to obtain potentially observational signatures of such type of hairy black hole-disk systems.

In a brief diversion outside GR, in Chapter 5 we considered a BH solution within the framework of $f(R)$ theories of gravity, known as Yukawa BH. Here, we studied constant angular momentum magnetized disks to assess the impact of deviations from GR on the structure and physical properties of the tori. We indeed observed morphological departures that are characteristic of those solutions. Moreover, we also computed the photon rings associated with the Yukawa BH and placed some observational constraints on the black hole parameters.

Capturing the effects of the accretion disk's self-gravity is relevant when the mass of the disk is comparable with the mass of the black hole around which the torus revolves. In Chapter 7 we studied the impact of including self-gravity in magnetized, Keplerian thick disks. Our study revealed morphological differences between test-fluid disks and self-gravitating disks. We also characterized the impact disks have on the metric of the spacetime for different black hole spin parameters and disk magnetizations.

Up to this point in the thesis we had only considered perfect fluid configurations. However under certain circumstances, dissipative effects can be important. For this reason, in Chapter 7 we introduced the presence of viscosity using a perturbative approach and considered a sequence of constant angular momentum magnetized disks in the Schwarzschild geometry. In this work we observed that the introduction of viscosity does not modify the magnetization of the disk (at least at first-order perturbation theory level) and that the correction

that viscosity introduces to the pressure and the energy density is negative. In addition, we also characterized the way viscosity modifies the structure of the disk, in particular in the region close to the cusp, placing upper bounds on the values of the model parameters.

Finally, in Chapter 8 we considered time evolutions of different constant angular momentum disks in a highly spinning Kerr BH background. In particular, we compared three ways of prescribing the initial data. One of them introduces the magnetic field as a perturbation of a non-magnetized solution. The other two are the Komissarov solution and a thermodynamically relativistic version of this solution in which the magnetic field is coupled with the fluid. Our study placed limits on the value of the initial magnetization of the disk for the first (somewhat inconsistent) approach. We also found agreement between the two consistent ways to prescribe the initial data. Moreover, the simulations exhibited angular momentum and magnetic field redistribution, in particular we found amplification of the magnetic field for mildly magnetized disks and decay of the magnetic field for the strongly magnetized cases. This hints at the existence of an equilibrium point for which the magnetic field will be approximately constant during the evolution.

Most of the results reported in this thesis have been obtained with a numerical code that I developed from scratch. This code has allowed me to build equilibrium solutions of magnetized disks in generic stationary and axisymmetric spacetimes. The code is constantly being expanded to account for additional physics and a number of projects are currently ongoing. In the near future we plan to release the code as an open-source tool available to the community.

Regarding extensions of the stationary models reported here, work to expand the magnetically polarized disks of Pimentel, Lora-Clavijo, and Gonzalez [2018] to the non-constant angular momentum case described in Gimeno-Soler et al. [2021] is already in progress. Additionally, models of magnetized disks are being computed around Proca stars, a class of horizonless exotic compact objects that have been proposed as black hole mimickers [Brito et al. 2016]. This type of bosonic stars allows to extend the disks close to the axis of rotation. This leads to the possibility of building the so-called *mixed stars* (stars formed of both bosonic fields and regular fermionic matter, see for instance [Di Giovanni et al. 2020]) within the framework of accretion disks. Additional ongoing work includes the extension of our results on viscous disks to the Kerr case. As the second-order gradients considered in Lahiri et al. [2021] include components of the Riemann tensor, we expect to find new effects when the Kerr geometry

is considered, particularly regarding the location of the cusp for disks around maximally rotating black holes. From a theoretical point of view, in collaboration with Dr. Patryk Mach, we are also interested in finding out the possibility of developing a framework to allow for poloidal magnetic fields in a consistent way like the one we use for toroidal fields. As poloidal fields are believed to be key for certain physical processes, as MRI and jet launching, this addition would be quite relevant.

Regarding potential comparisons with actual observations, the results from this thesis as well as our planned extensions, constitute a starting point. As a first step we plan to use *general relativistic radiative transfer* (GRRT) codes to obtain the shadows cast by the black hole that is illuminated by the light emitted by the accretion disk, an attempt we have started to pursue in collaboration with Drs. Ziri Younsi, Alejandro Cruz-Osorio, and Sayantani Lahiri. Still, considering an equilibrium disk solution is not very realistic, as actual accretion flows can be highly dynamic. Therefore, a natural next step in my investigation would be to evolve our initial models using evolution codes, both in the test-fluid approximation with BHAC, and in full GR using the *Einstein Toolkit* [Löffler et al. 2012]. These extensions would not only allow me to study the stability properties and physical processes of the initial models discussed in this thesis but also to use fully dynamical disk models to compute shadows with GRRT codes.

Bibliography

[1] B. P. Abbott et al. "Gravitational Waves and Gamma-Rays from a Binary Neutron Star Merger: GW170817 and GRB 170817A." In: *Astrophys. J. Lett.* 848.2, L13 (Oct. 2017), p. L13. DOI: 10.3847/2041-8213/aa920c. arXiv: 1710.05834 [astro-ph.HE].

[2] B. P. Abbott et al. "GW151226: Observation of Gravitational Waves from a 22-Solar-Mass Binary Black Hole Coalescence." In: *Phys. Rev. Lett.* 116.24 (2016), p. 241103. DOI: 10.1103/PhysRevLett.116.241103. arXiv: 1606.04855 [gr-qc].

[3] B. P. Abbott et al. "GW170608: Observation of a 19-solar-mass Binary Black Hole Coalescence." In: *Astrophys. J.* 851.2 (2017), p. L35. DOI: 10.3847/2041-8213/aa9f0c. arXiv: 1711.05578 [astro-ph.HE].

[4] B. P. Abbott et al. "GW170814: A Three-Detector Observation of Gravitational Waves from a Binary Black Hole Coalescence." In: *Phys. Rev. Lett.* 119.14 (2017), p. 141101. DOI: 10.1103/PhysRevLett.119.141101. arXiv: 1709.09660 [gr-qc].

[5] B. P. Abbott et al. "GWTC-1: A Gravitational-Wave Transient Catalog of Compact Binary Mergers Observed by LIGO and Virgo during the First and Second Observing Runs." In: *Phys. Rev. X* 9.3 (2019), p. 031040. DOI: 10.1103/PhysRevX.9.031040. arXiv: 1811.12907 [astro-ph.HE].

[6] B. P. Abbott et al. "Multi-messenger Observations of a Binary Neutron Star Merger." In: *Astrophysical Journal Letters* 848, L12 (Oct. 2017), p. L12. DOI: 10.3847/2041-8213/aa91c9. arXiv: 1710.05833 [astro-ph.HE].

[7] B. P. Abbott et al. "Observation of Gravitational Waves from a Binary Black Hole Merger." In: *Physical Review Letters* 116.6, 061102 (Feb. 2016), p. 061102. arXiv: 1602.03837 [gr-qc].

[8] B. P. Abbott et al. "Tests of general relativity with the binary black hole signals from the LIGO-Virgo catalog GWTC-1." In: *Phys. Rev. D* 100.10, 104036 (Nov. 2019), p. 104036. DOI: 10.1103/PhysRevD.100.104036. arXiv: 1903.04467 [gr-qc].

[9] B. P. Abbott et al. "GW170104: Observation of a 50-Solar-Mass Binary Black Hole Coalescence at Redshift 0.2." In: *Phys. Rev. Lett.* 118.22 (2017), p. 221101. DOI: 10.1103/PhysRevLett.118.221101. arXiv: 1706.01812 [gr-qc].

[10] B. Abbott et al. "GW170817: Observation of Gravitational Waves from a Binary Neutron Star Inspiral." In: *Phys. Rev. Lett.* 119.16 (2017), p. 161101. DOI: 10.1103/PhysRevLett.119.161101. arXiv: 1710.05832 [gr-qc].

[11] R. Abbott et al. "GW190521: A Binary Black Hole Merger with a Total Mass of 150 $M_{\odot}$." In: *Phys. Rev. Lett.* 125 (10 2020), p. 101102. DOI: 10.1103/PhysRevLett.125.101102. URL: https://link.aps.org/doi/10.1103/PhysRevLett.125.101102.

[12] R. Abbott et al. "GWTC-2: Compact Binary Coalescences Observed by LIGO and Virgo During the First Half of the Third Observing Run." In: (Oct. 2020). arXiv: 2010.14527 [gr-qc].

[13] R. Abbott et al. "GWTC-2.1: Deep Extended Catalog of Compact Binary Coalescences Observed by LIGO and Virgo During the First Half of the Third Observing Run." In: *arXiv e-prints*, arXiv:2108.01045 (Aug. 2021), arXiv:2108.01045. arXiv: 2108.01045 [gr-qc].

[14] R. Abbott et al. "Tests of general relativity with binary black holes from the second LIGO-Virgo gravitational-wave transient catalog." In: *Phys. Rev. D* 103 (12 2021), p. 122002. DOI: 10.1103/PhysRevD.103.122002. URL: https://link.aps.org/doi/10.1103/PhysRevD.103.122002.

[15] M. Abramowicz, M. Jaroszynski, and M. Sikora. "Relativistic, accreting disks." In: *Astron. Astrophys.* 63 (Feb. 1978), pp. 221–224.

[16] M. A. Abramowicz. "The Relativistic von Zeipel's Theorem." In: 21 (Jan. 1971), p. 81.

[17] M. A. Abramowicz, M. Calvani, and L. Nobili. "Runaway instability in accretion disks orbiting black holes." In: *Nature* 302 (Apr. 1983), pp. 597–599.

[18] M. A. Abramowicz and P. C. Fragile. "Foundations of Black Hole Accretion Disk Theory." In: *Living Reviews in Relativity* 16, 1 (Dec. 2013), p. 1. DOI: 10.12942/lrr-2013-1. arXiv: 1104.5499 [astro-ph.HE].

[19] F. Acker, R. B. de R. Borges, and B. Costa. "An improved WENO-Z scheme." In: *Journal of Computational Physics* 313 (May 2016), pp. 726–753. DOI: 10.1016/j.jcp.2016.01.038.

[20] N. Alipour, A. R. Khesali, and K. Nozari. "Dynamics of accretion disks in a constant curvature f(R)-gravity." In: *Astrophysics and Space Science* 361.7, 240 (July 2016), p. 240. DOI: 10.1007/s10509-016-2829-6.

[21] E. Anderson et al. *LAPACK Users' Guide*. Third. Philadelphia, Pennsylvania, USA: SIAM, 1999.

[22] A. M. Anile. *Relativistic fluids and magneto-fluids: With applications in astrophysics and plasma physics*. Cambridge University Press, 2005.

[23] P. Anninos, P. C. Fragile, and J. D. Salmonson. "Cosmos++: Relativistic Magnetohydrodynamics on Unstructured Grids with Local Adaptive Refinement." In: *Astrophys. J.* 635.1 (Dec. 2005), pp. 723–740. DOI: 10.1086/497294. arXiv: astro-ph/0509254 [astro-ph].

[24] P. Anninos et al. “COSMOSDG: An hp-adaptive Discontinuous Galerkin Code for Hyper-resolved Relativistic MHD.” In: *Astrophys. J. Suppl. Ser.* 231.2, 17 (Aug. 2017), p. 17. DOI: 10.3847/1538-4365/aa7ff5. arXiv: 1706.09939 [astro-ph.IM].

[25] M. Ansorg and D. Petroff. “LETTER TO THE EDITOR: Negative Komar mass of single objects in regular, asymptotically flat spacetimes.” In: *Classical and Quantum Gravity* 23.24 (Dec. 2006), pp. L81–L87. DOI: 10.1088/0264-9381/23/24/L01. arXiv: gr-qc/0607091 [gr-qc].

[26] M. Ansorg and D. Petroff. “Black holes surrounded by uniformly rotating rings.” In: *Phys. Rev. D* 72.2, 024019 (July 2005), p. 024019. DOI: 10.1103/PhysRevD.72.024019. arXiv: gr-qc/0505060 [gr-qc].

[27] L. Antón et al. “Numerical 3+1 General Relativistic Magnetohydrodynamics: A Local Characteristic Approach.” In: *Astrophys. J.* 637 (Jan. 2006), pp. 296–312. DOI: 10.1086/498238. eprint: astro-ph/0506063.

[28] A. Arvanitaki et al. “String axiverse.” In: *Phys. Rev. D* 81, 123530 (June 2010), p. 123530. DOI: 10.1103/PhysRevD.81.123530. arXiv: 0905.4720 [hep-th].

[29] L. Baiotti and L. Rezzolla. “Binary neutron star mergers: a review of Einsteins richest laboratory.” In: *Reports on Progress in Physics* 80.9, 096901 (Sept. 2017), p. 096901. DOI: 10.1088/1361-6633/aa67bb. arXiv: 1607.03540 [gr-qc].

[30] L. Baiotti et al. “Accurate simulations of the dynamical bar-mode instability in full general relativity.” In: *Phys. Rev. D* 75.4, 044023 (Feb. 2007), p. 044023. eprint: astro-ph/0609473.

[31] S. A. Balbus and J. F. Hawley. “A powerful local shear instability in weakly magnetized disks. I - Linear analysis. II - Nonlinear evolution.” In: *Astrophys. J.* 376 (July 1991), pp. 214–233.

[32] S. A. Balbus and J. F. Hawley. “A Powerful Local Shear Instability in Weakly Magnetized Disks. IV. Nonaxisymmetric Perturbations.” In: *Astrophys. J.* 400 (Dec. 1992), pp. 610–621. DOI: 10.1086/172022.

[33] J. M. Bardeen. “Rapidly rotating stars, disks, and black holes.” In: *Black Holes (Les Astres Occlus)*. Jan. 1973, pp. 241–289.

[34] J. Bekenstein. “Novel ’no scalar hair’ theorem for black holes.” In: *Phys.Rev.* D51 (1995), pp. 6608–6611. DOI: 10.1103/PhysRevD.51.R6608.

[35] E. Berger. “Short-Duration Gamma-Ray Bursts.” In: *Annu. Rev. Astron. Astrophys.* 52 (Aug. 2014), pp. 43–105. DOI: 10.1146/annurev-astro-081913-035926. arXiv: 1311.2603 [astro-ph.HE].

[36] O. M. Blaes. “Stabilization of non-axisymmetric instabilities in a rotating flow by accretion on to a central black hole.” In: *Mon. Not. R. Astron. Soc.* 227 (Aug. 1987), pp. 975–992.

[37] P. Bosch, S. R. Green, and L. Lehner. “Nonlinear Evolution and Final Fate of Charged Anti-de Sitter Black Hole Superradiant Instability.” In: *Physical Review Letters* 116.14, 141102 (Apr. 2016), p. 141102. DOI: 10.1103/PhysRevLett.116.141102. arXiv: 1601.01384 [gr-qc].

[38] D. B. Bowen et al. "Quasi-periodic Behavior of Mini-disks in Binary Black Holes Approaching Merger." In: *Astrophys. J. Lett.* 853.1, L17 (Jan. 2018), p. L17. DOI: 10.3847/2041-8213/aaa756. arXiv: 1712.05451 [astro-ph.HE].

[39] S. Brandt and B. Brügmann. "A Simple Construction of Initial Data for Multiple Black Holes." In: *Physical Review Letters* 78 (May 1997), pp. 3606–3609. eprint: gr-qc/9703066.

[40] S. R. Brandt and E. Seidel. "Evolution of distorted rotating black holes. I. Methods and tests." In: *Phys. Rev. D* 52.2 (July 1995), pp. 856–869. DOI: 10.1103/PhysRevD.52.856. arXiv: gr-qc/9412072 [gr-qc].

[41] Y. Brihaye and L. Ducobu. "Hairy black holes, boson stars and non-minimal coupling to curvature invariants." In: *Phys. Lett. B* 795 (2019), pp. 135–143. DOI: 10.1016/j.physletb.2019.06.006. arXiv: 1812.07438 [gr-qc].

[42] R. Brito et al. "Proca stars: Gravitating Bose–Einstein condensates of massive spin 1 particles." In: *Phys. Lett.* B752 (2016), pp. 291–295. DOI: 10.1016/j.physletb.2015.11.051. arXiv: 1508.05395 [gr-qc].

[43] M. Bugli et al. "Papaloizou-Pringle instability suppression by the magnetorotational instability in relativistic accretion discs." In: *Mon. Not. R. Astron. Soc.* 475.1 (Mar. 2018), pp. 108–120. DOI: 10.1093/mnras/stx3158. arXiv: 1707.01860 [astro-ph.HE].

[44] J. Calderón Bustillo et al. "Confusing Head-On Collisions with Precessing Intermediate-Mass Binary Black Hole Mergers." In: *Phys. Rev. Lett.* 126 (20 2021), p. 201101. DOI: 10.1103/PhysRevLett.126.201101. URL: https://link.aps.org/doi/10.1103/PhysRevLett.126.201101.

[45] J. Calderón Bustillo et al. "GW190521 as a merger of Proca stars: a potential new vector boson of 8.7×10^{-13} eV." In: *Phys. Rev. Lett.* 126.8 (2021), p. 081101. DOI: 10.1103/PhysRevLett.126.081101. arXiv: 2009.05376 [gr-qc].

[46] S. Capozziello and M. De Laurentis. *Invariance Principles and Extended Gravity: Theory and Probes*. Physics Research and Technology. Nova Science Publishers, 2010. ISBN: 9781616685003.

[47] S. Capozziello and V. Faraoni. *Beyond Einstein Gravity: A Survey of Gravitational Theories for Cosmology and Astrophysics*. Fundamental Theories of Physics. Springer Netherlands, 2010. ISBN: 9789400701656.

[48] S. Capozziello, A. Stabile, and A. Troisi. "Newtonian limit of f(R) gravity." In: *Phys. Rev. D* 76.10, 104019 (Nov. 2007), p. 104019. DOI: 10.1103/PhysRevD.76.104019. arXiv: 0708.0723 [gr-qc].

[49] S. Capozziello and M. de Laurentis. "Extended Theories of Gravity." In: *Phys. Rep.* 509.4 (Dec. 2011), pp. 167–321. DOI: 10.1016/j.physrep.2011.09.003. arXiv: 1108.6266 [gr-qc].

[50] V. Cardoso and P. Pani. "Testing the nature of dark compact objects: a status report." In: *Living Rev. Rel.* 22.1 (2019), p. 4. DOI: 10.1007/s41114-019-0020-4. arXiv: 1904.05363 [gr-qc].

[51] V. Cardoso et al. "The Black hole bomb and superradiant instabilities." In: *Phys.Rev.* D70 (2004), p. 044039. DOI: 10.1103/PhysRevD.70.049903, 10.1103/PhysRevD.70.044039. arXiv: hep-th/0404096 [hep-th].

[52] B. Carter. "Axisymmetric Black Hole Has Only Two Degrees of Freedom." In: *Phys. Rev. Lett.* 26 (6 1971), pp. 331–333. DOI: 10.1103/PhysRevLett.26.331. URL: https://link.aps.org/doi/10.1103/PhysRevLett.26.331.

[53] P. Cerdá-Durán, V. Quilis, and J. A. Font. "AMR simulations of the low T/|W| bar-mode instability of neutron stars." In: *Computer Physics Communications* 177.3 (Aug. 2007), pp. 288–297. DOI: 10.1016/j.cpc.2007.04.001. arXiv: 0704.0356 [astro-ph].

[54] M. Chabanov, L. Rezzolla, and D. H. Rischke. "General-relativistic hydrodynamics of non-perfect fluids: 3+1 conservative formulation and application to viscous black hole accretion." In: *Mon. Not. R. Astron. Soc.* 505.4 (Aug. 2021), pp. 5910–5940. DOI: 10.1093/mnras/stab1384. arXiv: 2102.10419 [gr-qc].

[55] A. Chael, R. Narayan, and M. D. Johnson. "Two-temperature, Magnetically Arrested Disc simulations of the jet from the supermassive black hole in M87." In: *Mon. Not. R. Astron. Soc.* 486.2 (June 2019), pp. 2873–2895. DOI: 10.1093/mnras/stz988. arXiv: 1810.01983 [astro-ph.HE].

[56] C.-K. Chan et al. "The Power of Imaging: Constraining the Plasma Properties of GRMHD Simulations using EHT Observations of Sgr A*." In: *Astrophys. J.* 799.1, 1 (Jan. 2015), p. 1. DOI: 10.1088/0004-637X/799/1/1. arXiv: 1410.3492 [astro-ph.HE].

[57] S. Chandrasekhar. "The Stability of Non-Dissipative Couette Flow in Hydromagnetics." In: *Proceedings of the National Academy of Science* 46.2 (Feb. 1960), pp. 253–257. DOI: 10.1073/pnas.46.2.253.

[58] D. Christodoulou. "Reversible and Irreversible Transformations in Black-Hole Physics." In: *Physical Review Letters* 25 (Nov. 1970), pp. 1596–1597.

[59] P. T. Chruściel, J. L. Costa, and M. Heusler. "Stationary Black Holes: Uniqueness and Beyond." In: *Living Reviews in Relativity* 15.1, 7 (May 2012), p. 7. DOI: 10.12942/lrr-2012-7. arXiv: 1205.6112 [gr-qc].

[60] L. G. Collodel, D. D. Doneva, and S. S. Yazadjiev. "Rotating tensor-multiscalar black holes with two scalars." In: *Phys. Rev. D* 102.8 (2020), p. 084032. DOI: 10.1103/PhysRevD.102.084032. arXiv: 2007.14143 [gr-qc].

[61] A. Cruz-Osorio, S. Gimeno-Soler, and J. A. Font. "Non-linear evolutions of magnetized thick discs around black holes: dependence on the initial data." In: *Mon. Not. R. Astron. Soc.* 492.4 (Mar. 2020), pp. 5730–5742. DOI: 10.1093/mnras/staa216. arXiv: 2001.09669 [gr-qc].

[62] A. Cruz-Osorio et al. "Magnetized discs and photon rings around Yukawa-like black holes." In: *Phys. Rev. D* 103.12, 124009 (June 2021), p. 124009. DOI: 10.1103/PhysRevD.103.124009. arXiv: 2102.10150 [astro-ph.HE].

[63] P. V. P. Cunha et al. "Chaotic lensing around boson stars and Kerr black holes with scalar hair." In: *Phys. Rev. D* 94.10 (2016), p. 104023. DOI: 10.1103/PhysRevD.94.104023. arXiv: 1609.01340 [gr-qc].

[64] P. V. P. Cunha et al. "Shadows of Kerr Black Holes with Scalar Hair." In: *Physical Review Letters* 115.21, 211102 (Nov. 2015), p. 211102. DOI: 10.1103/PhysRevLett.115.211102. arXiv: 1509.00021 [gr-qc].

[65] P. V. P. Cunha, C. A. R. Herdeiro, and E. Radu. "EHT constraint on the ultralight scalar hair of the M87 supermassive black hole." In: *Universe* 5.12 (2019), p. 220. DOI: 10.3390/universe5120220. arXiv: 1909.08039 [gr-qc].

[66] P. V. P. Cunha, C. A. R. Herdeiro, and E. Radu. "Spontaneously Scalarized Kerr Black Holes in Extended Scalar-Tensor–Gauss-Bonnet Gravity." In: *Phys. Rev. Lett.* 123.1 (2019), p. 011101. DOI: 10.1103/PhysRevLett.123.011101. arXiv: 1904.09997 [gr-qc].

[67] F. Daigne and J. A. Font. "The runaway instability of thick discs around black holes - II. Non-constant angular momentum discs." In: *Mon. Not. R. Astron. Soc.* 349 (Apr. 2004), pp. 841–868. DOI: 10.1111/j.1365-2966.2004.07547.x. eprint: astro-ph/0311618.

[68] S. Dain and M. E. Gabach-Clement. "Geometrical inequalities bounding angular momentum and charges in General Relativity." In: *Living Reviews in Relativity* 21.1, 5 (July 2018), p. 5. DOI: 10.1007/s41114-018-0014-7. arXiv: 1710.04457 [gr-qc].

[69] M. De Laurentis, I. De Martino, and R. Lazkoz. "Analysis of the Yukawa gravitational potential in f (R) gravity. II. Relativistic periastron advance." In: *Phys. Rev. D* 97.10, 104068 (May 2018), p. 104068. DOI: 10.1103/PhysRevD.97.104068. arXiv: 1801.08136 [gr-qc].

[70] I. De Martino et al. "Constraining f(R) gravity with Planck data on galaxy cluster profiles." In: *Mon. Not. R. Astron. Soc.* 442.2 (Aug. 2014), pp. 921–928. DOI: 10.1093/mnras/stu903. arXiv: 1310.0693 [astro-ph.CO].

[71] I. De Martino, R. Lazkoz, and M. De Laurentis. "Analysis of the Yukawa gravitational potential in f (R) gravity. I. Semiclassical periastron advance." In: *Phys. Rev. D* 97.10, 104067 (May 2018), p. 104067. DOI: 10.1103/PhysRevD.97.104067. arXiv: 1801.08135 [gr-qc].

[72] J.-P. De Villiers and J. F. Hawley. "A Numerical Method for General Relativistic Magnetohydrodynamics." In: *Astrophys. J.* 589.1 (May 2003), pp. 458–480. DOI: 10.1086/373949. arXiv: astro-ph/0210518 [astro-ph].

[73] J.-P. De Villiers and J. F. Hawley. "Global General Relativistic Magnetohydrodynamic Simulations of Accretion Tori." In: *Astrophys. J.* 592.2 (Aug. 2003), pp. 1060–1077. DOI: 10.1086/375866. arXiv: astro-ph/0303241 [astro-ph].

[74] J.-P. De Villiers and J. F. Hawley. "Three-dimensional Hydrodynamic Simulations of Accretion Tori in Kerr Spacetimes." In: *Astrophys. J.* 577.2 (Oct. 2002), pp. 866–879. DOI: 10.1086/342238. arXiv: astro-ph/0204163 [astro-ph].

[75] J. C. Degollado, C. A. R. Herdeiro, and E. Radu. "Effective stability against superradiance of Kerr black holes with synchronised hair." In: *Physics Letters B* 781 (June 2018), pp. 651–655. DOI: 10.1016/j.physletb.2018.04.052. arXiv: 1802.07266 [gr-qc].

[76] J. F. M. Delgado, C. A. R. Herdeiro, and E. Radu. "Horizon geometry for Kerr black holes with synchronized hair." In: *Phys. Rev. D* 97, 124012 (June 2018), p. 124012. DOI: 10.1103/PhysRevD.97.124012.

[77] J. F. M. Delgado, C. A. R. Herdeiro, and E. Radu. "Kerr black holes with synchronised scalar hair and higher azimuthal harmonic index." In: *Phys. Lett. B* 792 (2019), pp. 436–444. DOI: 10.1016/j.physletb.2019.04.009. arXiv: 1903.01488 [gr-qc].

[78] J. F. M. Delgado, C. A. R. Herdeiro, and E. Radu. "Kerr black holes with synchronized axionic hair." In: *Phys. Rev. D* 103.10 (2021), p. 104029. DOI: 10.1103/PhysRevD.103.104029. arXiv: 2012.03952 [gr-qc].

[79] J. F. M. Delgado et al. "Kerr–Newman black holes with scalar hair." In: *Phys. Lett. B* 761 (2016), pp. 234–241. DOI: 10.1016/j.physletb.2016.08.032. arXiv: 1608.00631 [gr-qc].

[80] J. Dexter and P. C. Fragile. "Observational Signatures of Tilted Black Hole Accretion Disks from Simulations." In: *Astrophys. J.* 730, 36 (Mar. 2011), p. 36. arXiv: 1101.3783 [astro-ph.HE].

[81] J. Dexter, J. C. McKinney, and E. Agol. "The size of the jet launching region in M87." In: *Mon. Not. R. Astron. Soc.* 421.2 (Apr. 2012), pp. 1517–1528. DOI: 10.1111/j.1365-2966.2012.20409.x. arXiv: 1109.6011 [astro-ph.HE].

[82] F. Di Giovanni et al. "Dynamical bar-mode instability in spinning bosonic stars." In: *Phys. Rev. D* 102 (12 2020), p. 124009. DOI: 10.1103/PhysRevD.102.124009. URL: https://link.aps.org/doi/10.1103/PhysRevD.102.124009.

[83] F. Di Giovanni et al. "Dynamical formation and stability of fermion-boson stars." In: *Phys. Rev. D* 102.8, 084063 (Oct. 2020), p. 084063. DOI: 10.1103/PhysRevD.102.084063. arXiv: 2006.08583 [gr-qc].

[84] F. Di Giovanni et al. "Dynamical formation of Proca stars and quasi-stationary solitonic objects." In: *arXiv preprint arXiv:1803.04802* (2018).

[85] T. Do et al. "Relativistic redshift of the star S0-2 orbiting the Galactic Center supermassive black hole." In: *Science* 365.6454 (Aug. 2019), pp. 664–668. DOI: 10.1126/science.aav8137. arXiv: 1907.10731 [astro-ph.GA].

[86] W. Dyba, W. Kulczycki, and P. Mach. "Self-gravitating perfect-fluid tori around black holes: Bifurcations, ergoregions, and geometrical properties." In: *Phys. Rev. D* 101 (4 Feb. 2020), p. 044036. DOI: 10.1103/PhysRevD.101.044036. URL: https://link.aps.org/doi/10.1103/PhysRevD.101.044036.

[87] W. Dyba, P. Mach, and M. Pietrzynski. "Toroidal magnetic fields in self-gravitating disks around black holes." In: *arXiv e-prints*, arXiv:2105.02494 (May 2021), arXiv:2105.02494. arXiv: 2105.02494 [gr-qc].

[88] W. E. East and F. Pretorius. "Superradiant Instability and Backreaction of Massive Vector Fields around Kerr Black Holes." In: *Physical Review Letters* 119.4, 041101 (July 2017), p. 041101. DOI: 10.1103/PhysRevLett.119.041101. arXiv: 1704.04791 [gr-qc].

[89] W. E. East. "Superradiant instability of massive vector fields around spinning black holes in the relativistic regime." In: *Physical Review D* 96.2 (2017), p. 024004.

[90] W. E. East, F. M. Ramazanoğlu, and F. Pretorius. "Black hole superradiance in dynamical spacetime." In: *Physical Review D* 89.6 (2014), p. 061503.

[91] B. Einfeldt. "On Godunov-type methods for gas dynamics." In: *SIAM Journal on Numerical Analysis* 25.2 (1988), pp. 294–318.

[92] A. Einstein. "Die Feldgleichungen der Gravitation." In: *Sitzungsberichte der Königlich Preußischen Akademie der Wissenschaften (Berlin), Seite 844-847.* (1915).

[93] Event Horizon Telescope Collaboration et al. "First M87 Event Horizon Telescope Results. I. The Shadow of the Supermassive Black Hole." In: *Astrophys. J. Lett.* 875.1, L1 (Apr. 2019), p. L1. DOI: 10.3847/2041-8213/ab0ec7. arXiv: 1906.11238 [astro-ph.GA].

[94] Event Horizon Telescope Collaboration et al. "First M87 Event Horizon Telescope Results. IV. Imaging the Central Supermassive Black Hole." In: *Astrophys. J. Lett.* 875.1, L4 (Apr. 2019), p. L4. DOI: 10.3847/2041-8213/ab0e85. arXiv: 1906.11241 [astro-ph.GA].

[95] Event Horizon Telescope Collaboration et al. "First M87 Event Horizon Telescope Results. VI. The Shadow and Mass of the Central Black Hole." In: *Astrophys. J. Lett.* 875.1, L6 (Apr. 2019), p. L6. DOI: 10.3847/2041-8213/ab1141. arXiv: 1906.11243 [astro-ph.GA].

[96] J. A. Faber and F. A. Rasio. "Binary Neutron Star Mergers." In: *Living Reviews in Relativity* 15 (July 2012). arXiv: 1204.3858 [gr-qc].

[97] V. Fish et al. "Observing-and Imaging-Active Galactic Nuclei with the Event Horizon Telescope." In: *Galaxies* 4 (Oct. 2016), p. 54. DOI: 10.3390/galaxies4040054. arXiv: 1607.03034 [astro-ph.IM].

[98] L. G. Fishbone and V. Moncrief. "Relativistic fluid disks in orbit around Kerr black holes." In: *Astrophys. J.* 207 (Aug. 1976), pp. 962–976. DOI: 10.1086/154565.

[99] J. A. Font and F. Daigne. "The runaway instability of thick discs around black holes - I. The constant angular momentum case." In: *Mon. Not. R. Astron. Soc.* 334 (Aug. 2002), pp. 383–400. DOI: 10.1046/j.1365-8711.2002.05515.x. eprint: astro-ph/0203403.

[100] F. Foucart et al. "Evolution of accretion discs around a kerr black hole using extended magnetohydrodynamics." In: *Mon. Not. R. Astron. Soc.* 456.2 (Feb. 2016), pp. 1332–1345. DOI: 10.1093/mnras/stv2687. arXiv: 1511.04445 [astro-ph.HE].

[101] P. C. Fragile and A. Sądowski. "On the decay of strong magnetization in global disc simulations with toroidal fields." In: *Mon. Not. R. Astron. Soc.* 467 (May 2017), pp. 1838–1843. DOI: 10.1093/mnras/stx274. arXiv: 1701.01159 [astro-ph.HE].

[102] P. C. Fragile et al. "Global General Relativistic Magnetohydrodynamic Simulation of a Tilted Black Hole Accretion Disk." In: *Astrophys. J.* 668 (Oct. 2007), pp. 417–429. arXiv: 0706.4303.

[103] J. Frank, A. King, and D. J. Raine. *Accretion Power in Astrophysics: Third Edition.* 2002.

[104] F. F. Freitas et al. "Ultralight bosons for strong gravity applications from simple Standard Model extensions." In: *arXiv e-prints*, arXiv:2107.09493 (July 2021), arXiv:2107.09493. arXiv: 2107.09493 [hep-ph].

[105] C. F. Gammie, J. C. McKinney, and G. Tóth. "HARM: A Numerical Scheme for General Relativistic Magnetohydrodynamics." In: *Astrophys. J.* 589.1 (May 2003), pp. 444–457. DOI: 10.1086/374594. arXiv: astro-ph/0301509 [astro-ph].

[106] B. Ganchev and J. E. Santos. "Scalar Hairy Black Holes in Four Dimensions are Unstable." In: *Physical Review Letters* 120.17, 171101 (Apr. 2018), p. 171101. DOI: 10.1103/PhysRevLett.120.171101. arXiv: 1711.08464 [gr-qc].

[107] A. García, D. Galtsov, and O. Kechkin. "Class of Stationary Axisymmetric Solutions of the Einstein-Maxwell-Dilaton-Axion Field Equations." In: *Phys. Rev. Lett.* 74 (Feb. 1995), pp. 1276–1279. DOI: 10.1103/PhysRevLett.74.1276.

[108] R. Genzel, F. Eisenhauer, and S. Gillessen. "The Galactic Center massive black hole and nuclear star cluster." In: *Reviews of Modern Physics* 82.4 (Oct. 2010), pp. 3121–3195. DOI: 10.1103/RevModPhys.82.3121. arXiv: 1006.0064 [astro-ph.GA].

[109] J. Ghanbari, S. Abbassi, and M. Ghasemnezhad. "The role of thermal conduction in magnetized viscous-resistive advection-dominated accretion flows." In: *Monthly Notices of the Royal Astronomical Society* 400.1 (Nov. 2009), pp. 422–428. DOI: 10.1111/j.1365-2966.2009.15467.x. arXiv: 0908.0325 [astro-ph.HE].

[110] A. M. Ghez et al. "Measuring Distance and Properties of the Milky Way's Central Supermassive Black Hole with Stellar Orbits." In: *Astrophys. J.* 689.2 (Dec. 2008), pp. 1044–1062. DOI: 10.1086/592738. arXiv: 0808.2870 [astro-ph].

[111] S. Gimeno-Soler and J. A. Font. "Magnetised Polish doughnuts revisited." In: *Astron. Astrophys.* 607 (2017), A68. DOI: 10.1051/0004-6361/201730935. arXiv: 1707.03867 [gr-qc].

[112] S. Gimeno-Soler et al. "Magnetized accretion disks around Kerr black holes with scalar hair: Constant angular momentum disks." In: *Phys. Rev. D* 99.4, 043002 (Feb. 2019), p. 043002. DOI: 10.1103/PhysRevD.99.043002. arXiv: 1811.11492 [gr-qc].

[113] S. Gimeno-Soler et al. "Magnetized accretion disks around Kerr black holes with scalar hair: Nonconstant angular momentum disks." In: *Phys. Rev. D* 104.10, 103008 (Nov. 2021), p. 103008. DOI: 10.1103/PhysRevD.104.103008. arXiv: 2106.15425 [gr-qc].

[114] P. Goldreich, J. Goodman, and R. Narayan. "The stability of accretion tori. I - Long-wavelength modes of slender tori." In: *Mon. Not. R. Astron. Soc.* 221 (July 1986), pp. 339–364. DOI: 10.1093/mnras/221.2.339.

[115] S. E. Gralla. "Can the EHT M87 results be used to test general relativity?" In: *Phys. Rev. D* 103 (2 2021), p. 024023. DOI: 10.1103/PhysRevD.103.024023. URL: https://link.aps.org/doi/10.1103/PhysRevD.103.024023.

[116] Gravity Collaboration et al. "A geometric distance measurement to the Galactic center black hole with 0.3% uncertainty." In: *Astron. Astrophys.* 625, L10 (May 2019), p. L10. DOI: 10.1051/0004-6361/201935656. arXiv: 1904.05721 [astro-ph.GA].

[117] Gravity Collaboration et al. "Detection of orbital motions near the last stable circular orbit of the massive black hole SgrA*." In: *Astron. Astrophys.* 618, L10 (2018), p. L10. DOI: 10.1051/0004-6361/201834294. arXiv: 1810.12641 [astro-ph.GA].

[118] Gravity Collaboration et al. "Detection of the Schwarzschild precession in the orbit of the star S2 near the Galactic centre massive black hole." In: *Astron. Astrophys.* 636, L5 (Apr. 2020), p. L5. DOI: 10.1051/0004-6361/202037813. arXiv: 2004.07187 [astro-ph.GA].

[119] T. Harko and F. Lobo. *Extensions of f(R) Gravity: Curvature-Matter Couplings and Hybrid Metric-Palatini Theory*. Cambridge Monographs on Mathem. Cambridge University Press, 2018. ISBN: 9781108428743.

[120] A. Harten, P. D. Lax, and B. v. Leer. "On upstream differencing and Godunov-type schemes for hyperbolic conservation laws." In: *SIAM review* 25.1 (1983), pp. 35–61.

[121] J. F. Hawley. "Three-dimensional simulations of black hole tori." In: *Astrophys. J.* 381 (Nov. 1991), pp. 496–507.

[122] J. F. Hawley, X. Guan, and J. H. Krolik. "Assessing Quantitative Results in Accretion Simulations: From Local to Global." In: *Astrophys. J.* 738.1, 84 (Sept. 2011), p. 84. DOI: 10.1088/0004-637X/738/1/84. arXiv: 1103.5987 [astro-ph.HE].

[123] C. Herdeiro and E. Radu. "Construction and physical properties of Kerr black holes with scalar hair." In: *Classical and Quantum Gravity* 32.14, 144001 (July 2015), p. 144001. DOI: 10.1088/0264-9381/32/14/144001. arXiv: 1501.04319 [gr-qc].

[124] C. Herdeiro and E. Radu. "Ergosurfaces for Kerr black holes with scalar hair." In: *Phys. Rev. D* 89.12, 124018 (June 2014), p. 124018. DOI: 10.1103/PhysRevD.89.124018.

[125] C. Herdeiro, E. Radu, and H. Rúnarsson. "Kerr black holes with Proca hair." In: *Classical and Quantum Gravity* 33.15, 154001 (Aug. 2016), p. 154001. DOI: 10.1088/0264-9381/33/15/154001. arXiv: 1603.02687 [gr-qc].

[126] C. Herdeiro et al. "Gravitating solitons and black holes with synchronised hair in the four dimensional O(3) sigma-model." In: *JHEP* 02 (2019), p. 111. DOI: 10.1007/JHEP02(2019)111. arXiv: 1811.11799 [gr-qc].

[127] C. Herdeiro et al. "Skyrmions around Kerr black holes and spinning BHs with Skyrme hair." In: *JHEP* 10 (2018), p. 119. DOI: 10.1007/JHEP10(2018)119. arXiv: 1808.05388 [gr-qc].

[128] C. A. R. Herdeiro and E. Radu. "Asymptotically flat black holes with scalar hair: A review." In: *International Journal of Modern Physics D* 24, 1542014-219 (June 2015), pp. 1542014–219. DOI: 10.1142/S0218271815420146. arXiv: 1504.08209 [gr-qc].

[129] C. A. R. Herdeiro and E. Radu. "Dynamical Formation of Kerr Black Holes with Synchronized Hair: An Analytic Model." In: *Physical Review Letters* 119.26, 261101 (Dec. 2017), p. 261101. DOI: 10.1103/PhysRevLett.119.261101.

[130] C. A. R. Herdeiro and E. Radu. "How fast can a black hole rotate?" In: *International Journal of Modern Physics D* 24, 1544022 (Nov. 2015), p. 1544022. DOI: 10.1142/S0218271815440228. arXiv: 1505.04189 [gr-qc].

[131] C. A. R. Herdeiro and E. Radu. "Kerr Black Holes with Scalar Hair." In: *Physical Review Letters* 112.22, 221101 (June 2014), p. 221101. DOI: 10.1103/PhysRevLett.112.221101. arXiv: 1403.2757 [gr-qc].

[132] C. A. R. Herdeiro, E. Radu, and H. Rúnarsson. "Kerr black holes with self-interacting scalar hair: Hairier but not heavier." In: *Phys. Rev. D* 92.8, 084059 (Oct. 2015), p. 084059. DOI: 10.1103/PhysRevD.92.084059. arXiv: 1509.02923 [gr-qc].

[133] C. A. Herdeiro et al. "The imitation game: Proca stars that can mimic the Schwarzschild shadow." In: *Journal of Cosmology and Astroparticle Physics* 2021.04 (Apr. 2021), p. 051. DOI: 10.1088/1475-7516/2021/04/051. URL: https://doi.org/10.1088/1475-7516/2021/04/051.

[134] K. Hioki and K.-I. Maeda. "Measurement of the Kerr spin parameter by observation of a compact object's shadow." In: *Phys. Rev. D* 80.2, 024042 (July 2009), p. 024042. DOI: 10.1103/PhysRevD.80.024042. arXiv: 0904.3575 [astro-ph.HE].

[135] W. A. Hiscock and L. Lindblom. "Generic instabilities in first-order dissipative relativistic fluid theories." In: *Phys. Rev. D* 31 (4 Feb. 1985), pp. 725–733. DOI: 10.1103/PhysRevD.31.725. URL: https://link.aps.org/doi/10.1103/PhysRevD.31.725.

[136] X. Hou et al. "Black hole shadow of Sgr A* in dark matter halo." In: *Journal of Cosmology and Astroparticle Physics* 2018.7, 015 (July 2018), p. 015. DOI: 10.1088/1475-7516/2018/07/015. arXiv: 1804.08110 [gr-qc].

[137] *http://gravitation.web.ua.pt/node/416*.

[138] I. V. Igumenshchev, R. Narayan, and M. A. Abramowicz. "Three-dimensional Magnetohydrodynamic Simulations of Radiatively Inefficient Accretion Flows." In: *Astrophys. J.* 592.2 (Aug. 2003), pp. 1042–1059. DOI: 10.1086/375769. arXiv: astro-ph/0301402 [astro-ph].

[139] K. Ioka and M. Sasaki. "Grad-Shafranov equation in noncircular stationary axisymmetric spacetimes." In: *Phys. Rev. D* 67.12, 124026 (June 2003), p. 124026. DOI: 10.1103/PhysRevD.67.124026. arXiv: gr-qc/0302106 [gr-qc].

[140] W. Israel. "Nonstationary irreversible thermodynamics: A Causal relativistic theory." In: *Annals Phys.* 100 (1976), pp. 310–331. DOI: 10.1016/0003-4916(76)90064-6.

[141] W. Israel. "Event Horizons in Static Vacuum Space-Times." In: *Phys. Rev.* 164 (5 1967), pp. 1776–1779. DOI: 10.1103/PhysRev.164.1776. URL: https://link.aps.org/doi/10.1103/PhysRev.164.1776.

[142] A. Janiuk et al. "Numerical simulations of black hole accretion flows." In: *arXiv e-prints*, arXiv:1805.11305 (May 2018), arXiv:1805.11305. arXiv: 1805.11305 [astro-ph.HE].

[143] M. Jaroszynski, M. A. Abramowicz, and B. Paczynski. "Supercritical accretion disks around black holes." In: 30 (1980), pp. 1–34.

[144] T. Johannsen and D. Psaltis. "Testing the No-hair Theorem with Observations in the Electromagnetic Spectrum. II. Black Hole Images." In: *Astrophys. J.* 718.1 (July 2010), pp. 446–454. DOI: 10.1088/0004-637X/718/1/446. arXiv: 1005.1931 [astro-ph.HE].

[145] H. C. L. Junior et al. "Can different black holes cast the same shadow?" In: *Physical Review D* 103.8 (2021). ISSN: 2470-0029. DOI: 10.1103/physrevd.103.084040. URL: http://dx.doi.org/10.1103/PhysRevD.103.084040.

[146] J. Karkowski et al. "General-relativistic rotation: Self-gravitating fluid tori in motion around black holes." In: *Phys. Rev. D* 97.10, 104034 (May 2018), p. 104034. DOI: 10.1103/PhysRevD.97.104034. arXiv: 1712.05673 [gr-qc].

[147] J. Karkowski et al. "Rotating systems, universal features in dragging and antidragging effects, and bounds of angular momentum." In: *Phys. Rev. D* 94.12, 124041 (Dec. 2016), p. 124041. DOI: 10.1103/PhysRevD.94.124041. arXiv: 1609.06586 [gr-qc].

[148] J. Karkowski et al. "Self-gravitating axially symmetric disks in general-relativistic rotation." In: *Phys. Rev. D* 97.10, 104017 (May 2018), p. 104017. DOI: 10.1103/PhysRevD.97.104017. arXiv: 1802.02848 [gr-qc].

[149] R. P. Kerr. "Gravitational Field of a Spinning Mass as an Example of Algebraically Special Metrics." In: *Physical Review Letters* 11 (Sept. 1963), pp. 237–238.

[150] M. Khuri and N. Xie. "Inequalities Between Size, Mass, Angular Momentum, and Charge for Axisymmetric Bodies and the Formation of Trapped Surfaces." In: *Annales Henri Poincaré* 18.8 (Aug. 2017), pp. 2815–2830. DOI: 10.1007/s00023-017-0582-1. arXiv: 1610.04892 [gr-qc].

[151] K. Kiuchi et al. "Gravitational Waves from the Papaloizou-Pringle Instability in Black-Hole-Torus Systems." In: *Physical Review Letters* 106.25, 251102 (June 2011), p. 251102. arXiv: 1105.5035 [astro-ph.HE].

[152] P. Kocherlakota et al. "Constraints on black-hole charges with the 2017 EHT observations of M87*." In: *Phys. Rev. D* 103.10 (2021), p. 104047. DOI: 10.1103/PhysRevD.103.104047. arXiv: 2105.09343 [gr-qc].

[153] S. Koide, K. Shibata, and T. Kudoh. "Relativistic Jet Formation from Black Hole Magnetized Accretion Disks: Method, Tests, and Applications of a General RelativisticMagnetohydrodynamic Numerical Code." In: *Astrophys. J.* 522.2 (Sept. 1999), pp. 727–752. DOI: 10.1086/307667.

[154] H. Komatsu, Y. Eriguchi, and I. Hachisu. "Rapidly rotating general relativistic stars. I - Numerical method and its application to uniformly rotating polytropes." In: *Mon. Not. R. Astron. Soc.* 237 (Mar. 1989), pp. 355–379. DOI: 10.1093/mnras/237.2.355.

[155] H. Komatsu, Y. Eriguchi, and I. Hachisu. "Rapidly rotating general relativistic stars. II - Differentially rotating polytropes." In: *Mon. Not. R. Astron. Soc.* 239 (July 1989), pp. 153–171. DOI: 10.1093/mnras/239.1.153.

[156] S. S. Komissarov. "Magnetized tori around Kerr black holes: analytic solutions with a toroidal magnetic field." In: *Mon. Not. R. Astron. Soc.* 368 (May 2006), pp. 993–1000. DOI: 10.1111/j.1365-2966.2006.10183.x. eprint: astro-ph/0601678.

[157] R. Konoplya, L. Rezzolla, and A. Zhidenko. "General parametrization of axisymmetric black holes in metric theories of gravity." In: *Phys. Rev. D* 93.6, 064015 (Mar. 2016), p. 064015. DOI: 10.1103/PhysRevD.93.064015. arXiv: 1602.02378 [gr-qc].

[158] O. Korobkin et al. "Stability of general-relativistic accretion disks." In: *Phys. Rev. D* 83.4, 043007 (Feb. 2011), p. 043007. arXiv: 1011.3010 [astro-ph.HE].

[159] O. Korobkin et al. "The runaway instability in general relativistic accretion discs." In: *Mon. Not. R. Astron. Soc.* 431 (May 2013), pp. 349–354. arXiv: 1210.1214 [astro-ph.HE].

[160] M. Kozlowski, M. Jaroszynski, and M. A. Abramowicz. "The analytic theory of fluid disks orbiting the Kerr black hole." In: *Astron. Astrophys.* 63 (Feb. 1978), pp. 209–220.

[161] W. Krivan and R. H. Price. "Initial data for superposed rotating black holes." In: *Phys. Rev. D* 58.10, 104003 (Nov. 1998), p. 104003. DOI: 10.1103/PhysRevD.58.104003. arXiv: gr-qc/9806017 [gr-qc].

[162] W. Kulczycki. *private communication.*

[163] W. Kulczycki, P. Mach, and E. Malec. "Stationary massive disks around black holes: Realistic equation of state and bifurcation." In: *Phys. Rev. D* 104.2, 024005 (July 2021), p. 024005. DOI: 10.1103/PhysRevD.104.024005. arXiv: 2103.15701 [gr-qc].

[164] W. Kulczycki, P. Mach, and E. Malec. "Two mass conjectures on axially symmetric black hole-disk systems." In: *Phys. Rev. D* 99.2, 024004 (Jan. 2019), p. 024004. DOI: 10.1103/PhysRevD.99.024004. arXiv: 1810.12134 [gr-qc].

[165] J. Kunz, I. Perapechka, and Y. Shnir. "Kerr black holes with parity-odd scalar hair." In: *Phys. Rev. D* 100.6 (2019), p. 064032. DOI: 10.1103/PhysRevD.100.064032. arXiv: 1904.07630 [gr-qc].

[166] H. Labranche, D. Petroff, and M. Ansorg. "The parametric transition of strange matter rings to a black hole." In: *General Relativity and Gravitation* 39.2 (Feb. 2007), pp. 129–143. DOI: 10.1007/s10714-006-0377-z. arXiv: gr-qc/0603059 [gr-qc].

[167] S. Lahiri. "Second order causal hydrodynamics in Eckart frame: using gradient expansion scheme." In: *Classical and Quantum Gravity* 37.7 (2020), p. 075010. ISSN: 1361-6382. DOI: 10.1088/1361-6382/ab712f. URL: http://dx.doi.org/10.1088/1361-6382/ab712f.

[168] S. Lahiri and C. Lämmerzahl. *A toy model of viscous relativistic geometrically thick disk in Schwarzschild geometry.* 2019. arXiv: 1909.10381 [gr-qc].

[169] S. Lahiri et al. "Stationary models of magnetized viscous tori around a Schwarzschild black hole." In: *Phys. Rev. D* 103.4, 044034 (Feb. 2021), p. 044034. DOI: 10.1103/PhysRevD.103.044034. arXiv: 2012.06835 [gr-qc].

[170] L. Landau and E. Lifshitz. *The Classical Theory of Fields.* Elsevier Science, 2013. ISBN: 9781483293288.

[171] N. Lin et al. "A parametrization to test black hole candidates with the spectrum of thin disks." In: *European Physical Journal C* 75, 599 (Dec. 2015), p. 599. DOI: 10.1140/epjc/s10052-015-3837-3. arXiv: 1512.00724 [gr-qc].

[172] F. Löffler et al. "The Einstein Toolkit: a community computational infrastructure for relativistic astrophysics." In: *Classical and Quantum Gravity* 29.11, 115001 (June 2012), p. 115001. arXiv: 1111.3344 [gr-qc].

[173] R. Lohner. "An adaptive finite element scheme for transient problems in CFD." In: *Computer Methods in Applied Mechanics and Engineering* 61.3 (Apr. 1987), pp. 323–338. DOI: 10.1016/0045-7825(87)90098-3.

[174] P. Mach and E. Malec. "General-relativistic rotation laws in rotating fluid bodies." In: *Phys. Rev. D* 91.12, 124053 (June 2015), p. 124053. DOI: 10.1103/PhysRevD.91.124053. arXiv: 1501.04539 [gr-qc].

[175] P. Mach et al. "Self-gravitating magnetized tori around black holes in general relativity." In: *Phys. Rev. D* 99.10, 104063 (May 2019), p. 104063. DOI: 10.1103/PhysRevD.99.104063.

[176] T. Matsumoto, T. Miyoshi, and S. Takasao. "A New HLLD Riemann Solver with Boris Correction for Reducing Alfvén Speed." In: *Astrophys. J.* 874.1, 37 (Mar. 2019), p. 37. DOI: 10.3847/1538-4357/ab05cb. arXiv: 1902.02810 [physics.comp-ph].

[177] J. C. McKinney and R. D. Blandford. "Stability of relativistic jets from rotating, accreting black holes via fully three-dimensional magnetohydrodynamic simulations." In: *Mon. Not. R. Astron. Soc.* 394.1 (Mar. 2009), pp. L126–L130. DOI: 10.1111/j.1745-3933.2009.00625.x. arXiv: 0812.1060 [astro-ph].

[178] J. C. McKinney, A. Tchekhovskoy, and R. D. Blandford. "General relativistic magnetohydrodynamic simulations of magnetically choked accretion flows around black holes." In: *Mon. Not. R. Astron. Soc.* 423.4 (July 2012), pp. 3083–3117. DOI: 10.1111/j.1365-2966.2012.21074.x. arXiv: 1201.4163 [astro-ph.HE].

[179] J. C. McKinney et al. "Three-dimensional general relativistic radiation magnetohydrodynamical simulation of super-Eddington accretion, using a new code HARMRAD with M1 closure." In: *Monthly Notices of the Royal Astronomical Society* 441.4 (2014), pp. 3177–3208.

[180] S. Mendoza and S. Silva. "The matter Lagrangian of an ideal fluid." In: *arXiv e-prints*, arXiv:2011.04175 (Nov. 2020), arXiv:2011.04175. arXiv: 2011.04175 [gr-qc].

[181] V. Mewes et al. "Numerical relativity simulations of thick accretion disks around tilted Kerr black holes." In: *Phys. Rev. D* 93 (6 Mar. 2016), p. 064055.

[182] V. Mewes et al. "On the dynamics of tilted black hole-torus systems." In: *Mon. Not. R. Astron. Soc.* 461.3 (Sept. 2016), pp. 2480–2489. DOI: 10.1093/mnras/stw1490. arXiv: 1605.02629 [astro-ph.HE].

[183] A. Mignone, M. Ugliano, and G. Bodo. "A five-wave Harten-Lax-van Leer Riemann solver for relativistic magnetohydrodynamics." In: *Mon. Not. R. Astron. Soc.* 393.4 (Mar. 2009), pp. 1141–1156. DOI: 10.1111/j.1365-2966.2008.14221.x. arXiv: 0811.1483 [astro-ph].

[184] Y. Mizuno et al. "The current ability to test theories of gravity with black hole shadows." In: *Nature Astronomy* 2 (Apr. 2018), pp. 585–590. DOI: 10.1038/s41550-018-0449-5. arXiv: 1804.05812 [astro-ph.GA].

[185] A. Mizuta et al. "Production of intense episodic Alfvén pulses: GRMHD simulation of black hole accretion discs." In: *Mon. Not. R. Astron. Soc.* 479.2 (Sept. 2018), pp. 2534–2546. DOI: 10.1093/mnras/sty1453. arXiv: 1707.08799 [astro-ph.HE].

[186] P. J. Montero, J. A. Font, and M. Shibata. "Influence of Self-Gravity on the Runaway Instability of Black-Hole-Torus Systems." In: *Physical Review Letters* 104.19, 191101 (May 2010), p. 191101. arXiv: 1004.3102 [gr-qc].

[187] P. J. Montero et al. "Dynamics of magnetized relativistic tori oscillating around black holes." In: *Mon. Not. R. Astron. Soc.* 378 (July 2007), pp. 1101–1110. DOI: 10.1111/j.1365-2966.2007.11844.x. eprint: astro-ph/0702485.

[188] E. R. Most et al. "On accretion disks formed in MHD simulations of black hole-neutron star mergers with accurate microphysics." In: *arXiv e-prints*, arXiv:2106.06391 (June 2021), arXiv:2106.06391. arXiv: 2106.06391 [astro-ph.HE].

[189] I. Muller. "Zum Paradoxon der Warmeleitungstheorie." In: *Z. Phys.* 198 (1967), pp. 329–344. DOI: 10.1007/BF01326412.

[190] R. Narayan, I. V. Igumenshchev, and M. A. Abramowicz. "Magnetically Arrested Disk: an Energetically Efficient Accretion Flow." In: *Publications of the ASJ* 55 (Dec. 2003), pp. L69–L72. DOI: 10.1093/pasj/55.6.L69. eprint: astro-ph/0305029.

[191] R. Narayan and I. Yi. "Advection-dominated accretion: A self-similar solution." In: *Astrophys. J. Lett.* 428 (June 1994), pp. L13–L16. DOI: 10.1086/187381. eprint: arXiv:astro-ph/9403052.

[192] R. Narayan et al. "GRMHD simulations of magnetized advection-dominated accretion on a non-spinning black hole: role of outflows." In: *Mon. Not. R. Astron. Soc.* 426 (Nov. 2012), pp. 3241–3259. DOI: 10.1111/j.1365-2966.2012.22002.x. arXiv: 1206.1213 [astro-ph.HE].

[193] B. Narzilloev et al. "Charged particle motion around a quasi-Kerr compact object immersed in an external magnetic field." In: *Phys. Rev. D* 99.10, 104009 (May 2019), p. 104009. DOI: 10.1103/PhysRevD.99.104009. arXiv: 1902.03414 [gr-qc].

[194] B. Narzilloev et al. "Dynamics of charged particles and magnetic dipoles around magnetized quasi-Schwarzschild black holes." In: *European Physical Journal C* 81.3, 269 (Mar. 2021), p. 269. DOI: 10.1140/epjc/s10052-021-09074-z. arXiv: 2103.11090 [gr-qc].

[195] S. Nishida and Y. Eriguchi. "A General Relativistic Toroid around a Black Hole." In: *Astrophys. J.* 427 (May 1994), p. 429. DOI: 10.1086/174153.

[196] S. C. Noble et al. "Primitive Variable Solvers for Conservative General Relativistic Magnetohydrodynamics." In: *Astrophys. J.* 641.1 (Apr. 2006), pp. 626–637. DOI: 10.1086/500349. arXiv: astro-ph/0512420 [astro-ph].

[197] S. Nojiri, S. D. Odintsov, and V. K. Oikonomou. "Modified gravity theories on a nutshell: Inflation, bounce and late-time evolution." In: *Phys. Rep.* 692 (June 2017), pp. 1–104. DOI: 10.1016/j.physrep.2017.06.001. arXiv: 1705.11098 [gr-qc].

[198] H. Olivares et al. "How to tell an accreting boson star from a black hole." In: *Mon. Not. R. Astron. Soc.* 497.1 (July 2020), pp. 521–535. DOI: 10.1093/mnras/staa1878. arXiv: 1809.08682 [gr-qc].

[199] H. Olivares Sánchez, O. Porth, and Y. Mizuno. "The Black Hole Accretion Code: adaptive mesh refinement and constrained transport." In: *Journal of Physics Conference Series*. Vol. 1031. Journal of Physics Conference Series. May 2018, p. 012008. DOI: 10.1088/1742-6596/1031/1/012008. arXiv: 1802.00860 [gr-qc].

[200] B. Paczyński and P. J. Wiita. "Thick accretion disks and supercritical luminosities." In: *Astron. Astrophys.* 500 (Aug. 1980), pp. 203–211.

[201] J. C. B. Papaloizou and J. E. Pringle. "The dynamical stability of differentially rotating discs with constant specific angular momentum." In: *Mon. Not. R. Astron. Soc.* 208 (June 1984), pp. 721–750.

[202] V. Paschalidis. "General relativistic simulations of compact binary mergers as engines for short gamma-ray bursts." In: *Class. Quant. Grav.* 34.8 (2017), p. 084002. DOI: 10.1088/1361-6382/aa61ce. arXiv: 1611.01519 [astro-ph.HE].

[203] R. F. Penna, A. Kulkarni, and R. Narayan. "A new equilibrium torus solution and GRMHD initial conditions." In: *Astron. Astrophys.* 559, A116 (Nov. 2013), A116. DOI: 10.1051/0004-6361/201219666. arXiv: 1309.3680 [astro-ph.HE].

[204] D. Pérez, G. E. Romero, and S. E. Perez Bergliaffa. "Accretion disks around black holes in modified strong gravity." In: *Astron. Astrophys.* 551, A4 (Mar. 2013), A4. DOI: 10.1051/0004-6361/201220378. arXiv: 1212.2640 [astro-ph.CO].

[205] O. M. Pimentel, F. D. Lora-Clavijo, and G. A. González. "Numerical General Relativistic MHD with Magnetically Polarized Matter." In: *Astrophys. J.* 861.2, 115 (July 2018), p. 115. DOI: 10.3847/1538-4357/aac6d0. arXiv: 1806.02266 [astro-ph.HE].

[206] O. M. Pimentel, F. D. Lora-Clavijo, and G. A. Gonzalez. "Analytic solution of a magnetized tori with magnetic polarization around Kerr black holes." In: *Astron. Astrophys.* 619, A57 (Nov. 2018), A57. DOI: 10.1051/0004-6361/201833736. arXiv: 1808.07400 [astro-ph.HE].

[207] O. Porth et al. "The black hole accretion code." In: *Computational Astrophysics and Cosmology* 4.1, 1 (May 2017), p. 1. DOI: 10.1186/s40668-017-0020-2. arXiv: 1611.09720 [gr-qc].

[208] O. Porth et al. "The Event Horizon General Relativistic Magnetohydrodynamic Code Comparison Project." In: *arXiv e-prints*, arXiv:1904.04923 (Apr. 2019), arXiv:1904.04923. arXiv: 1904.04923 [astro-ph.HE].

[209] D. Psaltis et al. "Gravitational Test Beyond the First Post-Newtonian Order with the Shadow of the M87 Black Hole." In: *Phys. Rev. Lett.* 125.14 (2020), p. 141104. DOI: 10.1103/PhysRevLett.125.141104. arXiv: 2010.01055 [gr-qc].

[210] L. Qian et al. "The Polish doughnuts revisited. I. The angular momentum distribution and equipressure surfaces." In: *Astron. Astrophys.* 498 (May 2009), pp. 471–477. DOI: 10.1051/0004-6361/200811518. arXiv: 0812.2467.

[211] F. M. Ramazanoglu and F. Pretorius. "Spontaneous scalarization with massive fields." In: *Phys. Rev. D* 93, 064005 (Mar. 2016), p. 064005. DOI: 10.1103/PhysRevD.93.064005.

[212] M. J. Rees. "Black Hole Models for Active Galactic Nuclei." In: *Annu. Rev. Astron. Astrophys.* 22 (Jan. 1984), pp. 471–506. DOI: 10.1146/annurev.aa.22.090184.002351.

[213] L. Rezzolla, O. Zanotti, and J. A. Font. "Dynamics of thick discs around Schwarzschild-de Sitter black holes." In: *Astron. Astrophys.* 412 (Dec. 2003), pp. 603–613. eprint: gr-qc/0310045.

[214] L. Rezzolla and O. Zanotti. *Relativistic Hydrodynamics*. 2013.

[215] L. Rezzolla et al. "Accurate evolutions of unequal-mass neutron-star binaries: properties of the torus and short GRB engines." In: *Classical and Quantum Gravity* 27, 114105 (June 2010), p. 114105. DOI: 10.1088/0264-9381/27/11/114105. arXiv: 1001.3074 [gr-qc].

[216] P. Romatschke. "New developments in relativistic viscous hydrodynamics." In: *International Journal of Modern Physics E* 19.01 (2010), 1–53. ISSN: 1793-6608. DOI: 10.1142/s0218301310014613. URL: http://dx.doi.org/10.1142/S0218301310014613.

[217] N. Sanchis-Gual et al. "Explosion and Final State of an Unstable Reissner-Nordström Black Hole." In: *Physical Review Letters* 116.14, 141101 (Apr. 2016), p. 141101. DOI: 10.1103/PhysRevLett.116.141101. arXiv: 1512.05358 [gr-qc].

[218] N. Sanchis-Gual et al. "Nonlinear Dynamics of Spinning Bosonic Stars: Formation and Stability." In: *Phys. Rev. Lett.* 123 (22 2019), p. 221101. DOI: 10.1103/PhysRevLett.123.221101. URL: https://link.aps.org/doi/10.1103/PhysRevLett.123.221101.

[219] N. Sanchis-Gual et al. "Synchronized gravitational atoms from mergers of bosonic stars." In: *Phys. Rev. D* 102.10, 101504 (Nov. 2020), p. 101504. DOI: 10.1103/PhysRevD.102.101504. arXiv: 2007.11584 [gr-qc].

[220] N. M. Santos et al. "Black holes with synchronised Proca hair: linear clouds and fundamental non-linear solutions." In: *JHEP* 07 (2020), p. 010. DOI: 10.1007/JHEP07(2020)010. arXiv: 2004.09536 [gr-qc].

[221] A. Sądowski et al. "Semi-implicit scheme for treating radiation under M1 closure in general relativistic conservative fluid dynamics codes." In: *Mon. Not. R. Astron. Soc.* 429 (Mar. 2013), pp. 3533–3550. DOI: 10.1093/mnras/sts632. arXiv: 1212.5050 [astro-ph.HE].

[222] Y. Sekiguchi and M. Shibata. "Formation of Black Hole and Accretion Disk in a Massive High-entropy Stellar Core Collapse." In: *Astrophys. J.* 737, 6 (Aug. 2011), p. 6. DOI: 10.1088/0004-637X/737/1/6. arXiv: 1009.5303 [astro-ph.HE].

[223] N. I. Shakura and R. A. Sunyaev. "Reprint of 1973A&A....24..337S. Black holes in binary systems. Observational appearance." In: *Astron. Astrophys.* 500 (June 1973), pp. 33–51.

[224] M. Shibata and Y. Sekiguchi. "Radiation Magnetohydrodynamics for Black Hole-Torus System in Full General Relativity: A Step toward Physical Simulation." In: *Progress of Theoretical Physics* 127 (Mar. 2012), pp. 535–559. arXiv: 1206.5911 [astro-ph.HE].

[225] M. Shibata and K. Taniguchi. "Coalescence of Black Hole-Neutron Star Binaries." In: *Living Reviews in Relativity* 14, 6 (Dec. 2011), p. 6. DOI: 10.12942/lrr-2011-6.

[226] M. Shibata and K. Taniguchi. "Coalescence of Black Hole-Neutron Star Binaries." In: *Living Reviews in Relativity* 14 (Aug. 2011).

[227] M. Shibata. "Rotating black hole surrounded by self-gravitating torus in the puncture framework." In: *Phys. Rev. D* 76.6, 064035 (Sept. 2007), p. 064035. DOI: 10.1103/PhysRevD.76.064035.

[228] M. Shibata and M. Sasaki. "Innermost stable circular orbits around relativistic rotating stars." In: *Phys. Rev. D* 58.10, 104011 (Nov. 1998), p. 104011. DOI: 10.1103/PhysRevD.58.104011. arXiv: gr-qc/9807046 [gr-qc].

[229] M. Shibata and S. L. Shapiro. "Collapse of a rotating supermassive star to a supermassive black hole: Fully relativistic simulations." In: *The Astrophysical Journal Letters* 572.1 (2002), p. L39.

[230] H. Shiokawa et al. "Global General Relativistic Magnetohydrodynamic Simulations of Black Hole Accretion Flows: A Convergence Study." In: *Astrophys. J.* 744.2, 187 (Jan. 2012), p. 187. DOI: 10.1088/0004-637X/744/2/187. arXiv: 1111.0396 [astro-ph.HE].

[231] C.-W. Shu and S. Osher. "Efficient Implementation of Essentially Non-oscillatory Shock-Capturing Schemes." In: *Journal of Computational Physics* 77 (Aug. 1988), pp. 439–471.

[232] D. M. Siegel and B. D. Metzger. "Three-Dimensional General-Relativistic Magnetohydrodynamic Simulations of Remnant Accretion Disks from Neutron Star Mergers: Outflows and r -Process Nucleosynthesis." In: *Phys. Rev. Lett.* 119.23, 231102 (Dec. 2017), p. 231102. DOI: 10.1103/PhysRevLett.119.231102. arXiv: 1705.05473 [astro-ph.HE].

[233] D. M. Siegel and B. D. Metzger. "Three-dimensional GRMHD Simulations of Neutrino-cooled Accretion Disks from Neutron Star Mergers." In: *Astrophys. J.* 858.1, 52 (May 2018), p. 52. DOI: 10.3847/1538-4357/aabaec. arXiv: 1711.00868 [astro-ph.HE].

[234] K. A. Sorathia, J. H. Krolik, and J. F. Hawley. "Magnetohydrodynamic Simulation of a Disk Subjected to Lense-Thirring Precession." In: *Astrophys. J.* 777.1, 21 (Nov. 2013), p. 21. DOI: 10.1088/0004-637X/777/1/21. arXiv: 1309.0290 [astro-ph.HE].

[235] T. P. Sotiriou and V. Faraoni. "f(R) theories of gravity." In: *Reviews of Modern Physics* 82 (Jan. 2010), pp. 451–497. DOI: 10.1103/RevModPhys.82.451. arXiv: 0805.1726 [gr-qc].

[236] A. A. Starobinsky. "Amplification of waves during reflection from a rotating black hole." In: *Zh. Eksp. Teor. Fiz.* 64 (1973), p. 48.

[237] N. Stergioulas. "Black hole spacetimes with self-gravitating, massive accretion tori." In: *Journal of Physics Conference Series*. Vol. 283. Feb. 2011, p. 012036. DOI: 10.1088/1742-6596/283/1/012036.

[238] N. Stergioulas. "An Improved Method for Constructing Models of Self-Gravitating Tori around Black Holes." In: *International Journal of Modern Physics D* 20.7 (Jan. 2011), pp. 1251–1263. DOI: 10.1142/S021827181101944X. arXiv: 1104.3685 [gr-qc].

[239] O. Straub et al. "Modelling the black hole silhouette in Sgr A* with ion tori." In: *Astron. Astrophys.* 543 (2012), A83. DOI: 10.1051/0004-6361/201219209. arXiv: 1203.2618 [astro-ph.GA].

[240] A. Tchekhovskoy, R. Narayan, and J. C. McKinney. "Efficient generation of jets from magnetically arrested accretion on a rapidly spinning black hole." In: *Mon. Not. R. Astron. Soc.* 418 (Nov. 2011), pp. L79–L83. DOI: 10.1111/j.1745-3933.2011.01147.x. arXiv: 1108.0412 [astro-ph.HE].

[241] The Event Horizon Collaboration. "First M87 Event Horizon Telescope Results. VIII. Magnetic Field Structure near The Event Horizon." In: *arXiv e-prints*, arXiv:2105.01173 (May 2021), arXiv:2105.01173. arXiv: 2105.01173 [astro-ph.HE].

[242] The LIGO Scientific Collaboration, the Virgo Collaboration, and R. Abbott. "Tests of General Relativity with Binary Black Holes from the second LIGO-Virgo Gravitational-Wave Transient Catalog." In: *Phys. Rev. D* 103 (12 June 2021), p. 122002. DOI: 10.1103/PhysRevD.103.122002. arXiv: 2010.14529 [gr-qc]. URL: https://link.aps.org/doi/10.1103/PhysRevD.103.122002.

[243] P. K. Townsend. "Black Holes." In: *arXiv e-prints*, gr-qc/9707012 (July 1997), gr–qc/9707012. arXiv: gr-qc/9707012 [gr-qc].

[244] F. H. Vincent et al. "A magnetized torus for modeling Sagittarius A* millimeter images and spectra." In: *Astron. Astrophys.* 574, A48 (Jan. 2015), A48. DOI: 10.1051/0004-6361/201424306. arXiv: 1406.0353 [astro-ph.GA].

[245] F. H. Vincent et al. "Astrophysical imaging of Kerr black holes with scalar hair." In: *Phys. Rev. D* 94.8, 084045 (Oct. 2016), p. 084045. DOI: 10.1103/PhysRevD.94.084045. arXiv: 1606.04246 [gr-qc].

[246] S. H. Völkel et al. "EHT tests of the strong-field regime of General Relativity." In: (Nov. 2020). arXiv: 2011.06812 [gr-qc].

[247] H. von Zeipel. "The radiative equilibrium of a rotating system of gaseous masses." In: *Mon. Not. R. Astron. Soc.* 84 (June 1924), pp. 665–683. DOI: 10.1093/mnras/84.9.665.

[248] Y.-Q. Wang, Y.-X. Liu, and S.-W. Wei. "Excited Kerr black holes with scalar hair." In: *Phys. Rev. D* 99.6 (2019), p. 064036. DOI: 10.1103/PhysRevD.99.064036. arXiv: 1811.08795 [gr-qc].

[249] M. Wielgus et al. "Local stability of strongly magnetized black hole tori." In: *Mon. Not. R. Astron. Soc.* 447 (Mar. 2015), pp. 3593–3601. DOI: 10.1093/mnras/stu2676. arXiv: 1412.4561 [astro-ph.HE].

[250] C. Will. *Theory and Experiment in Gravitational Physics*. Cambridge University Press, 2018. ISBN: 9781107117440. URL: https://books.google.com.mx/books?id=P8FtDwAAQBAJ.

[251] V. Witzany and P. Jefremov. "New closed analytical solutions for geometrically thick fluid tori around black holes. Numerical evolution and the onset of the magneto-rotational instability." In: *Astron. Astrophys.* 614, A75 (June 2018), A75. DOI: 10.1051/0004-6361/201732361. arXiv: 1711.09241 [astro-ph.HE].

[252] S. E. Woosley. "Gamma-ray bursts from stellar mass accretion disks around black holes." In: *Astrophys. J.* 405 (Mar. 1993), pp. 273–277.

[253] S. E. Woosley and J. S. Bloom. "The Supernova Gamma-Ray Burst Connection." In: *Annu. Rev. Astron. Astrophys.* 44.1 (Sept. 2006), pp. 507–556. DOI: 10.1146/annurev.astro.43.072103.150558. arXiv: astro-ph/0609142 [astro-ph].

[254] F. Yuan and R. Narayan. "Hot Accretion Flows Around Black Holes." In: *Annual Review of Astronomy and Astrophysics* 52 (Aug. 2014), pp. 529–588. DOI: 10.1146/annurev-astro-082812-141003. arXiv: 1401.0586 [astro-ph.HE].

[255] O. Zanotti and D. Pugliese. "Von Zeipel's theorem for a magnetized circular flow around a compact object." In: *General Relativity and Gravitation* 47, 44 (Apr. 2015), p. 44. DOI: 10.1007/s10714-015-1886-4. arXiv: 1412.6447 [gr-qc].

[256] O. Zanotti et al. "Dynamics of oscillating relativistic tori around Kerr black holes." In: *Mon. Not. R. Astron. Soc.* 356 (Feb. 2005), pp. 1371–1382. eprint: astro-ph/0411116.